SCUOLA DI DOTTORATO
UNIVERSITÀ DEGLI STUDI DI MILANO-BICOCCA

Dipartimento di / Department of

Fisica G. Occhialini

Dottorato di Ricerca in / PhD program Fisica e Astronomia Ciclo / Cycle XXXIII

Curriculum in Astrofisica

The astrophysics of black hole binaries in the era of gravitational wave astronomy

Cognome: Mangiagli Nome: Alberto

Matricola: 763573

Tutore / Tutor: Prof. Monica Colpi

Supervisor: Prof. Alberto Sesana

Coordinatore / Coordinator: Prof. Marta Calvi

ANNO ACCADEMICO / ACADEMIC YEAR
2019/2020

This page intentionally left blank.

To my parents for their invaluable support

Trevize said, "Listen to me again. Just outside the Galaxy are the Magellanic Clouds, where no human ship has ever penetrated. Beyond that are other small galaxies, and not very far away is the giant Andromeda Galaxy, larger than our own. Beyond that are galaxies by the billions".

- Foundation and Earth, *Isaac Asimov* -

Contents

List of Figures

List of Tables

List of Acronyms

S/N	Signal-to-Noise ratio
ΛCDM	Λ Cold Dark Matter
AGN	Active Galactic Nuclei
Athena	Advanced Telescope for High Energy Astrophysics
BH	Black Hole
BHB	Black Hole Binary
CE	Cosmic Explorer
CHE	Chemically Homogeneous Evolution
CMB	Cosmic Microwave Background
DECIGO	DECi-hertz Interferometer Gravitational-wave Observatory
DM	Dark Matter
EM	ElectroMagnetic
EMRI	Extreme Mass Ratio Inspiral
EOM	Equations Of Motion
EPTA	European Pulsar Timing Array
ESA	European Space Agency
ET	Einstein Telescope
GR	General Relativity
GRMHD	GR MagnetoHydroDynamics
GW	Gravitational Wave
GWB	GW Background
IMF	Initial Mass Function
IndIGO	Indian Initiative in Gravitational-wave Observations
ISCO	Innermost Stable Circular Orbit
JWST	James WebbSpace Telescop

KAGRA	Kamioka Gravitational Wave Detector
LDC	LISA Data Challenge
LIGO	Laser Interferometer Gravitational-Wave Observatory
LISA	Laser Interferometer Space Antenna
LSST	Large Synoptic Survey Telescope
MBH	Massive BH
MBHB	Massive Black Hole Binary
MCMC	Markov-Chain Monte Carlo
MOONS	Multi Object Optical and Near-infrared Spectrograph
NANOGrav	North American Nanohertz Observatory for Gravitational Waves
NASA	National Aeronautics and Space Administration
NS-NS	Neutron Star - Neutron Star
PE	Parameter Estimation
PHB	Primordial BH
PISN	Pair-Instability SNE
PN	Post-Newtonian
PPISN	Pulsation Pair-Instability SNe
PTA	Pulsar Timing Array
SAM	Semi-Analytical Model
SBHB	Stellar Black Hole Binary
SEVN	Stellar EVolution for N-body
SFR	Star Formation Rate
SKA	Square Kilometer Array
SN	SuperNova
SUA	Shifted Uniform Asymptotic
TAP	Transient Astrophysics Probe
VLT	Very Large Telescope
WFIRST	Wide Field Infrared Survey Telescop
ZAMS	Zero-Age Main Sequence

List of Publications

Most of the figures and results reported in this Thesis have already appeared on peer-reviewed journal. However the scope of this work is not to be a mere collection of results but to provide a consistent summary of the challenges and prospects that we will face in the future years in the field of GW astronomy. Up to date, my list of publications includes:

- Alberto Mangiagli, Antoine Klein, Matteo Bonetti, Michael L. Katz, Alberto Sesana, Marta Volonteri, Monica Colpi, Sylvain Marsat, Stanislav Babak. *Observing the inspiral of coalescing massive black hole binaries with LISA in the era of multimessenger astrophysics*. Physical Review D 102, 084056 doi: 10.1103/PhysRevD.102.084056

- Alberto Mangiagli, Matteo Bonetti, Alberto Sesana, Monica Colpi. *Merger rate of stellar black hole binaries above the pair instability mass gap*. The Astrophysical Journal Letter 883.1, L27. doi: 10.3847/2041-8213/ab3f33

- Tito Dal Canton, Alberto Mangiagli, Scott C. Noble, Jeremy Schnittman, Andrew Ptak, Antoine Klein, Alberto Sesana, Jordan Camp. *Detectability of modulated X-rays from LISA's supermassive black hole mergers*. The Astrophysical Journal 886, 146. doi: 10.3847/1538-4357/ab505a

- Alberto Mangiagli, Antoine Klein, Alberto Sesana, Enrico Barausse, Monica Colpi. *Post-Newtonian phase accuracy requirements for stellar black hole binaries with LISA*. Physical Review D 99, 064056. doi: 10.1103/PhysRevD.99.064056

I also contributed to the following works:

- Alberto Sesana, Natalia Korsakova *et al.*. *Unveiling the Gravitational Universe at μ-Hz Frequencies*. ArXiv: 1908.11391

- Monica Colpi *et al.*. *Athena-LISA Synergies*. Athena_LISA_Whitepaper_Iss1.0.pdf

- Vassiliki Kalogera *et al.*. *Deeper, Wider, Sharper: Next-Generation Ground-Based Gravitational-Wave Observations of Binary Black Holes*. arXiv:1903.09220

- Barack Leor *et al.*. *Black holes, gravitational waves and fundamental physics: a roadmap*. arXiv:1806.05195

Abstract

Black holes (BHs) are variegated and fascinating objects in Nature. Their realm extends from the stellar BHs with mass $\sim 10 - 10^2\,\mathrm{M}_\odot$ to the supermassive BHs of $10^{9-10}\,\mathrm{M}_\odot$ that reside in the center of galaxies. While the former are the expected outcome of stellar evolution, the latter are the results of multiple dark matter halo mergers in the standard ΛCDM scenario. When two BHs are close enough, they form a binary BHs (BHBs) and emit gravitational waves (GWs) that we can detect with our inteferometers.

Similarly to BHs, also BHBs can be divided into different sub-populations, each with its unique features and characteristics: stellar BHBs (SBHBs) form from the co-evolution of binary stars or in dense region, while massive BHBs (MBHBs) are the result of galaxy mergers.

The challenges of GW astronomy are still numerous and require different knowledge and expertise to be solved. For this reason, I start this Thesis presenting result for SBHBs in the initial chapters and moving to MBHBs in the end. Each chapter has its own brief introduction and discussion of the main results and conclusions.

In Chapter 1 I introduce some basic General Relativity (GR) concepts related to the emission of GWs. I summarise the current status of GW astronomy. I explain how GWs from BHBs can be easily modeled under some reasonable assumptions and report some formulas useful to understand the concepts of the following chapters.

In Chapter 2 I study the minimum Post-Newtonian (PN) order necessary to accurately track SBHBs in LISA and perform an unbiased parameter estimation. SBHBs are expected to spend a large number of cycles in band, therefore an accurate waveform is necessary to avoid biases in the binary parameters. I show that the main factor affecting the PN accuracy is the time to coalescence with systems closer to merger requiring higher PN contributions. I apply the previous result to a realistic population of SBHBs in LISA in order to draw more realistic estimates: I find that most of the sources can be modeled with just 2PN corrections while systems merging during LISA time mission require up to 2.5PN and 3PN contributions.

The topic of Chapter 3 is a model to describe SBHBs above the pair-instability

mass gap, i.e. BHs with mass $> 120\,M_\odot$. Under the assumption that the binary formation does not change beyond the mass gap, I estimate the detected rate for current detectors, ET and LISA. Finally I also suggest the possibility that the undetected sources form a new source of stochastic background in LISA.

In Chapter 4 I move to MBHBs, detectable only from space by LISA. I provide an introduction on MBHBs formation and evolution and the multimessenger possibilities. I also explain how we estimate source information with the so-called Fisher matrix formalism.

In Chapter 5 I present a work I contributed where we explore the possibility to detect a Doppler modulated X-ray emission during the inspiral of MBHBs. In the last stage of merger, X-ray emission is expected as the result of gas accretion on each BHs and the orbital motion of the binary might imprint a Doppler modulation on the electromagnetic (EM) emission in phase with the GW signal. The detection of this modulation would allow to pinpoint the exact source location in the relatively large error area provided by LISA. From our analysis, we estimate few modulation detections over the LISA time mission.

Finally in Chapter 6 I report the results for the parameter estimation of MBHBs *on the fly*, i.e. as function of time before coalescence. In particular I focus on sky position, luminosity distance, chirp mass and mass ratio and how their errors decrease as the system approaches merger. For the benefit of the community, I release also the complete set of data and analytical fits to describe the time evolution in the aforementioned parameters. Finally I discuss the multimessenger prospects.

Chapter 1

GWs from compact object binaries

In the history of Science, the first detection of gravitational waves, GW150914, [1–3] will have the same impact of the discover of Jupyter's Moons by Galileo Galilei in 1610.

When Galileo pointed his telescope at the sky, he did not probably realized the importance of his action and, especially, how far we would have come from that single blurry observation. After 400 years, we have explored the sky across its full electromagnetic spectrum, from γ-ray to radio, reaching a deep understanding of the laws that rule our Universe.

From 2015, GWs allow us to explore the Universe in an unmatched way, providing invaluable information on astrophysical and cosmological fields [4–7]. The first and second observing runs concluded with the detection of ten BHBs and one neutron star - neutron star (NS-NS) binary [4]. The NS-NS merger constitutes the first multimessenger event of a direct GW and EM detection and was covered by an extensive observational campaign [8–10].

Even if photons are easier to detect than GWs, the EM radiation interacts strongly with the matter between the source and our detectors, hampering the possibility to obtain information as the source distance increases. On the other side, Gravity is known to interact weakly therefore the detected signal is an accurate representation of what happened at the source and arrives unperturbed to our detectors.

As a consequence, with future detectors we will be able to detect BHB signals from when the Universe was less than 1 Gyr old. Moreover while the Cosmic Microwave Background (CMB) provide us information up to $\simeq 10^6$ yr from Big Bang, GWs allow us to push this time limit close to $\simeq 10^{-30}$ s after the Big Bang, exploring really the first wails of our Universe.

Since Einstein formulated GR theory, numerous experiments were performed to test its validity. All these experiments were performed in the so-called weak-field limit, where GR is employed to explain deviations for the Newtonian gravity

theory. The deflection of light observable during an eclipse, the precession of Mercury's orbit and the orbital period decay of the Hulse-Taylor pulsar [11] are just the most noticeable examples where GR successfully managed to explain the observation. However GWs allow us to test GR in its entirety, from the slow inspiral to the chaotic merger where the two BHs move at near half the speed of light and non-linear effects come to play.

Similarly to EM radiation, also for GWs we can talk of a 'gravitational spectrum' spanning frequencies from 10^{-9} Hz to 10^{4} Hz. Across this range, different detectors have been constructed or are planned to become operative in the coming years. Each detectors is targeted for particular type of sources in order to cover as better as possible this spectrum.

From 10 Hz up to the 10^{4} Hz, ground-based detectors as the twin LIGOs [12] and Virgo [13] are operative and reporting mergers from compact objects binaries regularly. More detectors are expected to join the LIGO/Virgo collaboration in the following years: the Japanese cryogenic interferometer KAGRA [14] is under commissioning, while the Indian inteferometer IndIGO [15] is under construction. These interferometers constitute an invaluable addition to the existing networks: observing the same signal with more detectors translate in a better parameter estimation (especially for the sky position of the source due to triangulation) and account also for possible hardware/software failures or maintenance in one or more detectors at the same time.

In the next years, Einstein Telescope (ET) [16] and Cosmic Explorer (CE) [17] are the third-generation interferometers planned to overcome the current detectors. These interferometers are expected to push the current sensitivity down of an order of magnitude and to be able to observe signals already at $3 - 5$ Hz.

However ground-based detectors are inevitably limited by seismic noise at low frequency. The solution currently adopted involves multiple inverted pendulums but, inevitably, we are limited at $\simeq 1$ Hz and the only solution is to move our interferometers into space.

Between 10^{-5} Hz and 1 Hz, LISA [18], selected by ESA as the third L3 mission in the Cosmic Vision Programme, is the planned space-based interferometer that will be able to detect a plethora of sources: SBHBs in their early inspiral, the merger of MBHBs and extreme mass ratio inspirals (EMRIs) are the most promising targets. Hopefully LISA will not be the only interferometer in space in the next years: Taiji [19] and TianQin [20] has been proposed by China in a similar frequency range while the Japanese DECIGO [21] should cover the gap between LISA and ground-based detector around 0.1 Hz.

To lower frequencies, $[10^{-9} - 10^{-7}]$ Hz pulsar timing array (PTA) experiments [22], as NANOGrav and EPTA, should detect in the next future the background from the coalescence of very MBHBs ($\simeq 10^{9} - 10^{10}\,\mathrm{M}_{\odot}$) looking at the time-of-

arrival of pulses from different pulsars [23].

In this chapter we present a brief overview of the theoretial aspects governing the emission of GWs from compact binaries and some notion of signal analysis. We defer to more detailed reviews and books [24–28] for further details.

The chapter is organized as follow: In Sec. 1.1 we review the basic concepts of the GW production and emission theory. In Sec. 1.2 we introduce the basic scaling relations of GW from compact binaries and some quantities useful to understand the results of following chapters. The discussion about the current and future status of GW detectors is deferred to Sec. 1.3.1 while in Sec. 1.3.2 we summarise the basic tools for detecting a GW signal.

1.1 Theoretical framework

GWs are space-time ripples propagating at the speed of light. A proper derivation from Einstein equations is beyond the scope of this Thesis: here we will focus for the major part on the physical aspects and observational properties of GWs, sketching the necessary theoretical steps.

Formally, the simplest approach to describe GWs requires expanding Einstein equations over a flat background metric and choosing a particular frame (the harmonic gauge) where the perturbation can be written as Green function [24].

Consider a flat metric $\eta_{\mu\nu} = \mathrm{diag}\{-1, 1, 1, 1\}$, the perturbation equations read[1]

$$\Box \bar{h}_{\mu\nu} = -\frac{16\pi G}{c^4} T_{\mu\nu} \tag{1.1}$$

where $\bar{h}_{\mu\nu} = h_{\mu\nu} - \frac{1}{2}\eta_{\mu\nu}h$, $\Box = \eta^{\mu\nu}\partial_\mu\partial_\nu$ is the d'Alambertian operator in flat-space time, $T_{\mu\nu}$ is the stress-energy tensor and $h_{\mu\nu}$ is the perturbation tensor. The harmonic gauge has the advantage of reducing the number of degrees of freedom of $h_{\mu\nu}$ from ten to six. A further reduction in the number of d.o.f. can be done, defining the 'traceless-transverse' gauge. In this way the perturbation tensor is fuction of only two polarizations, known as 'plus', h_+, and 'cross', $h_\times$.

GWs affects the proper distance between objects, i.e. objects get compressed and stretched when they interact with GWs. This effect can be seen on a ring of test particle. In Fig. 1.1 we show the effect of the propagation of a GW along the z-axis (out of the paper) on a test of ring particles in the (x, y) plane.

In electromagnetism no monopole radiation is admitted due to charge conservation. In GR mass and momentum conservation lead to the absence of monopole and dipole radiation. Therefore the first non-zero term in a multipoles expansion is the quadrupole one. This makes compact object binaries efficient emitters of GWs.

[1] In our convention, Greek indices take values $0, \ldots, 3$ while Latin letters denote spatial components, i.e. 1, 2, 3.

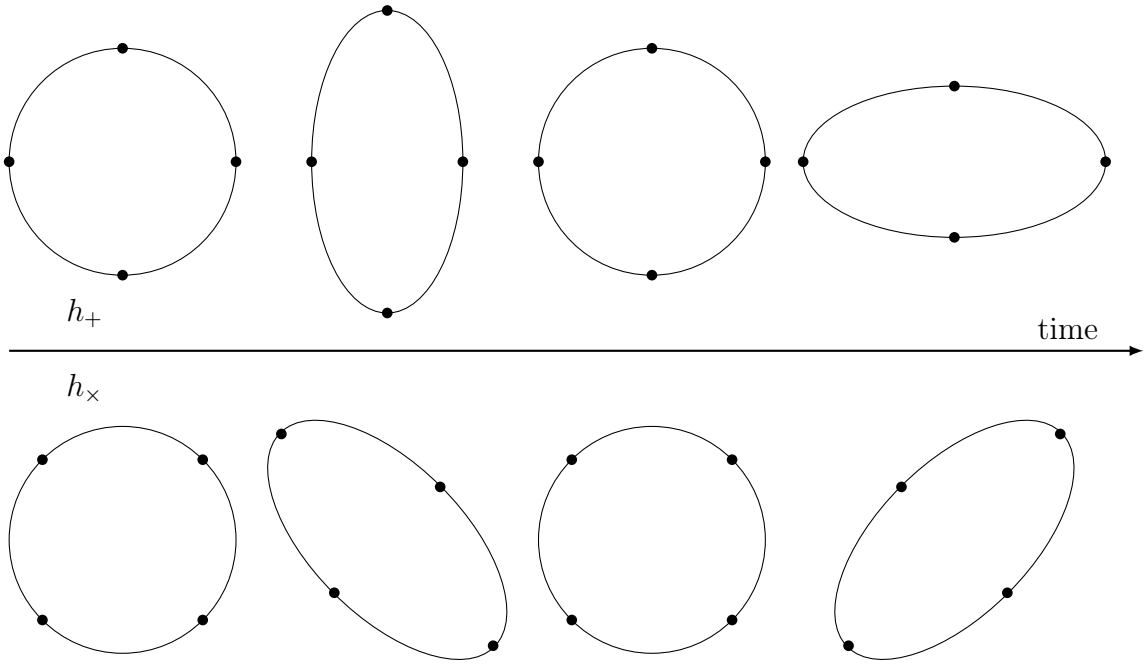

Figure 1.1: The effect of h_+ (upper panel) and $h_\times$ (lower panel) on a ring of test masses. The rings are shown at quarter of the period of the wave. Credits: N. Muttoni

[2] Since we are looking at a perturbation, we also need a time-varying quadrupole moment in order to generate GWs (a constant term would be reabsorbed with a redefinition of the potential energy). From Einstein equation, we can write

$$h_{ij}(t, \mathbf{x}) = \frac{1}{d}\frac{2G}{c^4}\ddot{Q}_{ij}(t - r/c) \tag{1.2}$$

where d is the distance of the source, $t_{\rm ret} \equiv t - r/c$ is the retarded time and $\ddot{Q}_{ij}$ is the second time derivative of the quadrupole moment of the source. We note that the term $G/c^4 \simeq 10^{-44}\mathrm{s}^2/(\mathrm{kg\,m})$ leads to incredibly weak GWs: for a binary systems in circular orbit with component masses m_1 and m_2 and separation a, $\ddot{Q}_{ij} \propto m_1 m_2 G/a$ so we need masses of $\simeq 10^4\,\mathrm{M}_\odot$ at a separation of 1 m to cancel out the G/c^4 term.

The strain h induces a deformation on an object of length L of the order

$$\Delta L \simeq hL \tag{1.3}$$

[2] In principle supernovae explosions are not expected to be spherically symmetric so they should emit GWs already at quadrupole moment however the overall strain would be small due to small departures from spherical symmetry.

where ΔL is the objects deformation. For typical astrophysical sources $h \simeq 10^{-21}$ so, if you consider the Earth radius ($L \simeq 6 \times 10^6$ m), the variation induced by the passage of GW is $\Delta L \simeq 10^{-14}$ m, slightly bigger than an atomic nucleus. Such a small length require accurate instruments for detection, representing the major challenge in GW astronomy for over 50 years.

1.2 Compact object binaries

Compact object binaries are perfect emitters of GW: their quadrupole term is non-zero and objects in binaries are accelerating (the second time derivative is also non-zero). We will discuss the different types of double compact objects in Chapter 3, while we limit here to generic considerations.

Their compactness, defined for a self-gravitating object as $\mathcal{C} \equiv GM_b/R_bc^2$ with M_b and R_b the mass and the radius of the body respectively, prevents the disruption of the two objects when they are too close to each other[3]. Indeed at merger compact object binaries are among the most luminous sources in the Universe, reaching a luminosity of $10^{56}\,\mathrm{erg\,s^{-1}}$.

The signal from a precessing compact object binary in quasi-circular orbit is described by 15 parameters: the two intrinsic components masses, m_1 and m_2, the colatitude $\cos\theta_N$ and longitude ϕ_N of the binary sky position[4] , the distance d, the two time-varying angles describing the orientation of the binary orbital angular momentum, θ_L and ϕ_L, the time to coalescence t_c, the initial phase ϕ_0, the magnitude of the two spins χ_1 and χ_2 and 4 angles describing their orientation relative to the binary plane.

Moreover we can define the total mass of the system $\mathrm{M_{tot}} = m_1 + m_2$ and the binary mass ratio $q = m_1/m_2$. Combining these two expressions, we introduce a more useful mass definition in GW astrophysics, the *chirp mass* $\mathcal{M}$ as

$$\mathcal{M} = \frac{(m_1 m_2)^{3/5}}{(m_1 + m_2)^{1/5}} = \nu^{3/5}\,\mathrm{M_{tot}} = \mu^{3/5}\,{\mathrm{M_{tot}}}^{2/5} \tag{1.4}$$

where $\nu = m_1 m_2/\,{\mathrm{M_{tot}}}^2$ is the symmetric mass ratio and $\mu = m_1 m_2/\,\mathrm{M_{tot}}$ is the reduced mass.

From Keplerian theory, the binary is orbiting with a frequency

$$\omega_s = \sqrt{\frac{G\,\mathrm{M_{tot}}}{R^3}} \tag{1.5}$$

[3]Note that NS can be tidally disrupted by BH if the BH is relatively light and rapidly rotating.
[4]If not stated otherwise, we refer to ecliptic coordinate.

where R is the orbital radius. At quadrupole approximation, we can write the two polarizations state as

$$\begin{aligned} h_+(t) &= \frac{4}{d}\left(\frac{G\mathcal{M}}{c^2}\right)^{5/3}\left(\frac{\pi f_{\rm gw}}{c}\right)^{2/3}\left(\frac{1+\cos^2\iota}{2}\right)\cos[2\omega_s t_{\rm ret}+\phi] \\ h_\times(t) &= \frac{4}{d}\left(\frac{G\mathcal{M}}{c^2}\right)^{5/3}\left(\frac{\pi f_{\rm gw}}{c}\right)^{2/3}\cos\iota\sin[2\omega_s t_{\rm ret}+\phi] \end{aligned} \tag{1.6}$$

where $f_{\rm gw} = \omega_s/\pi$ is the GW frequency and ι in the inclination angle between the line-of-sight and the normal to the orbital plane. Several considerations follow straightforwardly:

- The binary emits GW at twice the orbital frequency, i.e $\omega_{gw} = 2\omega_s$ due to the fact that the same mass configuration appears twice in the same orbital period.
- The two polarizations present different inclination contributions because binaries emit GWs preferentially in the direction of the angular momentum rather than on the orbital plane.
- At lowest quadrupole moment, $h \simeq \mathcal{M}^{5/3}$: we will see in Chapter 6 the consequences in term of parameter estimation.
- The strain decreases as the inverse of the distance of the source [5].

It is also useful to look at some hands-on formulas. From the balance equation between the energy carried by GWs and the loss of total energy of the binary, we can derive the relation between the time to coalescence τ and $f_{\rm gw}$ as [6]

$$\tau = \frac{5}{256}\frac{1}{(\pi f_{\rm gw})^{8/3}}\left(\frac{G\mathcal{M}}{c^3}\right)^{-5/3}. \tag{1.7}$$

At the same $f_{\rm gw}$, more massive systems are closer to coalescence. This can be explained thinking that, at first order approximation, the merger occurs when the BH horizons touch and the larger the mass of the BH is, the larger is its horizon.

From Eq. (1.7), we can also have an order of magnitude estimate of the amount of time that systems stay in band. For an equal mass binary with $m_1 = 30\,{\rm M}_\odot$, we observe the GW signal coming from the last few seconds before the merger when

[5] Our detectors are sensitive to the strain h rather than to the energy carried by GWs which decrease as $\simeq d^{-2}$.

[6] A similar expression can be derived also for eccentric binaries. In this case the coalescence time is shorten by a factor $(1-e_0^2)^{7/2}$ being e_0 the initial eccentricity because at the pericenter the objects will experience a strong acceleration and emit a burst of GWs.

it enters the band of current ground-based detectors at $f_{\rm gw} = 10\,{\rm Hz}$. If we move to LISA band, at $f_{\rm gw} = 5 \times 10^{-2}\,{\rm Hz}$, the same system is observed at $\tau = 0.26\,{\rm yr}$ from merger.
More massive systems with $m_1 = m_2 = 10^6\,{\rm M}_\odot$ can be observed one month before merger at $f_{\rm gw} = 10^{-4}\,{\rm Hz}$. We will see how this allow to perform parameter estimation for this type of sources during the inspiral, with important consequences for the search of possible EM counterparts.

Similarly we can also compute the number of cycles during the inspiral as

$$\mathrm{N_{cyc}} = \frac{1}{32\pi^{8/3}} \left(\frac{G\mathcal{M}}{c^3}\right)^{-5/3} \left(f_{\rm min}^{-5/3} - f_{\rm max}^{-5/3}\right) \tag{1.8}$$

From Eq. (1.8), we see that a system with $m_1 = m_2 = 30\,{\rm M}_\odot$ at $f_{\rm gw} = 5 \times 10^{-2}\,{\rm Hz}$ performs $\mathrm{N_{cyc}} \simeq 6 \times 10^5$ cycles in LISA band before exiting. In Chapter 2 we will see how the number of cycles poses serious requirement on the necessary waveform accuracy to track SBHB signals in LISA.

The expression and results presented so far are valid in the *low-velocity* limit, i.e. for non relativistic sources. In this regime, the GW wavelength is much larger than the typical size of the system, $\lambda_{\rm gw} \gg R$. This is indeed the case for systems far from coalescence (in the so-called *inspiral* phase): from Eq. (1.5), a binary with $m_1 = m_2 = 30\,{\rm M}_\odot$ emitting at $f_{\rm gw} = 10^{-2}\,{\rm Hz}$ ($\lambda_{\rm gw} = 10^{10}\,{\rm m}$), has a typical size of the order $R \simeq 10^8\,{\rm m}$.

From GR theory, there is minimum value of the radial separation between a test particle and a BH beyond which no stable orbits are allowed. This is referred as Innermost Stable Circular Orbit (ISCO). For a non-spinning BH we can write

$$r_{\rm ISCO} = \frac{6GM_{\rm BH}}{c^2}. \tag{1.9}$$

Clearly a long phase of stationary and semi-circular orbit can take place only at $r > r_{\rm ISCO}$. Therefore it is customarily assumed that the inspiral phase end at the corresponding frequency, $f_{\rm ISCO}$, defined as

$$f_{\rm ISCO} = \frac{1}{6^{3/2}2\pi} \frac{c^3}{G\,\mathrm{M_{tot}}}. \tag{1.10}$$

Plugging into Eq. (1.10) some values we obtain that for an equal mass binary with $m_1 = 30\,{\rm M}_\odot$ the $f_{\rm ISCO} \simeq 30\,{\rm Hz}$ that corresponds roughly to the frequency where current interferometers are most sensitive. Similarly for a binary with $\mathrm{M_{tot}} = 10^6\,{\rm M}_\odot$, we obtain $f_{\rm ISCO} \simeq 2 \times 10^{-3}\,{\rm Hz}$.

As the binary approaches coalescence these expressions are no longer valid and different methods must be adopted. In the *merger* phase, the two compact

objects are closely bound and GR non-linearity effects have to be take into account. This portion of the signal is usually modeled with Numerical Relativity (NR) simulations, covering the last few orbits. After the merger, the *ringdown* phase represents the stage where the remnant object dissipates its perturbation and returns into a stationary state. This phase is generally studied with perturbation theory techniques. In the past years a lot of effort has been spend in order to provide consistent expression for the GW signal across inspiral, merger and ringdown, resulting in different families of waveform that are adopted nowadays. Each waveform family typically focus on different aspects of binary modeling, as spin effects, eccentricity or the inclusion of higher harmonics, exploiting a time- or frequency-domain approach.

We are not going to provide an extensive overview of all the waveforms that are available at the time of writing (some reviews can be found at [29–31]). Among the possible approximant, the *Phenom* family has demonstrated to be a reliable and efficient tool for detection and parameter estimation. These phenomenological frequency-domain waveforms can track the GW signal from the deep inspiral to the ringdown. They have usually spin-aligned components (but see [32] for precession) and only the dominant mode ([33] for higher-mode contributions). Moreover these waveforms can be easily evaluated, making them a suitable choice for exploration of large parameter space. As an example, in Fig. 1.2 we report the GW signal computed for a system with $m_1 = m_2 = 30\,\mathrm{M}_\odot$ with the PhenomD as function of the time left before merger.

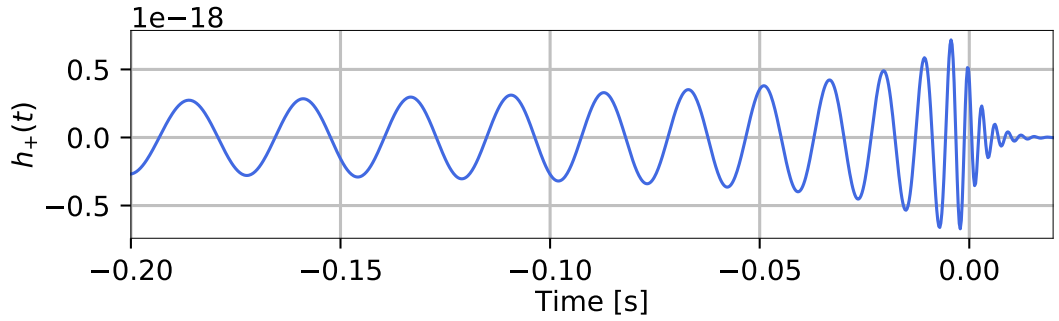

Figure 1.2: Late inspiral-merger-ringdown signal for an equal mass system with $m_1 = 30\,\mathrm{M}_\odot$ as function of the time left before merger.

Similarly to EM radiation, GWs are affected by the expansion of the universe, i.e. the GWs frequency is redshifted as $f_{\mathrm{gw,obs}} = f_{\mathrm{gw,s}}/(1+z)$ where z is the redsfhift of the emitting source and the pedix 'obs' ('s') refers to the observer

('source') frame. From Eq. (1.6) we can write

$$\begin{aligned} h_{+,\times} &\sim \frac{\mathcal{M}^{5/3}}{d} f_{\mathrm{gw,s}}^{2/3} \\ &\sim \frac{\mathcal{M}^{5/3}}{d} f_{\mathrm{gw,obs}}^{2/3} (1+z)^{2/3} \\ &\sim \frac{(\mathcal{M}(1+z))^{5/3}}{d(1+z)} f_{\mathrm{gw,obs}}^{2/3} \end{aligned} \tag{1.11}$$

where $\mathcal{M}_z = (\mathcal{M}(1+z))^{5/3}$ is the redshifted chirp mass and $d_L = d(1+z)$ is the luminosity distance of the source[7].

1.3 Signal theory

1.3.1 GW interferometers

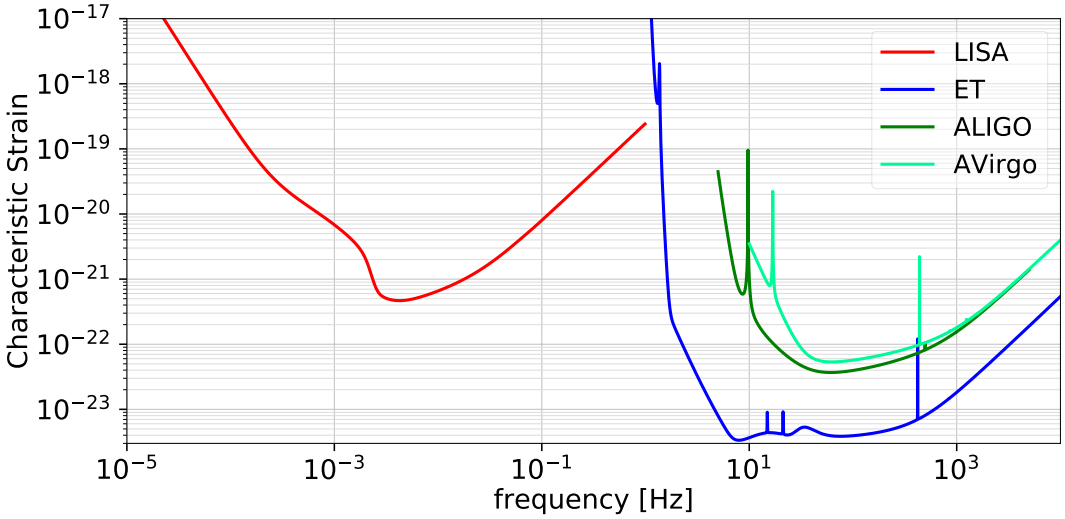

Figure 1.3: Characteristic strain of different interferometers as function of frequency.

The detection of GW signal is a hunt that lasted for 50 years. The first experiments that claim to detect GW adopted resonant bars: the idea is that GWs excite bar resonant frequencies and the change in length triggers piezoelectric sensors to

[7]Unless stated differently, for the rest of this Thesis we will refer to the observed frequency and we drop the subscript 'obs'.

produce a current signal. However resonant bar detectors were sensitive only to a small frequency range and had a small horizon distance, limited to the the size of our Galaxy. Even if some detections were claimed with resonant bar detectors, more refined analysis demonstrated that the observed signals were spurious artifacts of the detectors.

Interferometers are the instrument that are currently detecting GW signals. Their operation is based on the interference pattern produced by two different laser beams travelling inside the detector arms. The laser is splitted by a beam splitter into two beams that travel inside the detectors arms where partially reflecting mirrors create Fabry-Pérot cavities. Due to the fact that the interferometers work in destructive configuration, in the absence of a GW, no light is seen by the photodetector. Instead the passage of a GWs change the time of flight for the two laser beams and produce time-varying interference pattern.

The two LIGO were designed with 4 km armlength while Virgo armlength is just 3 km: since the length traveled by light affect the interference pattern, longer armlength increase the sensitivity of the detectors. Moreover the two LIGO were purposely built with one arm in the same direction to avoid the unfortunate case of a single detector signal. However, this configuration complicate the possibility to constrain the polarization states of the incoming signal. For this purpose, Virgo arms are tilted respect to the two LIGO, allowing for the detection of both polarizations [34].

In 2034, LISA will be launched and will follow an heliocentric Earth-trailing orbit with an opening angle of 20°. The constellation is made of three identical spacecrafts, set in an equilateral triangular configuration inclined of 60° respect to the ecliptic orbit, that rotate around their guiding center. The length of each arm is of 2.5×10^6 km in order to be sensitive in the $10^{-5} - 10^{-1}$ Hz frequency range. Such a large distance prevents the possibility to send the laser straight back from one spacecraft to another one and time delay interferometry has been developed to properly combined multiples signals [35]. In Fig. 1.3 we show the typical sensitivity range of the aforementioned instruments.

Interferometers present two major advantages respect to resonant bar detectors: they cover a wide range of frequencies, enabling the possibility to follow the signal during all the inspiral, and they can detect sources at cosmological distance, increasing the number of sources that we might be able to observe.

In Sec. 1.2, we described the two polarizations of a GW signal. However the detector input and output are scalar quantities. Therefore the two polarizations have to be convolved with the detector pattern functions that describe the interferometer sensitivity as function of the direction of the incoming signal $\hat{\boldsymbol{N}} = (\theta_N, \phi_N)$. Therefore the detector input can be defined as

$$h(t) = F_+(\theta_N, \phi_N, \psi)\, h_+(t) + F_\times(\theta_N, \phi_N, \psi)\, h_\times(t) \tag{1.12}$$

where F_+, $F_\times$ are the pattern function of the detector, (θ_N, ϕ_N) are the incoming direction of the signal (i.e. the declination and right ascension of the source) and ψ is the polarization angle describing the binary rotation in a plane perpendicular to the incoming direction. For a generic interferometer, we can write F_+, $F_\times$ as

$$\begin{aligned} F_+ &= \frac{1}{2}\left(1+\cos^2\theta_N\right)\cos 2\phi_N \cos 2\psi - \cos\theta_N \sin 2\phi_N \sin 2\psi \\ F_\times &= \frac{1}{2}\left(1+\cos^2\theta_N\right)\cos 2\phi_N \sin 2\psi + \cos\theta_N \sin 2\phi_N \cos 2\psi. \end{aligned} \tag{1.13}$$

The pattern functions takes the maximum value when the source is located right above the detector (at zenit) while the minimum is located in the plane of the detector and at 45° respect to the arm opening angle because a GW signal from this direction produces the same ΔL in the inteferometers arms, resulting in no relative variation.

These functions are quite smooth over the entire sky (with the exception of few blind spots). As a consequence, interferometers are not 'pointed' at the source as EM telescopes but they are more similar to microphones, listening in all directions. Still blind spots exist. For example, the first NS-NS merger [36] arrived in a blind spot of Virgo (incidentally this helped in reducing the sky position uncertainties). Increasing the number of detectors will decrease the number and the size of these blind spots, allowing for a great coverage of the sky.

Note also that Eq. (1.13) does not include time effect due to the detector moving during the observation. At first approximation, this can be applied for current detectors where GW signals are observed for less than one minute. However next-generation detectors, as ET or CE, will observe the inspiral of NS-NS binaries for minutes and, therefore, the rotation of the Earth might be taken into account. The same problem will appear in a more dramatic way with LISA. The combination of the orbital motion of the overall configuration and the rotation of the single spacecraft imprint unique features in the observed signals, as amplitude and phase modulation especially for long-lasting sources as SBHBs far from coalescence.

1.3.2 Signal-to-noise ratio

For most of the astrophysical sources, the signal is buried in the noise. In the presence of a GW signal the output of the detector can be written as $s(t) = h(t) + n(t)$ where $n(t)$ is the noise realisation in the detector[8]. If we consider standard astrophysical sources and the current sensitivity of interferometers, typically $|h| \ll |n|$.

[8]For simplicity we assume that $n(t)$ is stationary. We also assume a linear transfer function for the detector.

In order to extract the signal from the data strain, we adopt *matched filtering* techniques. The basic idea of these techniques is that it is possible to extract signal information if the form of the signal is known a prior. Indeed it can be shown that the best fit for a given signal is the signal itself[9]. We can define the signal-to-noise ratio as

$$S/N^2 = 4\int_{f_{\rm min}}^{f_{\rm max}} df\, \frac{|\tilde{h}(f)|^2}{S_n(f)} \tag{1.14}$$

where $\tilde{h}(f)$ is the Fourier transform of $h(t)$, $S_n(f)$ is the single-sided power spectral density (PSD), $f_{\rm min}$ the minimum frequency of the detector and $f_{\rm max}$ the maximum frequency of the GW signal. Note that since the S/N is adimensional, then $S_n(f)$ has dimension of Hz^{-1}.

The Fourier transform of Eq. (1.12) can be computed under the stationary phase approximation leading to the expression

$$\begin{aligned}\tilde{h}_+(f) &= \mathcal{A}\frac{\mathcal{M}_z^{5/6}}{d_L}(1+\cos^2\iota) f^{-7/6} e^{i\Psi(f)} \\ \tilde{h}_\times(f) &= \mathcal{A}\frac{\mathcal{M}_z^{5/6}}{d_L} 2\cos\iota f^{-7/6} e^{i\Psi(f)}\end{aligned} \tag{1.15}$$

where $\mathcal{A} = \frac{1}{\pi^{2/3}}\sqrt{5/96}$ and $\Psi(f)$ is the GW phase expressed as

$$\Psi(f) = 2\pi f(t_c + d/c) - \phi_0 - \frac{\pi}{4} - \frac{3}{4}\left(\frac{G\mathcal{M}_z}{c^3} 8\pi f\right)^{-5/3} \tag{1.16}$$

being t_c the retarded time at coalescence and ϕ_0 an arbitrary reference phase.

Eq. (1.14) can be re-written as

$$S/N = (\tilde{h}|\tilde{h}) \tag{1.17}$$

where the internal product $(\cdot|\cdot)$ is defined as

$$(a|b) = 4\,\mathrm{Re}\int_{f_{\rm min}}^{f_{\rm max}} df\, \frac{\tilde{a}^*(f)\tilde{b}(f)}{S_n(f)}, \tag{1.18}$$

where $a(t)$, $b(t)$ two real functions.

In this way we can easily write the S/N for a binary with random position, inclination and polarization as

$$S/N = wS/N_{\rm opt} \tag{1.19}$$

[9] This is the so-called 'Wiener filter'

where the $S/N_{\rm opt}$ is the optimal signal-to-noise ratio for a binary (i.e. zenit, face-on and $\psi = 0$) and w include all the angle dependencies as

$$w = \sqrt{F_+^2(1+\cos^2\iota)^2/4 + F_\times^2\cos^2\iota}. \tag{1.20}$$

We note that for an optimally located and oriented binary $w = 1$, while $w = 0$ if the detector has no response to the incoming signal [37].

The S/N is a useful quantity to establish the detectability of a given signal. Spurious noises in the detector might mimic the GW signal (especially for short-lasting sources) and produce a trigger: for a single detector a threshold value of $S/N_{\rm thres} = 8$ is considered reasonable [10]. Increasing the threshold will result in a reduction of the observed event as faint GW signals would be classified as noise artifacts. Therefore the choose of a $S/N_{\rm thres}$ is always a trade-off between the probability of false alarms and the horizon distance. For a network of detectors, the S/N values from each interferometer have to be summed in quadrature and customarily for LIGO/Virgo network the threshold value is $S/N_{\rm thres} = 12$ [11].

An useful expression to evaluate detector capabilities is the S/N averaged over the source location, inclination and polarization angles. Taking Eq. (1.13) and the inclination terms, we have to average

$$(1+\cos^2\iota)^2F_+^2 + 4\cos^2\iota F_\times^2. \tag{1.21}$$

For the inclination, we compute

$$\frac{1}{2}\int_{-1}^{1}(1+\cos^2\iota)^2 d\cos\iota = \frac{28}{15}, \tag{1.22}$$

and similarly for the $\cos^2\iota$ term. The average over the pattern function produce the same result for both polarizations, i.e.

$$\frac{1}{2\pi}\int_0^{2\pi}d\psi\,\frac{1}{2}\int_{-1}^{1}d\cos\theta_N\,\frac{1}{2\pi}\int_0^{2\pi}d\phi_N F_+^2 = \frac{1}{5}. \tag{1.23}$$

Therefore the average results in

$$\langle(1+\cos^2\iota)^2F_+^2 + 4\cos^2\iota F_\times^2\rangle = \frac{16}{25}. \tag{1.24}$$

From Eq. (1.15), the average amplitude can be written as

$$\begin{aligned}\langle\tilde{h}\rangle &= \frac{4}{5}\mathcal{A}\frac{\mathcal{M}_z^{5/6}}{d_L}f^{-7/6}e^{i\Psi(f)} \\ &= \frac{1}{\pi^{2/3}\sqrt{30}}\frac{\mathcal{M}_z^{5/6}}{d_L}f^{-7/6}e^{i\Psi(f)}\end{aligned} \tag{1.25}$$

[10] We note however that this condition depend from the type of signal and it is considered valid for signals from compact object binaries.

[11] This comes from a threshold value of $S/N_{\rm thres} = 8$ ($S/N_{\rm thres} = 4$) for the two LIGO (Virgo).

For LISA we also have to take into account the 60° arm opening angle due to its triangular configuration, reducing the strain of a factor $\sin(\pi/3)$. Moreover in LISA we also have to take into account the full response of the detector because the wavelength of the gravitational wave signal is comparable to the arm length: this is typically done taking into account the sensitivity, i.e. the sky position and polarization (not inclination) average sensitivity. The non sky-averaged sensitivity is connected to the sky-averaged noise spectral density as

$$S_n^{\rm NSA}(f) = \frac{3}{20} S_n^{\rm SA}(f). \tag{1.26}$$

Therefore in the quadrupole approximation, the averaged S/N in LISA can be computed as

$$\begin{aligned} S/N_{\rm ave} &= 2\left(\frac{\sqrt{3}}{2}\frac{1}{\pi^{2/3}\sqrt{30}}\right)\frac{\mathcal{M}_z^{5/6}}{d_L}\left[\int_{f_{\rm min}}^{f_{\rm max}} \frac{f^{-7/3}}{S_n^{\rm NSA}(f)}\right]^{1/2} \\ &= \sqrt{\frac{2}{3}}\frac{\mathcal{M}_z^{5/6}}{\pi^{2/3} d_L}\left[\int_{f_{\rm min}}^{f_{\rm max}} \frac{f^{-7/3}}{S_n^{\rm SA}(f)}\right]^{1/2} \end{aligned} \tag{1.27}$$

where we use $S_n^{\rm NSA}(f)$ to avoid the double average.

We can also obtain a general property for compact object binaries: from Eq.(1.27) we have

$$S/N \sim \frac{1}{d_L}\mathcal{M}_z^{5/6} S_0^{-1/2} f_0^{-2/3} \tag{1.28}$$

assuming that S_n has a constant value S_0 and that we start integrating from a minimum frequency f_0. From Eq.(1.6) we know that

$$h_0 \sim \frac{1}{d_L}\mathcal{M}_z^{5/3} f_0^{2/3} \tag{1.29}$$

and from Eq. (1.8) we can write

$$\mathrm{N_{cyc}} \sim \mathcal{M}_z^{-5/3} f_0^{-2/3}. \tag{1.30}$$

Substituting d_L and $\mathcal{M}_z$ in Eq. (1.28) with Eq. (1.29) and Eq. (1.30) respectively, we obtain

$$S/N \sim \frac{h_0}{(f_0 S_0)^{1/2}}\sqrt{\mathrm{N_{cyc}}}. \tag{1.31}$$

The term $(h_0/f_0 S_0)^{1/2}$ can be interpreted as the instantaneous S/N, i.e. integrated over a single GW cycle. However the integrated S/N receives a further contribution proportional to $\sqrt{\mathrm{N_{cyc}}}$ and for compact binaries $\mathrm{N_{cyc}} \gtrsim 10^2$. In other word, matched filtering techniques allow us to claim a detection even if the instantaneous S/N is still below the threshold detection if we have followed the signal for a sufficient number of cycles.

Chapter 2

Faithfulness requirement for SBHBs in LISA

In this Chapter we present a study on the waveform accuracy requirement to track SBHBs during their inspiral in LISA. Since SBHBs are expected to complete $N_{cyc} \simeq 10^6$ before moving outside LISA band, an accurate description of the GW signal is necessary to model the phase, to extract the signal from the noisy data and to perform an unbiased parameter estimation.

To model the signal, we adopt an inspiral-only waveform up to the 8PN order at leading order in the mass ratio. Therefore the question about the waveform accuracy translates in the minimum PN order necessary to keep track of the signal. We assume that the true signal is generated with all the PN contributions available and then compare the true signal against a set of template with increasing PN corrections.

We perform preliminary analysis exploring the effect of mass ratio, total mass and coalescence time. We then move to a more realistic situation and applied our code to a mock population of SBHBs in order to draw conclusions on the average waveform accuracy requirement for LISA.

The chapter is organized as follow: In Sec. 2.1 we introduce the concepts of data analysis necessary to claim the detection of a GW signal and to perform the parameter estimation. In Sec. 2.2 we describe the inspiral waveform adopted for this study. The same waveform will be adopted also to compute some of the results of the following chapters. In Sec. 2.3.1 we present the initial results from our exploration of the parameter space for different values of mass ratio, total mass and time to coalescence. In Sec. 2.3.2 we report the minimum accuracy requirement distribution when a realistic population of SBHBs is taken into account. Finally in Sec. 2.4 we discuss some caveats of our work together with future possible improvements. We also summarize our main findings.

The results presented here have been published in [38].

2.1 Signal theory introduction

In Sec. 1.3.2 we introduced the matched filtering techniques necessary to extract the GW signal buried in the noise. Matched filtering is often referred to as *optimal* filtering because the correlation between the detector output and the true signal provides the highest S/N value. However, in the analysis process, there are several effects that reduce the real S/N value. The template waveforms are approximated solutions to the GR equations, and therefore they cannot match the true waveform exactly. Moreover the parameters used to construct the template waveform are not the true source parameters. Both approximated waveforms and different parameters introduce systematic errors in detection and parameter estimation. Because of these effects the true signal is different from the actual template adopted.

From a geometrical viewpoint, it is useful to think to the set of all possible parameters as a parameter space. A waveform can be viewed as a function that takes a value from the parameter space to a signal space where the correlation is a well-defined internal product. Given a set of parameters, each waveform generates a signal that is cross-correlated with the detector output. Due to mismodeled waveforms, the true signal lies somewhere outside the template manifold used to search for it. Even if the template is a continuous analytical function of the parameters, the detector output cannot be correlated with an infinite number of template waveforms. It is therefore necessary to discretize the parameter space of the template waveform. Discretization is a trade-off between computational feasibility and detection efficiency, therefore, the step between two following template signals can not be, respectively, too large or too small. For example, there are more than 10^6 template for aligned-spin binaries with the current LIGO/Virgo sensitivity but the number is expected to increase with future upgrades [39, 40].

Due to the high computational requirements, the search for a GW signal in the detector output is usually performed hierarchically. The stretch of data is initially filtered with a sparse populated template manifold with a lower S/N threshold. The data that produced a lower S/N values are discarded as noise effect. The remaining data are filtered with a denser template manifold and an higher S/N threshold. The first step avoids the computation of too many correlations that would slow the overall analysis, while the last step ensures that no random noise realizations are claimed as true GW signal.

The theory behind data analysis have been developed by many authors starting from the early '90. Apostolatos [41] introduced the concept of *fitting factor* (FF) defined as the reduction in the S/N due to a mismatch between the true signal and the family of templates. The FF is equal to 1 if the signal and the template match perfectly, i.e. if the signal lies in the template manifold. If FF < 1, then the fitting factor represents the cross-correlation of a template waveform with a signal lying outside the manifold. Since the S/N scales with the inverse of the

luminosity distance, a reduction in the optimal value of the S/N implies a reduction in the observed event rate approximately of $1 - \mathrm{FF}^3$. A reasonable requirement is $\mathrm{FF} = 0.97$ that translates in a loss of 10% of the events due only to mismodeling.

Later Owen [40, 42] defined the match between two close templates in the template manifold, introducing a metric on the template manifold. In analogy to [41], in his work he defined the *minimal match* (MM) as the fractional S/N retained when the signal is exactly 'halfway' between two adjacent templates, assuming that the signal lies in the template manifold, i.e. the template waveform is identical to the true waveform. A template can be considered *effectual* if the correlation of the template with the GW signal, maximized over all the model parameters, is bigger than a threshold value. Differently, a template is *faithful* if the overlap between the true signal and the waveform, maximized only over the time and phase, is larger than a threshold value if computed with template parameters that are slightly different from the signal parameters [43]. Even if a template waveform can provide a good tool for detection, it is not granted that it can also be applied for parameter estimation. Detection and parameter estimation requirements are usually different [44]. For detection we require the model waveform to be similar enough to the true waveform to prevent loss in the detection rate (assuming that the template parameters are equal to the true ones). Instead, in order to perform parameter estimation we require that a detector can not distinguish the measurements made with two different waveforms, i.e. we require the intrinsic error due to mismodeling to be smaller than the statistical error.

In Sec. 1.3 we introduced the concept of optimal signal-to-noise ratio, S/N_{opt}. In practice, the filter function will be constructed from a template bank, no element of which will in general reproduce the true signal $h_t(t)$ exactly because of the systematic mismodeling mentioned above. Therefore, if one takes a filter function $K(f) \propto \tilde{h}(f)/S_n(f)$, where h is a given template, then the S/N will be

$$S/N = \frac{(h_t \,|\, h)}{(h \,|\, h)^{1/2}} = \mathcal{O}(h_t, h) S/N_{\mathrm{opt}} \,, \tag{2.1}$$

where we have introduced the overlap function

$$\mathcal{O}(h_t, h) \equiv \frac{(h_t|h)}{\sqrt{(h_t|h_t)(h|h)}} \,. \tag{2.2}$$

This function therefore quantifies the reduction in S/N due to the use of a sub-optimal template.

Clearly, if the S/N reduction due to the template mismodeling is too large, it could hinder detection of the signal. A measure of the S/N reduction relevant for detection is given by the *effectualness*, which is defined as the maximum overlap

function that can be obtained between a signal and the *whole* template bank (i.e. it is the overlap maximized over all possible template parameters). In practice, this means that we require that at least *one* template matches sufficiently well the signal, irrespective of the template parameters.

However, this condition is still too loose for parameter estimation, because for the latter we would rather need the template best matching the signal to correspond to source parameters "not too far" from the true ones. More precisely, a useful measure of the performance of a template family for parameter estimation is given by the *faithfulness*, i.e. the overlap maximized only over the coalescence time t_c and phase ϕ_c of the template, while adopting the true values for the other template parameters:

$$F \equiv \max_{t_c,\phi_c} \frac{(h|h_t)}{\sqrt{(h|h)(h_t|h_t)}}. \tag{2.3}$$

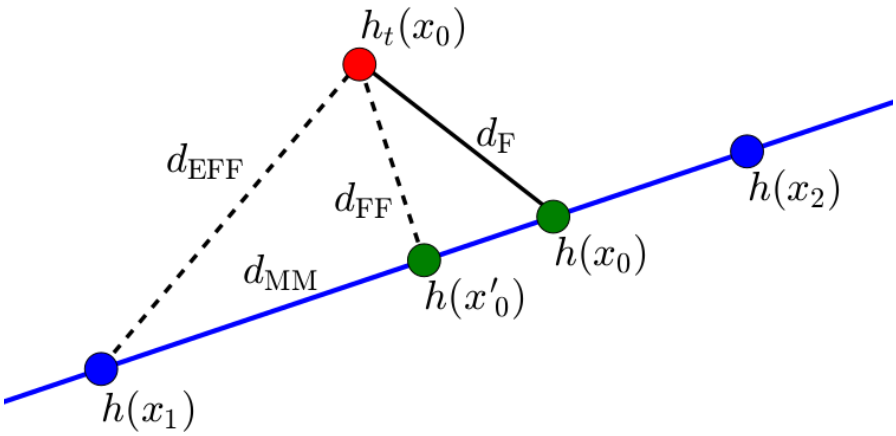

Figure 2.1: Schematic plot of a template manifold (blue line). The blue points $h(x_1)$ ad $h(x_2)$ represent two template signal. The red point $h_t(x_0)$ represent the true signal with x_0 being the real parameters of the source. The green point $h(x'_0)$ provide the maximum correlation with the true signal. $h(x_0)$ is the template signal constructed with the same parameters of the true signal but with a different waveform. The quantities $d_{\rm MM}$, $d_{\rm FF}$, $d_{\rm F}$ and $d_{\rm EFF}$ are defined in the text.

Defined as in Eq. (2.3), the faithfulness is a good way to test if a given template can be used for parameter estimation. Similarly to [44] and [31], Fig. 2.1 illustrates the concepts discussed up to this point. The blue line represents the template manifold on which the two template signals $h(x_1)$ and $h(x_2)$ are defined with parameter sets $x_1 \neq x_2$. Since the template manifold is constructed with approximated waveforms, the true signal $h_t(x_0)$ lies outside the template bank.

The point x_0' is chosen in such a way that the overlap between $h(x_1)$ and $h(x_0')$ corresponds to the *minimal match* as defined in [42]. The signal $h(x_0)$ is a template signal computed with the approximated waveform but with the same true parameters. Due to the difference between the template and the true waveform, $h_t(x_0)$ produces a higher overlap when correlated with $h(x_0')$, rather than $h(x_0)$. The quantities $d_{\rm MM} = 1-{\rm MM}$, $d_{\rm FF} = 1-{\rm FF}$, $d_{\rm F} = 1-{\rm F}$ are function, respectively, of the *minimal match*, the *fitting factor* and the *faithfulness*.

In a real search, $h_t(x_0)$ is correlated with a point $h(x_{\rm i})$. Therefore the quantity actually computed is more an *effective fitting factor* (EFF), with $d_{\rm EFF} = 1-{\rm EFF}$. If all these quantity are small, $d_{\rm EFF}$ is approximated as $d_{\rm EFF} \simeq d_{\rm MM} + d_{\rm FF}$. In order to avoid a large loss in detected events, we require $1-(1-d_{\rm EFF})^3 < 10\%$. Expanding, we obtain $d_{\rm EFF} < 3.5\%$. If the template bank has been constructed with $d_{\rm MM} = 3\%$, then $d_{\rm FF} < 0.5\%$. In a real search, we do not have access to the point of the template manifold closest to the true signal, but it is still true that $d_{\rm FF} < d_{\rm F}$ so the condition on $d_{\rm FF}$ is satisfied if $d_{\rm FF} < d_{\rm F} < 0.5\%$.

The threshold value of the faithfulness depends on the S/N. Since a mismodeled waveform introduces systematic errors in the parameter estimation, a reasonable requirement is to lower these errors below the statistical ones resulting from instrumental noise. The latter can be estimated from the covariance matrix, which is simply the inverse of the Fisher matrix[1] $\Gamma_{ij} = (\partial_i h|\partial_j h)$ (where i, j denote the waveform's parameters) in the high signal-to-noise ratio regime. In particular, in this regime the statistical errors decrease as S/N^{-1} [45], while the systematic errors are independent from the S/N.

In the high S/N regime, the expectation value of the faithfulness under the effect of statistical errors alone (i.e. resulting from the detector's noise and not from waveform mismodeling) in [46] is given by

$$\langle F\rangle \approx 1 - \frac{D-1}{2\,({\rm S/N})^2}\,, \tag{2.4}$$

where D is the number of parameters describing the template. In order to allow for an unbiased parameter estimation, the faithfulness of the templates needs to be less than the threshold given by Eq. (2.4). Similar requirements on F were obtained also in [44] as conditions on the amplitude and phase of the waveforms.

2.2 Inspiral-only waveform

The coalescence process of a BHB consists of three different phases: *inspiral*, *merger*, *ringdown*. In this study, we consider the inspiral phase only, as LISA can

[1] the Fisher matrix formalism and its application to the parameter estimation are discussed in more details in Sec. 4.2.

only detect the very early inspiral of SBHBs. During this phase, when the binary shrinks adiabatically and orbital velocities v are much smaller than the speed of light c, the equations of motion (EOM) are solved within the PN formalism, which consists of a series expansion in powers of v/c or, equivalently, a series expansion in powers of the dimensionless gravitational potential.

The idea behind PN theory is to compute the gravitational energy and GW luminosity of the binary up to high order and then combine the solution to obtain the phase of the system. One of the problem in the PN formalism arise in the actual computation of energy and luminosity: in principle one can solve the equation numerically or expand both term up to a given order. However these approaches lead to different solutions formerly know as TaylorTn approximants [31]. The PN approach is also known for its slow convergence to the real value. While $r_{\rm ISCO}$ can be easily computed in GR, in PN formalism we have to include up to the 8PN term in order to have an ISCO accurate at 1% [47]. As we approach the ISCO, the two BHs speed up and higher and higher PN corrections are required; eventually the PN formalism breaks down at ISCO where full GR effects have to taken into account. In LIGO/Virgo band, PN can not really be applied for systems with $\mathrm{M_{tot}} > 12\,\mathrm{M_\odot}$ because the ISCO moves in band (higher masses lead to smaller coalescence frequencies), the effect of different approximants become observable and the adiabatic approximation is no longer valid. However in LISA, SBHBs are still far from coalescence and the PN formalism can be applied safely.

At present, the EOM are known and can be solved up to 3.5PN order if the binary components are not spinning or if their spins are aligned/anti-aligned with the binary angular momentum, i.e. neglecting precession effects. If precession effects are taken into account, the EOM are known up to 2.5PN order, even if a closed form solution is still missing [29, 48, 49].

For this study, we use a Fourier-domain precessing waveform derived in [50], augmented to 8PN non-spinning order at leading order in the mass ratio $q \equiv m_2/m_1 \leq 1$ [51, 52]. We use a shifted uniform asymptotic (SUA [2]) description of the GW signal produced by a generically spinning binary system in LISA to avoid the divergent behavior predict in some cases by the stationary phase approximation. The spin-orbit equations are evolved numerically without compromising the computational cost of waveform generation. This method, being based on a PN description of the orbital evolution, is particularly suited to describe SBHB systems as observed by LISA as demonstrated in Tab. IV of [50] and in [46]. This waveform is therefore suitable to describe the inspiral of compact object binary but fails to reproduce the merger and ringdown portion of the signal. In geometric units ($G = c = 1$), the dimensionless parameter $v = \omega^{1/3}$ is our PN expansion parameter, where ω is the orbital frequency. We numerically evolve the following

[2] We will use this expression, 'SUA', to refer to this waveform in the next chapters

equations of motion:

$$M\dot{\phi} = v^3, \tag{2.5}$$

$$M\dot{v} = v^9 \sum_{n=0}^{16} a_n v^n, \tag{2.6}$$

$$M\dot{\hat{\boldsymbol{L}}} = -v^6 \left(\boldsymbol{\Omega}_1 + \boldsymbol{\Omega}_2\right), \tag{2.7}$$

$$M\dot{\boldsymbol{s}}_1 = \frac{m_2}{M} v^5 \boldsymbol{\Omega}_1, \tag{2.8}$$

$$M\dot{\boldsymbol{s}}_2 = \frac{m_1}{M} v^5 \boldsymbol{\Omega}_2, \tag{2.9}$$

where ϕ is the orbital phase of the system, $\hat{\boldsymbol{L}}$ is the unit vector parallel to the orbital angular momentum $\boldsymbol{L}$, $\boldsymbol{s}_i = \boldsymbol{S}_i/m_i$ are the individual reduced spins. Eq. (2.5) contains as key timescale the orbital time $\mathcal{O}(v^{-3})$, Eq. (2.6) the radiation reaction timescale $\mathcal{O}(v^{-8})$, while Eq. (2.7)-(2.9) describe the relativistic precession occurring on a timescale $\mathcal{O}(v^{-5})$. The vectors $\boldsymbol{\Omega}_i$ are defined in [50] and are orthogonal to $\boldsymbol{s}_i$, while $\boldsymbol{\Omega}_1 + \boldsymbol{\Omega}_2$ is orthogonal to $\boldsymbol{L}$. The coefficients a_n (with $0 \leq n \leq 7$) can also be found in [50] and are expressed in terms of powers of ν. They also contain terms related to both spin-orbit and spin-spin precession.

In the following, we will refer to a waveform constructed from these equations (Eq. (2.6)) truncated at order v^{9+2N} as an "N-PN waveform". In this, we follow the traditional PN order counting where the first non-vanishing term in an expression is called "Newtonian" or "leading PN order", and each further factor of v^2 adds one PN order to the term it multiplies. Our expressions for the vectors $\boldsymbol{\Omega}_i$ are valid at leading PN order for the terms quadratic in the spins, and at 2PN order (i.e. $\mathcal{O}(v^4)$ beyond the leading PN order) for the terms linear in the spins.

The constants a_n are valid for generic mass ratios and spin configurations at 2PN order, and are valid at linear order in the spins at 3.5PN order. While the constants a_n are currently not know for generic mass ratios up to 8PN order, in order to simulate a high PN order frequency evolution equation and compare waveforms at high PN orders, we use a hybrid approach to construct a_n for $n \geq 8$.

We first construct an 8PN relation between the orbital energy and the orbital frequency, $E(v)$, by including all generic terms up to 3.5PN [53], and adding subsequent PN terms in the extreme mass ratio limit by expanding the relation for test particle circular orbits in a Schwarzschild spacetime [51]:

$$E = \frac{1 - 2v^2}{\sqrt{1 - 3v^2}}. \tag{2.10}$$

While the binding energy is known at the linear order in the mass ratio at 6PN order [54, 55], using this more accurate result would not add much complexity to the EOM, and therefore we choose the simpler approximate result from Eq. (2.10).

We then perform the same construction to get the gravitational wave luminosity $\mathcal{L}(v)$, by including all generic terms at 3.5PN by leading order [53], and subsequent PN terms in the extreme mass ratio limit from [51]. We then use these two hybrid quantities to construct a simulated frequency evolution equation at 8PN beyond leading order by expanding the balance equation:

$$\frac{dv}{dt} = \frac{\mathcal{L}(v)}{dE/dv}. \tag{2.11}$$

To build the different waveforms that we compare in this work, we solve the equations of motion (2.5-2.9), truncating Eq. (2.6) at different PN orders, using a fifth order Cash-Karp Runge-Kutta method [56]. Using those solutions, we then construct the LISA response to a passing GW in the time-domain as

$$h(t) = \sum_{n=1}^{7} H_n(t) e^{-in(\phi+\phi_T)}, \tag{2.12}$$

where $H_n(t)$ are wave amplitudes for different GW harmonics that can be found at 2.5PN order for non-spinning systems in [57, 58] and contain the detector response to the GW polarizations in the low-frequency approximation [59], and ϕ_T is the Thomas precession phase accounting for the precession of the orbital plane in the detector frame and satisfies

$$\dot{\phi}_T = \frac{\cos\iota}{1-\cos^2\iota}\left(\hat{\boldsymbol{L}} \times \hat{\boldsymbol{N}}\right) \cdot \dot{\hat{\boldsymbol{L}}}, \tag{2.13}$$

where we remember that $\iota = \arccos(\hat{\boldsymbol{L}} \cdot \hat{\boldsymbol{N}})$ is the inclination angle and $\hat{\boldsymbol{N}}$ is the line-of-sight vector from the detector to the source.

We then use those results in a SUA transform to compute the gravitational wave signal, as in [50]:

$$\begin{aligned} \tilde{h}(f) = &\sum_{n=1}^{7} \sqrt{2\pi} T_n e^{i(2\pi f t_n - n\phi(t_n) - \pi/4)} \\ &\times \sum_{k=-3}^{3} b_k \mathcal{H}_n(t_n + kT_n), \end{aligned} \tag{2.14}$$

$$2\pi f = \dot{\phi}(t_n), \tag{2.15}$$

$$T_n = \ddot{\phi}^{-1/2}(t_n), \tag{2.16}$$

where

$$\mathcal{H}_n(t) = H_n(t) e^{-in\phi_T(t)}, \tag{2.17}$$

and the constants b_k satisfy

$$\sum_{k=-3}^{3} b_k = 1, \tag{2.18}$$

$$\sum_{k=1}^{3} b_k \frac{k^{2p}}{(2p)!} = \frac{(-i)^p}{2^{p+1}p!}, \quad 1 \leq p \leq 3, \tag{2.19}$$

$$b_k = b_{-k}. \tag{2.20}$$

2.3 Results

2.3.1 Exploration of parameter space

We run different simulations to verify the lowest PN order necessary to compute a faithful waveform. In all simulations we approximate the true signal h_t with a waveform constructed with 8PN phasing (which we assume as our reference waveform), and we simulate signals h at lower PN orders. Once both signals are obtained, we compute the faithfulness, F, according to Eq. (2.3), maximizing over the time and orbital phase. The resulting value is compared to a fiducial threshold of $F = 0.994$ corresponding to the situation where the intrinsic errors due to mismodeling are smaller than the statistical errors from the detector noise, for a waveform with a number of intrinsic parameters $D = 8$ and a signal with $S/N = 25$ [46]. When F is close to unity, roundoff errors can cause our code to yield $F \geq 1$, which is nonsensical. In order to circumvent this problem, whenever the faithfulness $F \geq 1$, we replace it with the largest double precision number strictly smaller than one, $F = 1 - \epsilon$ with $\epsilon \approx 1.1 \times 10^{-16}$.

We perform different simulations in order to fully characterize the faithfulness requirements for SBHB signals in LISA as a function of the relevant source parameters. We choose a fiducial SBHB with total mass $M = m_1 + m_2 = 60\,\mathrm{M}_\odot$, mass ratio $q = m_2/m_1 = 1$ and coalescence time $t_c = 4\,\mathrm{yr}$. For each set of simulations, we change only one of these parameters and keep the others fixed. We proceed as follows:

(I) We vary q, i.e. $q \in (0.1, 0.25, 0.5, 1)$;

(II) We vary the total mass of the system, i.e. $\mathrm{M_{tot}} = 60, 120, 200, 300\ \mathrm{M}_\odot$;

(III) We vary the coalescence time, i.e. we generate SBHB waveforms starting 4 years to 150 years before merger (we simulate systems that at the start of the LISA mission are 4 years to 150 years before merger).

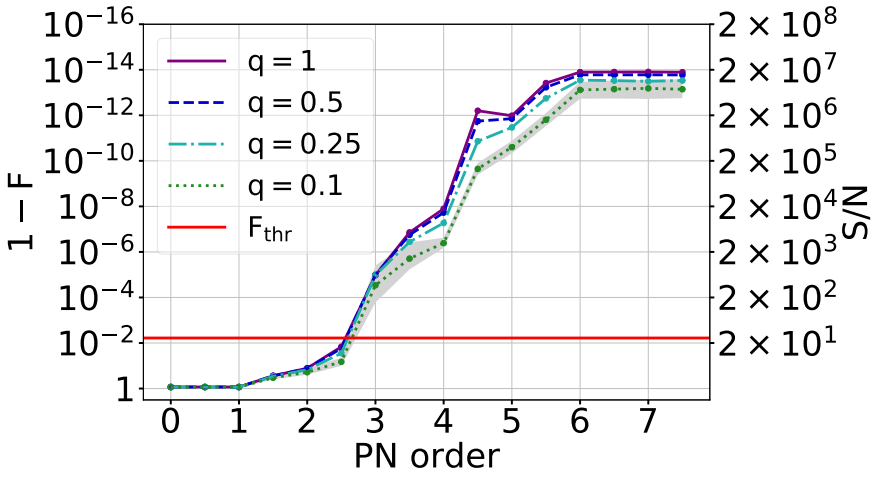

Figure 2.2: Results of the simulations for case (I), with four different values of the binary mass ratio, i.e. $q = 1, 0.5, 0.25, 0.1$. For each value of q, we show the unfaithfulness $(1-F)$ as a function of the waveform PN order. Each line represents the median over 10^3 simulated waveforms. For the case $q = 0.1$, we represent the region between the 16% and 84% quantiles (i.e. roughly the 1σ confidence region) by the shaded area. Dispersion around the median is similar in all cases. The horizontal red line is the threshold value $F = 0.994$, corresponding to a SBHB signal with $S/N = 25$ (on the right axes) and $D = 8$ waveform parameters.

In all cases, we consider spinning BHs, with spin magnitudes $\chi_{1,2}$ extracted from a flat distribution $0 < \chi_{1,2} < 1$ and spin directions, sky position, inclination and polarization uniformly distributed over a sphere. We further assume quasi-circular orbits. We notice that, due to the faithfulness definition, the luminosity distance is factored out. We run $N = 10^3$ random realizations for each sub-case to properly explore the parameter space.

Mass Ratio

In Fig. 2.2 we present the results of our runs as a function of q. The waveform is faithful at the adopted $F = 0.994$ threshold at PN orders larger than 3, almost irrespective of the value of q. In all cases, the inclusion of the 2.5PN dissipative term only is insufficient to produce the faithful waveform for SBHBs merging in 4 years, and the inclusion of the 3PN term is crucial for an unbiased parameter estimation. We notice that the convergence of the PN approximation is slower for lower mass ratios. This is a known characteristic of the PN approximation (see Fig. 1 in [60], or [61]), however it does not affect our conclusions.

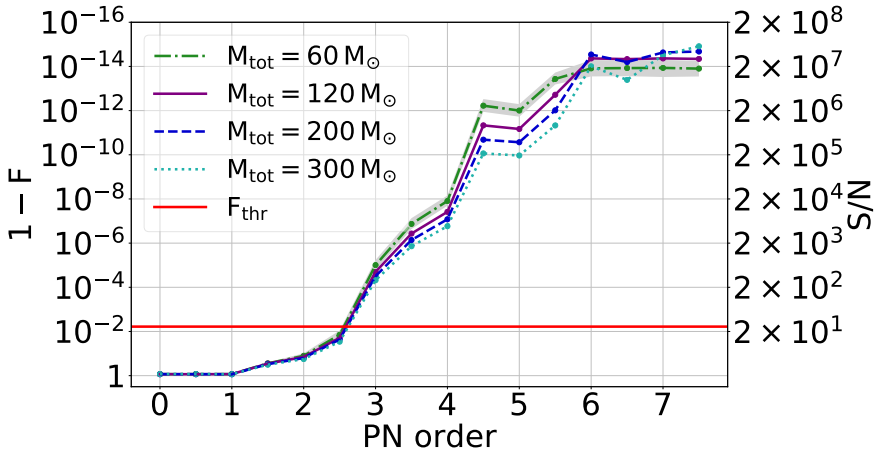

Figure 2.3: Same as Fig. 2.2 for case (II), i.e. for different values of the total binary mass. For the case $M_{tot} = 60\ M_\odot$, we represent the region between the 16% and 84% quantiles by the shaded area. Dispersion around the median is similar in all cases.

Total Mass

We now investigate the dependence of the faithfulness on the total mass of the SBHB. More massive SBHBs reach coalescence at lower frequencies. Therefore, in the LISA band, these sources are detectable when they are closer to coalescence and we would expect to have to include higher PN orders to properly describe the signal, as relativistic effects become more important. However, for a fixed coalescence time more massive systems also emit at lower frequencies, therefore the number of cycles we need to match decreases. So even if the systems are slightly more relativistic, we have to match fewer cycles for the same observation time. Which one of these effects dominate the dependence of the PN requirements on the total mass will thus have to be determined from our simulations.

Our results are illustrated in Fig. 2.3 for binaries with total mass from $M_{tot} = 60\ M_\odot$ to $M_{tot} = 300\ M_\odot$. We observe that the requirement on the faithfulness is already satisfied by a 3PN waveform, even for the more massive binaries. Note that for a fixed PN order the faithfulness between the template and the reference waveform slightly decreases with the total binary mass. However, even if we were to observe systems close to coalescence for a long time, the faithfulness requirement would still be satisfied by a 3PN waveform, with a weak dependence from the total binary mass.

Coalescence Time

Finally, we consider SBHBs with different coalescence times, t_c. In the previous cases, we fixed $t_c = 4\,\mathrm{yr}$, however we expect these sources to only represent a small sub-sample of the population that LISA will observe. Most of the SBHBs will be observed in their inspiral phase, several years before coalescence at a typical frequency of $10^{-2}\,\mathrm{Hz}$ [62]. These sources will be slowly chirping in the LISA band and will not coalesce in the LIGO/Virgo band during the mission lifetime. Since these systems are far from coalescence, we expect lower PN order waveforms to be sufficient to properly describe and follow the signal.

For each run, we fix different coalescence times, from $t_c = 10\,\mathrm{yr}$ to $t_c = 150\,\mathrm{yr}$. Results are shown in Fig. 2.4. SBHBs binaries with $t_c = 10,\ 25,\ 50,\ 75\,\mathrm{yr}$ can be properly described with just 1.5PN waveforms. Systems with $t_c = 100\,\mathrm{yr}$ can be described accurately with just a 1PN waveform and, finally, systems with $t_c = 150\,\mathrm{yr}$ are well described by Newtonian (i.e. 0PN) waveforms. Since the PN accuracy requirement is 0PN for systems with $t_c = 150\,\mathrm{yr}$, we conclude that also systems with longer merger time can be properly described by the same waveform accuracy.

In summary, we find that in order to guarantee that systematic waveform errors do not bias the recovery of SBHB parameters, 3PN templates are sufficient throughout the relevant parameter space. From our analysis, the most important factor to determine the lowest PN corrections necessary to properly describe SBHB signals is the coalescence time. Even if the binary mass components and mass ratios are expected to vary, their effect on waveform accuracy requirements is negligible. We also run each sub-case under the assumption of non spinning SBHBs and find no significant differences.

2.3.2 Implication for population of SBHBs

The goal of this study is to assess the waveform requirements for faithful signal reconstruction of the SBHBs detected by LISA. It is therefore useful to apply our analysis to expected SBHB populations, informed by the current LIGO/Virgo constraints.

We consider three population models, differing in the assumed SBHB mass function. In the first model, binary component masses are independently extracted from a log-flat distribution, with the only constrain that the total mass of the system has to lie in the range $[10\ \mathrm{M}_\odot, 100\ \mathrm{M}_\odot]$, with $m_1,\ m_2 > 5\ \mathrm{M}_\odot$ [63, 64]. In the second and third model, the mass of the primary BH is obtained from a Salpeter distribution [65] in the range $[5\ \mathrm{M}_\odot, 100\ \mathrm{M}_\odot]$, and the secondary mass is drawn from a flat distribution in the range $[5\ \mathrm{M}_\odot, m_1]$ and $[\max(5\ \mathrm{M}_\odot, m_1/3), m_1]$ respectively. For each model we simulate 10 realizations of the expected SBHB

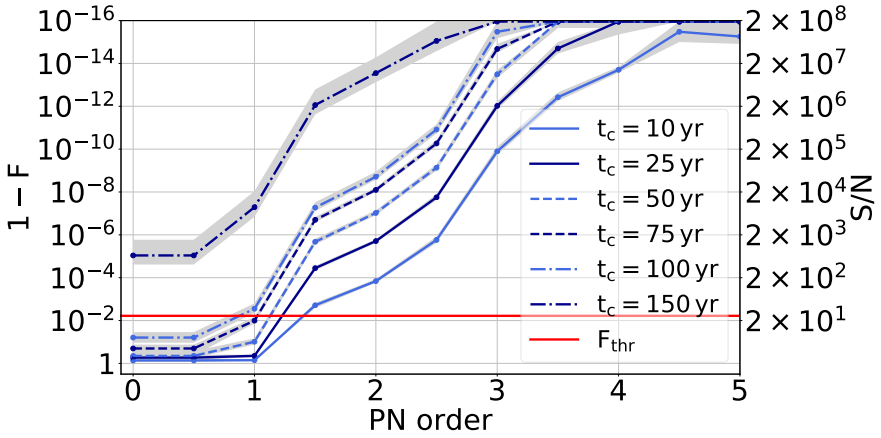

Figure 2.4: Same as Fig. 2.2 for case (III), i.e. for different coalescence times. For each case, we represent the region between the 16% and 84% quantiles by the shaded area.

population by drawing the local SBHB merger rate from the posterior distribution estimated by the LIGO O1 observations for either a log-flat or a Salpeter mass function, as reported in Fig. 11 of [66]. The merger rate is assumed to be constant in redshift (this does not have a major impact on LISA SBHB sources which are mainly at $z < 0.5$ anyway). The population of SBHB observed by LISA as a function of mass, redshift and frequency is then computed as described in [62], assuming circular binaries.

This procedure yields $N_{cat} = 30$ synthetic catalogs of SBHBs emitting in the LISA band. The GW signals from those systems are then integrated over the assumed 4 year LISA mission lifetime and the S/N is computed. We consider detectable, and thus retain, only events with $S/N > 8$ [3]. The 30 catalogs yield an average number of ≈ 100 SBHBs detectable by LISA above threshold.

In this population analysis, we do not consider a single threshold value for the faithfulness as in Section 2.3. Instead, we compute the faithfulness requirement for each event, based on its S/N, and we estimate the required PN order in the waveform model accordingly. In practice we proceed as follows:

- for each event we compute the S/N in the LISA detector with the SUA waveform (assuming a random sky location, inclination and polarization);
- from the S/N we compute the faithfulness threshold from Eq. (2.4);

[3] Clearly increasing the S/N threshold for detection [67] will decrease the number of sources; however our conclusion will not be drastically affected

- we take the 8PN waveform as the true model signal and compute the faithfulness of waveforms at increasing PN orders until its value gets larger than the threshold.

We repeat this procedure for all individual events with $S/N > 8$ in all 30 catalogues. We found similar results for the three population models. This had to be expected, since we have demonstrated in Section 2.3 that waveform requirements are largely independent of the mass and mass ratio of the SBHBs. Therefore, in the following we present results only from the first population, i.e. averaged over 10 catalogues.

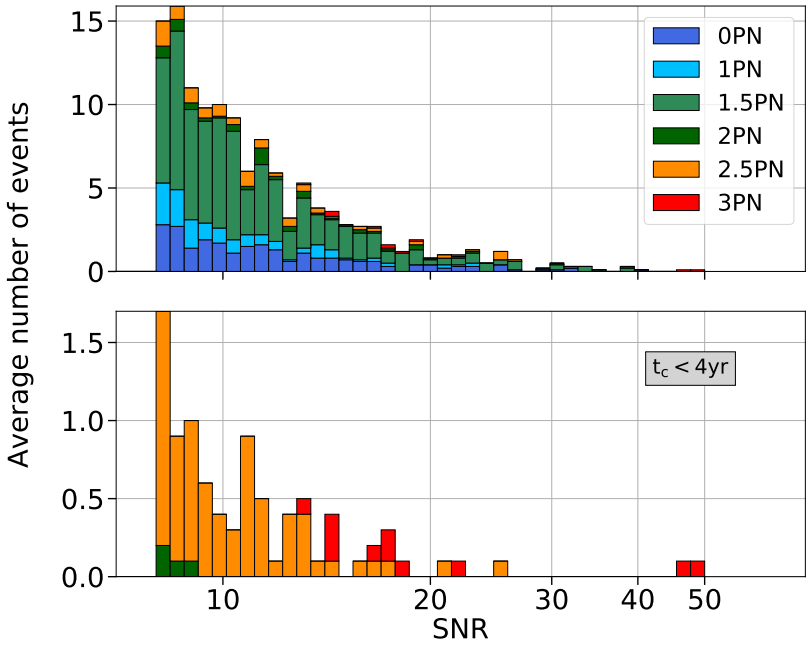

Figure 2.5: Top panel: stacked S/N distribution for PN sub-populations, labeled with different colors. Each bin is divided by the number of catalogs in our simulations, $N_{cat} = 10$, to provide mean estimates. Bottom panel: same distribution but selecting only systems with $t_c < 4\,\mathrm{yr}$. The PN sub-populations are constructed computing the faithfulness for each event and considering the lowest PN order satisfying the threshold value, from Eq. (2.4).

Fig. 2.5 shows the average number of sources as a function of S/N, color-coded according to the PN accuracy requirement. The upper panel shows that for the majority of SBHBs, 1.5PN waveforms are sufficient. Indeed, it is clear that

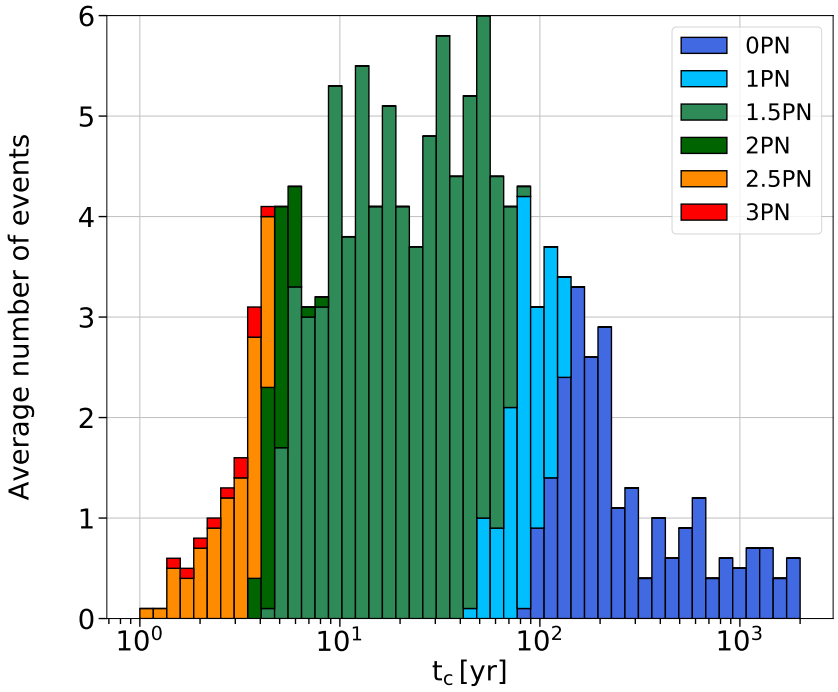

Figure 2.6: Stacked coalescence time distribution for each sub-population, color-coded as indicated in figure.

the vast majority ($\approx 90\%$) of the SBHBs are described accurately by using low PN waveform (PN < 2) with only a small fraction of sources requiring 2.5PN or higher-PN waveforms. The lower panel shows that the sub-population of SBHBs with $t_c < 4\,\mathrm{yr}$, i.e. those crossing to the LIGO/Virgo band within the LISA lifetime, generally require 2.5PN and 3PN waveforms. In fact 90% (80%) of the SBHBs requiring 3PN (2.5PN) waveforms fall in this sub-population. We also observe that the PN requirements are largely independent of the S/N for the global population, while for systems merging within the mission lifetime, more stringent PN requirements correspond to larger S/N values.

In Fig. 2.6 we plot the average number of sources as a function of time to coalescence, again color-coded according to the PN order required for a faithful recovery of the signal. As expected from the previous results, longer coalescence times imply less stringent requirement on the PN waveform accuracy necessary to track the signal phase. Indeed PN sub-populations are quite sharply separated in terms of coalescence time. For $t_c < 4\,\mathrm{yr}$ the main contribution comes from the 2.5PN and 3PN sub-populations. In the interval $4\,\mathrm{yr} < t_c < 10\,\mathrm{yr}$, SBHBs require 2PN and 1.5PN corrections to be appropriately described. As can be seen in the

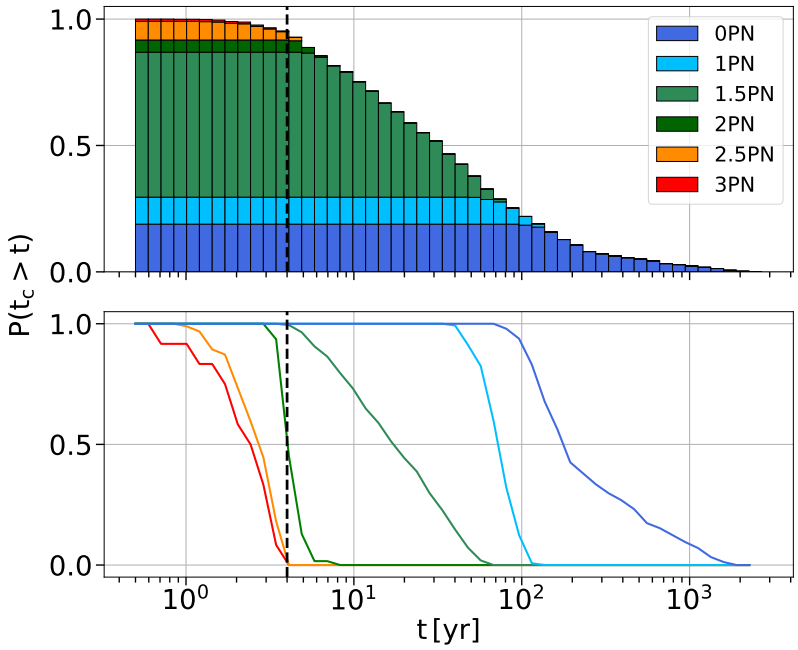

Figure 2.7: Stacked cumulative coalescence time distribution for the complete catalogs (top panel) and for each PN sub-population (lower panel), color-coded as indicated in figure. The vertical dashed black line represents $t_c = 4\,\mathrm{yr}$.

top panel of Fig. 2.5, the larger sub-population is the 1.5PN one, which dominates the distribution for $t_c \in [10, 100]\,\mathrm{yr}$, with an important contribution from the 1PN population for $t_c \simeq 100\,\mathrm{yr}$. For longer t_c, most systems can be modeled by 0PN waveforms.

We also computed the cumulative distribution of sources as a function of coalescence time, divided according to the required PN order in waveform modeling. The result is presented in Fig. 2.7. The upper panel shows the cumulative stacked distribution, color-coded for the different PN sub-populations. The lower panel shows the cumulative distribution separately for each PN sub-population. As expected from the previous results, all systems can be described using 3PN waveforms. Both the 3PN and 2.5PN sub-populations only contribute to the overall distribution for $t_c < 4\,\mathrm{yr}$. The rest of the population (i.e. binaries with $t_c > 4\,\mathrm{yr}$, accounting for $\sim 90\%$ of the overall sample) can be described by 2PN waveforms. About 75% of the population lies at $t_c > 10\,\mathrm{yr}$ and requires 1.5PN waveform accuracy or lower; only 25% of the detected SBHBs have $t_c > 100\,\mathrm{yr}$ and can be mostly described by Newtonian waveforms. In the lower panel, we can see the fraction of each sub-

population at a given time. Again, the 3PN and 2.5PN sub-populations behave similarly and their support is almost completely inside $t_c < 4$ yrs. Similarly the 2PN sub-population shows support up to $t_c < 10\,\mathrm{yr}$, while the 1.5PN one extends up to $t_c \simeq 70\,\mathrm{yr}$. The 1PN and 0PN sub-populations show open support up to $t_c \simeq 10^2\,\mathrm{yr}$ and $t_c \simeq 10^3\,\mathrm{yr}$ respectively.

These findings provide useful hints on the trade-off between the waveform accuracy necessary to follow the binary phase during the inspiral and the information recovered from the parameter estimation. Based on our simulations, we find that low PN templates can efficiently recover about 90% of the signals allowing faithful and fast parameter estimation. However, for the multiband SBHBs merging within the mission lifetime, 3PN waveforms will be necessary to provide unbiased parameters and to precisely inform ground based detectors. In the scenario of a ten years LISA time mission, we will be able to detect a larger number of systems at lower frequencies thus increasing the number of SBHBs for which low-PN waveform are sufficient.

2.4 Discussion and summary

In this paper, we assumed circular orbits, since GW emission tends to circularize binary systems [68]. We can write the eccentricity in function of the orbital separation as

$$e \simeq \left(a \frac{g(e_0)}{a_0} \right)^{19/12} \tag{2.21}$$

where a_0 and e_0 are the original semi-major axis and eccentricity, respectively, and $g(e) = (1 + 121e^2/304)^{870/2299} e^{12/19}/(1 - e^2)$. If we consider a system with total mass $\mathrm{M_{tot}} = 60\,\mathrm{M_\odot}$ at an initial frequency $f_0 = 0.1\,\mathrm{Hz}$ ($\mathrm{a_0} = 4 \times 10^7\,\mathrm{m}$) with an initial eccentricity of $e_0 = 0.9$, by the time the two objects reach a separation of ten times larger than their radius $\simeq 10^3\,\mathrm{Km}$, the eccentricity has become $e \simeq 0.038$.

However, their residual eccentricity may not be negligible [69, 70], and therefore a study similar to ours has to be performed also for eccentric SBHBs. We recall that the effect of eccentricity is to speed up the inspiral time and increase the effect of relativistic corrections. Therefore, we expect that eccentric binaries will require higher PN orders to be properly modeled. For our results, this would imply a larger contribution from the high PN sub-population in Fig. 2.6. Moreover, from stellar evolution simulations we expect the presence of a mass gap in the black hole mass distribution [71, 72] between $[60, 120]\ \mathrm{M_\odot}$, which we do not consider in this work. Nevertheless, this gap may be filled by "second generation" black holes in cluster formation scenarios [73, 74].

We determined the PN accuracy requirements necessary to properly track a SBHB signal during the inspiral phase in the LISA band. Our key findings can be

summarised as follow:

- For systems merging within the mission lifetime, a 3PN waveform is sufficient to perform unbiased parameter estimation.
- Total mass and mass ratio play a minor role in the requirement for PN accuracy; similarly spin effects and spin precession are found negligible as precession timescales are exceedingly long in these systems.
- Systems with longer coalescence time require less accurate templates to be properly modeled. In particular, assuming a 4 year LISA mission, systems with $t_c = 5$, 10, 50, 75 yr require only a 1.5PN accurate waveform. Systems with $t_c = 100\,\mathrm{yr}$ and $t_c = 150\,\mathrm{yr}$ can be properly modeled by 1PN and Newtonian (i.e. 0PN) waveforms respectively or adopting the same approach for galactic binaries [75].
- For SBHB population models, most of the detectable sources will be properly described by low PN waveforms (PN ≤ 2), while systems merging within the mission lifetime will require 2.5PN and 3PN waveform phasing.
- The coalescence time distribution shows PN sub-populations reasonably separated in coalescence time, with systems requiring higher PN accuracy appearing only at small t_c.
- The cumulative distribution of the coalescence time for each PN sub-population shows in particular that for systems merging after the end of the LISA mission ($t_c > 4\,\mathrm{yr}$) 2PN waveforms can be used to provide unbiased parameter estimation, with even lower PN orders needed as t_c further increases.

Overall, our results provide an estimate of the waveform accuracy necessary to track the GW phase without compromising the recovered information. Even though all detectable SBHB signals can be properly described by 3PN waveforms, for a large fraction of sources 2PN waveforms alone will already satisfy the conditions for unbiased parameter estimation. Thus, our results may help the data analysis community in the construction of efficient and computationally viable algorithms.

Chapter 3

SBHBs above the pair-instability mass gap

In this chapter we present a study on the possibility to detect stellar black hole binaries above the so-called *pair-instability* mass gap. Starting from the star formation rate (SFR) and metallicity evolution across cosmic time, we build a coherent and simple approach to describe BHs above the mass-gap. We consider 4 different scenarios: one pessimistic and one optimistic in order to constrain our model and two intermediate ones.

In order to evolve the stars we adopted the code SEVN ([72] and references therein) that can evolve stars up to $350\,\mathrm{M}_\odot$ and metallicity $Z = 2 \times 10^{-4}$. Our approach is based on evolving *single* stars instead of binary stars.

Assuming mass ratio and time delay distributions, we compute the intrinsic merger rate of three distinct sub-populations: 'below-gap' binaries with both $m_1, m_2 < 60\,\mathrm{M}_\odot$, 'across-gap binaries' with $m_1 > 120\,\mathrm{M}_\odot$ and $m_2 < 60\,\mathrm{M}_\odot$ and 'above-gap' binaries with $m_1, m_2 > 120\,\mathrm{M}_\odot$. Our results for 'across-gap' and 'above-gap' binaries are based on the ansatz that the underlying physics of binary formation and evolution does not change beyond the gap.

We convolve each sub-population with the detector sensitivity of current and future interferometers to compute the expected detected rates. Finally we also computed the expected stochastic background signal from unresolved 'across-gap' and 'above-gap' binaries in LISA.

The chapter is organized as follow: in Sec. 3.1.1 we review the concept of stellar evolution theory while in Sec. 3.1.2 we summarise the main formation channels that are expected to form SBHBs. In Sec. 3.1.3 we highlight the motivation of our work. The description of the SFR, metallicity and IMF prescriptions adopted is reported to Sec. 3.2.1 while in Sec. 3.2.2 we present the approach to compute the actual rates. In Sec. 3.3.1 we present our results for current and future interferometers for the three sub-populations and different models. In Sec. 3.3.2 we forecast our

predictions for LISA. In Sec. 3.4 we discuss the main assumptions and caveats of our work. Finally in Sec. 3.5 we summarise our main conclusions.

Most of the results presented here have been published in [76].

3.1 Binary formation and evolution

3.1.1 Stellar evolution theory

Neutron stars and black holes are the relics of massive stars with mass $> 10\,\mathrm{M}_\odot$. Thanks to fusion reactions, massive stars are able to synthesize heavier elements, ending up with an iron core. When the iron core is driven above the Chandrasekhar mass limit, fusion reactions can no longer support the star, balancing the gravitational force. The core itself contracts, experiencing photodissociation and neutronization processes. In this last stage, a supernova (SN) explosion is triggered by the fallback of the star envelop on the dense neutron-core. The remnant is a hot and dense NS. If the mass star is in between $15 \lesssim M/\,\mathrm{M}_\odot \lesssim 30$, the supernova explosion is in part suppressed and some of the ejected material fall back to the remnant NS. If the mass is too large, the NS collapse into a BH. Finally, if the mass of the star is $\gtrsim 30\,\mathrm{M}_\odot$ the gravitational potential suppresses the supernova explosion and the star directly collapses in a BH. The results of these processes is a gap between NS and BH around $2 - 5\,\mathrm{M}_\odot$ [77].

There are two main properties driving the evolution of a star: its mass M, and its metallicity Z [1]. We have already sketched the role of mass. Metallicity affects in particular the mass of the remnant BH, especially in the late stage of its life. Metal rich stars lose a significant portion of their envelope due to strong stellar winds, because the typical cross-section of heavier element is larger than the hydrogen one. When heavy elements interact with the hydrogen in the envelope, they can scatter with it and, eventually unbind it from the star, reducing the total mass.

Moreover the type of SN is expected to affect the final BH mass. In the standard scenario, if the Helium core of the star is above a critical mass ($\simeq 30\,\mathrm{M}_\odot$), the star experiences strong pulses leading to a significant loss of mass before explosion. This scenario is known as *pulsational pair-instability SNe* (PPISNe). However if enough energy is realesed during fusion reactions, the star might be disrupted and no remnant at all is expected: this scenario is usually referred to as *pair-instability SNe* (PISNe, [78]). Finally, if the the Helium core is enough massive $\gtrsim 135\,\mathrm{M}_\odot$, star avoids both scenarios and undergoes directly collapse.

[1] We define the metallicity as logarithm in power of ten of the iron to hydrogen abundance ratio.

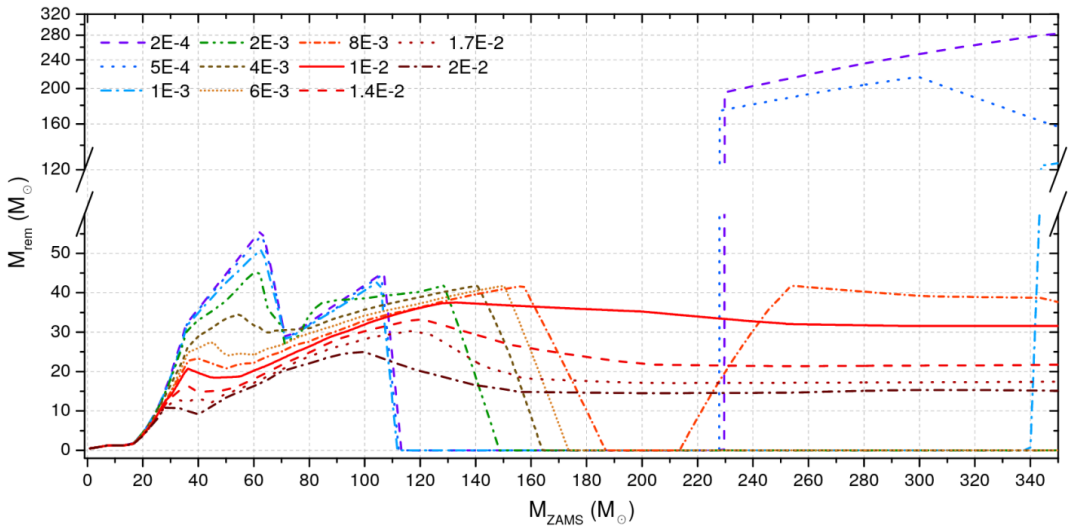

Figure 3.1: Mass of the remnant BH (M_{rem}) as function of Zero-Age Main Sequence (ZAMS) star mass (M_{ZAMS}) when we include the PPISNe and PISNe effects. Each color represents different value of metallicity. Here $Z_\odot = 2 \times 10^{-2}$. Credits to [72].

In Fig. 3.1, we highlight the combination of all the aforementioned effects in shaping the BH mass distribution for different values of metallicities as function of the Zero-Age Main Sequence (ZAMS) star mass [2]. Low metallicity stars tend to form more massive BHs: a star with $M_{ZAMS} = 260\,M_\odot$ ends up in a BH with $M_{rem} \simeq 15\,M_\odot$ ($M_{rem} \simeq 200\,M_\odot$) if its metallicity is $Z = 2 \times 10^{-2}$ ($Z = 5 \times 10^{-4}$).

Another effect of PPISNe is to increase the number of BH in the LIGO/Virgo range between $20 \lesssim M_{rem}/M_\odot \lesssim 50$ for all progenitor masses. Indeed, before GW detections, BHs were reported only as companion of stars in low mass X-ray binaries. This BH population shows a mass distribution centered around $8\,M_\odot$. Even if slightly more massive BHs have been reported with this technique, their masses are all below $20\,M_\odot$ due to the metallicity of their progenitor stars.

It is also evident the effect of PISNe for stars with $120 \lesssim M_{ZAMS}/M_\odot \lesssim 230$ and $Z \lesssim 8 \times 10^{-3}$: these stars are not expected to produce any remnant, leaving a gap in the BH mass distribution (shown as a break in the y-axis). If the star is enough massive ($M_{ZAMS} > 230\,M_\odot$) and with low-metallicity ($Z \lesssim 5 \times 10^{-4}$), it directly collapses in a massive BH ($M_{rem} > 120\,M_\odot$).

[2]The ZAMS star mass corresponds to the mass when the star enters the main sequence on the Hertzsprung-Russell diagram.

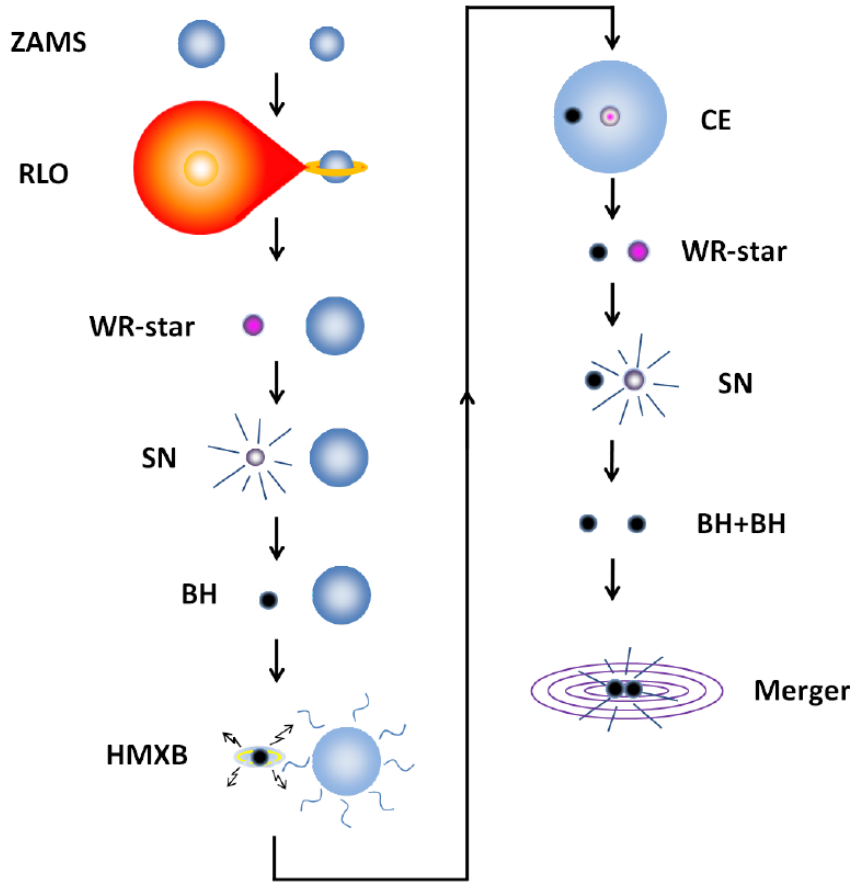

Figure 3.2: The formation of a BHB from the isolated binary channel. RLO: Roche-lobe overflow; WR-star: Wolf-Rayet star; HMXB: high-mass X-ray binary. Credits to [79].

3.1.2 Formation channels

Two main formation channels have been proposed for SBHBs, i.e. the isolated binary channel [80–84] and the dynamical channel [85–90]. Each scenario presents its unique traits and features that shape the final mass and redshift distribution of merging SBHBs. BHBs formed from isolated binaries are expected to have spins aligned to the orbital angular momentum and small orbital eccentricities [68, 91] . Otherwise, if two BHs bound after a dynamical encounter, their spins will be isotropically oriented [92] . Moreover many-body interactions can trigger Kozai-Lidov oscillations and produce large eccentricities that can be detected at low-frequency with LISA [69, 93–97] or even at merger time in LIGO/Virgo band [74, 98–101]. The two scenarios predict also different contributions to the total

merger rate. Field scenario merger rates are comparable to the LIGO/Virgo rates while BHBs from clusters are expected to contribute up to $\simeq 10\%$ to the total [37, 102–106]. During the years, other possible formation channels have been proposed:

- In the chemically homogeneous evolution (CHE) [107–109], two stars are tidally locked in a close binary. This configuration leads to fast rotating stars with efficient internal mixing that keep the stars chemically homogeneous during most of its life.

- BHBs might also form in Active Galactic Nuclei (AGNs) where the interaction between the binary and the gaseous disk might enhance the number of mergers and leave distinct imprints in the mass and spin distributions [110, 111].

- Primordial BHs (PHB) born from the collapse of density inhomogeneities might constitute a non-negligible fraction of the current dark matter content of the Universe: these PBHs might eventually merge and be indistinguishable from the BHBs formed via the astrophysical scenarios [112].

Here we focus mostly on the isolated binary channel. The evolution of stars in binary is still a poorly understood process. Apart from the physical processes driving the evolution of each stars individually, stars in binary exchange energy and angular momentum in non-trivial way.

In Fig. 3.2 we report a scheme to illustrate the stages from the ZAMS binary to the compact object binary (in this case a SBHB). The most massive star in a binary is the first to evolve outside the main sequence branch: in the last stage of its life, the star expands, filling its Roche lobe, and mass is transferred to the secondary stars that starts accreting. Eventually the donor star ends up in a SN explosion that could potentially unbind the binary preventing the formation of a compact objects binary. However if the donor star is massive, it directly collapses in a BH or produces a weak supernova explosion: in this case the binary is likely to survive and a compact object (either a BH or a NS) is present. After some time, even the second star evolves in a red giant, engulfing the compact object with a *common envelope*. During this phase, the two bodies migrate to the center, transferring orbital energy and angular momentum to the external envelope. If enough energy is released the star merges with the compact object, otherwise it ends up in a close orbit, without its envelope[3]. Finally even the second star undergoes SN explosion, however, thanks to the fact that the objects are closer than the previous explosion, the binary is more likely to survive this step. If the stars binary survived up to this point, then it has become a compact object binary.

[3]Clearly if not enough energy is released, the two compact objects end up being too far for GW to be efficient and drive them to coalescence in a Hubble time

If the two objects are relatively close, GW emission will lead them to merger in a Hubble time. The coalescence time for this system range from few Myr to Gyr following a log-flat distribution. However there are large uncertainties on the common envelop phase, on the internal mixing and on the angular momentum transport resulting in wide range for the predicted rate. Clearly if not enough energy is released during the common envelope phase, the two compact objects end this stage being too far for GW to efficient drive them to coalescence in a Hubble time.

This formation scenario is explored by population synthesis codes like StarTrack [113], MOBSE [114] and Compass [115], taking as input parameters the mass of the two stars, the orbital and the eccentricity of the orbit. Their mass distributions and rates are consistent with the constraints from LIGO/Virgo observations [4].

The large astrophysical uncertainties translate in large error bars for the rates of different types of compact objects. For BHBs the intrinsic current rates ranges between $9.7-101\,\mathrm{Gpc^{-3}\,yr^{-1}}$, while for NS-NS binary the interval is $110-3840\,\mathrm{Gpc^{-3}\,yr^{-1}}$. The rate for BH-NS binary merger is even more uncertain because up so far no unambiguously detection has been made (even if some detection might be consistent [116, 117]) and the current upper limit is $610\,\mathrm{Gpc^{-3}\,yr^{-1}}$.

The detected rates take into account the detector sensitivity and therefore produce different results: even if the number of NS-NS merger is higher, the horizon distance for this type of source is small due to their relatively low mass. On the other side, BHBs can be detected up to higher redshift. For BHBs, we expect several hundreds of events per year and just a few events for NS-NS and BH-NS binaries [37].

3.1.3 Motivations of this work

Stellar evolutionary models predict that a gap in the BH mass distribution should naturally form as the result of stellar evolution. LIGO/Virgo are sensitive in this mass range, so we expect to be able to detect a BHB with component mass in the gap [118].

Clearly, the dynamical scenario provide a natural way to fill the gap. If "second generation" BH [73], i.e. the BH formed after the merger of two previous BHs, is retained inside the cluster, multiple encounters might lead it to coalesce again with another BH. However, the dynamical scenario predict lower rates than the isolated channel. Moreover, [119] and [120] proposed that massive stars with small core and large envelope masses might collapse, thus avoiding the pair-instability phase and producing BHs in the mass gap. Even CHE and AGN formation scenarios might be able to fill partially this gap.

Due to the theoretical and observational evidences, several authors have already

explored the possibility of a gap in the BH mass distribution. Using only the first 3.9 detections, [121] find preliminary evidence of a gap at $40\,M_\odot$ and conclude that a gap is necessary, if no heavy BHBs are detected, to avoid BHs mass distribution too steep. Moreover, if the BH mass distribution follow a Salpeter distribution, it will require $\gtrsim 60$ BHBs detections to invalidate the power-law index, unless no BH exist above the gap. [122] conclude that we should be able to put constrain on the presence of a gap in the BH mass distribution after $\lesssim 20$ detections. They also predict the occurrence of PPSN might lead to a peak close to the lower edge of the BH mass distribution.

For the rest of the current chapter we will refer to three different sub-populations:

(I) *below-gap* binaries $\rightarrow m_1 < 60\,M_\odot$, $m_2 < 60\,M_\odot$;

(II) *across-gap* binaries $\rightarrow m_1 > 120\,M_\odot$, $m_2 < 60\,M_\odot$;

(III) *above-gap* binaries $\rightarrow m_1 > 120\,M_\odot$, $m_2 > 120\,M_\odot$.

'Below-gap' binaries are the binaries that LIGO/Virgo have already observed during the first, second and third run. 'Across-gap' binaries present a massive BHs with a light companion, with a typical $q < 0.4$. In 'above-gap' binaries both BHs are above the pair-instability mass gap. The latter population is particularly interesting because such massive BHS have been invoked in the literature as possible seeds for the formation and growth of the supermassive BHs that we currently see accreting at high redshift [123, 124]. Moreover, up to now, most of population synthesis codes are unable to evolve massive star ($M_{ZAMS} > 150\,M_\odot$) in binaries due to the aforementioned uncertainties , stopping around $\simeq 100 - 150\,M_\odot$ [125–127] [4]. However, from Fig. 3.1, it is clear that this limit prevents the possibility to synthesize BHs above the mass gap with the current codes.

Moreover 'across-gap' and 'above-gap' binaries are optimal sources for LISA or ET due to the larger total mass compared to the standard SBHBs detected by LIGO/Virgo. Under some assumption, 'above-gap' binaries might even be the dominant multiband SBHBs detected by LISA due to the long inspiral and the large number of cycles performed in band.

Finally, in the past, many studies [129, 130] explored the possibility of a stochastic background from the first generation of stars, usually known as POPIII stars. An additional source of BHBs above the pair-instability mass gap might improve the background strain and, eventually, be comparable to the expectation for 'below-gap' SBHBs.

[4] See also [109, 128] for more recent results from populations synthesis code for SBHB in the pair-instability mass gap.

3.2 Formalism and setup

3.2.1 SFR, metallicity and IMF

In this study, we employ two models referred as *optimistic* and *pessimistic*. The reason behind these names come from the assumptions on three quantities:

(I) star formation rate, SFR;

(II) mean metallicity evolution, $\langle Z \rangle$, across cosmic time;

(III) initial mass function (IMF).

We obtained two additional models mixing these quantities as later described.

The SFR represents the amount of mass converted in stars and it is typically given in unit of comoving volume and year. In the literature different prescriptions can be found.[5] For example Madau and Fragos [132] propose an expression for the SFR as

$$\mathrm{SFR(z)} = \mathrm{a}\,\frac{(1+\mathrm{z})^{\mathrm{b}}}{1+[(1+\mathrm{z})/\mathrm{c}]^{\mathrm{d}}}\ \mathrm{M}_{\odot}\,\mathrm{Mpc}^{-3}\,\mathrm{yr}^{-1} \tag{3.1}$$

with $a = 0.01$, $b = 2.6$, $c = 3.2$ and $d = 6.2$. This expression is based on UV and infrared surveys [133], adopted to better reproduce novel observations $4 \lesssim z \lesssim 10$ [134] and a Kroupa IMF [135].

Strolger et al. [136] proposed a different formulation (later adopted in [102]) as

$$\mathrm{SFR(t)} = \mathrm{a}\,(\mathrm{t}^{\mathrm{b}}\mathrm{e}^{-\mathrm{t}/\mathrm{c}} + \mathrm{d}\,\mathrm{e}^{\mathrm{d}(\mathrm{t}-\mathrm{t}_0)/\mathrm{c}})\,\mathrm{M}_{\odot}\,\mathrm{Mpc}^{-3}\,\mathrm{yr}^{-1} \tag{3.2}$$

where t is the cosmic time in Gyr measured in the rest-frame, t_0 is the age of the universe and the parameter values are $a = 0.182$, $b = 1.26$, $c = 1.865$, $d = 0.071$. This expression is a modified version of the one presented in [137] and corrected for the data from several surveys [138].

The mean metallicity represents the metal to hydrogen ratio. Since metals are the results of stellar reactions, the metallicity is lower at high redshift when the Universe was young and few stars have polluted the galactic environment.

Also for this quantity several expressions can be found in the literature. Madau and Fragos [132] propose to fit the average metallicity of newly formed stars as

$$\log_{10}\langle Z/Z_{\odot}\rangle = a_s - c_s z^{d_s} \tag{3.3}$$

where $a_s = 0.153$, $c_s = 0.074$ and $d_s = 1.34$. Madau and Dickinson [133] proposed also a mean metallicity evolution for the intergalactic medium as

$$\log_{10}\langle Z(z)\rangle = 0.5 + \log_{10}\left(\frac{y(1-R)}{\rho_b}\int_z^{20}\frac{97.8\times10^{10}\mathrm{SFR}(z')}{H(z')}dz'\right) \tag{3.4}$$

[5] In [131] different SFR prescriptions are presented based on the observation of luminous galaxies and on the rate of gamma-ray bursts with a possible early POPIII population.

with a net metal yield $y = 0.019$, a return fraction $R = 0.27$, a barion density $\rho_b = 2.77 \times 10^{11} \Omega_b h_0^2$ $\mathrm{M}_\odot\,\mathrm{Mpc}^{-3}$ with $h_0 = 0.7$. For the cosmological quantities $H(z) = H_0 E(z)(1+z)$ with $H_0 = 70\,\mathrm{Km\,s^{-1}\,Mpc^{-1}}$ and $E(z) = \sqrt{\Omega_m(1+z)^3 + \Omega_k(1+z)^2 + \Omega_\Lambda}$ with $(\Omega_b,\, \Omega_m,\, \Omega_k,\, \Omega_\Lambda) = (0.045,\, 0.3,\, 0,\, 0.7)$. However we would like to stress the difference between these two expressions: while Eq. (3.3) represents the mean metallicity of newly formed stars, Eq. (3.4) describes the metal content of all the barions in the Universe. For our study the former expression is the correct one because galaxies are biased region for the star formation therefore their metal content is higher than the pristine intergalactic medium. Assuming Eq. (3.4) might lead to a lower metallicity and, possibly, to an incorrect estimate on the number of BH and their mass distribution. In order to take into account this characteristic, we shifted Eq. (3.4) in order to match Eq. (3.3) at $z = 0$, to model a possible rapid decline of the metallicity between the present and redshift $z \simeq 4$ and to provide a lower limit to our models. At each time step in redsfhit, we assume a log-normal distribution of metallicity around $\langle Z(z) \rangle$ with $\sigma = 0.5$ dex as standard deviation.

An example of the SFR and metallicity prescriptions adopted for our study are reported in Fig. 3.3. Both SFRs match quite well at low-redshift, thanks to the abundance of data and observation, while, at high redshift the models vary of $\simeq 2$ order of magnitudes. Similar arguments apply also for the metallicity evolution.

Since for the first model both the SFR and the metallicity are taken from Madau and Fragos [132], it is labeled as "mSFR-mZ". The second model takes the SFR from Strolger et al. [136] and the metallicity is *shifted*, so it is labeled as "sSFR-sZ". We consider two intermediate models, labelled "mSFR-sZ" and "sSFR-mZ" and obtained combining the SFR and the metallicity prescriptions.

The initial mass function (IMF) describes the number of stars formed for bin of unit mass. We consider a power-law expression as [135, 139]:

$$dN/dM = \xi(M, \alpha) \propto \begin{cases} M^{-1.3} & \text{for } \mathrm{M/M_\odot} \in [0.08, 0.5] \\ M^{-2.2} & \text{for } \mathrm{M/M_\odot} \in [0.5, 1.0] \\ M^{-\alpha} & \text{for } \mathrm{M/M_\odot} \in [1.0, 350]. \end{cases} \tag{3.5}$$

with $\alpha = 2.7$ for the "mSFR" model and $\alpha = 2.35$ for the "sSFR" one. From these arguments it is clear that the "mSFR-mZ" can be considered as the pessimistic model and "sSFR-sZ" as the optimistic one: the former has a higher mean metallicity evolution (BHs are lighter), lower SFR and steeper IMF (we form less star).

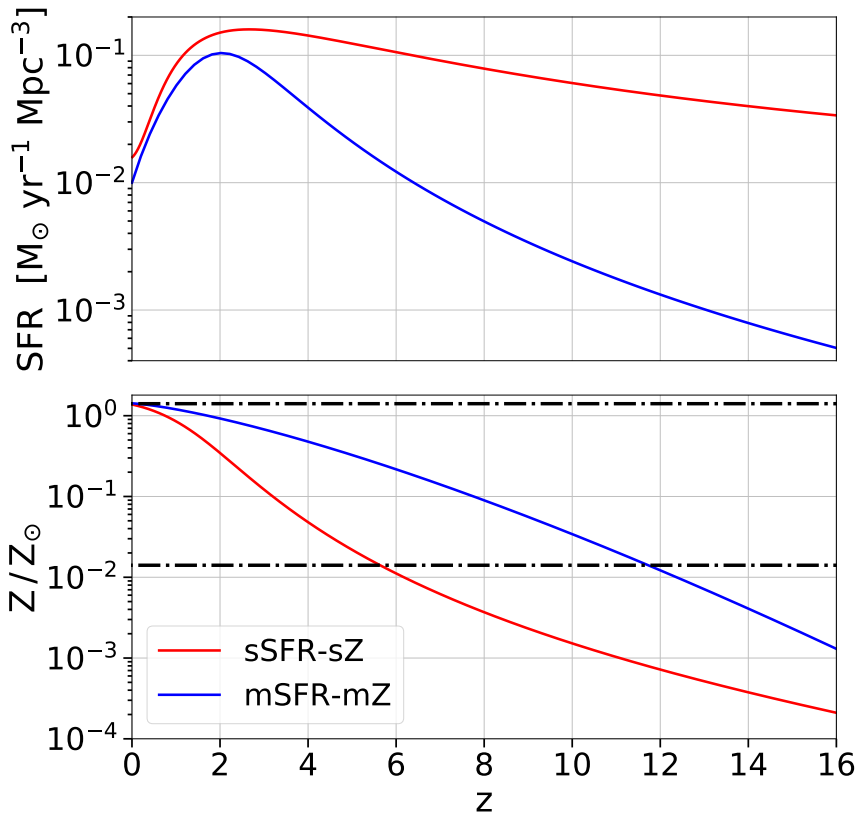

Figure 3.3: SFR (upper-panel) and mean metallicity (lower-panel) of the galaxy population $\langle Z \rangle$ (we choose solar metallicity $Z_\odot = 0.0142$) for the models mSFR-mZ (blue lines) and sSFR-sZ (red lines) as function of redshift. The dashed-dotted lines in the lower panel show the range of metallicity that can be evolved with SEVN. Stars with metallicity exceeding this range are considered to follow the same evolution of stars in the lowest/highest metallicity bin.

3.2.2 Merger rate computations

The differential comoving volume number density formation rate of progenitor stars as a function of cosmic time, mass and redshift is

$$\frac{\mathrm{d}^3 n_\star}{\mathrm{d}t \mathrm{d}\log M_\star \,\mathrm{d}\log Z} = \frac{f_\star(\alpha)}{\langle m_\star(\alpha)\rangle} \mathrm{SFR}(t) \times p(\log M_\star) \times p(\log Z). \tag{3.6}$$

Here $f_\star$ and $m_\star$ are the fraction of simulated binaries and the average IMF mass as defined by Eq. (6-7) of [130] and $p(\log M_\star)$, $p(\log Z)$ are the probability densities of stellar mass and metallicity.

Both $f_\star(\alpha)$ and $< m_\star(\alpha) >$ depend from the IMF and they can be expressed as

$$f_\star(\alpha) = \frac{\int_8^{350} \xi(m,\alpha)\, dm}{\int_{0.1}^{350} \xi(m,\alpha)\, dm} \tag{3.7}$$

and

$$< m_\star(\alpha) >= \frac{\int_{0.1}^{350} \xi(m,\alpha)\, m\, dm}{\int_{0.1}^{350} \xi(m,\alpha)\, dm}. \tag{3.8}$$

We separately compute the IMF probability distribution $p(\log M_\star)$ as:

$$p(\log M_\star) = \int_M^{M+\Delta \log M} \xi(M',\alpha)\, dM' \tag{3.9}$$

where log in the log based 10 logarithm. We also compute the metallicity probability distribution $p(\log Z)$ for each time step as:

$$p(\log Z) = \int_Z^{Z+\Delta \log Z} \frac{1}{\sqrt{2\pi\sigma^2}\, Z'} \exp\left(\frac{[\log(Z') - \log(Z_{\rm mean})]^2}{2\sigma^2}\right) dZ'. \tag{3.10}$$

Note that, while the IMF probability distribution is always the same, the metallicity probability distribution changes at each time bin due to the increase of mean metallicity across cosmic time.

We perform N $= 10^3$ steps in mass and metallicity to properly explore the parameter space. For a given interval $(\Delta \log_{10} M, \Delta \log_{10} Z)$, we evolve a single star with SEVN to determine its final state and final mass. Stars with metallicity exceeding our range are treated as stars at the lowest or highest metallicity available. For simplicity, we consider only stars with BH as final state. This allows us to map Eq. (3.6) into the BH formation rate density, $\mathrm{d}^2 n/(\mathrm{d}t\, \mathrm{d}m_1)$. The mass of the primary BH, m_1, is drawn from this distribution. We note that the progenitor density in a given time interval is typically translated in a remnant density to a later time. This takes into account the specific lifetime of a star in the given interval $(\Delta \log_{10} M, \Delta \log_{10} Z)$.

To convert the birth rate of BHs into the merger rate of BHBs we need two additional assumptions: i) all BHs are in binaries and the mass of the secondary BH is drawn from a flat mass ratio $q = m_2/m_1 < 1$ distribution in the range [0.1, 1] [6] and ii) mergers take place at a time $t_m = t + \tau_d$ where the delay time τ_d is distributed according to $p(\tau_d) \propto \tau_d^{-1}$ [127, 141] between $\tau_{d,\,\rm min} = 50\,$Myr and $\tau_{d,\,\rm max} = t_{\rm Hubble}$ [131], where $t_{\rm Hubble}$ is the Hubble time.

We note that from assumption i), there might be binaries with m_2 falling in the mass gap. However these binaries are discharged and the whole population is

[6] We also investigate the possibility if a flat mass ratio distribution in the range [0.5,1] [140].

re-normalized to guarantee that the total mass density of allowed BHBs is equal to $\int \mathrm{d}\log m_1\, m_1[\mathrm{d}^2n/(\mathrm{d}t\,\mathrm{d}\log m_1)]$. Since m_1 covers all the BH mass spectrum, this re-normalization does not affect in particular one sub-population respect to others.

Therefore, similarly to mass and metallicity, we compute the probability distribution for time delay and mass ratio to obtain the number density of BHBs merging per unit of mass, time and mass ratio.

The rate density per comoving volume of merging BHBs is therefore given by:

$$\frac{\mathrm{d}^3n}{\mathrm{d}t_m\,\mathrm{d}\log m_1\,\mathrm{d}q} = \mathcal{C}\int_{t<t_m}\int \frac{\mathrm{d}^4n}{\mathrm{d}t\,\mathrm{d}\tau_d\,\mathrm{d}\log m_1\,\mathrm{d}q}\delta(t_m-(t+\tau_d))\mathrm{d}\tau_d\mathrm{d}t \tag{3.11}$$

where $\mathcal{C}$ is a normalization constant to re-scale the intrinsic BHB merger rate in the local Universe to

$$\int_{5\,\mathrm{M}_\odot}^{50\,\mathrm{M}_\odot}\mathrm{d}\log m_1\int \mathrm{d}q\frac{\mathrm{d}^3n}{\mathrm{d}t_m\,\mathrm{d}\log m_1\,\mathrm{d}q}\bigg|_{z=0} = 50\,\mathrm{Gpc}^{-3}\,\mathrm{yr}^{-1}, \tag{3.12}$$

close to the best estimate provided by the LIGO-Virgo O2 run [142]. This a posteriori normalization is needed because we started from the SFR and assumed, up so far, that all massive stars form BHBs. However this is not true due to the uncertainties discusses in 3.1.1.

We checked, however, that both the resulting BHB merger rate density as a function of redshift and the mass function of merging BHBs below the pair-instability gap are in good agreement with sophisticated population synthesis models found in the literature [e.g. 119].

Since we are more interested in massive SBHBs above the pair-instability mass gap, we define their merger rate as

$$\mathcal{R}(z_m) = \int_{120\,\mathrm{M}_\odot}^{\infty}\mathrm{d}\log m_1\int \mathrm{d}q\frac{\mathrm{d}^3n}{\mathrm{d}t_m\,\mathrm{d}\log m_1\,\mathrm{d}q}. \tag{3.13}$$

Depending on q value, we define the sub-classes of 'across-gap' ($m_2 < 60\,\mathrm{M}_\odot$) and 'above-gap' ($m_2 > 120\,\mathrm{M}_\odot$) SBHBs. From our choice of the mass gap range, 'across-gap' binaries are characterized by $q < 0.5$ and 'above-gap' binaries by $q \gtrsim 0.4$.

The number of detections per year is computed as

$$\mathcal{R}_{\mathrm{det}} = \int \mathcal{R}(z_m)\frac{1}{1+z_m}\frac{\mathrm{d}V_c}{\mathrm{d}z_m}p_{\mathrm{det}}\,\mathrm{d}z_m \tag{3.14}$$

where $(1+z_m)^{-1} = \mathrm{d}t_m/\mathrm{d}t_m^{\mathrm{obs}}$ accounts for the time dilation due to cosmic expansion between the source and the observer frames and $\mathrm{d}V_c/\mathrm{d}z_m$ is the differential comoving volume shell.

The quantity $p_{\rm det}$ represents the probability to detect a binary with (m_1, q, z_m) with randomic sky-positions and binary inclination [143]. Assuming a fixed threshold $S/N_{\rm thr}$, $p_{\rm det}$ can be expressed as the cumulative distribution function of the ratio between the $S/N_{\rm thr}$ and $S/N_{\rm opt}$ [37], i.e.

$$p_{\rm det} = P\left(\frac{S/N_{\rm thr}}{S/N_{\rm opt}}\right) = P(w) \tag{3.15}$$

where P denote the cumulative distribution function and we use Eq. (1.19) for the last equality.

Eq. (3.14) is ideal to compute the detection rate for ground-based detectors. However, LISA will observe multiband and persistent sources, that will remain in band for long time. Therefore it is necessary to take into account the initial frequency at which the source is emitting. The distribution of inspiralling sources in the LISA band is given by

$$\frac{{\rm d}N}{{\rm d}\log m_1\,{\rm d}q\,{\rm d}z\,{\rm d}\ln f_{\rm gw}} = \frac{{\rm d}^3 n}{{\rm d}t_m\,{\rm d}\log m_1\,{\rm d}q}\frac{{\rm d}V_{\rm c}}{{\rm d}z}\frac{{\rm d}t_m}{{\rm d}\ln f_{\rm gw}}, \tag{3.16}$$

where ${\rm d}t_m/{\rm d}\ln f_{\rm gw}$ is given by differentiating eq. (1.7) [68] as

$$\frac{{\rm d}t_m}{{\rm d}\ln f_{\rm gw}} = \frac{5}{96\pi^{8/3}}\left(\frac{c^3}{G\mathcal{M}}\right)^{5/3}(f_{\rm gw}(1+z))^{-8/3}. \tag{3.17}$$

Here $f_{\rm gw}$ is the observed GW frequency. In this study we consider only circular binary because GWs are known to circularize the orbit.

From Eq. (3.16) we draw 10 Monte Carlo realisations of the SBHB distribution in the range $[10^{-4}, 10^{-1}]$ Hz. We assume that the sampled SBHBs represent the distribution of sources at the beginning of LISA mission. Finally we repeat the draw for each SBHB population model described in subsec. 3.2.1.

We evolve each source forward in time assuming GW-driven dynamics and evaluate their S/N at the exit of LISA band or at the end of time mission. For each value of m_1, q and $z_{\rm m}$, we compute the S/N assuming random sky positions, polarization and inclinations angles. We also assume non-spinning BHs. For ground-based detectors, we estimate the S/N with the LALsuite [144], modeling the inspiral-merger-ringodown signal with the IMRPhenomD waveform [145, 146]. For LIGO during O1/O2, we choose $S/N_{\rm thr} = 8$ while for LIGO/Virgo at design sensitivity and ET we assume $S/N_{\rm thr} = 12$. Similarly for LISA, we adopted the IMRPhenomC waveform [147] to compute the S/N and considered a source detected if its S/N was above $S/N_{\rm thr} = 8$. Amongst the detected events in LISA, we select the multiband events ($\tau < 4\,{\rm yr}$) and check if they can also be detected with LIGO/Virgo or ET. We also explore a possible extended LISA time mission of 10 years.

For O2 LIGO sensitivity, we adopt the curve labelled as 'mid' in [148]. We also consider Advanced LIGO [aLIGO, 149], Advanced Virgo [AdVirgo, 13] and Einstein Telescope [ET-D, 150]. For LISA we adopt the curve described in [151].

Finally we also compute the level of the stochastic GWB generated by the inspiralling SBHBs, combining the 'across-gap' and 'above-gap' sub-populations. The stochastic GWBs computed by summing in quadrature the characteristic strains of the unresolved sources and its $S/N_{\rm gwb}$ is estimated as in Thrane and Romano [152] and Sesana [153]:

$$(\mathrm{S/N_{gwb}})^2 = T \int \gamma(f_{\rm gw}) \frac{h^4_{c,\rm gwb}}{f^2_{\rm gw} S_n(f_{\rm gw})^2} \mathrm{d}f_{\rm gw} \tag{3.18}$$

where $T = 4$ yr is the LISA mission required lifetime, $h^2_{c,\rm gwb}(f_{\rm gw}) = 2 f_{\rm gw} S_h(f_{\rm gw})$ (being $S_h(f_{\rm gw})$ the power spectral density of the signal), and $\gamma(f_{\rm gw}) = 1$ [see Fig. 4 in 152]. We also estimate the strength of the GWB via its GW energy density parameter as

$$\Omega_{\rm gw}(f_{\rm gw}) = \frac{2}{3} \left(\frac{\pi f_{\rm gw} h_{c,\rm gwb}}{H_0} \right)^2 . \tag{3.19}$$

3.3 Results

3.3.1 Implications for ground-based detectors

In Fig. 3.4 we report the number density of SBHBs formed with SEVN versus chirp mass for different metallicity values.

The three sub-populations cover different chirp mass ranges: the maximum chirp mass for 'below-gap' binaries is $\simeq 50\,\mathrm{M}_\odot$, while 'across-gap' ('above-gap') binaries have chirp mass ranging in $\mathcal{M}/\,\mathrm{M}_\odot \in [40, 100]$ ($\mathcal{M}/\,\mathrm{M}_\odot \in [100, 240]$). We note that a maximum chirp mass of $\simeq 50\,\mathrm{M}_\odot$ is compatible with results from independent synthesis code [154].

'Across-gap' and 'above-gap' sub-populations come from very low-metallicity stars $\langle Z \rangle < 1.2 \times 10^{-3}$, while 'below-gap' binaries are consistent with that of [119] (see their Fig. D2). In particular we match better the maximum chirp mass from metal-rich stars ($\langle Z \rangle > 8 \times 10^{-3}$) rather than the ones from metal-poor progenitors $\langle Z \rangle < 8 \times 10^{-3}$. In the latter case, we obtain slightly heavier BHs with $\mathcal{M} \in [40,\, 50]\,\mathrm{M}_\odot$, but this is expected due to the difference between our approach and binary evolution.

We also notice that, due to our choice on the mass ratio, the source-frame chirp mass distributions show no evident gap across the three sub-populations. The number density of BHBs varies of 1-2 order of magnitude between the most extreme models because of the different SFR, metallicity evolution and IMF.

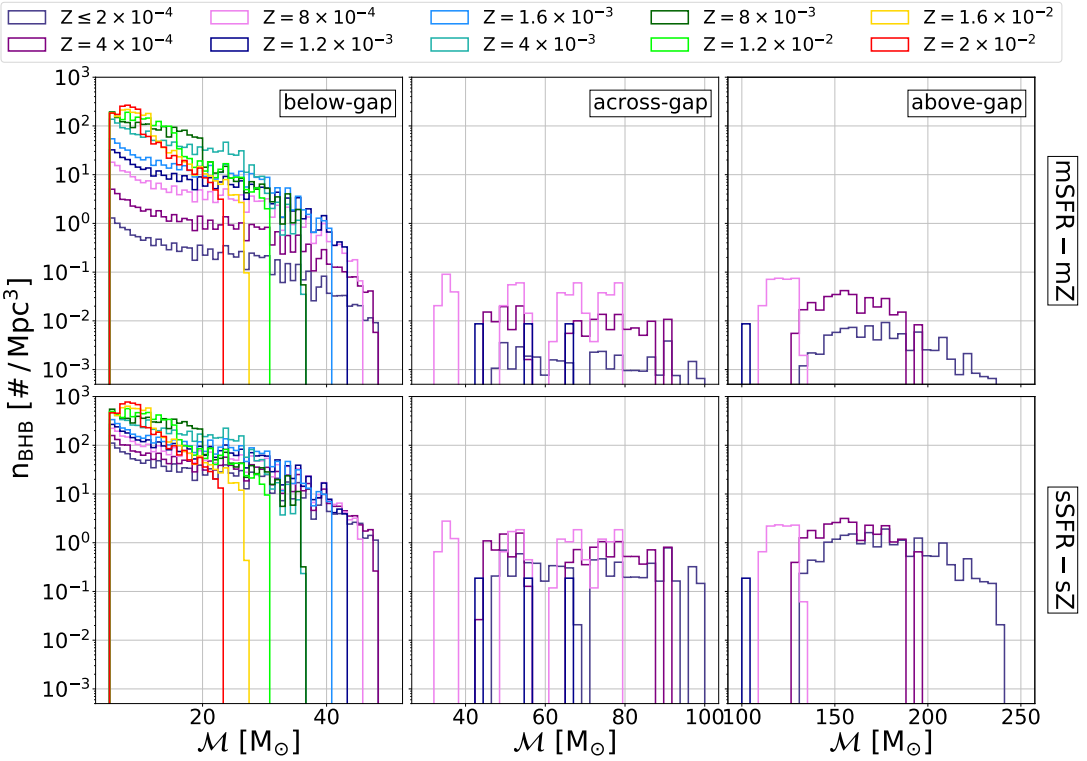

Figure 3.4: Number density of BHBs formed (per unit comoving volume of Mpc^{-3}) versus their $\mathcal{M}$. Each color represents different metallicity as labeled in the upper section of the plot. From left to right: 'below-gap', 'across-gap' and 'above-gap' binaries. From top to bottom: mSFR-mZ and sSFR-sZ (intermediate models not shown).

In Fig. 3.5 we show the intrinsic merger rate (i.e. the number density of mergers per unit of comoving volume and year) for our optimistic and pessimistic models. For a deeper insight we split the total merger rate into the contribution from each sub-populations. The total merger rate is dominated by 'below-gap' binaries during all the cosmic history. Due to the normalization imposed with Eq. (3.12), both sSFR-sZ and mSFR-mZ models predict the same intrinsic merger rate at $z = 0$. The merger rates remain similar up to $z \simeq 2$ but end up with more than an order of magnitude of difference at $z \simeq 10$.

Moving to 'across-gap' and 'above-gap' sub-populations, their merger rates are three (four) orders of magnitude lower than the one from 'below-gap' binaries for the sSFR-sZ (mSFR-mZ) model. At $z = 0$ there is roughly a difference of one order of magnitude between the predictions of the two models. However in both models the 'above-gap' sub-population leads to slightly more mergers than the

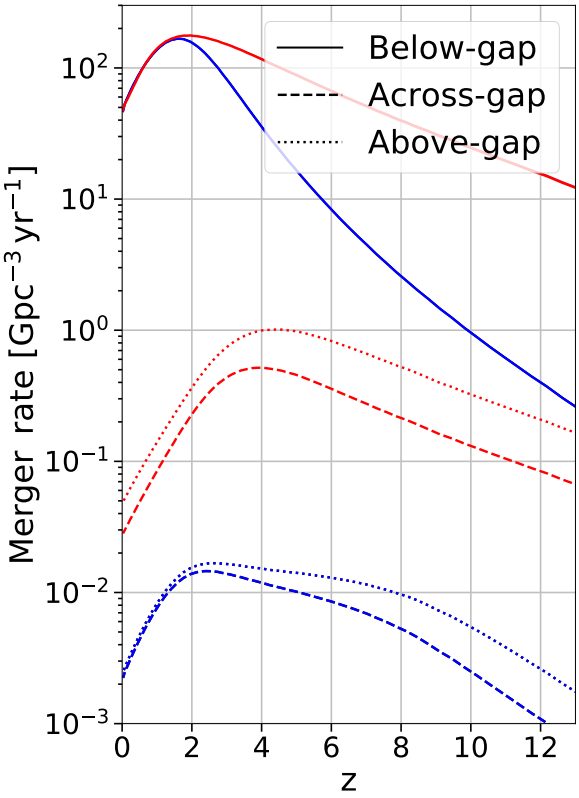

Figure 3.5: Intrinsic merger rate (in unit of comoving Gpc^{-3} and year) versus redshift for the sSFR-sZ model (red lines) and mSFR-mZ (blue lines). The merger rate is decomposed into the BHB sub-populations: 'below-gap' (solid lines), 'across-gap' (dashed lined) and 'above-gap' (dotted lined).

'across-gap'. The two mixed models (mSFR-sZ and sSFR-mZ, not shown) give intermediate results, as expected.

From the intrinsic merger rate, it is possible to compute the detected number rate, i.e. the number of events detected per year, following Eq. (3.14). The result are reported in Tab. 3.1 for O1/O2, LIGO/Virgo at design sensitivity and ET. The non detection of BHBs from the 'across-gap' and 'above-gap' sub-populations is consistent with our estimates. In the pessimistic scenario, LIGO/Virgo at design sensitivity should detect less than 1 event per year and just a handful of events in the sSFR-sZ model. Intermediate models predict $\lesssim 1\,\mathrm{yr}^{-1}$ ($\simeq 2\,\mathrm{yr}^{-1}$) events from the 'across-gap' ('above-gap') sub-populations. The detected rates increase of more than an order of magnitude with ET for all models and sub-populations. For the 'above-gap' sub-population the expected number of events ranges from

Detection rates	Models							
	mSFR-mZ		sSFR-sZ		sSFR-mZ		mSFR-sZ	
	'across'	'above'	'across'	'above'	'across'	'above'	'across'	'above'
Rate O1/O2 (S/N > 8) [yr^{-1}]	0.001	0.001	0.01	0.03	0.005	0.007	0.003	0.005
Rate LIGO/Virgo design (S/N > 12) [yr^{-1}]	0.1	0.4	0.9	6.9	0.4	1.9	0.3	1.6
Rate ET (S/N > 12) [yr^{-1}]	8.1	10.7	212.8	458.5	61.7	116.3	39.8	68.2
Detected events in 4 yr								
LISA events (S/N > 8)	0.2	1.3	2.9	42.5	0.6	12.9	0.3	8.6
LISA events (S/N > 8 & $T_{\mathrm{gw}} < 4\,\mathrm{yr}$)	< 0.1	0.8	0.5	19.3	< 0.1	5.8	< 0.1	4.6
LIGO/Virgo multiband events (S/N > 12)	< 0.1	0.5	0.4	8.8	< 0.1	2.9	< 0.1	1.9
ET multiband events (S/N > 12)	< 0.1	0.8	0.5	19.3	< 0.1	5.8	< 0.1	4.6
S/N_{gwb} background in LISA	2.7		81.5		18.9		14.8	
Detected events in 10 yr								
LISA events (S/N > 8)	0.6	6.2	6.2	152.1	1.9	33.0	1.7	27.0
LISA events (S/N > 8 & $T_{\mathrm{gw}} < 10\,\mathrm{yr}$)	0.1	3.6	1.5	102.6	0.3	22.1	0.6	18.2
LIGO/Virgo multiband events (S/N > 12)	1	1.6	1.2	34.7	0.2	8.6	0.5	5.6
ET multiband events (S/N > 12)	0.1	3.6	1.5	102.6	0.3	22.1	0.6	18.2
S/N_{gwb} background in LISA	3.7		117.8		26.9		21.4	

Table 3.1: Upper panel: Number of mergers detected per year by O1/O2, LIGO/Virgo at design sensitivity and ET for our four different models as labelled in the text. Middle panel: Number of event over four years for LISA, number of events merging within four years to allow multiband observation with LIGO/Virgo at design sensitivity and with ET. Lower panel: Number of event over ten years for LISA, number of multiband events merging within ten years. Last row gives the S/N from the stochastic GW background (summing 'across-gap' and 'above-gap' sub-populations) for the four models. For each model, left (right) column refers to 'across-gap' ('above-gap') binaries.

$\simeq$ [10, 460] yr^{-1}. Moreover, due to the improved sensitivity, ET will be able to detect 'across-gap' binaries even in the pessimistic scenario.

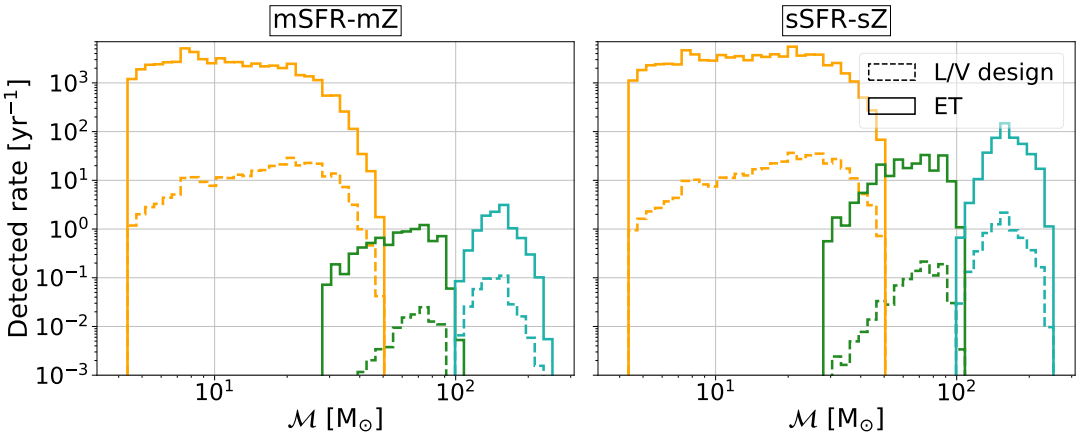

Figure 3.6: Detected rate versus $\mathcal{M}$ for LIGO/Virgo at design sensitivity and ET according to the label. Yellow(green)[blue] lines correspond to 'below-gap' ('across-gap') ['above-gap'] binaries. Left: mSFR-mZ model. Right: sSFR-sZ model

In fig. 3.6 we report the detected rates as function of $\mathcal{M}$ for the optimistic and pessimistic model and the three sub-populations. Independently from the model, the distributions of 'below-gap' binaries detected with LIGO/Virgo are skewed toward higher chirp mass ($\mathcal{M} \simeq 30\,\mathrm{M}_\odot$) due to the detector sensitivity. With ET, the distributions of 'below-gap' binaries are log-flat. The distributions of detected 'across-gap' binaries peak at the highest chirp mass value available for this sub-population, while 'above-gap' binaries are detected with an average $\mathcal{M} \simeq 150\,\mathrm{M}_\odot$.

3.3.2 Prospects for LISA

Since SBHBs are long-living sources in LISA band, their initial frequency plays an important role in their detectability. In order to cast predictions for all our models for LISA, we take into account the starting frequency and sample our average distributions to produce catalogs of SBHB mergers. Each binary is therefore characterized by its redshift, mass of the primary BH, mass ratio and initial frequency in LISA band. We checked that our samples were consistent with our distributions. For each combination of model and sub-population, we perform 10 realizations. In Fig. 3.7 we compare our samples to our distributions for the 'above-gap' sub-population in the pessimistic scenario. The sampled binaries match the expected distributions for primary mass, redshift, mass ratio and observed frequency. As

expected, systems merging in less than four years come from the high frequency portion of the distribution.

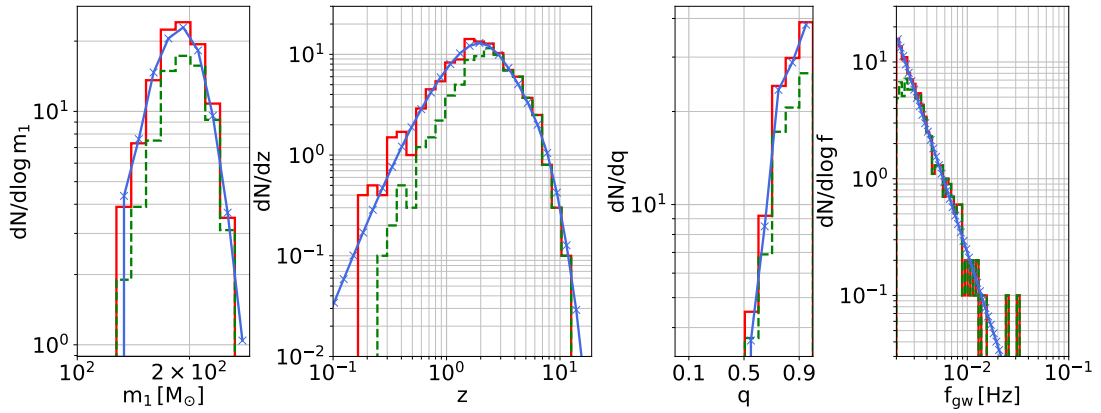

Figure 3.7: Comparison between the distribution of the sample binaries (red lines) and the average distribution (blue lines). Green histograms correspond to multi-band events, i.e. $\tau < 4\,\mathrm{yr}$.

From here we focus on the 'across-gap' and 'above-gap' sub-populations because they represent the novelty of our work. In Fig. 3.8 we show the overall properties of the events observed by LISA with $S/N > 8$, assuming four year time mission. In this figure we are combining the numbers from the 'across-gap' and 'above-gap' sub-populations. For both models, the majority of events concentrates at $z \lesssim 0.5$, with a fraction extending up to $z \approx 1.5$. There is roughly an order of magnitude of difference between the optimistic and pessimistic models. Moreover multiband binaries (i.e $\tau < 4\,\mathrm{yr}$) can be detected to slightly higher redshift.

The chirp mass distribution for the sSFR-sZ model exhibits two peaks corresponding to the 'across-gap' (left peak) and 'above-gap' (right peak) sub-populations. The different heights of the peaks is due to selection effects because it is easier to detect more massive binaries with mass ratio close to unity. It is also clear that we do not expect any multiband event in 4 years from the 'across-gap' sub-population in the pessimistic model. This is due to the aforementioned selection effects and because unequal mass systems evolve slower than equal mass ones.

The detected sources have an initial $f_{\rm gw} \in [10^{-3}, 10^{-2}]\,\mathrm{Hz}$. Only a handful of events are detected at $f_{\rm gw} < 10^{-3}\,\mathrm{Hz}$ in the optimistic scenario, because low frequency sources do not emit enough GWs to produce a signal-to-noise ratio above threshold. Moreover multi-band sources peak at greater frequency respect to persistent ones.

For both model, the merging time distribution of the detected events peak at LISA time mission because systems closer to coalescence produce larger S/N

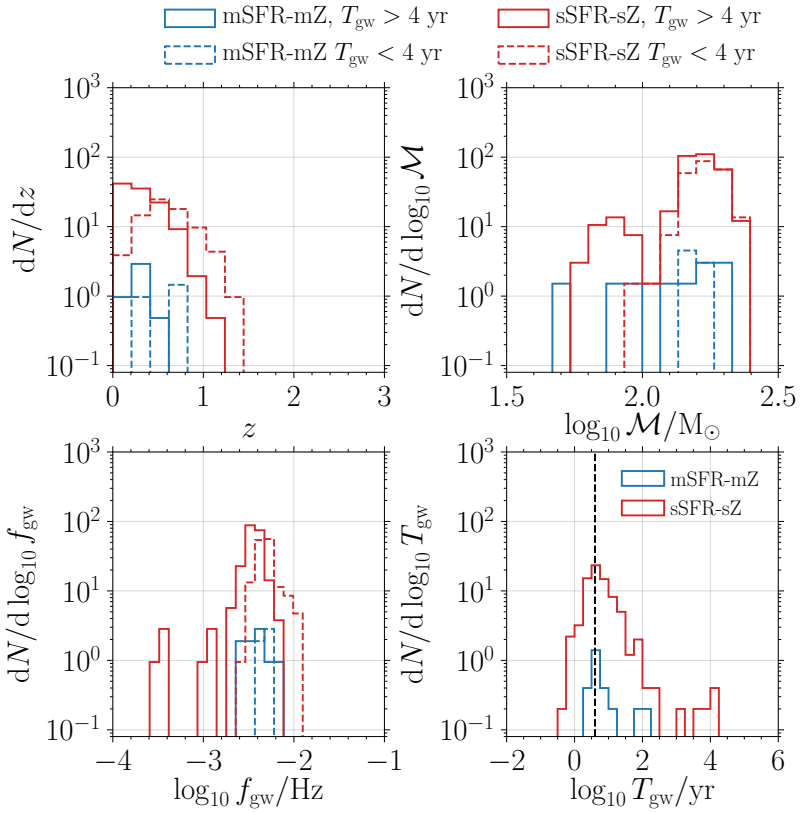

Figure 3.8: Differential number of detected 'across-gap' and 'above-gap' events with LISA from models mSFR-mZ (blue) and sSFR-sZ (red) as a function of redshift, rest-frame chirp mass, observed GW frequency and time to coalescence. Line style and colour code are labelled in the figure. The black dashed line in the lower-right panel corresponds to $T_{\rm gw} = 4\,\mathrm{yr}$

.

if observed for long time. The trade-off between these two effects produce the aforementioned peak (look also at Fig.1 in [155]).

In Tab. 3.1 we report the number of events from the 'across-gap' and 'above-gap' sub-population in LISA for each model considered. For a 4 year time mission, LISA will be able to detect between $\simeq$ 1.5 and 43 events from the pessimistic and optimistic model, respectively. Intermediate models predict $\simeq$ 10 events. The number of events merging in less than 4 years is smaller but still of order unity even for the pessimistic scenario, while the optimistic model predicts $\simeq$ 20 events. These systems will merge at higher frequencies in the LIGO/Virgo band, however, due to their relative high masses, only half of them will be detected by ground-based detectors. The number of events range from $\simeq$ 0.5 for the pessimistic scenario to

$\simeq 10$ for the optimistic one. However, if ET will be operative, all multiband events detected in LISA will also be detected by ET. For a 10 years LISA time mission, the number of events increases by a factor of $\gtrsim 3$. The increases time mission leads to a gain in S/N as $\sim \sqrt{10/4}$. Since $S/N \propto d_L^{-1}$, the accessible volume is almost four times larger and, therefore, the number of detected events increases of a similar quantity.

For the case with a flat mass ratio distribution for $q \in [0.5, 1]$, we find that the rate from the 'above-gap' sub-populations increase of ≈ 2 while we lose completely the possibility to form 'across-gap' binaries.

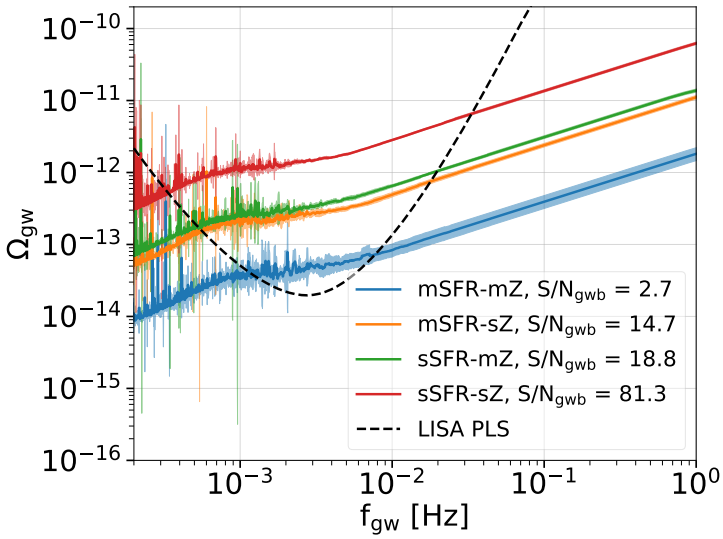

Figure 3.9: GW energy density parameter as function of frequency for the four models as labelled. The dotted-dashed black line represents the LISA power-law sensitivity (PLS) curve from [156] and computed fixing a threshold of $\mathrm{S/N}_{\mathrm{gwb}} = 1$.

In Fig. 3.9 we show the energy density of the stochastic GWB – Ω_{gw}, from Eq. (3.19)– produced combining 'across-gap' and 'above-gap' binaries for all the considered models. In the same figure, we report also the expected background signal-to-noise ratio for each scenario. Apart from the pessimistic model, the signal is loud enough to be detected. In particular for the optimistic scenario, the background signal is comparable to that expected from 'below-gap' BHB and galactic binary populations [e.g. 153, 157]. Our estimate is also consistent with the upper limits reported after the end of the first and second run from the LIGO/Virgo collaboration [158, 159].

3.4 Discussion

The possibility to form and detect SBHBs above the pair-instability mass gap is an intriguing scenario. However our models rely on a set of assumptions that need to be carefully taken into account when evaluating results.

We assumed that our IMF extends up to $350\,M_\odot$ because we want to form massive metal-poor stars that may eventually end in BHs above the mass gap. However the IMFs extend usually up to $\simeq 150\,M_\odot$ [135]. The formation and evolution of such massive stars is still uncertain however there are observational evidence that the IMF might extend to $M \gtrsim 300\,M_\odot$ [160]. Even if we know that such massive stars form, their IMF might follow a steeper distribution above $150\,M_\odot$. This would leave unchanged our conclusion for the 'below-gap' sub-populations but would reduce the number of 'across-gap' and 'above-gap' binaries, depending on the actual slope. However we note that, if massive stars do not form, the merger rate for 'above-gap' and 'across-gap' binaries from this channel has to be zero. In this way future detections of massive BHBs can empirically prove that massive stars form and, eventually, provide constrains on the IMF slope.

The SFR and the mean metallicity evolution described in Sec. 3.2.1 are averaged over all the Universe. This is a necessary approximation for our study but it does not take into account the cosmic evolution of stellar metallicity and its dependence on the galactic environment [161, 162]. Since dwarf galaxies evolve slower, their metallicity can be lower than their massive counterpart at present day. This could in principle change the distribution of BHB mergers across the cosmic time, increasing the number of massive BHBs merging close to us. Moreover even if dwarf galaxies contribution to the number of star formed is smaller, they are more numerous in number than massive galaxies.

Our results are also affected by large uncertainties on the evolution of massive stars in binaries, especially on internal mixing, angular momentum transport. It is also unclear what could happen during the common envelope phase when both stars are more massive than $150\,M_\odot$. In our study we assumed that the same processes rule both the 'below-gap' and the 'above-gap' evolution in the same way. However this might not be truly in principle: massive stars might lose more mass during the common envelope, resulting in lighter BHs. Moreover fast rotating stars might produce a torus around the remnant BH [163], resulting is slightly less massive BHs but still above the mass-gap.

'Above-gap' are perfect targets for multiband observation because they spend many cycles in LISA band before chirping to the high frequency portion of the spectrum where ET will detect them. Sky position and chirp mass are expected to be determined with great accuracy in LISA. To quantify this statement we run

a Fisher Matrix code[7] on the population of 'above-gap' in LISA. To model the signal, we adopted the inspiral-only precessing waveform described in Sec. 2.2. Thanks to the large number of cycles and the orbital motion of the detector, these sources are localized with a median precision of $\lesssim 10\,\mathrm{deg}^2$. The single component redshifted masses are constrained to better than 1% percent. Due to the low S/N, the luminosity distance is poorly determined with a median uncertainty of $\lesssim 30\%$. Spins would be essentially unresolved.

In addition 'above-gap' SBHBs might also be targets for possible EM counterpart search. If a torus from the progenitor stars is formed around the binary, the gas might accrete on the binary or on the remnant BH. LISA will be able to greatly localize these sources in the sky and the detected systems will be preferentially face-on/off so if a jet is launched along the angular momentum of the binary, it might point directly toward us. In Fig. 3.10 we report the fraction of detected 'above-gap' binaries for the sSFR-sZ model in LISA. As expected, due to the relatively low S/N, most of the source detected will be preferentially aligned with the line of sight of the observer.

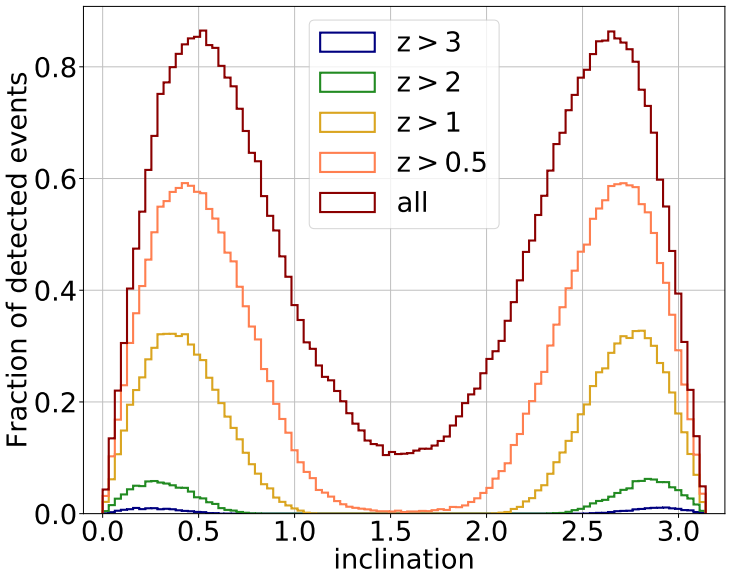

Figure 3.10: Fraction of detected 'above-gap' binaries as function of the binary inclination for the optimistic model.

Finally, during the third observing run the LIGO/Virgo collaboration reported the detection of a signal coming from two very massive BHs with $m_1 = 85^{+21}_{-14}\,\mathrm{M}_\odot$ and $m_2 = 66^{+17}_{-18}\,\mathrm{M}_\odot$ [118]. These BHs are definitely inside the mass gap and

[7]For an exhaustive discussion about the Fisher Matrix see Sec. 4.2

therefore can not be treated by our model. Indeed systems like that are expected to come from dynamical environment or AGN disk [164, 165]. However this is consistent with the observation of multiple formation channels during the third observation run and highlight the necessity to combine different approaches in order to explain the detected distribution [166].

3.5 Summary

In this chapter we develop a simple approach to describe SBHBs above the pair-instability mass gap. The main caveat of our work is the evolution of stars in binary as single stars. Our results are consistent for the population of 'below-gap' binaries but there is no further evidence that the same is true also for SBHBs above the mass gap. In order to bracket uncertainties we implemented a pessimistic and optimistic model with different SFR, mean metallicity evolution and IMF prescriptions. We considered two additional models obtained by mixing the previous one. Stellar physics, BH mass ratio and time delay distribution are the same for all models. For each models, we computed the expected number of mergers from the three sub-populations with the current interferometer, LIGO/Virgo at design sensitivity, ET and LISA. We also computed the expected signal-to-noise ratio produced by unresolved sources in LISA.

Our results can be summarised as follow:

- We reproduce results from more accurate population synthesis code for 'below-gap' binaries. This is an important check to asses the validity of our work. Moreover our rates for 'across-gap' and 'above-gap' sub-population are consistent with a non-detection with the current ground-based detector.

- Our code is extendable to different prescription (i.e. alternative SFR, metallicity evolution, mass ratio and time delay distributions) and can be easily upgradable with new results from population synthesis codes or detections from O3.

- In the pessimistic scenario LIGO/Virgo at design sensitivity should detect less than 1 event per year from 'across-gap' and 'below-gap' sub-populations. The number of events increases to $\simeq 7(\simeq 1)$ for 'above-gap'('across-gap') binaries in the optimistic model. Due to the increased sensitivity, ET should detect $\simeq 10$ events per year even in the pessimistic model, while for the optimistic we expect more than $\simeq 200$ sources per year.

- Moving to low frequency band, LISA will be able to detect 'above-gap' binaries even in the pessimistic scenario. A significant portion ($\simeq 50\%$) of the

detected events in LISA coalesce in less than four year, making them the perfect multi-band sources. In the high frequency section of the spectrum, only $\simeq 50\%$ of the multiband events are detected by LIGO/Virgo at design sensitivity, while ET will detect all of them.

- The unresolved 'across-gap' and 'above-gap' binaries might form a stochastic background in LISA band for $f < 10^{-3}\,\mathrm{Hz}$. In the pessimistic scenario the S/N is to small to be detected but for the optimistic and intermediate models is comparable to the stochastic background expected from 'below-gap' SBHB and galactic binaries.

Overall our results suggest that SBHBs above the pair-instability mass gap might indeed be detectable in the following years with third generation detectors. On the contrary, a non-detection will pose strong constrain on the stellar evolution mechanisms for massive stars in binaries. Moreover SBHBs above the mass-gap at high redshift might have acted as seed for the growth and evolution of the supermassive BHBs that we observe nowadays at the center of galaxies.

Chapter 4

MBHBs and multimessenger astrophysics

This chapter has the scope to provide an overview on two topics that will be the subject of the last two chapters of the Thesis. No results are presented here. In Sec. 4.1 we review the current knowledge on MBHB formation and evolution across cosmic time with a particular focus on the multimessenger potentials combining GW and EM radiation. In Sec. 4.2 we introduce the basic concepts of parameter estimation of a GW signal, in particular for MBHBs in LISA.

4.1 MBHBs in cosmological framework

Massive BHBs (MBHBs) with masses in the range $10^5 - 10^7\,M_\odot$ are key sources for LISA. In the current scenario, MBHs are hosted at the center of galaxies. Even if their formation and evolution is still uncertain and poorly understood, we observe MBHs emitting powerful EM radiation when the Universe was still really young [167–169]. How such massive BHs have formed in such a short amount of time is still an open question and even larger uncertainties affect our understanding of how MBHs evolve and interact with their host galaxy. In the next decade, LISA proposes to shed light on the origin and growth of MBHBs during the Universe evolution [170–178].

In the standard ΛCDM scenario, the structure formation occurs in a bottom-up scenario where DM halos experience multiple mergers along the cosmic history. As a consequence, also the galaxies hosted in each halos undergo the same physical process. If most galaxies host a MBH, the natural outcomes of the current standard cosmological model is that a large number of MBHBs have formed across all epochs [179–184].

Even if the MBHB formed, the path to coalescence is long and complex. One

of the current major issue is the possibility that the coalescence due to emission of GW might take longer than the Hubble time. In Sec. 3.1.2 we saw that, for SBHBs, this problem is typically solved within the common envelope scenario. Clearly a similar solution can not be applied to MBHBs and other mechanisms have to play a role in bringing the two MBHs close enough in order to make GW emission an efficient process.

When two galaxies merge, each MBH migrates toward the center of the merger thanks to the dynamical friction [185] between the MBH and single stars. In each encounter a MBH and a star exchange momentum and kinetic energy and, if the MBH moves on average faster than the stars, the stars gain velocity while the MBH sink in the galactic potential due to the net drag force.

As the two MBH sink toward the center, the number of stars available to scatter decreases and the dynamical friction becomes inefficient. At this stage, MBHs are usually bound in a close orbit but still far from coalescence. The velocity of the MBHs increase and only the three-body interaction between the MBHB and nearby stars might further shrink the orbit. This process is referred to as stellar hardening. During close fly-by, stars acquire energy and angular momentum, reducing the MBHB separation but preventing the possibility of further interactions. In this way, the number of stars that might potentially interact with the binary decreases (the so called 'loss-cone') and also this process becomes inefficient.

At this point the binary has a separation of $\simeq 1\,\mathrm{pc}$. If we assume a binary with $m_1 = m_2 = 10^6\,\mathrm{M}_\odot$ and use Eq. (1.7) to compute the time left before merger in the case of pure GW emission we obtain $\tau \simeq 10^{18}\,\mathrm{yr}$, which is much larger than the Hubble time. Alternatively, GWs are known to subtract energy and angular momentum of the binary shrinking the orbit as [68]

$$\frac{da}{dt} = -\frac{64}{5c^2}\left(\frac{G\,\mathrm{M_{tot}}}{c\,a}\right)^3 \frac{q}{(1+q)^2} \tag{4.1}$$

where a is the semi-major axis of the binary. Integrating this equation we can compute the minimum separation a binary should have in order to merge in less than the Hubble time,. t_H, i.e.

$$a_\mathrm{gw} = 1.2 \times 10^9 \left(\frac{\tau}{t_\mathrm{H}}\right)^{1/4} \left(\frac{\mathrm{M_{tot}}}{\mathrm{M}_\odot}\right)^{3/4} \mathrm{m} \tag{4.2}$$

For a binary with $\mathrm{M_{tot}} = 3 \times 10^6\,\mathrm{M}_\odot$, Eq. (4.2) produce a minimum separation of $a_\mathrm{gw} \simeq 2 \times 10^{-3}\,\mathrm{pc} \ll 1\,\mathrm{pc}$.

Many mechanisms have been proposed to overcome the final parsec problem: non spherically symmetric galactic potentials might induce more stars to enter the loss-cone and interact with the MBHBs; in gas-rich environment, the torque

produced by a gaseous circumbinary disk on the binary can subtract angular momentum, leading to a tighter configuration[1]; in the hierarchical scenario a third MBH can interact with the stalled MBHB and subtract enough energy and angular momentum via three-body interaction [186].

The poor knowledge of the physics behind MBHBs assembly and evolution leads to large uncertainties in the predicted rate of MBHB mergers. To perform these estimates, "semi-analytical models" (SAMs) have been developed and applied with great success. SAMs evolve DM halos along the cosmic history, following the "Press and Schechter" formalism in order to keep a reasonable computational cost. MBHs are growth from high redshift seeds to reproduce observational constrains as high-redshift quasar. Along the cosmic history BHs are evolved taking into account accretion and mergers of the hosting DM halos. Eventually MBHBs can form and coalesce thanks to the aforementioned effects. Finally SAMs provide the rate and distribution of the merging MBHBs, with typical values in the range $\simeq 10 - 300$ events for a 4 year LISA time mission [186, 187].

MBHBs are among the loudest source of GWs that will be accessible by LISA up to very high redshift. In Fig. 4.1 we report contours of constant S/N across the $\mathrm{M_{tot}} - z$ plane[2]. LISA will be able to detect intermediate MBHBs between $\simeq 10^3 - 10^4\,\mathrm{M_\odot}$ up to very high redshift with $S/N \simeq 10 - 20$. MBHBs with $10^5 - 10^7\,\mathrm{M_\odot}$ will merge in the bucket of LISA sensitivity with $S/N \gtrsim 500$ up to $z < 4$, thanks also to the long inspiral phase. At higher masses, MBHBs with $\simeq 10^8 - 10^9\,\mathrm{M_\odot}$ will be detected only with the ringdown portion of the signal.

Moreover MBHBs in the range $10^5 - 10^7\,\mathrm{M_\odot}$ are detected days or week before coalescence. In Fig. 4.2 we report contours of advanced detection time in the $\mathrm{M_{tot}} - z$ plane. For each combination of $\mathrm{M_{tot}}$ and z we computes the sky-averaged S/N and saved the frequency at which we reached $S/N = 8$. The frequency is later converted in time before merger with Eq. (1.7). As expected as we increase the total mass of the system, the coalescence frequency decrease and the detection is pushed close to the merger. Similarly, MBHBs merging when the Universe was still young are redshifted to lower frequencies, leaving less time to claim detection. Systems with $\mathrm{M_{tot}} \in [10^3, 10^5]\,\mathrm{M_\odot}$ are detected one month before merger if the sources are at $z < 2$. However the existence of these intermediate MBHs is still uncertain and, due to the scale relation between the mass of the central BH and the host galaxy, we expect a small amount of gas around them available for accretion. Therefore the possible EM counterparts might be faint and undetectable. Close ($z < 2$) MBHBs with $\mathrm{M_{tot}} \in [10^5, 10^7]\,\mathrm{M_\odot}$ can be detected weeks before merger. Once detected, alerts can be sent to telescopes (similarly to the current pipeline

[1] We note that this mechanism can not be applied in the case of dry merger.

[2] These plots are typically called "waterfall plot" and provide an estimate of the capabilities of a detector or network of detectors.

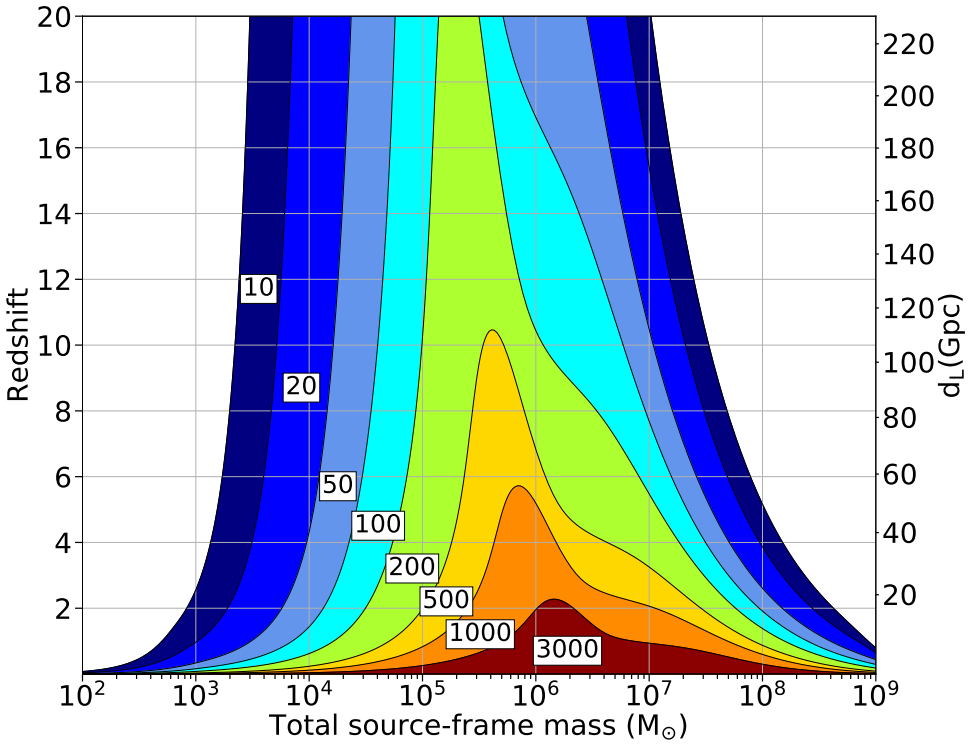

Figure 4.1: Contours of constant S/N for LISA assuming the baseline described in Sec. 6.2 in the $M_{tot} - z$ plane, assuming $q = 1$ and non-spinning BHs.

for LIGO/Virgo triggers) to point the sky position provide by LISA and search for a possible EM counterparts.

Combining the previous considerations, it is clear why MBHBs are key sources for multimessenger astrophysics: the merger is expected to happen in gas-rich environment therefore an EM counterpart can be triggered thanks to the interaction between the binary and the surrounding material; LISA will detect MBHBs in the range $10^5 - 10^7\,M_\odot$ with incredibly large values S/N, allowing for accurate parameter estimation of the sky position and luminosity distance of the source; SAMs predict a reasonable number of events during the LISA time mission even in the pessimistic scenario so a fairly sample of detected MBHB should be available for search of possible EM signature.

The possible EM signature associated to the GW signal from MBHB merger is still puzzling and unknown but, in principle, EM radiation can be triggered at any stage of the merger, i.e. during the inspiral, merger and post-merger phase [188–191]. Although it is well established that the MBHB torque opens a cavity in the circumbinary disk, it has been recently pointed out that gas leaks through the disk edge feeding minidisks around the binary all the way to the final coalescence [192].

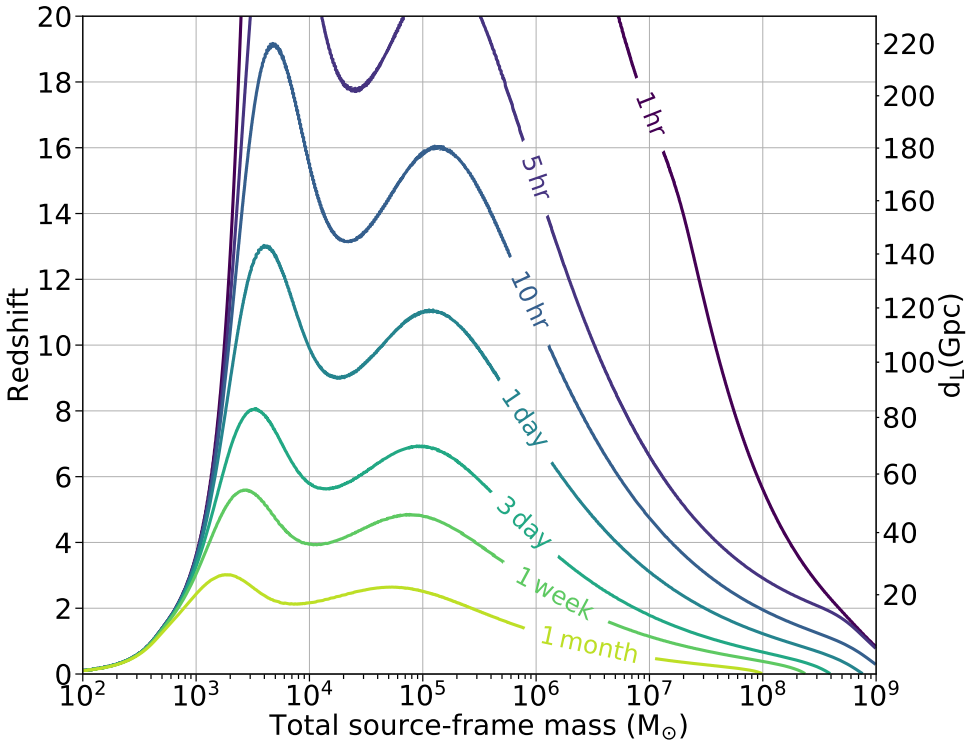

Figure 4.2: Contours of advanced detection time for LISA assuming the baseline described in Sec. 6.2 in the $M_{tot} - z$ plane, assuming $q = 1$ and non-spinning BHs.

Full GRMHD simulations suggest that the circumbinary disk, the streams feeding the minidisks and the minidisks themselves contribute to variable EM emission at all wavelengths [193]. During the inspiral thermal soft X-rays might be produced by the inner rim of the circumbinary disk while corona emission from each BHs minidisk might generate hard X-ray emission. The high energy emission coming from minidisks can be modulated by the binary orbital phase [194] to an extent that might be possibly observed by future X-ray probes [195, 196]. After the merger, the gas might fall on the remnant BH, shedding light on the time-scale between the merger of the MBHB and the rebirth of the AGN. However, the gas itself might hinder the detection of an EM counterpart if the AGN is obscured by the surrounding environment. If the remnant BH receive a kick in the plane at formation [197], months or years after the merger we might observe the recoiling BH accreting the circumbinary disk gas.

The multimessenger potential relies in the additional science that can be achieved combining GW and EM signals. For example, Athena [198] is a large X-ray telescope selected as the 2nd Large class mission of the ESA program. Combining Athena and LISA observations we might in principle observe the very prompt

emission after the merger of a MBHB, the origin of relativistic jets from MBHs and their initial evolution with the galactic environment, constrain the cosmological parameters [199] and perform test on the propagation speed of GWs [200].

4.2 Parameter estimation of GW signal

The science outcomes depend strictly on LISA ability to estimate source parameters. Parameter estimation is a complex and computationally expensive task.

Bayes theorem allows us to infer information on the source parameters, $\bar{\theta}$, taking into account the observation and our prior knowledge on the system parameters, i.e.

$$p(\bar{\theta}|d) = \frac{\mathcal{L}(d|\bar{\theta})\pi(\bar{\theta})}{\mathcal{Z}} \tag{4.3}$$

where $p(\bar{\theta}|d)$ is the posterior distribution for the binary parameters, $\mathcal{L}(d|\bar{\theta})$ is the likelihood of performed the observation d given the parameters $\bar{\theta}$, $\pi(\bar{\theta})$ is the prior distribution and quantify our knowledge a priori and $\mathcal{Z}$ is a normalization constant called 'evidence' defined as

$$\mathcal{Z} = \int d\bar{\theta}\, \mathcal{L}(d|\bar{\theta})\pi(\bar{\theta}). \tag{4.4}$$

For the purpose of the parameter estimation, the evidence is mostly useless. However $\mathcal{Z}$ plays an important role in model selection analysis, where different models are compared to establish which is more consistent with the set of observed data[3]. The prior distribution $\pi(\bar{\theta})$ encapsulate our prior knowledge on the binary parameters that we expect to detect: for example, simulations and observations might inform us on the typical masses and spin distribution before LISA mission. The same GW detected events might form a prior, once enough signals are detected.

If we want to provide the maximum value of the posterior distribution, we have to maximize the product between the likelihood and the prior (or just the likelihood, in case of uniform prior).

We focus on the particular case of a GW signal. Assuming the noise as Gaussian and stationary leads to Gaussian-like likelihood, i.e.

$$\mathcal{L}(d|\bar{\theta}) \propto \exp\left(-\frac{1}{2}(d - h(\bar{\theta})|d - h(\bar{\theta}))\right) \tag{4.5}$$

[3]One detail often omitted is that both prior and likelihood depend on a specific model. For example, the estimated parameters for the detected events by LIGO/Virgo assume GR as the correct gravity theory (even if it is possible to search for deviations).

where we adopted the scalar product defined in Eq. (1.18). The full posterior distribution can be expressed as

$$p(\bar{\theta}|d) \propto \pi(\bar{\theta}) \exp\left((h(\bar{\theta})|d) - \frac{1}{2}(h(\bar{\theta})|h(\bar{\theta}))\right). \tag{4.6}$$

This quantity contain all the necessary information to perform the parameter estimation. In case of a GW signal sampling this posterior distribution might be a burdensome task. We saw in Sec. 1.2 that the typical BHBs is described by 15 parameters, therefore we have to explore a 15 dimensional parameter space in order to find the maximum likelihood value: it is clear that if we choose to evaluate the likelihood only at 10 different points for each parameter, the total amount of evaluation is already practically impossible.

Brute force approach is not the best solution with multidimensional search. To overcome this problem, Markov-Chain Monte Carlo (MCMC) have been developed to provide efficient and reliable estimate of the source parameter. MCMC algorithms explore the parameter space with test particles (known as 'walkers'): at each iteration, the probability for a walker to jump to another point is weighted against the previous jump in order to move toward values that maximize the likelihood. For the parameter estimation of GW signal in LISA, the LISA Data Challenge (LDC) project is being developed and it constitutes now the largest and most updated library available to obtain the information needed to tackle these problems.

In the high signal-to-noise ratio limit, we can derive an easy expression for the likelihood and for the parameter errors. If the S/N is large, the error on the parameters is expected to be small and the likelihood can be considered as a gaussian distribution centered around the true values. For simplicity, we also assume uniform prior, even if at high S/N the shape of the prior becomes irrelevant. Under these assumptions, we can write the true parameter $\bar{\theta}^a$ as

$$\bar{\theta}^a = \theta^a_{ML} + \Delta\theta^a, \tag{4.7}$$

where θ^a_{ML} is the value that maximize the likelihood. Then we can substitute Eq. (4.7) in Eq. (4.6) and expand in power of $\Delta\theta^a$ to obtain

$$p(\bar{\theta}|d) \propto \exp\left(-\frac{1}{2}\Gamma_{ab}\Delta\theta^a\Delta\theta^b\right) \tag{4.8}$$

where Γ_{ab} is the so-called 'Fisher information matrix', defined as

$$\Gamma_{ab} \equiv \left(\frac{\partial h}{\partial\theta^a}\middle|\frac{\partial h}{\partial\theta^b}\right). \tag{4.9}$$

Here $\partial h/\partial\theta^a$ is the partial derivative of the GW waveform respect to the parameter θ^a evaluated at the injected value. Since LISA can be seen as two independent detectors, we construct the total Fisher matrix as the sum of the Fisher matrix for each detector as

$$\Gamma_{ab} = \Gamma^{\rm I}_{ab} + \Gamma^{\rm II}_{ab}\,. \tag{4.10}$$

The correlation matrix is the inverse of the Fisher matrix, $\Sigma = \Gamma^{-1}$. The expected statistical error on a single parameter $\Delta\theta^a$ is computed from the corresponding diagonal element of the correlation matrix as

$$\Delta\theta^a \equiv \sqrt{\langle(\delta\theta^a)^2\rangle} = \sqrt{\Sigma^{aa}}. \tag{4.11}$$

Several authors have studied LISA's capability to localize the source and to measure its parameters [178, 197, 201–211]. Most of these works focused on estimating the binary parameters from the full signal, i.e. from the inspiral to the ringdown, while only few of them explored LISA capability to constrain the source parameters as a function of the time to coalescence [197, 207–209].

Lang and Hughes [207] estimated the uncertainties in the sky position and luminosity distance for a set of MBHBs as function of the time to coalescence exploring the relative impact of spin-precession in the last days before merger. They found that spin-precession reduces the error in the major and minor axis of the error ellipse by a factor $1.5 - 9$ at the end of the inspiral. A similar improvement was found for the luminosity distance. Notably, from their simulations, LISA should be able to localize MBHB with total intrinsic mass $\lesssim 4 \times 10^6\,{\rm M}_\odot$ at $z = 1$ with a precision of $\simeq 10\,{\rm deg}^2$ already one month before merger. They also found that LISA would localize with better precision sources lying outside the Galactic plane. Kocsis *et al.* [197] performed a similar analysis, adopting the 'harmonic mode decomposition' method to compute the 3D localization volume as a function of time to coalescence. They also included a detailed discussion of the possible EM counterparts one could expect from MBHBs and their implications for wide- and narrow-field instruments. Trias and Sintes [208] adopted a full post-Newtonian waveform, and found an overall improvement in the parameter estimation for massive MBHB (${\rm M}_{\rm tot} > 5 \times 10^6\,{\rm M}_\odot$). In particular the inclusion of amplitude corrections leads to earlier warning and improved sky-position accuracy as a function of time to coalescence for massive unequal MBHBs. McWilliams *et al.* [209] explored LISA ability to constrain the sky-position and luminosity distance of non-spinning equal mass systems using the full inspiral-merger-ringdown waveform and including the orbital motion of the detector plus the three-channel LISA response. They found a final median sky-position error of $\simeq 3\,{\rm arcmin}$ for a system with total intrinsic mass of $2 \times 10^6\,{\rm M}_\odot$ at $z = 1$.

4.3 Summary

In this chapter we presented the set of knowledges necessary to understand the results of the two final chapters. We summarised how MBHBs are expected to form and grow from dark matter perturbations in the high-redshift Universe and the current problems related to the last stage of their inspiral. We also highlighted LISA ability to detect MBHBs to high redshift with large S/N values days or week before the merger. We also introduced the basic ideas behind the parameter estimation of a GW signal. Even if the formal approach require the application of Bayes theorem, under reasonable assumptions the Fisher matrix formalism can be safely applied, greatly reducing the computational cost of this task. We concluded with a brief overview of the studies that explored LISA ability to constrain MBHB parameters during the inspiral.

Chapter 5

Premerger localization of MBHBs in LISA

Among the possible EM signatures associated to the coalescence of MBHBs, the X-ray might be the most promising one. In particular in this chapter we focus on the possibility to detect a premerger modulated X-ray emission in phase with the GW signal.

In the standard formalism, in the last stage of the merger, MBHBs are expected to excavate a void region in the circumbinary disk and minidisk should form around each BHs, especially for unequal mass systems where the lighter BH orbit close to the inner edge of the circumbinary disk. If the system is edge-on, the X-ray emission might experience Doppler-shift modulation that is in phase with the GW signal. Detecting both the modulated premerger emission and the GW signal would allow to pinpoint the exact galaxy and provide early warning to observe the very prompt emission.

In the next decade, one of the proposed mission designed to observe EM transient is the NASA Transient Astrophysics Probe (TAP) [212]. TAP is planned to have fast slew rate and to be positioned around the L_2 Lagrangian point, thus reducing the possibility to be blocked during the observation. Moreover, TAP is equipped with an X-Ray Telescope (XRT) sensitive in the band $[0.5, 2]\,\mathrm{KeV}$ with a field of view (FOV) of $\simeq 1\,\mathrm{deg}^2$, 2 second timing precision and 5 arcsec angular resolution.

Even if the possibility to detect an EM counterpart to the GW signal is intriguing, there are several difficulties:

- Even if LISA is able to detect MBHB days or week before merger, the sky position recovered at such early times is too large to be feasible explored with the FOV of X-ray telescope. LISA is able to localize the source with a precision of $\lesssim 1\,\mathrm{deg}^2$ only close to the merger, leaving a short interval of

time to provide alert to EM facilities, unless the system is close ($z < 0.5$);

- The EM emission is still uncertain: the orbital motion and accretion might produce 'chirping' X-ray signal as the GW one [200]. However the observed flux strongly depend by the feeding rate of the minidisk, the accretion details, the surrounding environment and the amount of X-ray radiation produced;

- Due to the large error area provided by LISA, there will be additional confusion sources in the region scanned by TAP.

In this chapter we explore the possibility to detect the X-ray modulated emission in phase with the GW signal. Assuming a 4 year time mission and reasonable rate for the number of MBHB mergers, we compute the number of detected modulations. We also vary our assumption and test different observing scenarios to establish the optimal trade-off between observing time and modulation detections.

The chapter is organized as follow: In Sec. 5.1 we describe our simulation setup. In Sec. 5.2.1 we explore the results for the baseline configuration in terms of detected modulations for different MBHBs. In Sec. 5.2.2 we vary each assumption of the baseline assumption and compare possible observational strategies. In Sec. 5.3 we conclude and summarise our findings.

The results presented in this chapter have been published in [195].

5.1 Simulation setup

The shape of the MBHBs mass distribution detectable with LISA is still uncertain. The most promising sources for detecting an EM counterpart are nearby and relatively massive systems in the range $10^5 - 10^7\,\mathrm{M}_\odot$. For the sake of simplicity we choose to focus on three particular systems with $(\mathrm{M}_{\rm tot}, q) = [(5\times10^5\,\mathrm{M}_\odot, 1), (5\times10^6\,\mathrm{M}_\odot, 1), (5\times10^6\,\mathrm{M}_\odot, 0.1)]$ extending up to $z = 3.5$ (above this value the possibility to detect an EM modulation is basically negligible). To compute the actual number of mergers per year we approximated the merger rate density presented in [178]. We further assume non-spinning BHs in circular orbit.

In this study we adopt two GW waveforms. We adopt the PhenomC to compute the S/N as the signal accumulates in band. We set as minimum frequency $f = 10^{-5}\,\mathrm{Hz}$ and claim the signal detection when then S/N is above a threshold value of 10. When the signal is detected, we perform parameter estimation with the Fisher matrix approach. For this step, we adopt the same inspiral-only precessing waveform (SUA) described in Sec. 2.2. This waveform is optimal for the parameter estimation because it includes higher harmonics and spin-precession effects: both these effects are know to reduce degeneracies between parameters especially close to merger.

While the system approaches coalescence, regular updates will be sent from LISA back to Earth. In this way the parameter estimation would further improve and, in particular, the sky position of the source will reduce. We assume to receive regular update from LISA every 2 days: this might be a bit conservative but it takes into account the time required to download the data, re-point LISA antennas and perform the PE estimation. The inspiral-only waveform loses validity close to merger but it's sufficiently accurate during all the inspiral. We convert the frequency in the time left before merger using Eq. (2.7) of Lang and Hughes [207].

We take the sky position uncertainties provided by LISA and compute sky localization probabilities in the HEALPix format [213], drawing points from a 3-variate Gaussian distribution with a covariance provided by the Fisher matrix.

We assume the LISA sensitivity curve labeled as "ESACall v1.1" configuration in the "LISA strain curves" document, assuming six-laser link, 2.5×10^6 km armlenght and the reprocessed data from the LISA Pathfinder mission.

EM counterpart modeling

The next step is the modeling of the X-ray lightcurve expected. A complete description of the EM emission can be performed only with GRMHD code, that takes to much time to be efficiently adopted for our scope. Moreover the current available simulations cover only the last few orbit before the merger, while we are interested in the emission during the whole inspiral phase. For the EM, we consider a single minidisk around one of the two BHs in binary because overdensities in circumbinary disk are expected to feed one BH at time [194]. We also neglect the emission from the circumbinary disk.

To perform a fast and efficient search, we modeled the observed flux as

$$F = \mu \frac{XL}{4\pi d_L^2} \tag{5.1}$$

where L is the Eddington luminosity. The two factors μ and X take into account the modulation due to the orbital motion and the conversion between bolometric Eddington luminosity and X-ray luminosity, respectively. We model the effect of orbital motion as

$$\mu = 1 + 3\sin(\iota)\cos(\psi)v \tag{5.2}$$

where we remember that ι is the binary inclination, ψ the polarization angle and v is the orbital velocity. As expected, since we are looking for Doppler modulation, for face-on systems $\mu = 1$ and no modulation can be observed. The conversion factor X is expressed as

$$X = 0.1 + \frac{1}{a} \tag{5.3}$$

where a is the binary orbital separation (in gravitational radii). The factor 0.1 is based on observation of AGN and spectroscopic survey [214–216]. The factor a^{-1} represents the coronal heating due to the increase of available magnetic energy close to merger [217] or to streams of gas from the circumbinary disk to the single minidisk [218].

Tiling and search for modulation

The sky localization area provided by LISA is divided is tiles that are observed with the XRT telescope, assuming a FOV of $1\,\mathrm{deg}^2$. The total area is observed up to a given coverage, excluding the possibility of being blocked by the Sun or Earth. Each tile is observed for $10^4\,\mathrm{s}$ before moving to the next one with lower probability. Once the total coverage is reached, the search starts again from the highest probability tile. However, when LISA provide a new sky localization, a new set of tiles is generated and the process resumes from the beginning. For TAP we assume a slew rate of $1\,\mathrm{deg/s}$ and $10\,\mathrm{s}$ to start a new observation after a slew. Even if TAP has different instruments on board, we assumed at the beginning that 100% of time is spent observing LISA sources.

We considered a more realistic scenario adding background photon with a constant rate of $7.2 \times 10^{-5}\,\mathrm{s}^{-1}$ and a non-constant term with $2 \times 10^{-6}\,\mathrm{s}^{-1}$. Photons are sampled from the total time series obtained combining these three fluxes. To test the presence of modulation, we adopt the Kuiper's test [219]: we focus mainly on the periodicity and compare the phase of the accumulated lightcurve with the expected modulation coming from the orbital motion of the binary. We claim the detection when the p-value drops below 0.003 ($\simeq 3\sigma$ significance). When the detection is claimed other telescopes will point the source and confirm or dismiss the modulation so 3σ is a consistent threshold.

5.2 Results

5.2.1 Results from baseline configuration

We assume a standard baseline for LISA and TAP observations:

- $10^4\,\mathrm{s}$ exposure time for each XRT tile;
- 50% coverage of LISA sky localization area;
- XRT starts observation when LISA claim detection;
- 100% of available time is spent on a single source.

After presenting the baseline results, we will relax each of the aforementioned assumptions in order to model more realistic observing scenarios.

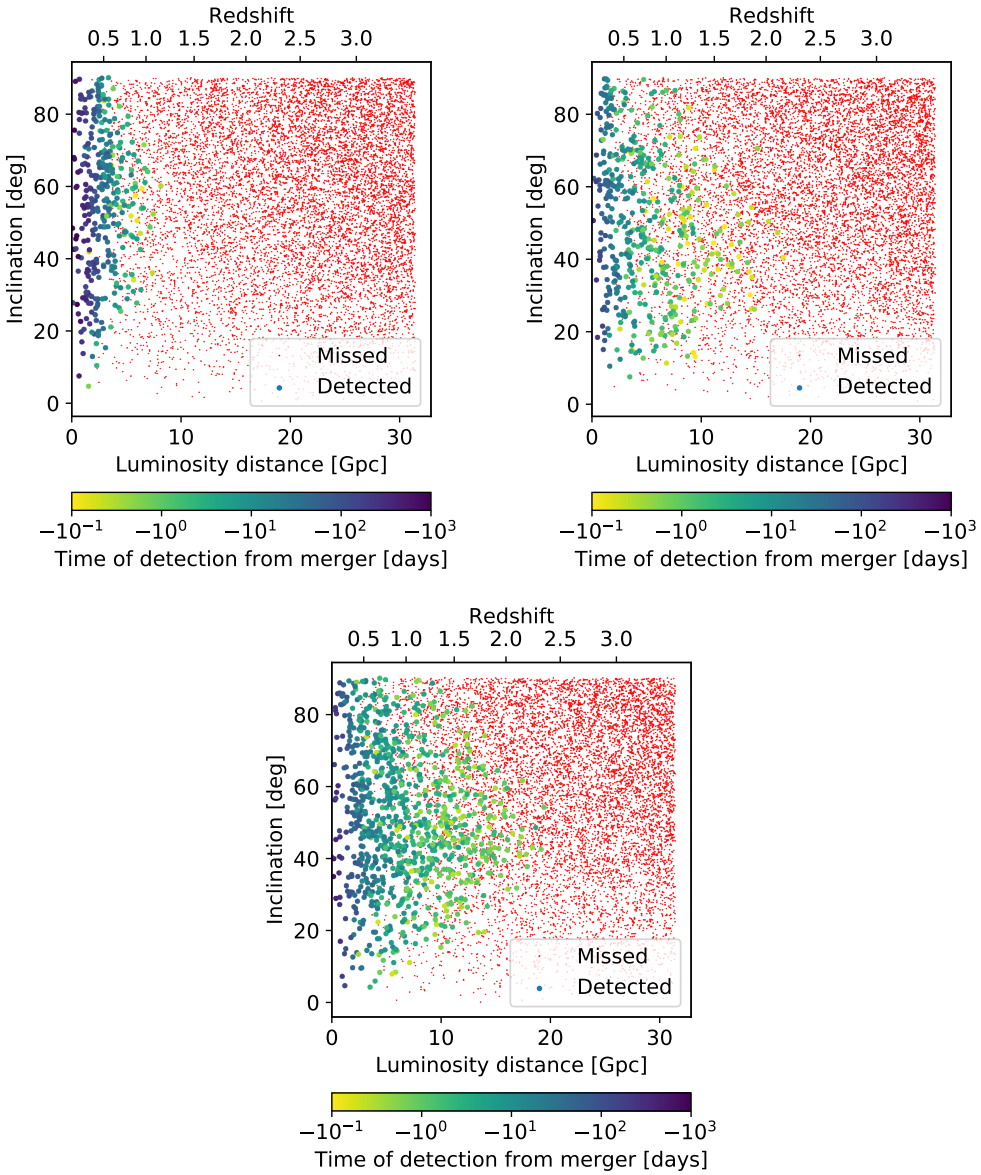

Figure 5.1: Distribution in the inclination-d_L plane of sources whose X-ray modulation is detected (viridis large points) or missed (red small points). Darker colors means earlier detection time. Upper-left panel: $(5\times10^5\,\mathrm{M}_\odot, 1)$. Upper-right panel: $(5\times10^6\,\mathrm{M}_\odot, 1)$. Bottom panel: $(5\times10^6\,\mathrm{M}_\odot, 0.1)$.

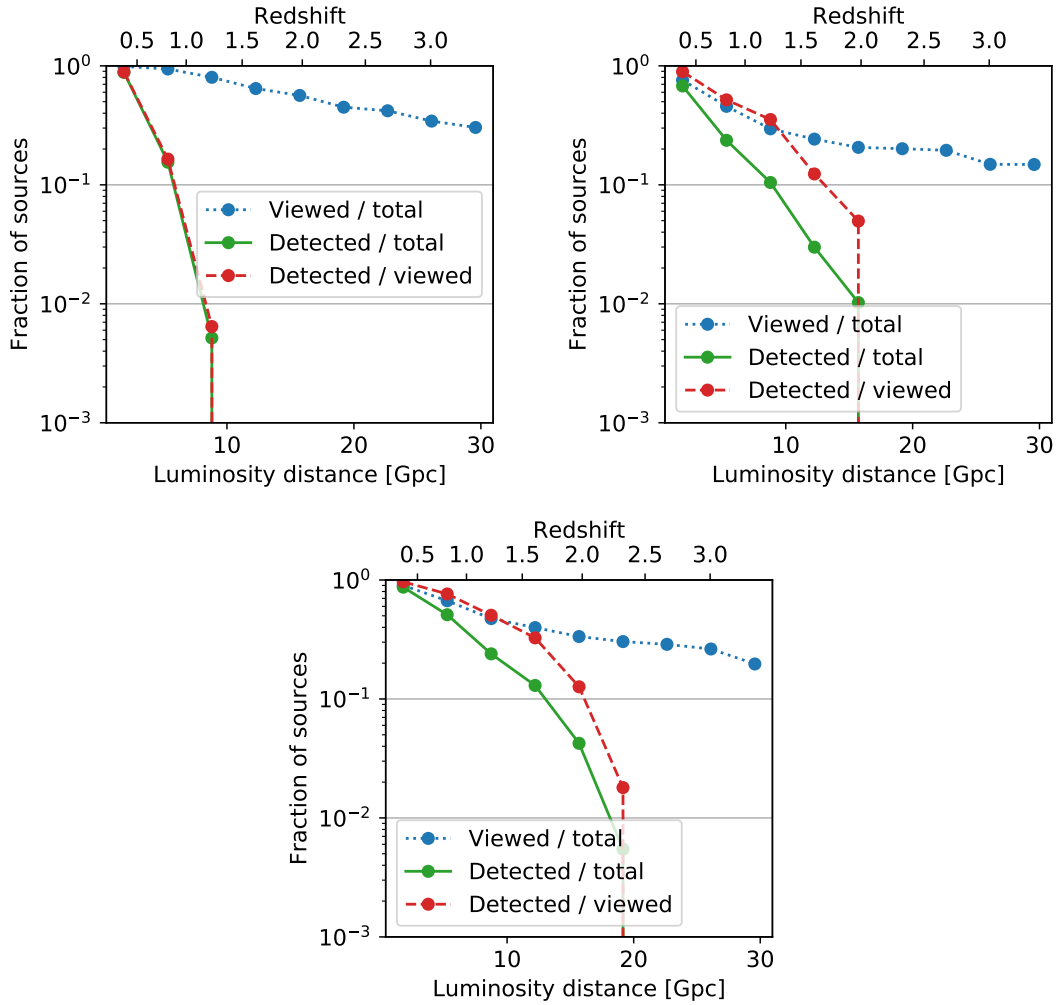

Figure 5.2: Fraction of viewed or detected systems as function of luminosity distance. Upper-left panel: $(5 \times 10^5\,\mathrm{M}_\odot, 1)$. Upper-right panel: $(5 \times 10^6\,\mathrm{M}_\odot, 1)$. Bottom panel: $(5 \times 10^6\,\mathrm{M}_\odot, 0.1)$. Here 'total' refers to all events detectable with LISA (i.e $S/N > 8$), while 'detected' refers to systems for which an EM modulation is claimed.

In Fig. 5.1 we report the systems for which a modulation is detected in function of inclination and luminosity distance for the three aforementioned systems [1]. As expected, for close systems ($z < 0.5$), the modulation is detected even $\simeq 100$ days

[1]Here 'detected' refers to the EM modulation; all these systems are detected as GW sources in LISA.

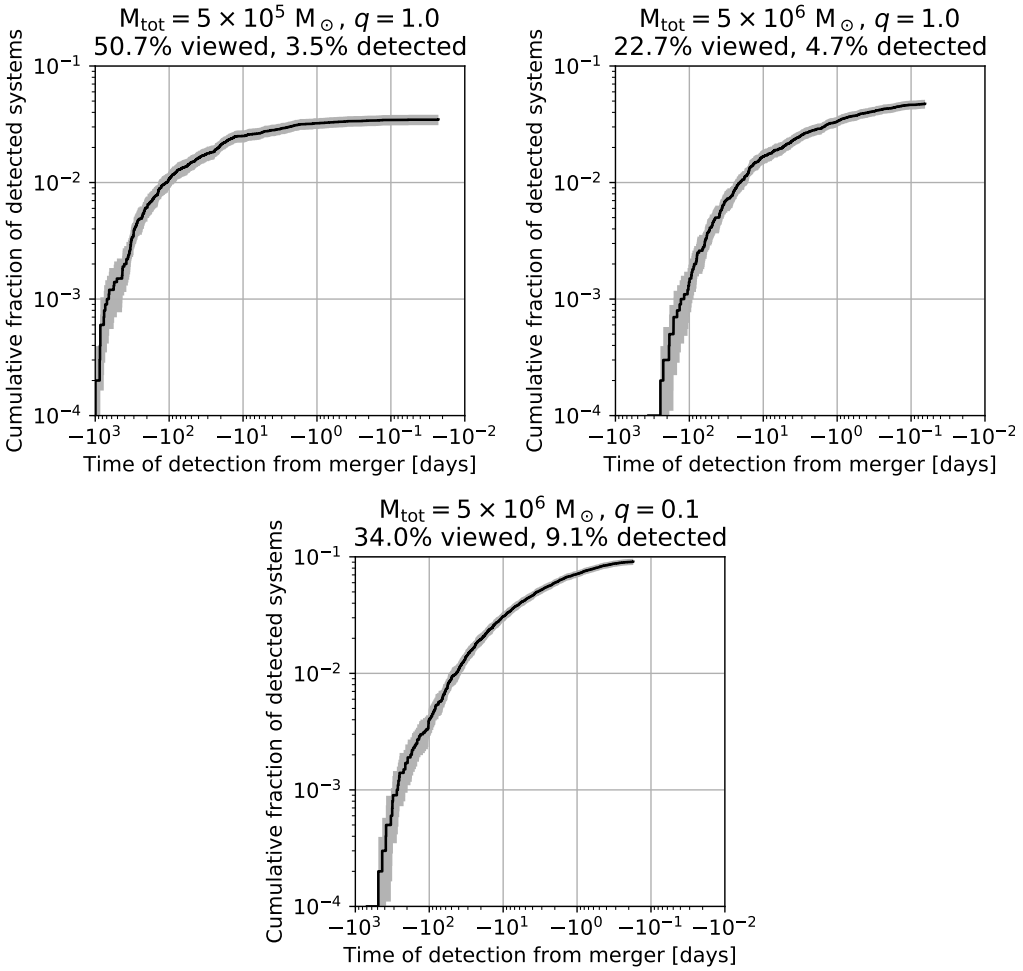

Figure 5.3: Cumulative distribution of systems whose X-ray modulation is detected at the reported time. Shaded areas correspond to 95% confidence interval. Upper-left panel: $(5 \times 10^5\,\mathrm{M}_\odot, 1)$. Upper-right panel: $(5 \times 10^6\,\mathrm{M}_\odot, 1)$. Bottom panel: $(5 \times 10^6\,\mathrm{M}_\odot, 0.1)$.

before merger due to the small LISA sky localization and the number of photons received. As we increase the luminosity distance, the modulation is detected closer to merger and no modulation at all is claimed for systems at $z > 2.5$. For the unequal mass case the modulation is detected up to higher redshift respect to the equal mass systems thanks to the higher harmonics in the GW waveform that allow to recover a small area from LISA data. For all systems, the modulation is typically detected at $\iota \simeq \pi/4$ due to the fact that for face-on systems the modulation is absent while for edge-on systems we lose a polarization state and,

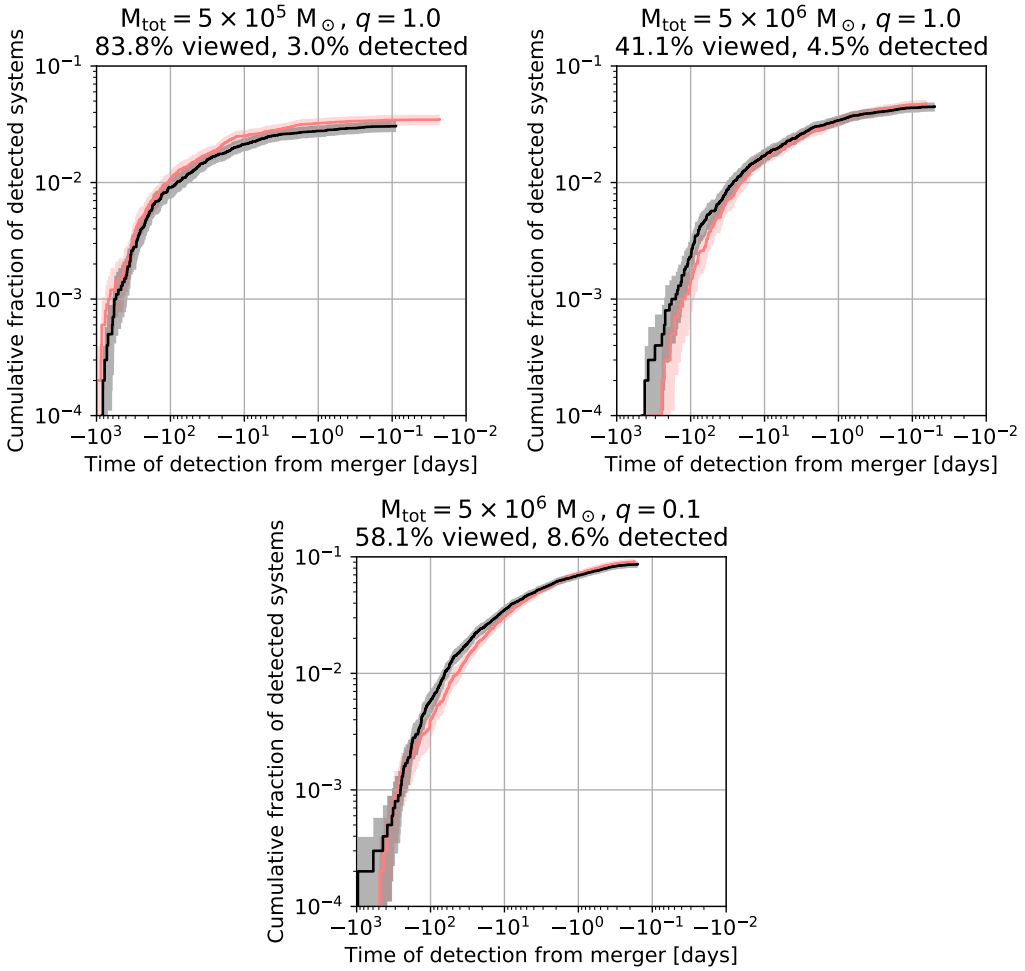

Figure 5.4: Cumulative distribution of systems whose X-ray modulation is detected at the reported time. Grey distributions: XRT exposure is reduced to 10^3 s. Red distributions: baseline configuration. Upper-left panel: $(5 \times 10^5\,\mathrm{M}_\odot, 1)$. Upper-right panel: $(5 \times 10^6\,\mathrm{M}_\odot, 1)$. Bottom panel: $(5 \times 10^6\,\mathrm{M}_\odot, 0.1)$.

therefore, the error on the binary location increases.

A system can be just 'viewed' if XRT observes the tile where the system is located but does not detect any modulation. It might happen however that the sky position estimate provided by LISA is so large that the system is not even 'viewed' once. In Fig. 5.2 we report the fraction of viewed and detected events as function of luminosity distance. As the distance increases, the number of systems for which a modulation is detected decreases due to the large error area and to the small flux received. Lighter systems are viewed up to higher redshift because they

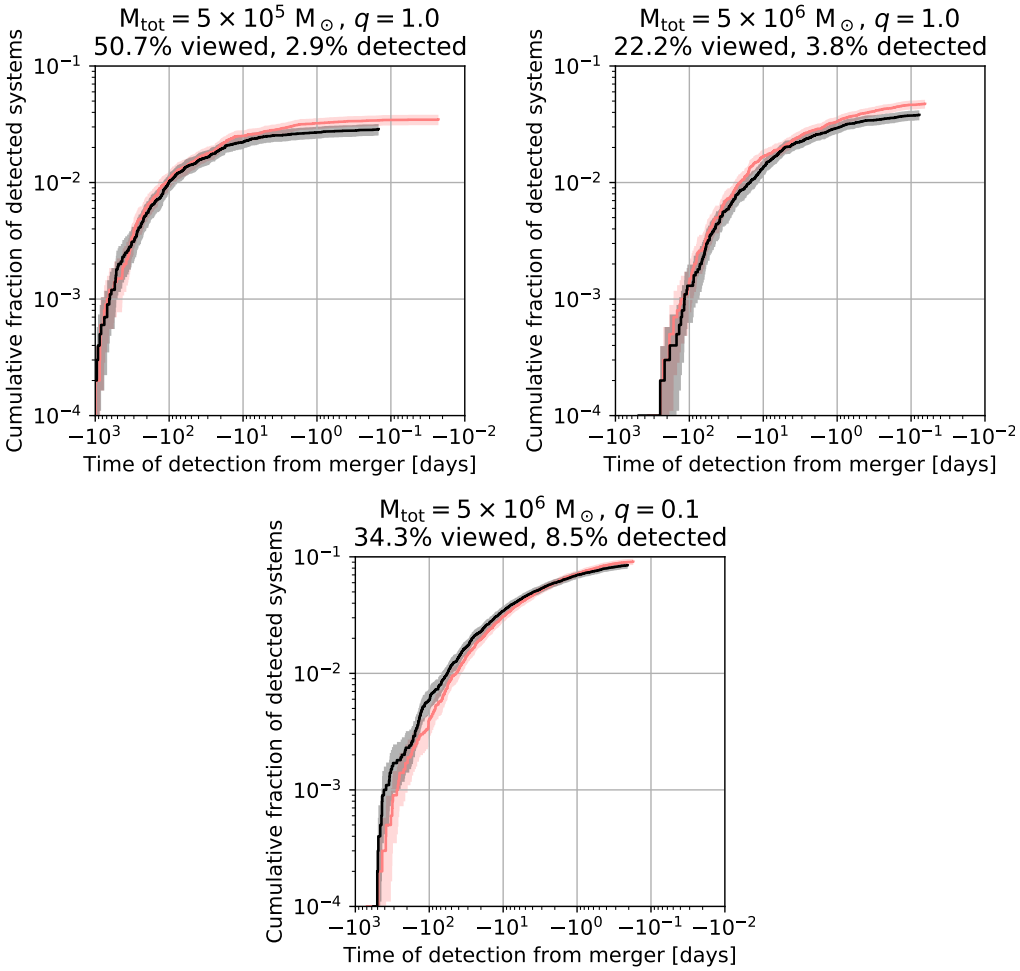

Figure 5.5: Cumulative distribution of systems whose X-ray modulation is detected at the reported time. Grey distributions: LISA area is covered to 95%. Red distributions: baseline configuration. Upper-left panel: $(5 \times 10^5\,\mathrm{M}_\odot, 1)$. Upper-right panel: $(5 \times 10^6\,\mathrm{M}_\odot, 1)$. Bottom panel: $(5 \times 10^6\,\mathrm{M}_\odot, 0.1)$.

are better localize. However the fraction of of detected systems extends to higher redshift for heavier MBHBs thanks to the larger X-ray flux produced.

In Fig. 5.3 we plot the cumulative distribution of detected events as function of time left before merger when the detection of modulation is claimed. More than 50% of light systems are seen at least once by TAP. For heavier systems, the fraction of viewed systems reduces to 23% and 34% for the $q = 1$ and $q = 0.1$ scenario respectively. The higher fraction of viewed systems for the unequal mass case is due to the better sky localization provided by LISA. Moving to the fraction

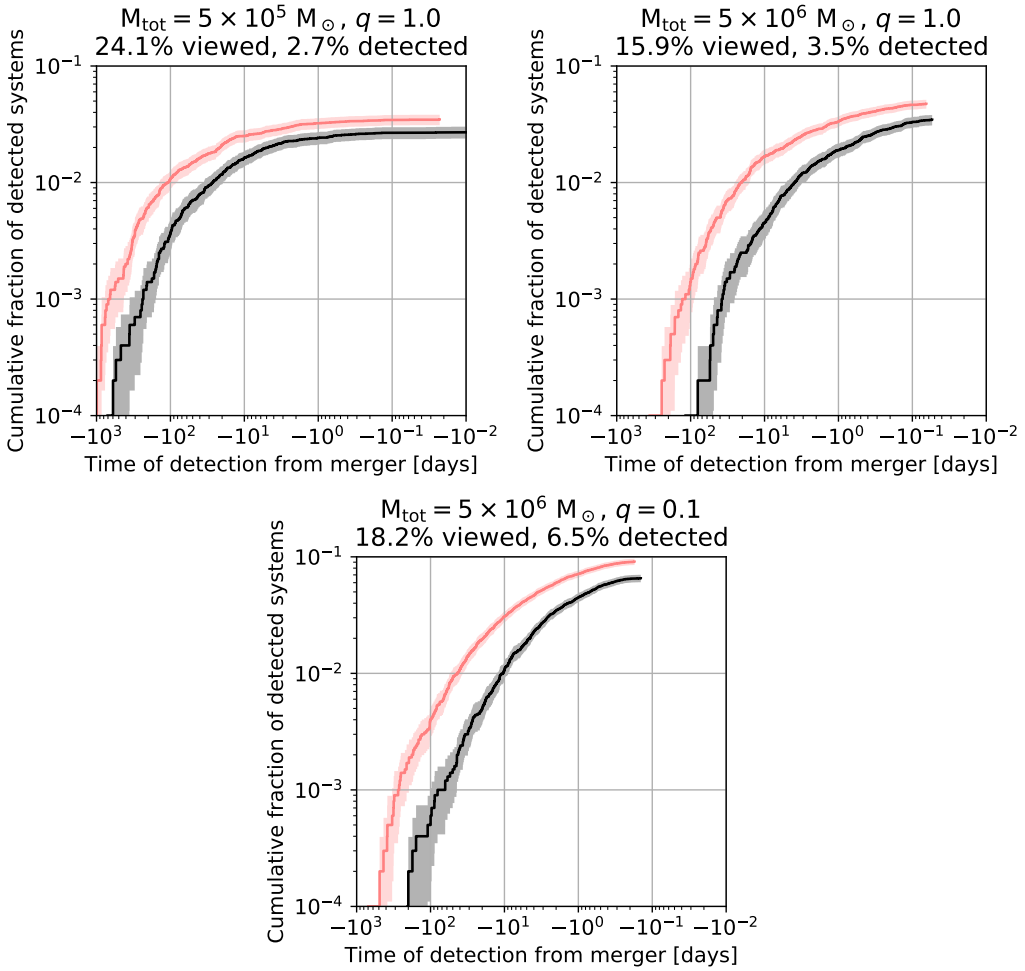

Figure 5.6: Cumulative distribution of systems whose X-ray modulation is detected at the reported time. Grey distributions: LISA area is smaller than 20 $\deg^2$ when TAP starts the observation. Red distributions: baseline configuration. Upper-left panel: $(5 \times 10^5\,M_\odot, 1)$. Upper-right panel: $(5 \times 10^6\,M_\odot, 1)$. Bottom panel: $(5 \times 10^6\,M_\odot, 0.1)$.

of systems for which the modulation is detected, heavy unequal MBHB provide the highest detection rate with $\simeq 9\%$ of detection over the whole sample thanks to the particular binary configuration. For equal light (heavy) systems the modulation is detected only in the 3.5% ($\simeq 5\%$) of cases. However light binaries provide higher detection rates at $\simeq 100$ days from merger than heavy systems.

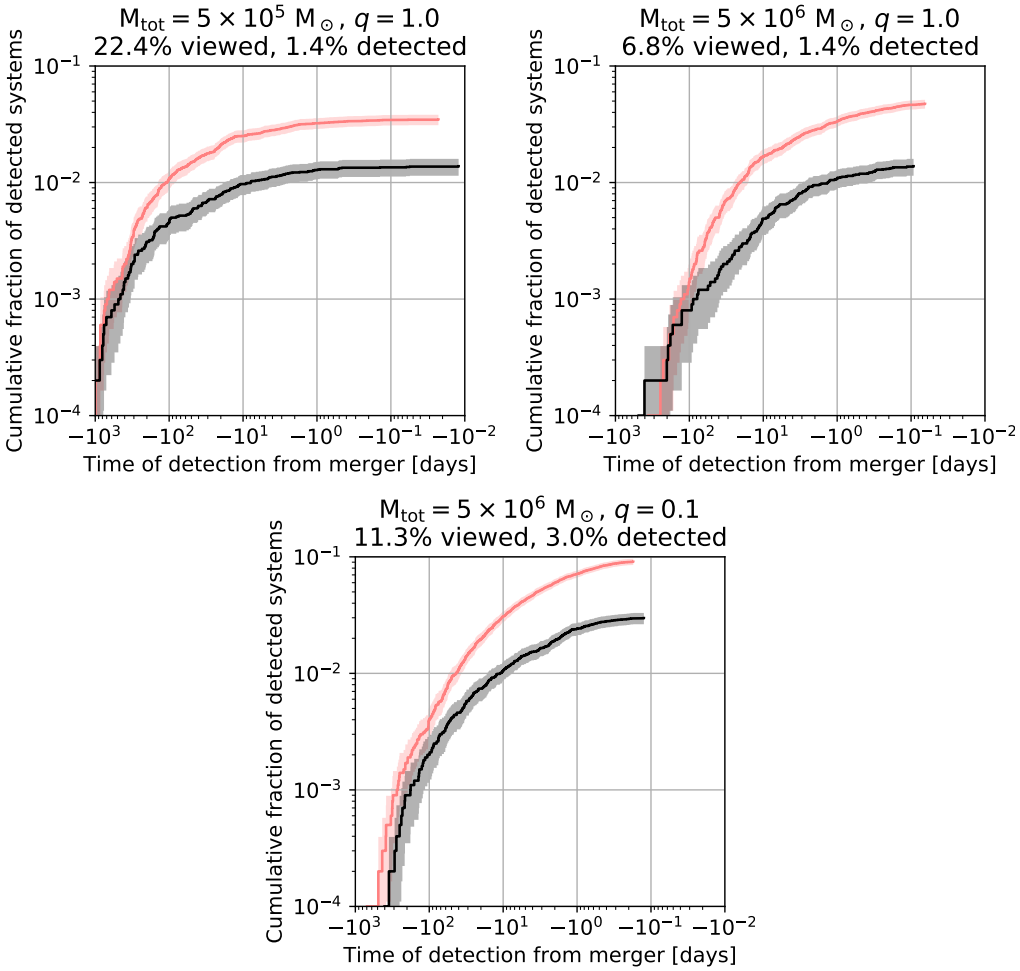

Figure 5.7: Cumulative distribution of systems whose X-ray modulation is detected at the reported time. Grey distributions: TAP observes LISA sources only for 10% of the available time. Red distributions: baseline configuration. Upper-left panel: $(5 \times 10^5\,\mathrm{M}_\odot, 1)$. Upper-right panel: $(5 \times 10^6\,\mathrm{M}_\odot, 1)$. Bottom panel: $(5 \times 10^6\,\mathrm{M}_\odot, 0.1)$.

5.2.2 Exploring alternative configurations

In the following we are going to change the baseline assumptions separately and analyse how our detection rates are affected. We start shortening the exposure time for each tile from 10^4 s to 10^3 s. The results are in Fig. 5.4. This configuration lead to an increase of the fraction of viewed systems however the detection rates remain unaffected: even if we observe the tiles with increased frequency, we are

collecting less photons to claim detection. We obtain similar results if we increase the coverage of LISA area to 95% because for most binaries, there is not enough time to reach this coverage between receiving LISA updates. The results for this configuration are reported in Fig. 5.5.

When LISA claim a detection, the area recovered is usually larger than $100\,\mathrm{deg}^2$. With the baseline configuration, we are able to observe an area of $\simeq$ 17 deg^2 before a new set of tiles is produced. The amount of time spent to observe the system from detection might be allocated to observe other LISA sources. In Fig. 5.6 we show the cumulative fraction of detected events if we start TAP observation when LISA area drops below $20\,\mathrm{deg}^2$. The fraction of viewed systems reduces by a factor of 2 however the detected fraction is less affected: lighter systems are the least affected with a detection of 2.7%, while for heavy system the modulation is detected in the 3.5% (6.5%) for equal (unqueal) MBHBs.

In our baseline configuration, we assume that TAP spends all the available time observing a single LISA source. However this will not be the case due to the other science objectives of the mission. In addition, more than one MBHBs could be detected at the same time. For these reasons, we test a last configuration setting a dead time of $9 \times 10^4\,\mathrm{s}$ to simulate a more realistic scenario. In this way only $\simeq 10\%$ of TAP time is spent observing a single LISA source. The result are showed in Fig. 5.7. Overall the fraction of detected systems is reduced by a factor $\simeq 3$ or all masses. However there is still a small fraction of systems ($\simeq 0.1\%$) detected at early time.

We take the merger rate of MBHBs from Fig. 3 of Klein et al. [178] up to $z = 3.5$ considering the "popII" and "q3-nod" models. In this way we obtain $\simeq 10\,\mathrm{yr}^{-1}$ events in LISA that translated in GW detection because all these events are detected in LISA as shown in Fig. 4.1. Combining this information with the total amount of systems simulated for each simulation, we can compute the rate of modulation detection and the amount of time required by each simulation. We can take the total time spent by XRT observing tiles and rescale it for the total amount of time of the simulation in order to provide the fraction of TAP time spent observing MBHB. This information is reported in Fig. 5.8 where we combine the detection rate and the required observing time for each of the observing strategies. The baseline configuration leads to the highest detection rate but it also require the most amount of observing time (for the light binary with $\mathrm{M_{tot}} = 5 \times 10^5\,\mathrm{M_\odot}$ we even need two identical TAP). As expected even from the previous results, the configurations with reduced exposure time and extended coverage produce no significant difference respect to the baseline strategy. Starting the observation when the area provided by LISA is smaller than $20\,\mathrm{deg}^2$ reduces the detection rate of $\simeq 30\%$ for all systems, but decreases the amount of time spent observing LISA source by an order of magnitude. Similarly, reducing the allocation time frees time

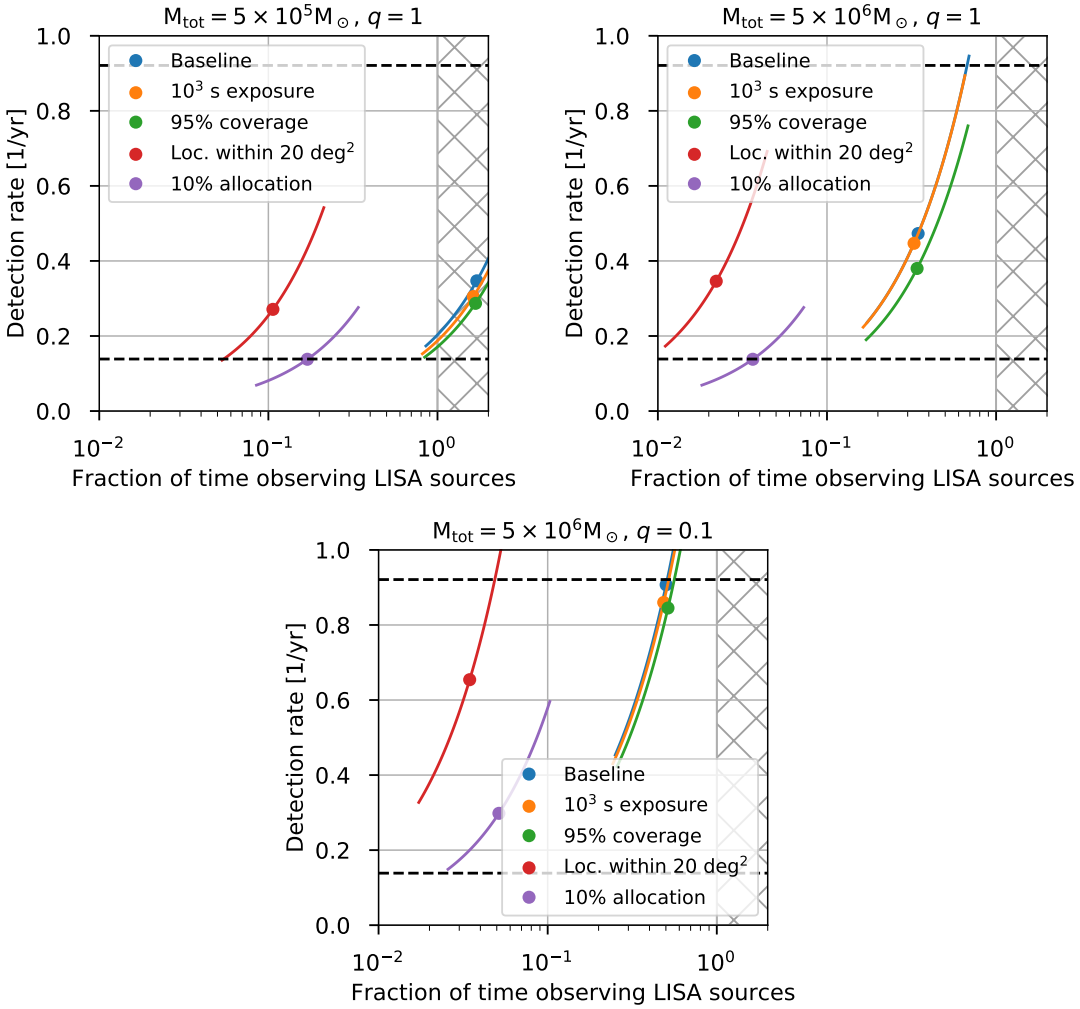

Figure 5.8: Modulation detection rate as function of the time spent observing LISA sources for baseline and different configurations as labeled in legend. For each configuration, the lines represent the effect of varying the merger rate by a factor of 2 in both directions. The dashed horizontal black lines represent the 50% and 99% probabilities of one or more detections assuming a 5 yr LISA time mission. The hatched portion of the plots represents the regime where more than one TAP is required. Upper-left panel: $(5 \times 10^5\,\mathrm{M}_\odot, 1)$. Upper-right panel: $(5 \times 10^6\,\mathrm{M}_\odot, 1)$. Bottom panel: $(5 \times 10^6\,\mathrm{M}_\odot, 0.1)$.

to observe other sources but lowers the number of detection of a factor $\simeq 2(3)$ for equal (unequal) mass system. We also notice that the choice of which source

observing will depend on the outcome of the full parameter estimation in LISA and on our model for the X-ray emission: we can impose further constrains once we estimate the luminosity distance of the source, inclination angle, component masses and spins magnitude and orientation. From the EM side, more accurate X-ray emission models might suggest the optimal conditions for the generation of a counterpart.

5.3 Discussion and summary

In this chapter we explored the possibility to detect an EM Doppler modulation in phase with the GW signal exploiting LISA and TAP combined observations. We assume three different sub-populations up to redshift $z \simeq 3.5$ with $(\mathrm{M_{tot}}, q) = [(5\times10^5\,\mathrm{M_\odot}, 1), (5\times10^6\,\mathrm{M_\odot}, 1), (5\times10^6\,\mathrm{M_\odot}, 0.1)]$ and we investigated LISA ability to constrain source position in the inspiral. The recovered area is then divided in tiles and scanned by TAP to search for an X-ray emission modulated by the orbital motion of the binary. As MBHBs approach coalescence, the recovered area decreases but the time left to claim detection reduces. We derived the number of detection that we expect over a 5 yr time mission under a baseline configuration. We later changed each of the baseline assumptions to explore different and more realistic scenarios.

Red noise is expected to contaminate the X-ray emission and unrelated bright sources will be present in LISA sky localization area. From an initial study, we conclude that bright and highly variable red-noise sources might produce a significant amount of false positives. Real lightcurves will be more complicated and include additional effect as intrinsic variability that might further complicate our analysis and reduce the expected number of detection. We also remove the expected contribution from circumbinary disk but further studies are necessary to validate this assumption. Moreover, not all MBHB mergers might produce AGN-like emission and some might even be obscured by the surrounding gas. Clearly both scenarios would lower our detection estimates.

The precession of MBHB orbital plane due to spin misalignment or unequal mass ratio might add further modulations to the EM emission. However at the end of inspiral most of the BHs are expected to have spin aligned with the orbital angular momentum, reducing the effect of precession [177, 220].

We summarize our results here:

- For light and close ($z < 0.5$) systems the modulation can be detected even $\simeq 100$ days before merger due to the accurate sky position provided by LISA.
- Overall massive and unequal systems are promising to detect an EM modulation thanks to the larger X-ray flux and stronger modulation. Also higher

harmonics might help breaking degeneracies and further reduce LISA area.

- Almost independently from the mass, the modulation is preferentially detected for systems with $\iota \simeq 45°$ due to the combination of the GW strain and the modulation itself (null for face-on MBHBs).

- Light systems are viewed in larger percentage respect to massive systems. However the modulation is detected for $\simeq 9\%$ of cases for massive and unequal systems, compared to just $\simeq 3.5\%$ for light MBHBs.

- Reducing the exposure time or increasing the coverage of LISA area leads to no significant changes in the the detected rates.

- The fraction of detections if we start TAP observations when LISA area drops below $20\,\mathrm{deg}^2$ reduces by $\simeq 30\%$ with light systems being the less affected. Similarly, reducing the observation time of LISA sources to the 10% of the total available time leads to a reduction of a factor 3 in the number of detections for all masses.

- Taking into account the actual rates of MBHB, we find that the optimal configuration to detect an EM modulation without unrealistic assumptions on TAP might be to start XRT observations when LISA area drops below $20\,\mathrm{deg}^2$.

Assuming to detect ~ 10 MBHBs per year over a 5 yr time mission, we expect to be able to detect few EM modulations. The detection will most likely come from massive systems with unequal component masses and inclined to $\simeq 45°$ respect to the line of sight.

Chapter 6

Parameter estimation of MBHBs in LISA

In this chapter we present a detailed analysis on LISA abilities to constrain MBHB source parameters as they approach coalescence, i.e. during the inspiral. In particular we focus on the sky position, luminosity distance, chirp mass and mass ratio. To properly explore the parameter space, we consider systems with $\mathrm{M_{tot}} \in [10^5, 3 \times 10^7]\,\mathrm{M_\odot}$ and $z \in [0.1, 4]$. For each combination of total mass and redshift we perform $N = 10^4$ realizations. The signal is computed with the inspiral precessing waveform described in Sec. 2.2 to exploit spin precession and higher harmonics effects in breaking parameter degeneracies. For a small sample of selected events, we also compare our results against two independent MCMC codes. We also explore the case of a possible degradation in the low-frequency portion of LISA sensitivity. We manage to fit our results with analytical formulas with few input parameters (the time left before merger, total mass and redshift) to provide the median, 68 and 95 percentiles of our distributions. With the formulas, we further explore multimessenger possibilities across the full EM spectrum.

The chapter is organized as follow: in Sec. 6.1 we introduce the main motivations of our work. In Sec. 6.2.1 we present a detailed overview of the current LISA sensitivity with a possible low-frequency degradation. In Sec. 6.2.2 we describe the framework of our simulations. In Sec. 6.3 we perform preliminary tests to asses the validity of our code. In Sec. 6.4.1 we present the results for the estimate on sky position, luminosity distance, chirp mass and mass ratio. In Sec. 6.4.2 we validate our approach against MCMC simulations. In Sec. 6.4.3 we introduce the formulas to fit our results. In Sec. 6.4.4 we implement the previous formulas to look at LISA abilities to constrain source parameters in whole simulation space. In Sec. 6.4.5 we discuss the multimessenger possibility offered by LISA. In Sec. 6.5 we analyzed the contribution of mass ratio, time to coalescence, spin magnitude, inclination and binary position in shaping the uncertainty distributions. In Sec. 6.6 we perform

a comparison with the old LISA sensitivity curve. In Sec. 6.7 we look at LISA abilities to constrain binary inclination. Finally in Sec. 6.8 we summarize our main findings.

The results presented in this chapter have been published in [221].

6.1 Motivations

All the studies in Sec. 4.2 were performed with the *classic* LISA design, with a five-million kilometer constellation and a low frequency sensitivity extending down to 10^{-5} Hz. Following the re-design of the LISA mission, the armlength of the interferometer is reduced to 2.5 million kilometers, featuring a steeper low frequency sensitivity extending possibly down to 2×10^{-5}Hz, based on the in-flight LISA Pathfinder performance [222]. Loss in the low frequency sensitivity, as compared to the *classic* LISA, leads to a shorter (detectable) duration of the GW signal and, therefore, to some degradation of our abilities to localize the sources. It also implies that more weight is given to the merger and post-merger part of the signal. In light of these changes, it is therefore necessary to reassess earlier findings to establish the performance of the current design in producing *on the fly* estimates of source parameter errors.

Moreover the parameter space of merging MBHBs is vast, and its full exploration with MCMC techniques is time consuming. Several studies as [223, 224] demonstrated that parameter estimation via Fisher information matrix evaluation reproduces reasonably well MCMC results for high S/N sources, which are the targets of this study. Although Fisher matrix-based estimates allow to drastically cut down computational cost, there is still the need to perform large set of simulations and, up to now, there is no public available code for this. Berti *et al.* [204] provided analytical formulas for the mass and distance errors for non-spinning MBHB with total mass $\mathrm{M_{tot}} = 2 \times 10^6\,\mathrm{M_\odot}$ but for the old LISA design and as function of redshift, not as function of time to coalescence.

Therefore the additional scope of our work is to provide a vast library of LISA parameter estimates as a function of time to merger for MBHBs. All results are obtained by consistently evaluating the Fisher matrix of the signal as the source evolves, and are tested, for a subset of selected sources, against full MCMC calculations. To the benefit of the community, we provide analytical formulas to describe how parameter estimates improve *on the fly*, i.e. while the MBHB is approaching the merger. We perform an extensive set of simulations exploring the parameter space of MBHBs in the mass range $10^5\,\mathrm{M_\odot} < \mathrm{M_{tot}} < 3 \times 10^7\,\mathrm{M_\odot}$ at $z < 4$ and fit the results with polynomial expressions. The resulting formulas are cast in terms of three variables: the total (intrinsic) mass of the system, the redshift of the source and the (observed) time to coalescence.

We also release the full set of data on which these formulas are based. The data can be found on the GitHub repository https://github.com/amangiagli/Fits-for-parameter-estimation-of-MBHBs-in-LISA.

6.2 Analysis framework

6.2.1 LISA observatory

For the LISA sensitivity curve, we adopt a six-link laser configuration labeled as "Payload Description Document Allocation" in the "LISA strain curves" document [1] and described also in [225]. The total noise power spectral density in a single LISA data channel is modeled as

$$S_n(f) = \frac{1}{L^2}\left(P_{\rm OMS}(f) + \frac{4P_{\rm acc}(f)}{(2\pi f)^4}\right)\times \\ \times\left(1+\frac{6}{10}\left(\frac{f}{f_*}\right)^2\right) + S_c(f)\,\mathrm{Hz}^{-1} \tag{6.1}$$

with $L = 2.5\,\mathrm{Gm}$, $f_* = 19.09\,\mathrm{mHz}$ and

$$P_{\rm OMS}(f) = (1.5\times10^{-11})^2\left(1+\left(\frac{2\,\mathrm{mHz}}{f}\right)^4\right)\mathrm{m}^2\mathrm{Hz}^{-1}, \tag{6.2}$$

$$P_{\rm acc} = (3\times10^{-15})^2\left(1+\left(\frac{0.4\,\mathrm{mHz}}{f}\right)^2\right)\times \\ \times\left(1+\left(\frac{f}{8\,\mathrm{mHz}}\right)^4\right)\mathrm{m}^2\mathrm{s}^{-4}\mathrm{Hz}^{-1} \tag{6.3}$$

In addition to the instrument noise, unresolved galactic binaries are expected to form a confusion background noise below $\lesssim 1\,\mathrm{mHz}$. While the LISA mission progresses, more galactic binaries will be detected and this noise source will reduce. We model the background noise contribution as

$$S_c(f) = Af^{-7/3}e^{-Kf^\alpha}[1+\tanh(-\gamma(f-f_k))]\mathrm{Hz}^{-1} \tag{6.4}$$

where $A = (3/10)\,3.26651613\cdot10^{-44}$ and $\alpha = 1.18300266$. Parameters K, γ, f_k change as the mission progresses and their values are reported in Tab. 6.1 [226].

[1] see also https://atrium.in2p3.fr/nuxeo/nxpath/default/Atrium/sections/Public/LISA@view_documents?tabIds=%3A

T_{obs}	K	γ	f_k[mHz]
1 day	941.315118	103.239773	11.5120924
3 months	1368.87568	1033.51646	4.01884128
6 months	1687.29474	1622.04855	3.47302482
1 year	1763.27234	1686.31844	2.77606177
2 years	2326.78814	2068.21665	2.41178384
4 years	3014.30978	2957.74596	2.09278117
10 years	3749.70124	3151.99454	1.57362626

Table 6.1: Coefficients describing the expected stochastic galactic background as a function of mission duration.

For simplicity, our fiducial sensitivity assumes the long-wavelength approximation and, therefore, it does not include the high frequency oscillations. Nevertheless, most of the sources in the parameter space explored in this study emit GWs with $f < 0.05\,\mathrm{Hz}$ so we expect it to be a valid approximation.

LISA sensitivity is set by the mission requirement in the range $10^{-4} - 1\,\mathrm{Hz}$ [227]: besides the extrapolation from Eq. 6.1, we also consider a less favorable version of the curve in the low-frequency region ($f < 2 \times 10^{-4}\,\mathrm{Hz}$). The new curve is obtained adding an additional source of noise in the acceleration term, i.e

$$P_{\mathrm{acc,\,degr}} = P_{\mathrm{acc}} \times \left(1 + \left(\frac{0.1\,\mathrm{mHz}}{f}\right)^2\right) \tag{6.5}$$

and substituting this new acceleration noise to the one in eq. 6.1 [228].

The degraded sensitivity affects mostly high-redshift heavy MBHBs ($\mathrm{M_{tot}} > 10^6\,\mathrm{M_\odot}$) for which the detection is claimed close to merger. An example is provided in Fig. 6.1 where we show a zoom-in of Fig.4.2 for heavy systems together with the results assuming the degraded sensitivity. For a MBHB with $\mathrm{M_{tot}} = 10^8\,\mathrm{M_\odot}$, the detection can be claimed 5 hrs before merger if the source is located at $z < 3$ with the standard sensitivity. However claiming the detection with the same time interval before merger is achievable only for sources at $z \lesssim 1.3$ for the degraded curve. Similar considerations apply also for systems with $\mathrm{M_{tot}} = 10^7\,\mathrm{M_\odot}$: the detection can be claimed 3 days before merger if the system is at $z \lesssim 2$ ($z \lesssim 1$) for the standard (degraded) sensitivity. As expected, the detection time of lighter systems with $\mathrm{M_{tot}} = 10^6\,\mathrm{M_\odot}$ is mostly unaltered by the degraded sensitivity.

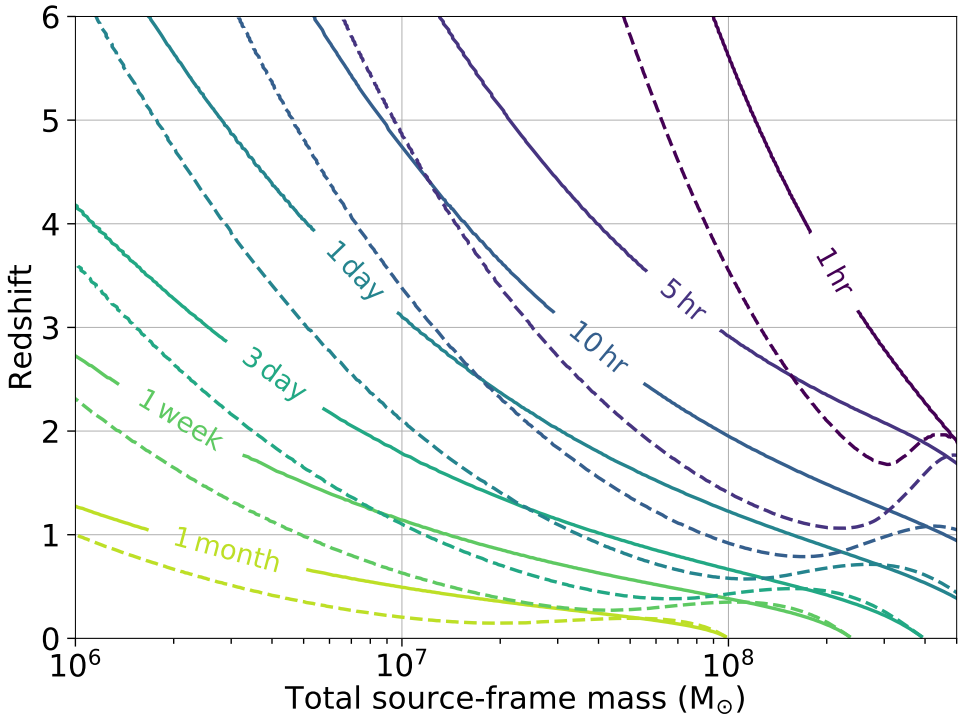

Figure 6.1: Contours of advanced detection time for LISA assuming the baseline configuration (solid lines) and the degraded sensitivity (dashed line) in the $M_{tot} - z$ plane, $q = 1$ and non-spinning BHs.

6.2.2 Simulation setup

For the results presented in this chapter we adopt the following waveforms to describe the GW signal:

(I) A general precessing inspiral-only waveform based on the shifted uniform asymptotics (SUA) method, described in Sec. 2.2. To summarize, the waveform is computed in the frequency domain for the inspiral part only. This model contains higher order harmonics and allows arbitrary orientation of spins (including orbital precession due to spin-orbit coupling). This waveform is used in the computation of the parameter uncertainties based on the Fisher information matrix, and to obtain the main results of this paper;

(II) PhenomC [147], a spin-aligned inspiral-merger-ringdown waveform. This model includes only the dominant harmonic and ignores the orbital precession. It is used only to evaluate the signal-to-noise ratio for the full signal and to rescale the uncertainties on sky position and luminosity distance at merger;

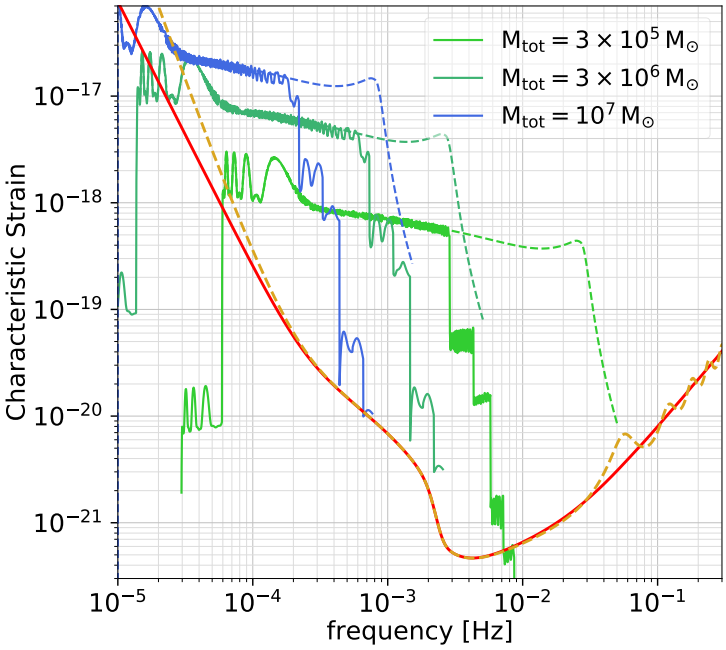

Figure 6.2: Example of GW signals in the LISA band for three MBHBs with source-frame total mass as labeled at redshift $z = 1$. The solid red curve corresponds to the instrument sensitivity, while dashed golden line corresponds to the sensitivity with an additional noise contribution at low frequencies. Blue and green curves represent the typical tracks for non-spinning MBHBs: dashed lines correspond to PhenomC waveform, while solid lines to the only-inspiral waveform. For the plot, we assume $q = 0.5$, $\iota = \psi = \pi/4$, $\theta_N = \cos(\pi/4)$, $\phi_N = \pi/4$, $t_c = 4\,\mathrm{yr}$. For this figure, the stochastic background from the galactic binaries has been set to the level after 4 years of mission. The steps in solid signals correspond to the switch off of different harmonics at the end of inspiral

(III) PhenomHM waveform [229] which also describes inspiral, merger and ring-down parts of the GW signal. Similarly to PhenomC, this model ignores orbital precession but takes into account higher order harmonics. It is used in assessing parameters uncertainties within Bayesian (Markov chain Monte-Carlo) approach.

The first model is the most complete and gives the best estimates for the inspiral part of the GW signal. All three models are reliable in estimating uncertainties in the intrinsic parameters of binary systems (masses, magnitude of spins). Extrinsic parameters (such as distance, orbital inclination, sky position) are quite degenerate in PhenomC model, higher order harmonics and orbital pre-

cession break this degeneracy (at least partially), this is the reason behind using SUA-based inspiral-only and inspiral-merger-ringdown PhenomHM models in the parameter estimation.

In Fig. 6.2 we plot the non sky-averaged sensitivity curves adopted in this work with typical GW signals.

We adopt SUA as waveform to carry on the inspiral parameter estimation at different (observed) times to merger. In particular we stop the waveform at 1 month, 1 week, 3 days, 1 day, 10 hours, 5 hours and 1 hour before coalescence. We compute the 2D sky position error ellipse $\Delta\Omega$ following [230] (see Eq. 4.13) so that the probability for the source to lie outside this region is e^{-1} where e is the source position ellipse eccentricity. The uncertainties on chirp mass and mass ratio are simply propagated as:

$$\begin{aligned}\left(\frac{\Delta\mathcal{M}}{\mathcal{M}}\right)^2 &= \left(\frac{m_1}{\mathcal{M}}\right)^2\left(\frac{\partial\mathcal{M}}{\partial m_1}\right)^2\Sigma^{\ln m_1,\ln m_1} \\ &+ \left(\frac{m_2}{\mathcal{M}}\right)^2\left(\frac{\partial\mathcal{M}}{\partial m_2}\right)^2\Sigma^{\ln m_2,\ln m_2} \\ &+ 2\left(\frac{m_1 m_2}{\mathcal{M}^2}\right)\left(\frac{\partial\mathcal{M}}{\partial m_1}\right)\left(\frac{\partial\mathcal{M}}{\partial m_2}\right)\Sigma^{\ln m_1,\ln m_2}\end{aligned} \tag{6.6}$$

where Σ is the inverse of the Fisher matrix as defined in Sec. 4.2 and similarly for the mass ratio, replacing $\mathcal{M}$ with q (here ln refers to the natural logarithm).

To model the effect of merger and ringdown in the parameter estimation (labeled as 'merger' in our figures), we rescale the sky position and luminosity distance uncertainties at 1 hour before merger as [178]

$$\Delta\Omega_{\rm merger} = \Delta\Omega_{\rm 1h} \times \left[\frac{(S/N)_{\rm SUA}}{(S/N)_{\rm PhC}}\right]^2 \tag{6.7}$$

$$\Delta d_{L,\,\rm merger} = \Delta d_{L,\,\rm 1h} \times \left[\frac{(S/N)_{\rm SUA}}{(S/N)_{\rm PhC}}\right] \tag{6.8}$$

where $S/N_{\rm SUA}$ is the S/N accumulated with the waveform SUA at the end of the inspiral, and $S/N_{\rm PhC}$ is the one computed with the PhenomC waveform.

To asses the validity of our approach, we compare the sky position uncertainties computed with our approach against MCMC simulations for a small subset of 20 samples. To sample the posterior distributions $p(\overline{\theta}|d)$ we adopt two MCMC algorithms: `PTMCMCSampler` [231] without parallel tempering and `ptemcee` [232] with parallel tempering. Using `PTMCMCSampler` without parallel tempering allows sampling the posterior around the true values in a very efficient way, while in the second method we explore the global posterior (including secondary modes) using GPUs [233]. For the first algorithm we adopt uniform distribution in chirp mass,

while for the second one uniform distribution in total mass. The other parameters are sampled the same way for both treatments: uniform distribution in mass-ratio, source volume, binary orientation, polarization, phase and spin magnitude from -1 to 1. For all 20 systems, we use the zero noise realization and adopted the PhenomHM waveform [229], that takes into account higher modes, merger-ringdown phases but ignores precession. Those systems were randomly drawn from our parameter space with the only requirement to have a sky localization uncertainties $\Delta\Omega < 10\,\mathrm{deg}^2$ at 5 hours before merger. For simplicity, we remove the contribution of the galactic background from Eq. (6.1).

A primary goal of the presented work is to provide analytical fits to describe how parameter uncertainties decrease as the signal is accumulated. Therefore we choose to report the median errors, without focusing on the fraction of systems for which a given parameter can be measured up to a certain precision [178]. For the same reason, we do not consider in this work semianalytical models ([234] and later expansions).

A final caveat on the reported uncertainties : the error on the luminosity distance for sources at $z > 0.25$ is expected to be dominated by weak lensing, due to the matter distribution between us and the source [235, 236]. We do not include the effect of weak lensing in our analysis, therefore the reported uncertainties on the luminosity distance and redshift refer to the pure GW measurements.

We run different sets of simulations to properly explore the parameter space. We keep fixed the total (source frame) mass of the system for a set of redshifts. We consider:

(I) $\mathrm{M_{tot}} = 10^5, 3\times10^5, 5\times10^5, 7.5\times10^5, 10^6, 3\times10^6, 5\times10^6, 7.5\times10^6, 10^7, 3\times 10^7\ \mathrm{M_\odot}$;

(II) $z = 0.1, 0.3, 0.5, 1, 2, 3, 4$;

The mass ratio is randomized in [0.1, 1], while the time to coalescence is drawn in [0, 4] yr. Spin magnitudes are flat distributed in [0, 1]. Sky position, angular momentum angles and spin orientations are uniformly distributed over a sphere. Since we want to explore how parameter estimation improves as function of time to coalescence we did not take into account the possibility that LISA stops taking data while a signal is chirping in band. Unless otherwise noted, for each combination of total mass and redshift, we perform $\mathrm{N} = 10^4$ random realizations.

6.3 Preliminary benchmarks

Since we aim to rescale the S/N computed with the SUA waveform at the end of the inspiral with the one computed with the PhC, we start checking that the

two waveforms produce comparable S/N values. In Fig. 6.3 we report the median and 68 percentile S/N values as function of GW frequency for a system with $\mathrm{M_{tot}} = 2 \times 10^6\,\mathrm{M_\odot}$ at $z = 1$. At $f_{\rm gw} \lesssim 10^{-3}\,\mathrm{Hz}$, the S/N distributions are consistent. Far from coalescence, spin effects and higher harmonics are negligible so we should not expect a large difference in the S/N from the two waveforms. The PhenomC waveform takes contribution also from the merger and ringdown portion of the GW signal and gives rise to larger S/N values for $f_{\rm gw} \gtrsim 10^{-3}\,\mathrm{Hz}$.

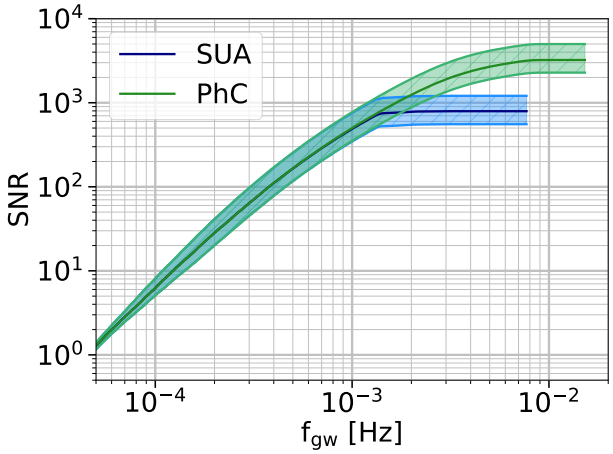

Figure 6.3: S/N as function of frequency for a system with $\mathrm{M_{tot}} = 2 \times 10^6\,\mathrm{M_\odot}$ at $z = 1$. Color according to legend.

We compute the derivatives numerically so we check that our choice of the infinitesimal increment, $\Delta\theta$, for each parameters does not introduce bias in the Fisher matrix. Derivatives can be computed as [237]

$$\frac{\partial h}{\partial \theta} = \frac{h(\theta + \Delta\theta) - h(\theta - \Delta\theta)}{2\Delta\theta}. \tag{6.9}$$

In principle we would like to set $\Delta\theta$ as small as possible, however we have to take into account the digit precision we can reach within our machine. Indeed an infinitesimal value will be seen as exactly zero and the derivative will diverge. To check the optimal $\Delta\theta$ interval for each parameter, we look at the norm of the difference between derivatives computed with close $\Delta\theta$, i.e $|h_i - h_{i-0.5}|/|h_i|$ where i denotes $\Delta\theta = 10^{-i}$. The idea is to choose $\Delta\theta$ values in such a way that the difference between two close delta values is small and 'constant' as function of frequency. This test is not to be considered rigorous but provide and efficient and clear way to set the infinitesimal value for each parameter.

In Fig. 6.4 we report the aforementioned quantity as function of frequency for several values of i for the m_1 parameter (in units of solar mass) of a MBHB with $\mathrm{M_{tot}} = 3 \times 10^6\,\mathrm{M_\odot}$ and $q = 0.5$.

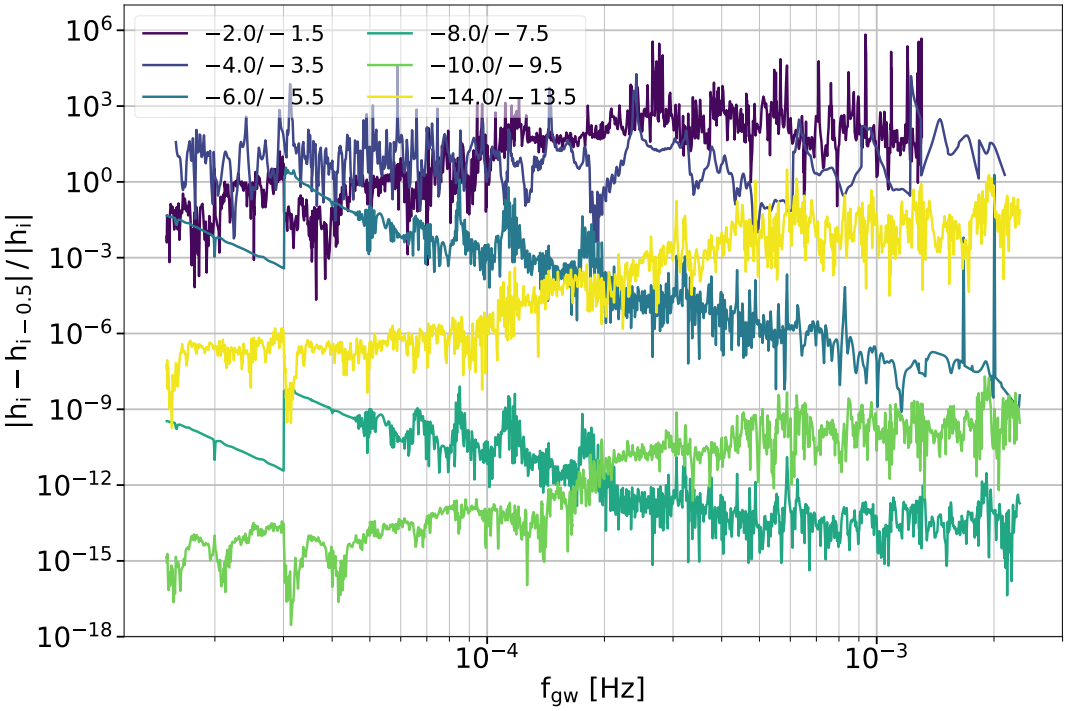

Figure 6.4: Derivative differences for the m_1 parameter as function of frequencies for different values of the infinitesimal increment $\Delta\theta$.

As expected the differences computed with small $\Delta\theta$ values are inconsistent and even larger than 1 for $f_{\rm gw} \gtrsim 10^{-4}$ Hz. The cases for $\Delta\theta = 10^{-6}$ and $\Delta\theta = 10^{-8}$ produce small differences but the behavior at low-frequency show numerical artifacts. The ideal value to compute the derivative is $\Delta\theta \simeq 10^{-10}$ due to the small absolute difference between close deltas. As expected, if we further reduce the value of $\Delta\theta$, the difference increases again moving to the same range of $\Delta\theta = 10^{-6}$.

To avoid possible problems when computing the inverse of the Fisher matrix numerically, we implement an additional check. Following [187], we accept the inverse of the Fisher matrix only if

$$\max_{i,j} |I^{ij}_{\rm num} - \delta^{ij}| < \epsilon_{\rm min} \tag{6.10}$$

where $I^{ij}_{\rm num}$ is the "numerical identity matrix" obtained multiplying the Fisher matrix by its inverse and δ^{ij} is the standard Kronecker delta function. We set

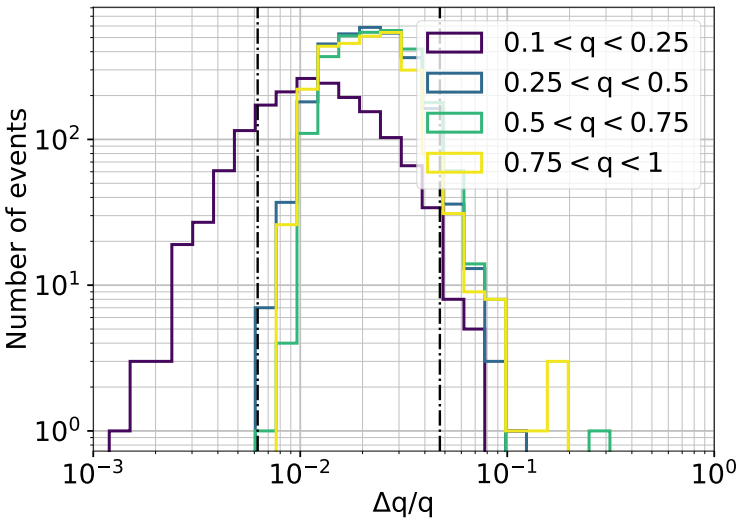

Figure 6.5: Distribution of $\Delta q/q$ uncertainties for different values of mass ratio for a system with $\mathrm{M_{tot}} = 3 \times 10^6\,\mathrm{M_\odot}$ at $z = 1$. Dashed vertical lines correspond to 95 percentile of the whole distribution.

$\epsilon_{\rm min} = 10^{-3}$. Fisher matrix that do not satisfy this condition are rejected and new binary parameters are extracted. We also check that this additional condition on the Fisher matrix does not introduce any bias in the distribution of the initial parameters.

Finally we expect higher harmonics to break degeneracies close to merger and for small mass ratio values. In Fig. 6.5 we report the $\Delta q/q$ uncertainties for a system with $\mathrm{M_{tot}} = 3 \times 10^6\,\mathrm{M_\odot}$ at $z = 1$ for different mass ratio values. As expected, small mass ratio values ($0.1 < q < 0.25$) lead to better constraints on the binary mass ratio while the bulk of events in the 95 percentile region is formed mostly by systems with $q > 0.25$.

6.4 Results

6.4.1 Inspiral parameter estimation of MBHBs

In Fig. 6.6 we show the time evolution of the S/N, the sky-position and luminosity distance estimate for the three systems. Light binaries live longer in the LISA band and accumulate a median $S/N \simeq 20$ already 1 month before coalescence, compared to S/N of $\simeq 5$ and $\simeq 3$ of intermediate and heavy systems respectively. As systems approach merger, the S/N increases. Including the full signal ('merger'), light systems have similar S/N to heavy ones. However, due to the form of LISA

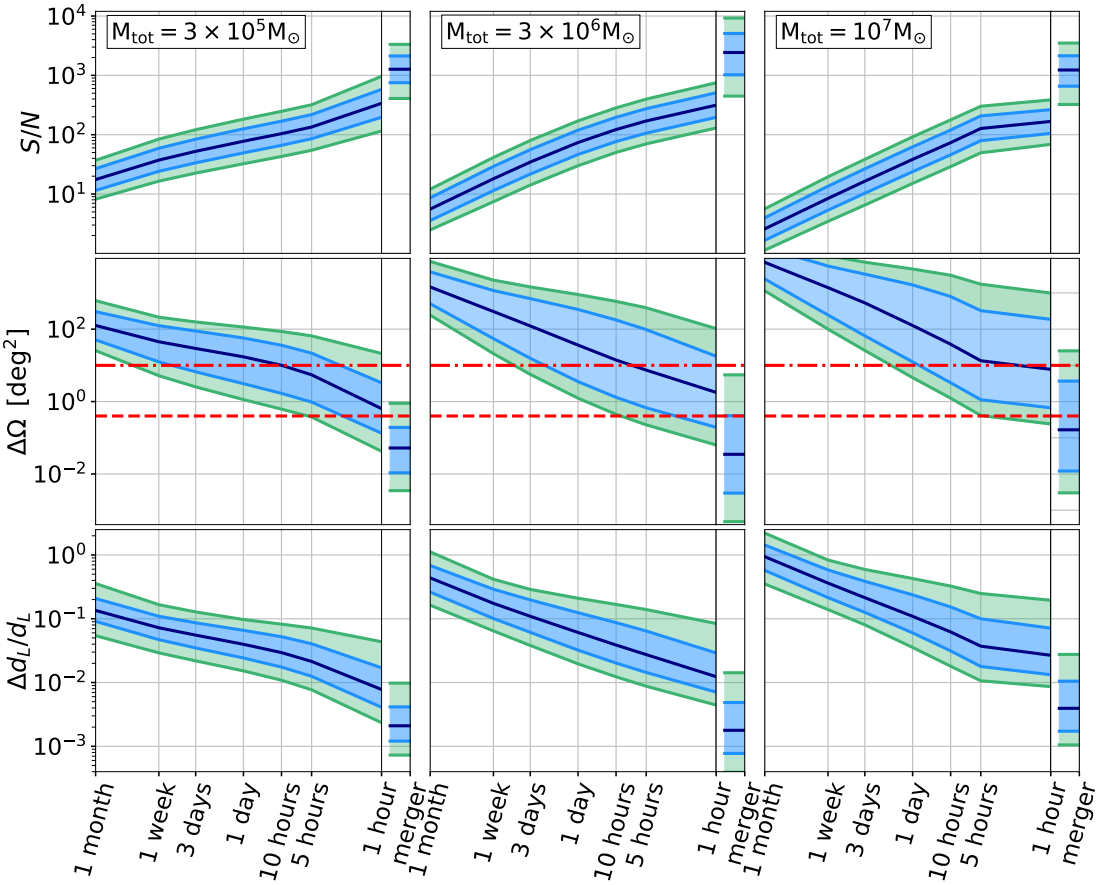

Figure 6.6: Accumulated S/N, sky-position and luminosity distance uncertainties as function of time to coalescence for light (left column), intermediate (central column) and heavy (right column) systems. All sources are located at $z = 1$. Blue line corresponds to the median of the distribution, while light blue and green areas correspond to the 68 and 95 percentiles. For each case, we also plot the S/N, the sky position and luminosity distance uncertainties when the full signal is considered ('merger'), inferred according to the scaling in Eq. (6.7)-(6.8). In the mid panels, the dashed and dotted-dashed horizontal red lines correspond to the field of view of Athena and LSST of 0.4 deg^2 and 10 deg^2 respectively. For all cases, while the S/N monotonically increases, the median of the distributions decreases, leading to a progressively more accurate parameter estimation. However with time the uncertainties around the median value broaden, implying different levels of parameter estimation accuracy for sources with the same mass and redshift. This is especially true for the sky localisation.

sensitivity curve, the S/N contribution from merger and ringdown for intermediate

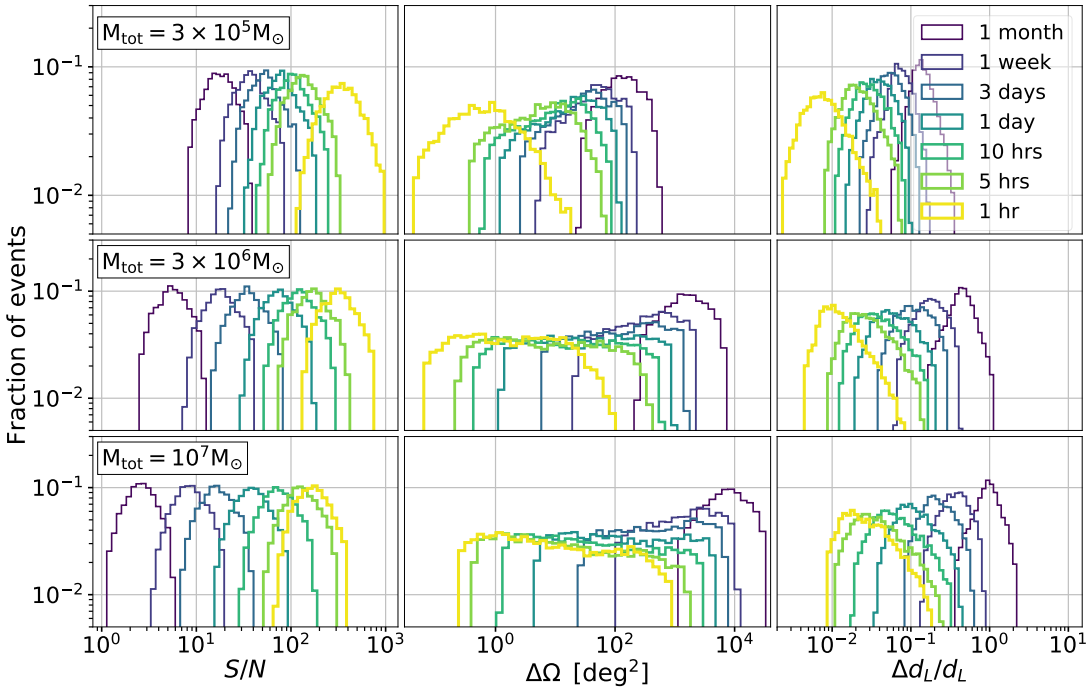

Figure 6.7: S/N, $\Delta\Omega$ and $\Delta d_L/d_L$ distributions of the 95 percentile corresponding to different times to coalescence as indicated in the legend. The total source-frame mass and redshift are as in Fig. 6.6. Upper panels: light systems. Central panels: intermediate systems. Lower panels: heavy systems.

systems leads to a final value of $S/N \simeq 2 \times 10^3$.

Turning to sky localization, lighter systems are typically better localized than heavier ones, especially at earlier time. Light binaries are localized with a median accuracy of $\simeq 100\,\mathrm{deg}^2$ already 1 month before coalescence, due to the modulations imprinted by the detector orbital motion and the higher S/N. As the binary approaches coalescence, the signal accumulates and the uncertainties in the sky localization reduce to $\simeq 10\,\mathrm{deg}^2$ at 10 hours before merger. A similar improvement is also present at shorter timescales, i.e from 10 hours to 1 hour, where the uncertainty drops to $\simeq 1\,\mathrm{deg}^2$, since in this phase the accumulated S/N increases rapidly and spin precession effects come into play. By rescaling the area at the end of the inspiral according to Eq. (6.7), we find final sky localization uncertainties of $\lesssim 0.1\,\mathrm{deg}^2$. Intermediate systems are localized less precisely with a recovered area of $\simeq 10^3\,\mathrm{deg}^2$ 1 month prior to merger. This is due to the lower S/N values. The angular resolution at 1 hour from merger is comparable to that of light systems with a median value of $\simeq 2\,\mathrm{deg}^2$. Eventually, the S/N is dominated by the merger and ringdown part of the signal, allowing a further improvement to the binary's lo-

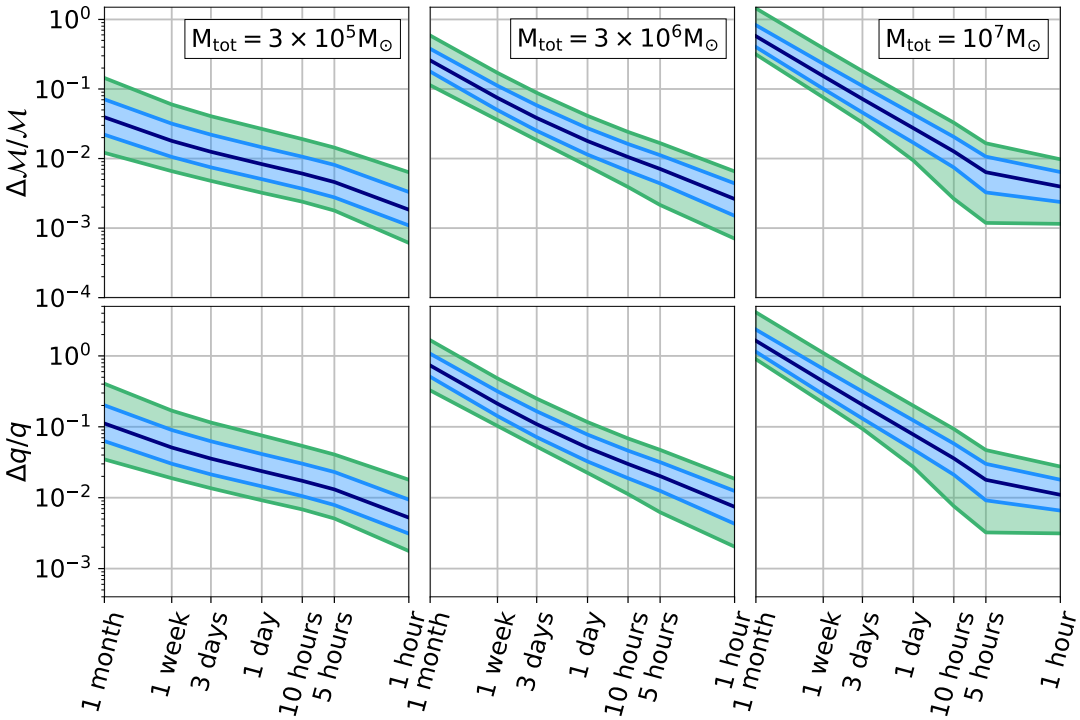

Figure 6.8: Chirp mass and mass ratio relative uncertainties as a function of time to coalescence for the same systems considered in Fig. 6.6.

cation and bringing the median value down to $\simeq 0.04\,\mathrm{deg}^2$. Similar considerations apply to heavy MBHBs. The sky position is essentially unconstrained 1 month before coalescence, mostly due to the very low S/N. By the end of the inspiral, the source can be localized with a median uncertainty of $\simeq 10\,\mathrm{deg}^2$, further reduced to $\lesssim 0.2\,\mathrm{deg}^2$ when the full signal is accounted for.

The luminosity distance for light systems can be determined at 10% and 0.8% level at 1 month and 1 hour from merger, respectively. Similarly to sky localization, the distance determination early in the inspiral is severely degraded when moving to more massive binaries. Nonetheless at the end of the inspiral, the distance for the intermediate and heavy systems can be measured with $\simeq 1\%$ and $\simeq 3\%$ median precision, respectively. Rescaled uncertainties including merger and ringdown are around $0.2-0.4\%$ for all systems. We remind that the reported error in luminosity distance do not include the weak lensing error and, therefore, are to be considered as optimistic.

We note that for intermediate (heavy) mass systems the S/N is still below 10 at 1 month (1 week) from coalescence, therefore the Fisher matrix formalism should be applied with caution. However, at these early times and for these systems, the

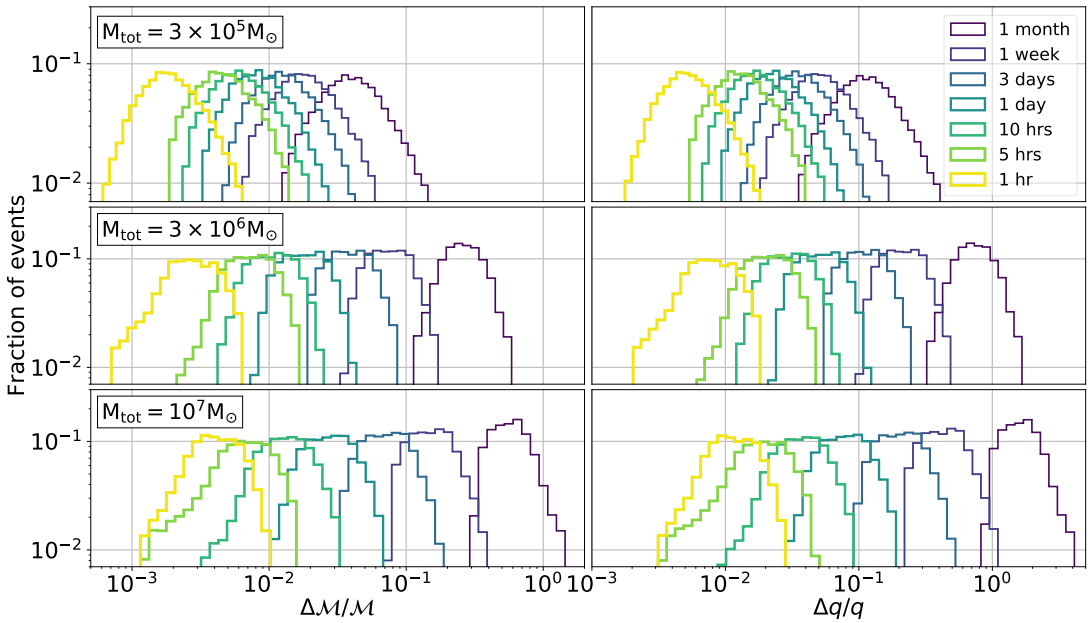

Figure 6.9: Chirp mass and mass ratio uncertainty distributions of the 95 percentile corresponding to different times to coalescence as indicated in the legend. Total source-frame mass and redshift as for the systems in Fig. 6.8.

sky localization is so poor that it is hardly of any use when in search for a potential EM counterpart.

So far, we have discussed median values for the uncertainties on the parameters, but the full distribution is also of importance to interpret our results. Since we fix only the total mass and redshift, we expect that part of the uncertainties is inherited by the spread of the additional parameters affecting the binary signal. We defer to Sec. 6.5 for an in-depth exploration of how each binary parameter shapes the 68 and 95 percentile distribution, while we here only summarize the overall trends and the main findings. As in previous studies, we find that the sky position estimate depends strongly on the true source position in the sky. Even if orbital modulations help to reduce the source position errors at earlier time, it becomes unimportant at the end of the inspiral. However, most of the S/N is accumulated close to merger and, therefore, the final S/N will be small if the binary is located in a low sensitivity region.

While the S/N distributions are similar at all times and for all masses, higher mass systems display broader sky location distributions. Light (heavy) systems distributions extend over 2.5 ($\simeq 4$) order of magnitude at 1 hour before merger. Moreover far from coalescence the source position distributions show similar widths of $\simeq 1$ order of magnitude, almost independent from the total mass of the system.

This is due to the fact that, typically, at that time the system has low S/N so the actual true location of the source has a mild impact. Heavy systems show also larger uncertainties in the luminosity distance close to merger than light and intermediate ones.

In Fig. 6.7 we show the 95 percentile distributions at each time for the three cases: light, intermediate and heavy binaries. The S/N distributions look symmetrically distributed in log around the median at all times and for all systems. Also the sky position uncertainty distributions look similar at 1 month for all the three cases. When the binary approaches coalescence the median sky-position uncertainty decreases but the distribution widens. Light system distributions remain similar over all the inspiral with no major shape changes, while heavy mass system distributions flatten and skew towards lower uncertainties. For the intermediate and heavy systems the position uncertainty distributions are uniform at 1 day and 10 hours from coalescence. However these distributions are skewed to lower values at 5 hours and a 1 hour before merger with stronger effects for heavy mass systems. We find that systems with lower values of the sky location uncertainties are those with low mass ratio and high spin magnitude of the primary BH due to the inclusion of higher harmonics and spin precession effects. The wide spread for heavy systems is due to fast accumulation of most of their S/N very close to the merger where LISA can be seen as static. The error in extrinsic parameters is particularly sensitive to the source position and orientation leading to a large spread. Luminosity distance distributions are similar for all the three cases. While they are symmetric far from coalescence, higher mass systems distributions are skewed towards lower luminosity distance uncertainties at late times.

In Fig. 6.8 we show the chirp mass and mass ratio relative uncertainties for the three cases as function of time to coalescence. For light systems, the chirp mass is determined to few percent accuracy already 1 month from coalesce and it can be constrained to $\simeq 0.2\%$ at the end of the inspiral. This is due to the fact that chirp mass is inferred by phasing the signal during the inspiral, and lighter systems spend more time and wave cycles in band. Moving to higher mass systems, the median uncertainties shift to higher values without, however, a significant loss in LISA ability to constrain the chirp mass, especially at late times. The chirp mass is determined at $\simeq 30\%$ ($\simeq 60\%$) precision at 1 month for intermediate and heavy systems and to less than 1% at 1 hour from coalescence for both cases.

The mass ratio is constrained to 10% precision already 1 month from coalescence and $\simeq 0.5\%$ 1 hour from merger for light systems. The mass ratio is basically undetermined 1 month from coalescence for intermediate and heavy systems, and only at the end of the inspiral the uncertainties reduce to $\simeq 1\%$ level for both cases.

Fig. 6.9 shows the 95% percentile distributions for the chirp mass and mass

ratio uncertainties. Overall, these distributions are narrower around the median compared to those describing the sky position. The chirp mass distributions for light binaries is symmetric around the median values at all times. However intermediate and heavy systems chirp mass uncertainties distributions are uniform inside the 95% interval at early times and skewed close to merger. We check again that the systems contributing to smaller uncertainties are the ones with small mass ratio ($q < 0.4$). Similar considerations apply also to the mass ratio distributions, which are symmetric for the light systems, and skewed for intermediate and heavy ones.

6.4.2 MCMC comparison

In Fig. 6.10 we report the distributions for the log of the ratios between the sky position uncertainties computed following our primary approach (`fisher`) and the results for the two MCMC simulations (`ptemcee` and `PTMCMCSampler`). The distribution of the ratio between `fisher` and `ptemcee` display two sub-populations with a mean value of $\simeq 0.11$. We find that the systems for which the `fisher` approach produces better sky-position uncertainties than `ptemcee` show small mass ratio, i.e. $q < 0.3$. Similar considerations hold also for the comparison between `fisher` and `PTMCMCSampler` areas, with a mean value of 0.05. We also compare the two MCMC estimates to check if the differences between the two implementations of the same technique are compatible with the one coming from `fisher`. In this case the `ptemcee` produces typically smaller areas than the `PTMCMCSampler` approach with a mean value of $\simeq -0.06$, close to the value coming from the comparison between `fisher` and `PTMCMCSampler`. Use of global parameter exploration with `ptemcee` results in finding the secondary mode for some systems.

The secondary modes correspond to the antipodal or reflected points, depending on the actual system considered, of the real binary position in the sky. Including the whole signal with the high frequency response of the detector and higher harmonics break degeneracies during the parameter estimation process [211] and disfavor these secondary modes. In most of these cases, the secondary mode has lower statistical significance. Removing from the analysis the points with secondary mode in the sky position has no strong impact in the ratio distributions[2].

For each of the aforementioned 20 cases we perform an additional check comparing median sky position uncertainties from two independent Fisher matrix codes, the one adopted for this study and another one from Marsat *et al.* [211] without spin-precession. We keep fixed the total mass of the system, mass ratio, redshift

[2]For one system, the sky position posterior distribution from `ptemcee` has not enough samples to make proper estimation, therefore blue histograms in the upper and lower panels have 19 entries.

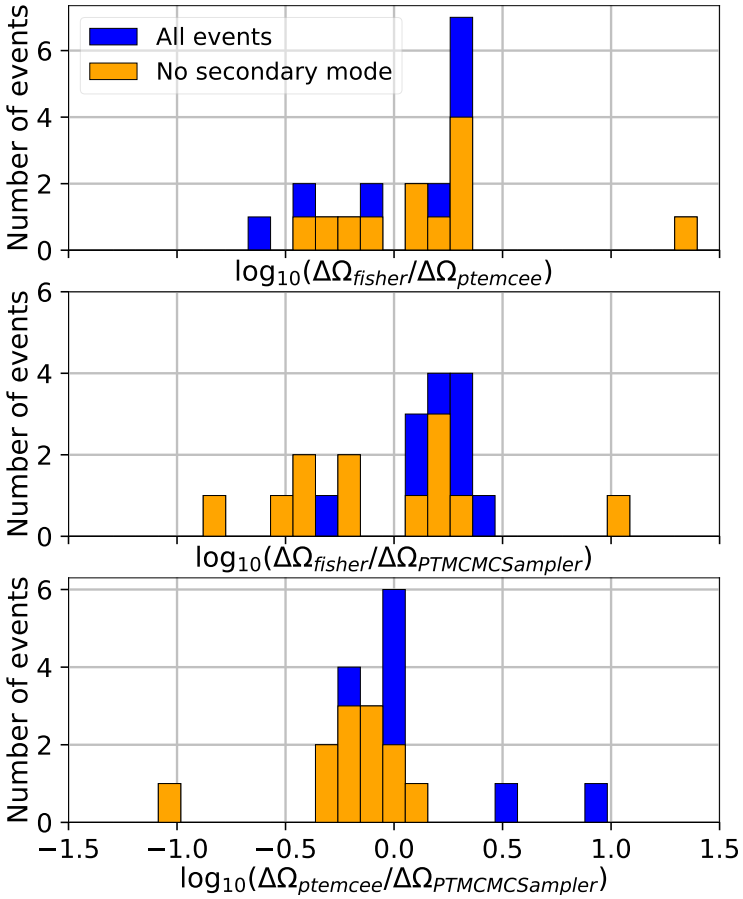

Figure 6.10: Sky localization log uncertainty ratio distribution obtained comparing different methods. Blue histograms refers to the whole set of 20 points, while orange histograms refer only to cases without secondary mode in the sky-position. Upper panel: `fisher` and `ptemcee`. Middle panel: `fisher` and `PTMCMCSampler`. Lower panel: `ptemcee` and `PTMCMCSampler`.

and spin magnitude while we randomize over sky position, polarization, inclination, time to coalescence and initial phase. For each case we perform N = 10^3 realizations. In Tab. 6.2 we report the mean value of the ratio between the median sky position uncertainties obtained from the code adopted in this study and the alternative one, $\mathcal{R}^{\Delta\Omega}$, at different times from merger and when the full signal is included ('merger'). From 1 month and up to 3 days to merger, the code used for this study recover median sky position uncertainties $\simeq 3$ times larger, while the opposite happen for times close to merger. Overall the agreement between the two results is quite good, especially at 1 day from merger. The results from the code adopted in this study are better at the last stages of inspiral due to the inclusion

Time	$\mathcal{R}^{\Delta\Omega}$
1 month	3.15
1 week	2.05
3 days	1.54
1 day	0.84
10 hours	0.47
5 hours	0.30
1 hour	0.87
merger	0.35

Table 6.2: Mean value of the ratio between the sky position uncertainties computed with the same Fisher adopted in this study and the one from Marsat *et al.* [211] at different times from merger and when the full signal is included ('merger').

of spin-precession that break degeneracies close to merger.

6.4.3 Analytical fits to parameter estimation uncertainties

Having discussed the trends of the parameter estimation and precision for our selected sources, we now turn to the main aim of this study: provide *ready-to-use fitting formulas* that allow to infer on the fly the properties of an emerging LISA source (sky localization, distance determination, chirp mass and mass ratio in particular). For sky position and luminosity distance we provide additional formulas when the full signal is considered to inform astronomers of a potential counterpart for targeted and instructed searches.

Since we propose to provide multidimensional formulas to model error uncertainties as the signal accumulates in band, we need to find a reasonable balance between the number of input parameters required and the accuracy of the proposed formulas. In other words we desire a formula that takes as input only few key parameters and matches reasonably well simulation results. The (observed) time left before binary coalescence has to be one of the input parameters. We also need the total (intrinsic) mass of the binary and the redshift of the source, since they will both affect the relative strain of the signal in the detector. Although the amplitude of the GW signal scales with the system chirp mass [24], we choose to adopt the total mass of the system as input parameter since it is the quantity normally used within the astrophysical community.

In principle, the parameter estimation depends on all the other binary parameters , i.e mass ratio, sky position, time to coalescence, spins, inclination, polarization and initial phase. Including all of them would dramatically increase

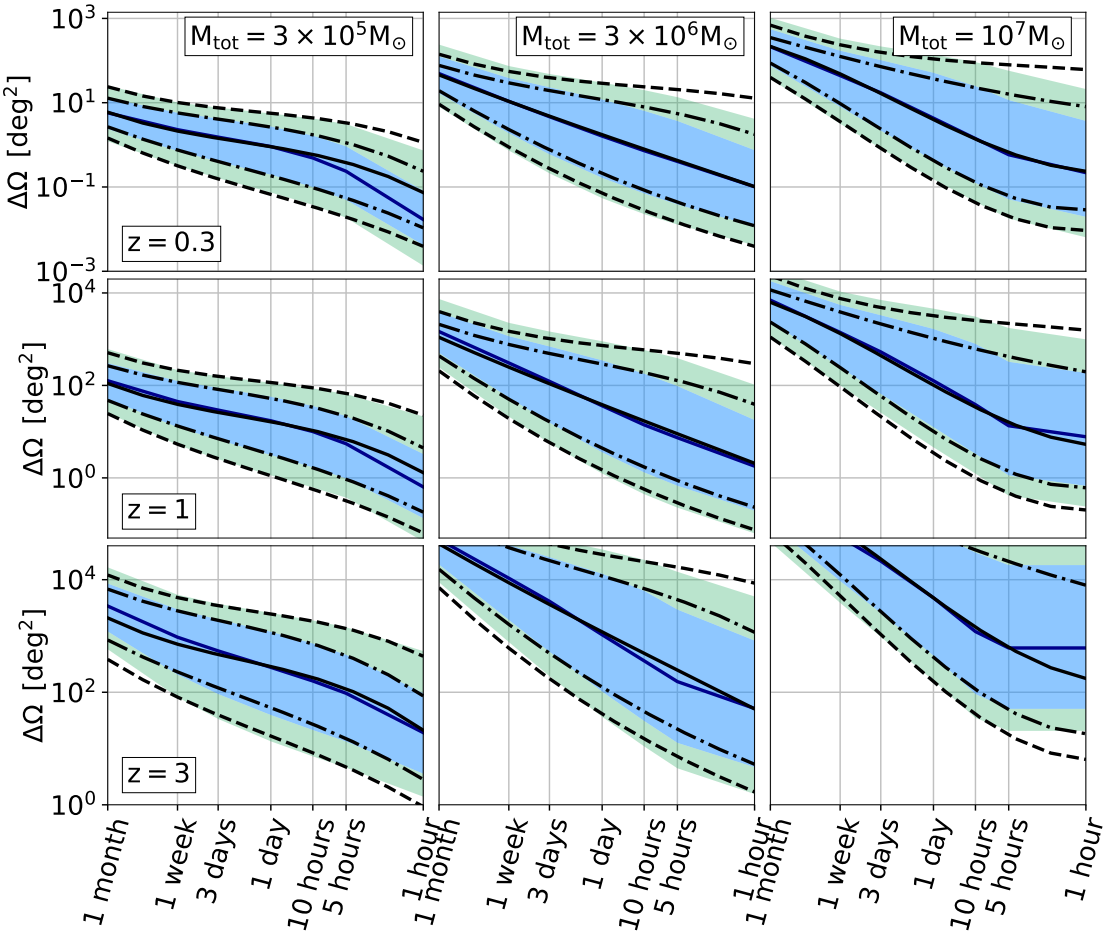

Figure 6.11: Time evolution of sky position uncertainties obtained with the Fisher Matrix approach compared to that recovered employing fits from Eq. (6.11) - (6.12). Blue lines correspond to the median of distribution while blue and green areas to the 68 and 95 percentiles. Solid, dashed-dotted, and dashed lines correspond to the fit outcome for the median, 68% and 95% regions, respectively. Each column refers to a different source-frame MBHB total mass as labeled. Upper panels: MBHB at $z = 0.3$; middle panels: $z = 1$; lower panels: $z = 3$.

the complexity of the fitting functions.

Averaging over some of the aforementioned parameters is also justified by what is expected in a real situation. MBHBs will be isotropically distributed in the sky, with uniform randomly distributed inclination and polarization. The situation is less clear for spin magnitude and directions. MBHs gain their mass mostly from accretion, which affects their spin in different ways depending on the coherency of the accretion flow [238–242]. Mutual spin orientations in MBHBs are further

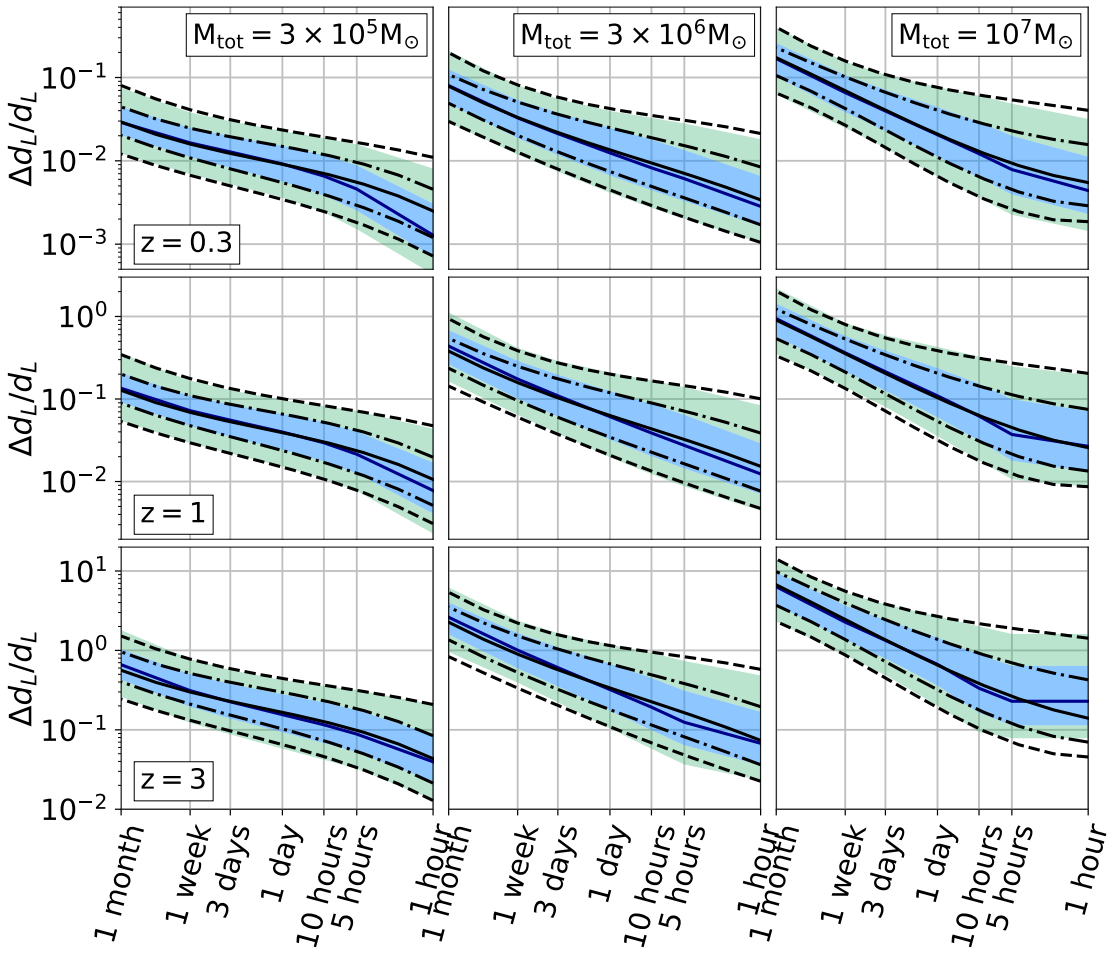

Figure 6.12: Same as Fig. 6.11, but for the luminosity distance relative uncertainties.

determined by their close environment; 'dry' mergers (where the binary evolution is primarily driven by stars) generally result in random spin orientations [243], whereas 'wet' mergers (where the evolution is driven by gas) promote spin magnitude growth and spin-orbit alignment [244–246].

In Sec. 6.5 we explore in more detail how these parameters affect the sky position, luminosity distance, chirp mass and mass ratio uncertainties. However, we briefly note here that none of them produces clear trends, with the exception of the true sky position of the source and therefore we chose to average over all of them and keep only three input parameters for our formulas, i.e. the total (intrinsic) mass of the system, its redshift and the (observed) time to coalescence.

Given total mass M_{tot} at redshift z, the evolution of parameter uncertainty ΔX

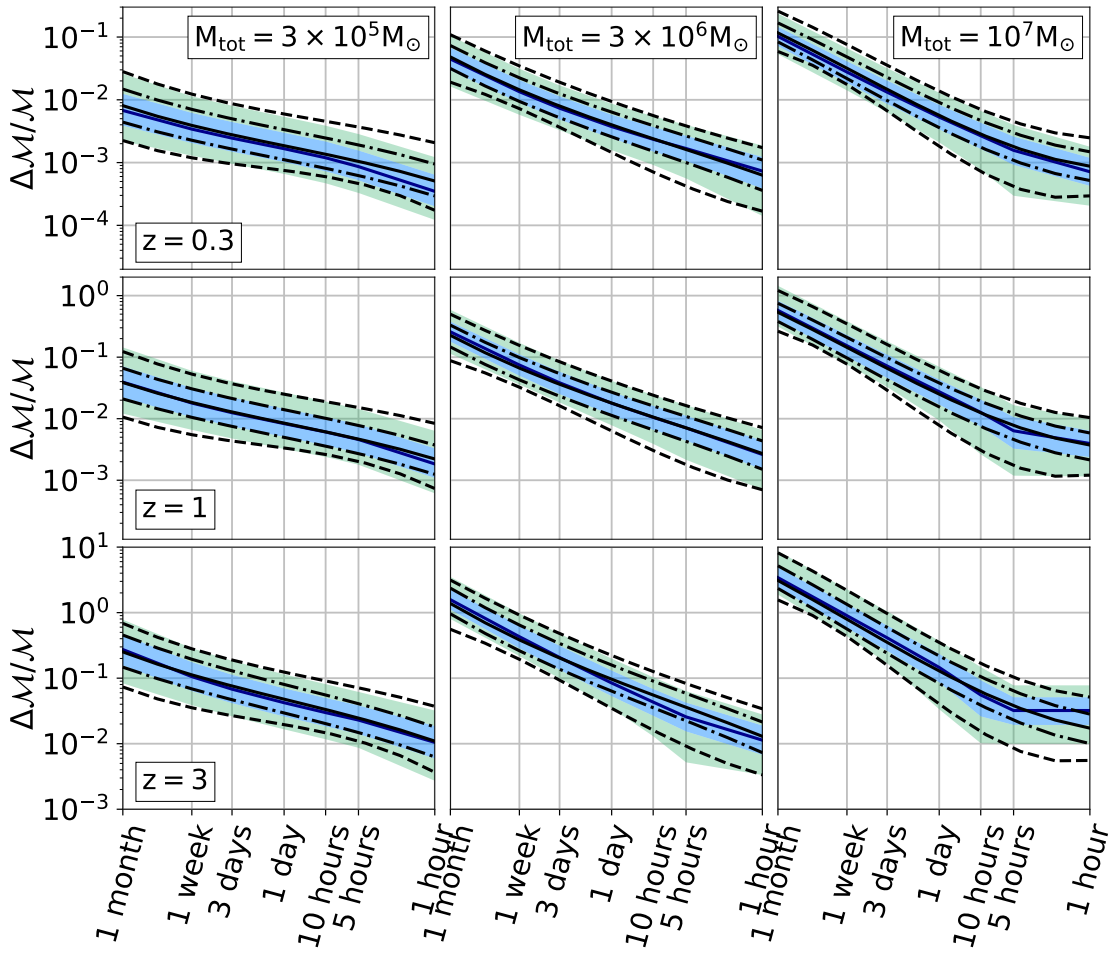

Figure 6.13: Same as Fig. 6.11, but for the chirp mass relative uncertainties.

from 1 month to 1 hour before merger is described as $\log_{10} \Delta X = \mathcal{F}(\log_{10} \mathrm{t_c}, \log_{10} \mathrm{M_{tot}}, z)$, where $\mathcal{F}$ is a third degree polynomial expression of $\log_{10} \mathrm{t_c}$ and $\log_{10} \mathrm{M_{tot}}$ with a supplementary dependence on redshift. We tested different expressions varying the number of parameters and we find that the following expressions are the best compromise. We initially fit values at constant redshift and then add a redshift dependence to take into account the uncertainties evolution. In practice we use the form

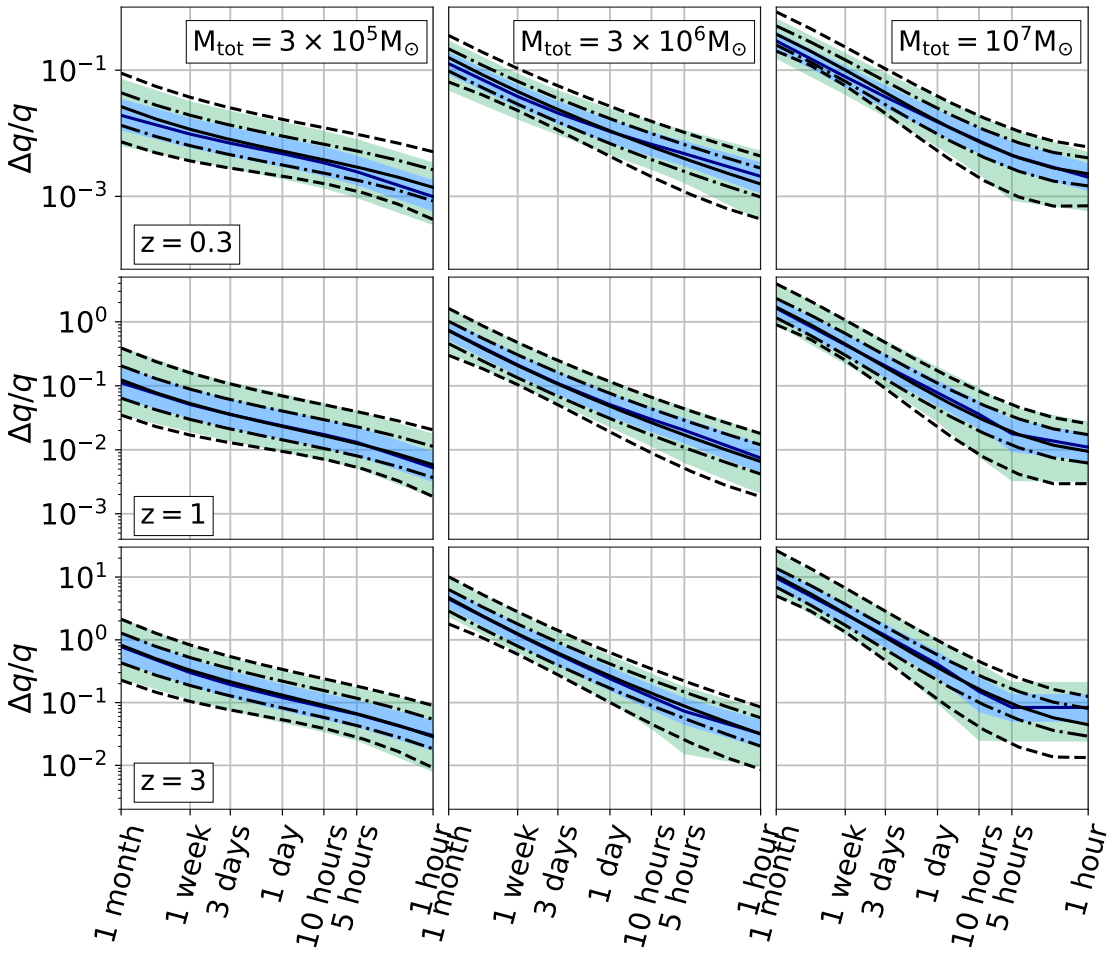

Figure 6.14: Same as Fig. 6.11, but for the mass ratio relative uncertainties.

$$
\begin{aligned}
\log_{10} \Delta X = {} & c_1 + c_2\, y + c_3\, y^2 + c_4\, y^3 \\
& + c_5\, x + c_6\, x\, y + c_7(z,\, y)\, x\, y^2 \\
& + c_8\, x\, y^3 + c_9\, x^2 + c_{10}\, x^2\, y \\
& + c_{11}\, x^2\, y^2 + c_{12}\, x^2\, y^3 + c_{13}\, x^3 \\
& + c_{14}\, x^3\, y + c_{15}\, x^3\, y^2 \\
& + c_{16}\, x^3\, y^3 + z_c \left(\frac{z - 0.5}{0.25\, z + 0.25} \right),
\end{aligned}
\tag{6.11}
$$

where $x = \log_{10}(\mathrm{t_c}/\mathrm{sec})$, $y = \log_{10}(\mathrm{M_{tot}}/\mathrm{M_\odot})$ and z is the source redshift. $c_1, \ldots, c_{16}$ and z_c are numerical coefficients whereas $c_7(z,\, y)$ is a function of mass and redshift

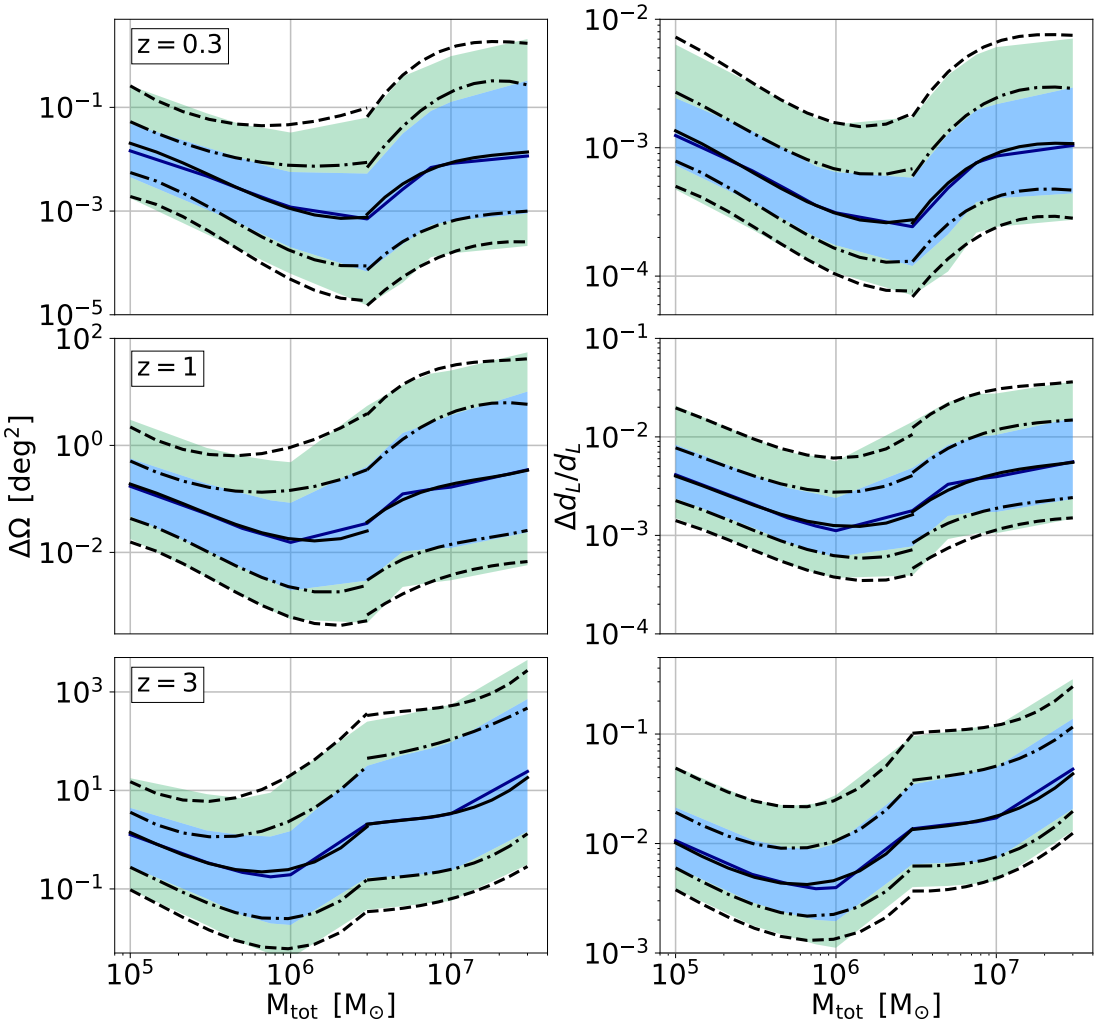

Figure 6.15: Sky localization (left column) and luminosity distance (right column) uncertainties at merger obtained with the Fisher Matrix approach compared to fits from Eq. (6.14) - (6.15) as function of the total mass of the binary. Color code and line style as in Fig. 6.11. Upper panels: $z = 0.3$. Middle panels: $z = 1$. Lower panels: $z = 3$.

only, dependent on more four coefficients

$$c_7(z,\, y) = d_1 + d_2\, y \\ d_3\, z + d_4\, z\, y. \tag{6.12}$$

Here we express c_7 as function of redshift and total mass however this is not true in general. For each case, we choose which parameter should be a combination of

the previous input parameters by looking at the one that could match better the simulations. $\mathcal{F}$ is therefore a function of 21 numerical coefficients.

For the four key parameters discussed in the previous section – $\Delta X = \Delta\Omega/\mathrm{sr}$, $\Delta \mathrm{d_L}/\mathrm{d_L}$, $\Delta\mathcal{M}/\mathcal{M}$, $\Delta q/q$ – we adopt Eq. (6.11) to fit the median, 68% and 95% confidence interval of the uncertainties in the LISA measurements. We report the value of the coefficients for the median, 68% and 95% confidence regions for the uncertainties on the sky localization and luminosity distance in Tab. A.1. The value for the chirp mass and mass ratio fits are reported in Tab. A.2. In these table the coefficients computed according to Eq. (6.12) are labeled with '[z, $\log_{10}$ $\mathrm{M_{tot}}$]'.

For the degraded sensitivity curve we include two additional coefficients in Eq. (6.12), i.e.

$$\begin{aligned} c_{7,\mathrm{degr}}(z,\, y) = d_1 + d_2\, y \\ d_3\, z + d_4\, z\, y \\ d_5\, z^2 + d_6\, z^2\, y \end{aligned} \tag{6.13}$$

and replace the term $(z-0.5)$ in Eq. (6.11) with $(z-1)$ to better fit the simulation results. The additional coefficients are reported in the aforementioned GitHub repository.

Even if we perform simulations of systems with $\mathrm{M_{tot}} \in [10^5,\, 3\times10^7]\ \mathrm{M_\odot}$ and $z \in [0.1, 4]$, our formulas can be applied only on a slightly smaller subset: they are valid for systems with $\mathrm{M_{tot}} \in [10^5,\, 10^7]\ \mathrm{M_\odot}$ and $z \in [0.3, 3]$ because we choose to focus on providing formulas that can be used for the expected majority of LISA sources.

In the following, we provide a visual comparison between the analytical fits and the results of the Fisher matrix simulations for binaries with $\mathrm{M_{tot}} = 3\times10^5,\, 3\times10^6,\, 10^7\,\mathrm{M_\odot}$ (i.e. the 'light', 'intermediate' and 'heavy' systems considered in the previous subsection) placed at $z = 0.3$, $z = 1$ and $z = 3$.

In Fig. 6.11 we show results for the sky localization. Overall there is a good agreement between our fits and the outcomes of our simulations. However the fits overestimate the sky position uncertainty for light systems at $z = 0.3$ 1 hour from merger by a factor 3-4. This is because the precision in the source position for low-redshift light systems has a steep improvement close to merger, where the accumulated S/N leads to a shrinkage of the localization area of an order of magnitude on a short timescale (from 5 hours to 1 hour before merger). We lose some precision when fitting the 69 and 95 percentile upper limit for intermediate and heavy systems, especially at $z = 0.3$. If the system is massive and at high redshift the orbital timescale at the ISCO is comparable to 1 hour and, since we truncate our waveform when the MBHB separation reaches $6\,\mathrm{M_{tot}}$ as we are not able to explore shorter time intervals. For this reason the sky position uncertainties are flat from 5 hours to 1 hours for massive and distant sources.

In Fig. 6.12 we perform the same comparison for the luminosity distance. Also for this parameter, our fits reproduce well the simulation outcomes with the exception of light systems at $z = 0.3$ and heavy systems at $z = 3$ both at 1 hour from coalescence. However here the results for the median from the fit differ from the simulation values only by a factor of 2.

Finally, in Fig. 6.13 and Fig. 6.14 we compare our formulas for the chirp mass and mass ratio to the simulation results. Again the fits match quite well the Fisher outcomes with the same caveats of the sky position and luminosity distance. The larger differences between our fits and the simulations are usually a factor 2.

We also provide fits to the sky position and luminosity distance uncertainties for the full signal, computed from Eq. (6.7)-(6.8). Since for this case we do not have the time dependence, we reduce the number of coefficient necessary for the fit. As a consequence we are able to extend the validity of these formulas to the full parameter space explored, i.e. the formulas describing the sky position and luminosity distance uncertainties when the full signal is considered are valid for $\mathrm{M_{tot}} \in [10^5,\, 3\times 10^7]\ \mathrm{M_\odot}$ and $z \in [0.1, 4]$.

In this case, however, the noise due to Galactic binaries becomes important. Since the merger-ringdown S/N is accumulated over a relatively narrow range of frequencies, the impact of the galactic foreground is highly mass-dependent and to obtain an acceptable fit we have to split the mass range in two sub-intervals, namely $[10^5,\, 3\times 10^6]\ \mathrm{M_\odot}$ and $[3\times 10^6,\, 3\times 10^7]\ \mathrm{M_\odot}$. The formulas are the same for the two ranges but, clearly, the coefficients are different. As for the inspiral, one of the coefficients is given by a nested function of redshift. Using again $y = \log_{10}(\mathrm{M_{tot}}/\mathrm{M_\odot})$ and the redshift z, uncertainties can be expressed as

$$\begin{aligned}\log_{10}\Delta X = {} & \frac{z}{m_1(z)} + \\ & + m_2\, z + m_3\, y + m_4\, z^2 \\ & + m_5\, y^2 + m_6\, z^3 + m_7\, y^3 \\ & + m_8\, z\, y + m_9\, z^2\, y + m_{10}\, z\, y^2\end{aligned} \tag{6.14}$$

where

$$\begin{aligned}m_1(z) = {} & n_1 + n_2\, z \\ & n_3\, z^2 + n_4\, z^3 + n_5\, z^4,\end{aligned} \tag{6.15}$$

and $\Delta X = \Delta\Omega/\mathrm{sr},\ \Delta d_L/d_L$. Similar to what done for the fits for the inspiral part of the signal, we provide expressions also for the 68% and 95% intervals. We report the coefficient value for the sky position and luminosity distance for $\mathrm{M_{tot}} \in [10^5,\, 3\times 10^6]\ \mathrm{M_\odot}$ in Tab. A.3 and for $\mathrm{M_{tot}} \in [3\times 10^6,\, 10^7]\ \mathrm{M_\odot}$ in Tab. A.4.

For the degraded sensitivity curve we keep the same expression without adding any further coefficients. Also these coefficients can be found on the GitHub repository.

In Fig. 6.15 we compare the above fits to the full inspiral-merger-ringdown sky location and luminosity distance errors obtained for our set of simulations, at three different redshifts. At $M_{tot} = 3 \times 10^6$ there is a small gap between the fits due to the fact that we focus on fitting the overall behaviour in both sub-intervals rather than requiring the continuity of the equation at their point of contact. Overall our formulas follow closely the distributions of sky location and luminosity distance uncertainties .

6.4.4 Time progression of parameter estimation

The analytical fits provided in the previous section can be used to generate 'advanced warning' contour plots across the parameter space. In practice, one can fix a desired precision of a given parameter and ask how long prior to merger such precision is achieved across the mass-redshift parameter space. This is particularly useful, for example, to assess under which circumstances and for which sources a specific instrument is appropriate to search for a counterpart, or to pre-select *on the fly* candidates from existing galaxy catalogs in the expected mass and redshift ranges to concentrate follow-up efforts on the most promising candidates. We now show the contour maps of each parameter and discuss specific examples of their use in the next section.

In the two panels of Fig. 6.16 we plot the remaining time prior to coalescence for progressively smaller values of the sky position uncertainty. For example, a MBHB with $M_{tot} = 10^6\,M_\odot$ at $z \simeq 0.6$ ($z \simeq 1.5$) can be localized within $\Delta\Omega = 10\,\mathrm{deg}^2$ ($100\,\mathrm{deg}^2$) 2 days before merger. However the source has to be at $z < 0.5$ ($z \simeq 1.1$) for a 1 week earlier alert. Note that in this and in the following figures, contours are produced using the fit to the median values of the parameter estimation. As shown in Fig. 6.6, the sky location estimate is subjected to large uncertainties, which affects also the contour plots and in turn the redshift at which a source can be localized with a solid angle at a given time prior coalescence. An example of this is given in the upper panel of Fig. 6.16 and refers to localization of $10\,\mathrm{deg}^2$, 2 days before merger. Depending on the specific parameters at the source, the redshift at which a MBHB with $M_{tot} = 10^6\,M_\odot$ can be localized with a $10\,\mathrm{deg}^2$ accuracy 2 days before merger ranges from $\simeq 0.3$ up to 1.2. The lower panel of Fig. 6.16 shows that median localizations of $1\,\mathrm{deg}^2$ or better ($0.4\,\mathrm{deg}^2$) can only be achieved 5 hours (1 hour) before merger for MBHBs at $z \lesssim 0.5$. Again depending on the source parameters, the redshift at which a MBHB with $M_{tot} = 10^6\,M_\odot$ can be localized within $0.4\,\mathrm{deg}^2$ 1 hour before merging ranges similarly from less than 0.3 up to about 1.3.

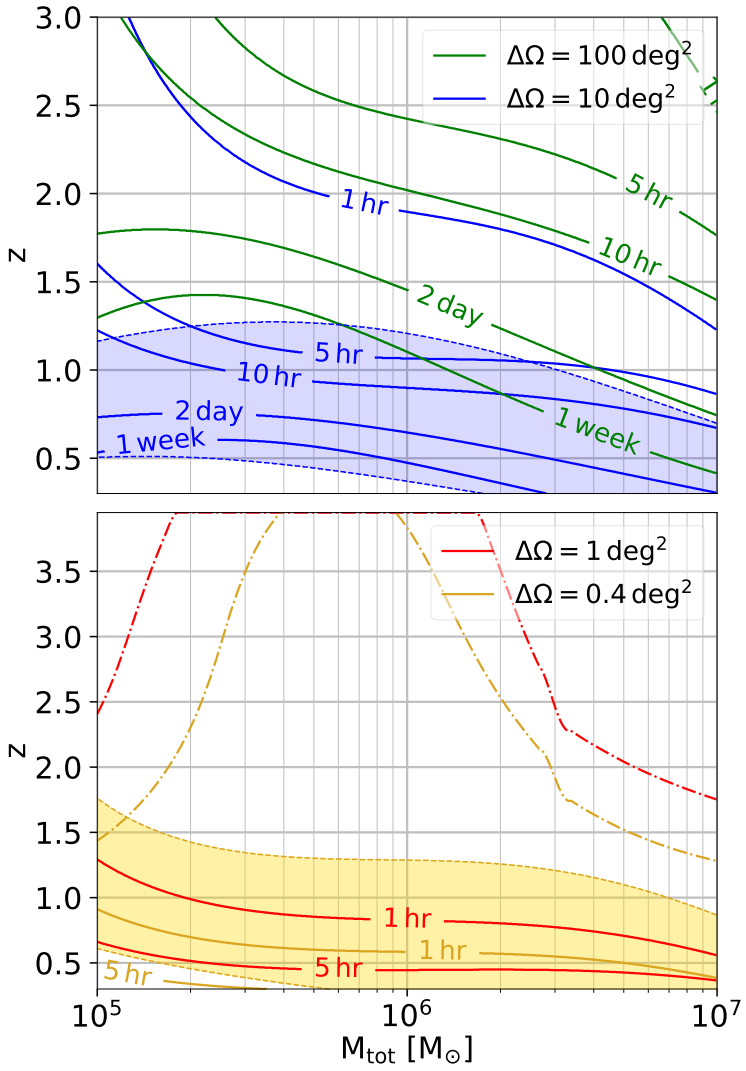

Figure 6.16: Contours of constant 'remaining' time in the $(\mathrm{M_{tot}}, z)$ plane, for selected values of the median sky localization reached during the binary inspiral, as indicated in the legend. The shaded blue (yellow) area in the top (bottom) panel corresponds to the 68 percentile of the distribution around the median value of $\Delta\Omega = 10\,\mathrm{deg}^2$ 2 days before merger ($\Delta\Omega = 0.4\,\mathrm{deg}^2$ 1 hour before merger). In the bottom panel the dash-dotted red (yellow) line gives the line of constant $\Delta\Omega$ equal to $1\,\mathrm{deg}^2$ ($0.4\,\mathrm{deg}^2$) when we account for the full signal, i.e. including the 'merger'.

However measurements improve right after merger, when the full signal is considered in the parameter estimation. This is shown by the dashed-dotted lines,

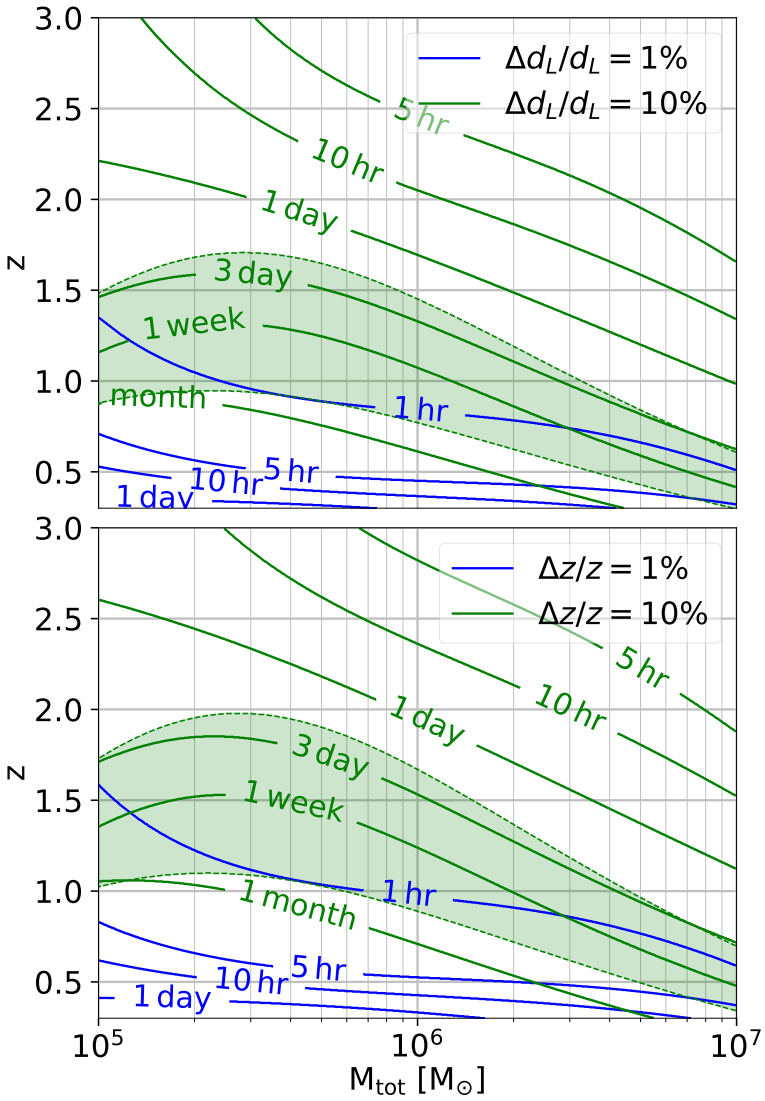

Figure 6.17: Contours of constant 'remaining' time in the (M_{tot}, z) plane for two selected values of the precision on the luminosity distance (upper panel) and redshift (lower panel) estimates reached during the binary inspiral, as indicated in the legend. The green area corresponds to the 68 percentile of the relative uncertainty distribution on d_L (upper panel) and $\Delta z/z$ (lower panel), calculated 1 week before coalescence, assuming $\Delta d_L/d_L = 10\%$ and $\Delta z/z = 10\%$, respectively.

which highlight how sources in the interval between a few $10^5\,M_\odot$ up to a few $10^6\,M_\odot$ can be localized to sub$-\,\mathrm{deg}^2$ precision beyond $z = 3$.

The results of the same type of analysis for the luminosity distance are presented in Fig. 6.17. For a MBHB with $M_{tot} = 10^6\,M_\odot$, 10% d_L precision can be

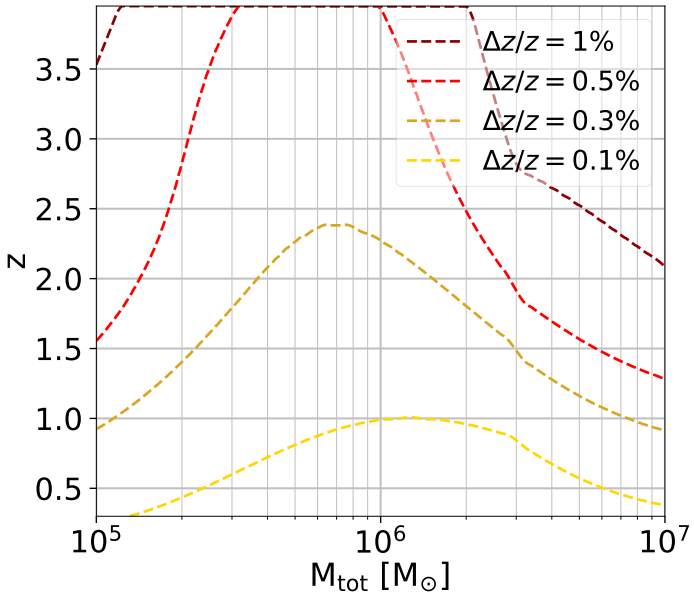

Figure 6.18: Lines of constant $\Delta z/z$ as labeled in the plot in the $(\mathrm{M_{tot}}, z)$ plane when we account for the full signal, i.e. including the 'merger'. Also here we are neglecting lensing errors.

generally achieved one week (10 hours) before merger at redshift $z \approx 1$ ($z \approx 2$). Getting to the 1% precision level, however, is much more challenging during the inspiral, and is generally possible only few hours before merger for systems at $z \lesssim 1$. Albeit to a lesser extent than sky localization, results still depend on the specific parameter of the source, with the uncertainty range marked by the green shade in Fig. 6.17. For example, the luminosity distance of a particularly favorable MBHB with $\mathrm{M_{tot}} = 10^6\,\mathrm{M_\odot}$ can be measured with 10% precision 1 week before merger even if it is at $z \approx 1.5$. For an unfavorable system, the same performance is achieved only if it is located at $z \approx 0.8$.

Following Eq.(3.7) in [204] and assuming a fixed cosmology ($\Delta H_0 = \Delta\Omega_\Lambda = 0$), we convert the error on luminosity distance in a redshift error and give the result in the lower panel of Fig. 6.17. For a system with $\mathrm{M_{tot}} = 10^6\,\mathrm{M_\odot}$ the redshift can be determined to 10% precision 1 week before merger if the source lies in $z \in [0.9, 1.6]$. For the same binary 1% accuracy is attained 1 hour (10 hours) prior merging for $z \sim 1$ ($z \sim 0.4$). Redshift uncertainties clearly mirror those on the luminosity distance.

In Fig. 6.18 we report the $\Delta z/z$ uncertainties when the full signal is considered. Systems with $\mathrm{M_{tot}} \simeq 10^6\,\mathrm{M_\odot}$ are localized with a precision of $\Delta z/z \simeq 0.1\,(0.3)\%$

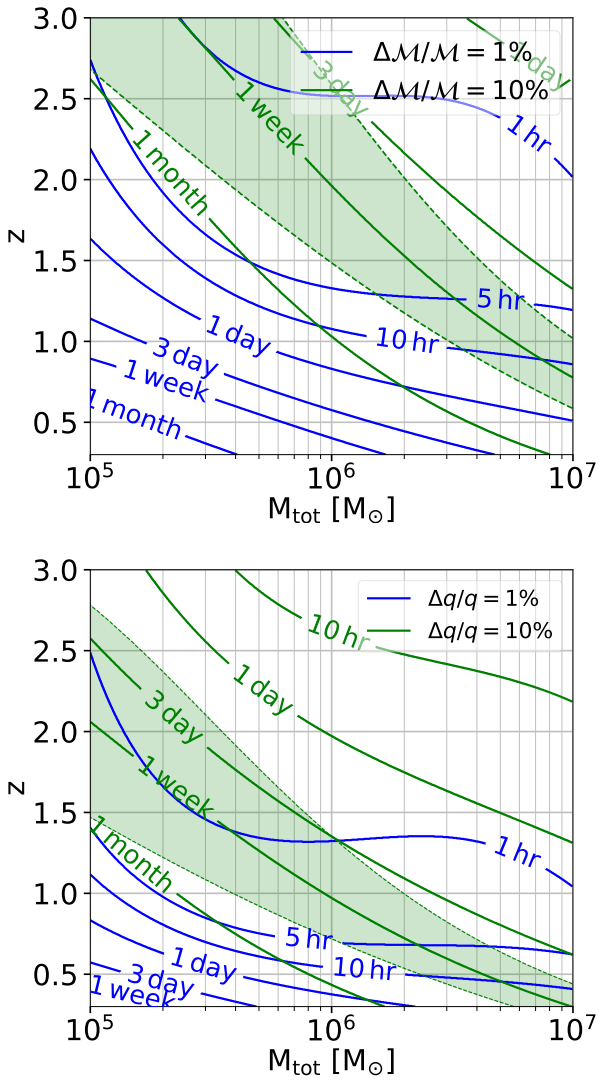

Figure 6.19: Contours of constant 'remaining' time in the (M_{tot}, z) plane for selected values of the median relative error for chirp mass (upper panel) and mass ratio (bottom panel) as labeled. Green and blue lines refer to a precision of 10% and 1%, respectively. The green area in each panel corresponds to the 68 percentile of the uncertainty distribution on $\mathcal{M}$ and q evaluated 1 week before coalescence assuming a precision of 10%.

up to $z \lesssim 1\,(2.3)$. Except for the most massive systems ($M_{tot} > 3 \times 10^6\,M_\odot$), the redshift of all MBHB mergers can be determined by LISA to a precision of 1% up to $z \simeq 4$.

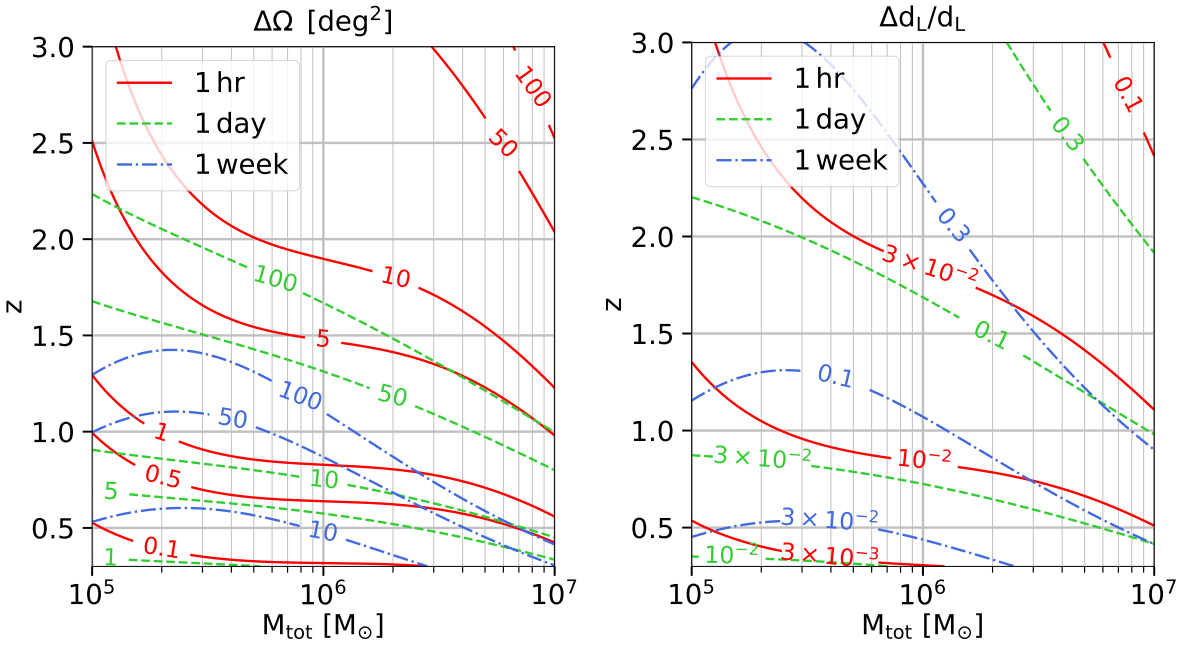

Figure 6.20: Contours of constant sky position (left panel) and luminosity distance (right panel) uncertainties in the (M_{tot}, z) plane. Continue (dashed) [dotted-dashed] lines correspond to 1 hour (1 day) [1 week] before merger.

We stress again that the reported uncertainties in the luminosity distance do not take into account the weak lensing error. The lensing limit our error $\Delta d_L/d_L \simeq 1\%$ already at $z = 1$. At $z = 0.5, 1, 2$ this translates to a $\Delta z/z \simeq 0.83\%, 0.81\%, 0.82\%$ respectively

Finally, in Fig. 6.19 we plot the same time contour levels in progression, i.e. those times at which a parameter is determined at 1% and 10% precision for the source's intrinsic parameters; namely chirp mass and mass ratio.

As expected, when increasing the total mass of the system or the source redshift, the amount of time left, when the required precision is reached, is reduced for both parameters (note that this is not always the case for extrinsic parameters discussed before). Starting from the upper panel, LISA could constrain the chirp mass at 1% (10%) 1 week from coalescence for a system with $M_{tot} = 10^6\,M_\odot$ at $z \simeq 0.4$ ($z \simeq 2$).

Overall, the chirp mass is basically determined with 10% precision 1 day before merger for the whole parameter space considered in this study and even 1 month before merger for sources with $M_{tot} \lesssim 10^6\,M_\odot$ out to $z \lesssim 1$. However we stress that, even for the chirp mass determination, there are large uncertainties in the progression of times to coalescence. The chirp mass of systems with $M_{tot} = 10^7\,M_\odot$

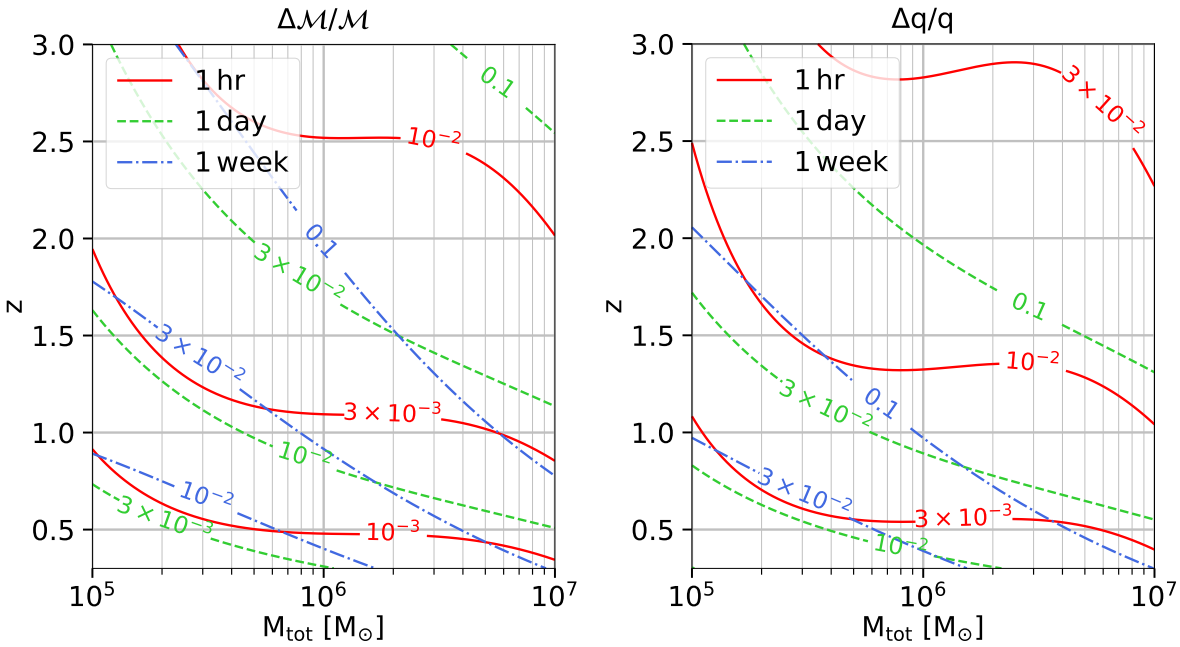

Figure 6.21: Same as Fig. 6.20 for chirp mass (left panel) and mass ratio (right panel) uncertainties.

can be determined with 10% precision 1 week prior merger if the redshift of the source is $z \in [0.6, 1]$, depending on the exact parameters. For a systems with $M_{tot} = 10^6\,M_\odot$ the same is true but out to much larger redshifts, $z \in [1.5, 2.5]$.

In the bottom panel of Fig. 6.19 we see that LISA can constrain the mass ratio for a MBHB with $M_{tot} = 10^6\,M_\odot$ with a precision of 1% (10%) at 10 hours before merger if the source is at $z \simeq 0.5$ ($z \simeq 2.5$). With the exception of more massive systems ($M_{tot} > 3 \times 10^6\,M_\odot$) at relatively high redshift ($z > 2.5$), the mass ratio should be measured with an accuracy of 10% when there are still 10 hours left before the merger. Also in this case, we highlight that the reported contours are affected by large uncertainties: the mass ratio of a MBHB with $M_{tot} = 10^5\,M_\odot$ ($M_{tot} = 10^6\,M_\odot$) can be determined to 10% precision 1 week before the merger if the source redshift is $\simeq [1.5, 2.7]$ ($\simeq [0.7, 1.4]$).

In Fig. 6.20 we plot sky position and luminosity distance contour levels of uncertainties at different times before merger. A system with $M_{tot} = 10^6\,M_\odot$ is localized with a median value of $10\,deg^2$ ($5\,deg^2$) 1 week (1 day) before merger if the system is located at $z \simeq 0.5$. All systems are localized within $10\,deg^2$ 1 hour before merger if they are at $z < 1.5$. The same is true for an accuracy of $\simeq 0.5\,deg^2$ if the systems lie at $z \lesssim 0.6$. Moving to the right panel, the luminosity distance of all systems with $M_{tot} \in [10^5, 10^6]\,M_\odot$ is constrained to 10% (1%) 1

week (1 hour) before merger if the systems are at $z \lesssim 1$. For heavy systems with $M_{tot} = 10^7\,M_\odot$ the same precision is reached only if the binary is at $z < 0.5$. Note that, for simplicity, here are not showing the uncertainties in the median values as in Fig. 6.16-6.19.

Finally in Fig. 6.21 we show the same contour levels at different time from coalescence for the chirp mass and mass ratio uncertainties. The chirp mass for all systems is determined to 0.1% (1%) precision if the systems are located at $z < 0.5$ ($z < 2.5$) at 1 hour from merger. $\Delta\mathcal{M}/\mathcal{M} \simeq 1\%$ precision is reached one week before merger only for binaries with $M_{tot} \lesssim 10^6\,M_\odot$ located at $z < 0.5$. The mass ratio is constrained to 0.3% 1 hour before merger for all systems if the source is located at $z < 0.5$. One day before merger a 3% precision is reached only for light systems only if they are at $z \lesssim 1$.

6.4.5 Multi-messenger potential

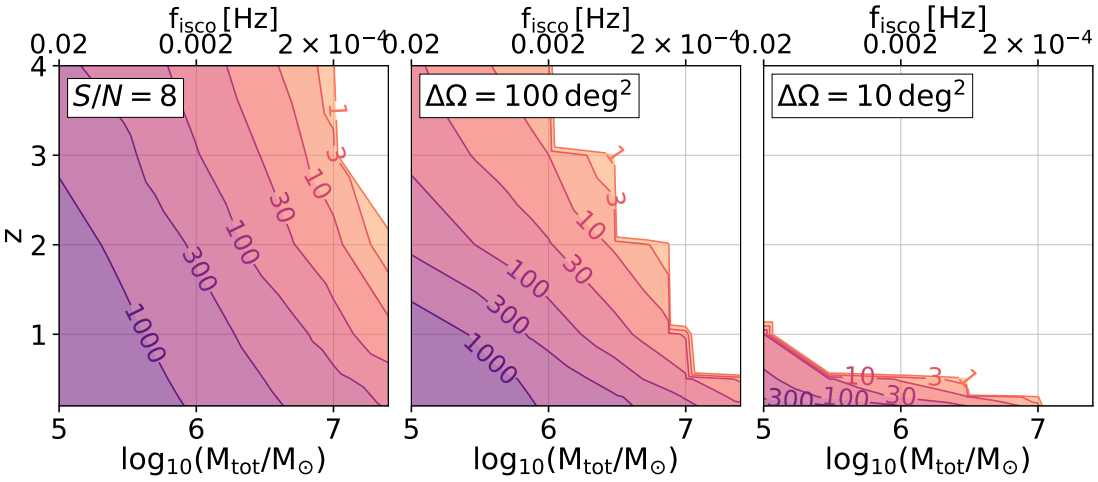

Figure 6.22: Contours of number of cycles spent by sources in the time interval ranging from the moment at which $S/N = 8$ (left panel), $\Delta\Omega = 100\,\mathrm{deg}^2$ (central panel) and $\Delta\Omega = 10\,\mathrm{deg}^2$ (right panel) up to ISCO as function of total mass and redshift. The values of $f_{\rm ISCO}$ are computed in the source-frame.

The analytic fits and results presented in the previous section are useful tools to explore potential synergies between LISA and EM telescopes, to select the best instrumentation to perform early warning searches and follow-ups, and to devise optimal survey strategies. Especially *on the fly*, the necessity of covering relatively large sky localization areas (generally of several deg^2) calls for wide field of view (FOV) instruments. Spanning the EM spectrum, primary candidates for fruitful synergies that are expected to be operational at the time LISA fly are the Square

Kilometre Array (SKA, [247]) in the radio, the Large Synoptic Survey Telescope (LSST, [248]) in optical and *Athena* in X-ray. We briefly discuss the potential of each of them in the following, deferring a more systematic investigation to future work.

Starting from the high frequencies, *Athena* is an X-ray satellite selected as ESA L2 mission and due to fly at the same time as LISA. [3] The WFI instrument on board has a FOV of $0.4\,\mathrm{deg}^2$, reaching a soft X-ray flux limit of $\approx 3 \times 10^{-16}$erg cm^{-2} s^{-1} in 100 ks (about 1 day) of exposure [249]. This roughly corresponds to the received flux from a $10^6\,\mathrm{M}_\odot$ MBH accreting at the Eddington limit at $z \approx 2$. As clear from Fig. 6.16, only systems at $z \lesssim 0.5$ can be localized within $0.4\,\mathrm{deg}^2$ during the inspiral, and only few hours before merger, which provides just enough time to repoint Athena in the source direction before the merger occurs. However, post-merger localization is generally better than the FOV of *Athena* out to $z \gtrsim 3$. Considering also the long exposure times required, *Athena*'s is therefore optimal to search for post-merger signatures [196] associated, e.g. to the emergence of a relativistic jet [250]. Particularly favorable are low redshift sources, which will allow a single field pointing of *Athena* few hours before merger, enabling the detection of a putative X-ray flash at merger (e.g. [251]).

At the low frequency end, SKA will be surveying the radio sky. In its first operational stage, SKA1-MID is expected to have a FOV of $1\,\mathrm{deg}^2$, reaching a detection flux limit of $2\,\mu$Jy in 1 hour integration time[4]. In this case, considerations similar to those made for *Athena* apply. SKA1-MID will be optimally suited to identify the launch of a post-merger radio jet. The subsequent stage, SKA2-MID, is more uncertain, but the goal is to improve both the sensitivity and FOV by roughly factor of ten, getting to $0.1\,\mu$Jy over $10\,\mathrm{deg}^2$, allowing effective pre-merger searches, at least out to $z \approx 1$.

Moving to the optical, LSST can also play primary partnership role with LISA. In its $9.6\,\mathrm{deg}^2$ FOV, this telescope can reach a limiting magnitude of about 24.5 in mere 30 seconds of pointing [252], sufficient to detect a $10^6\,\mathrm{M}_\odot$ MBH accreting at the Eddington rate out to $z \approx 1.5$. Note that the survey speed easily allows to cover in just five minutes the $\Delta\Omega = 100\,\mathrm{deg}^2$ with which LISA sources out to $z \approx 1.5$ are expected to be localized two days before merger. A viable strategy would then be to survey the whole area every few minutes with LSST for the last two days of inspiral, which would allow to construct an ≈ 1000 point light curve of each object within the (evolving) LISA error box. Note that in this time, the MBHB will complete several orbits, resulting in a large number of GW cycles. For a given time to coalescence, the corresponding GW frequency f_t can be obtained

[3] We refer the reader to https://www.cosmos.esa.int/documents/678316/1700384/Athena_LISA_Whitepaper_Iss1.0.pdf for a preview on this theme.

[4] https://www.skatelescope.org/technical/info-sheets/

using Eq. (2.7) of [230]. Then, ignoring higher post-Newtonian corrections, an estimate of the number of GW cycles experienced by a binary when it sweeps from f_t to ISCO is given by

$$N_{\rm cyc} = \frac{1}{32\pi^{8/3}} \left(\frac{c^3}{G\mathcal{M}_z}\right)^{5/3} (f_t^{-5/3} - f_{\rm ISCO}^{-5/3}) \tag{6.16}$$

where $f_{\rm ISCO} = c^3/[6\sqrt{6}\pi G \mathrm{M}_{\rm tot}(1+z)]$.

In Fig. 6.22 we show in the mass-redshift plane, the number of cycles left to merger when a source first accumulates $S/N = 8$ in the LISA band, and when it is localized within 100 deg^2 and 10 deg^2, respectively. The right panel shows that a 3×10^5 M$_\odot$ MBHB at $z = 1$ still needs to complete 100 orbits when it is localized within 10 deg^2 about ten hours before merger. If any EM periodicity rises during the GW chirp, LSST will have the potential to effectively uncover it. We note that similar arguments apply to SKA2-MID, which might potentially detect a periodic signal due to e.g. a precessing radio jet.

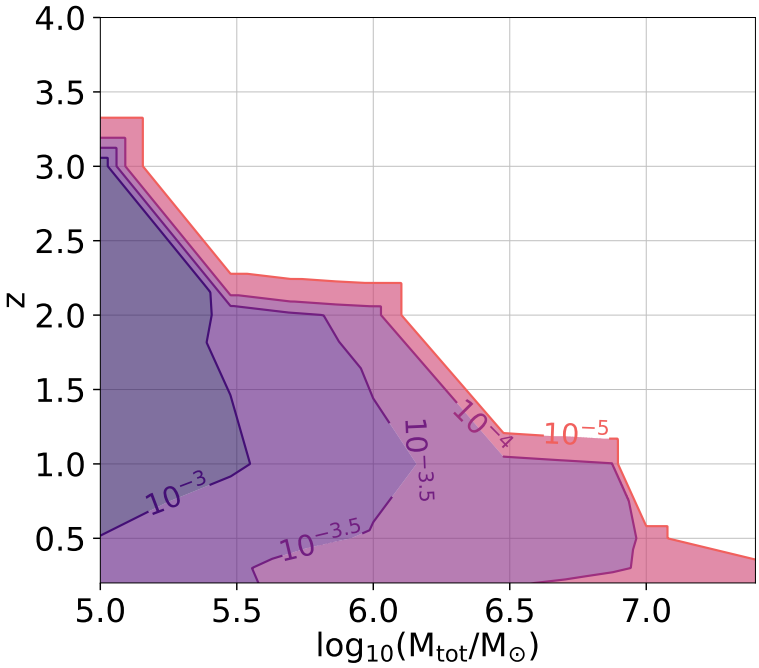

Figure 6.23: Contours of observed frequency f_f when sources are localized with $\Delta\Omega = 10\,\mathrm{deg}^2$ accuracy as function of total mass in the source frame and redshift.

We can further correlate the frequency f_t at which the median of $\Delta\Omega$ equals 10 deg^2 with the binary separation in units of the binary Schwarzschild radius $r_{\rm schw} = 2GM_{\rm tot}/c^2$

$$\frac{a}{r_{\rm schw}} \simeq 40 \left(\frac{10^{-3}{\rm Hz}}{f_t}\right)^{2/3} \left(\frac{10^5\,{\rm M}_\odot}{M_{\rm tot}}\right)^{2/3} \tag{6.17}$$

to show that light binaries are sufficiently separated that minidisks that may form around each black hole might leave a periodic imprint on the EM light cure in the approach to merger. In Fig. 6.23 we show contour lines of constant f_t when $\Delta\Omega = 10\,{\rm deg}^2$ as a function of redshift and total mass in the source frame.

We note that few days before merger, the distance and mass of the GW source is typically known within 10% precision, as shown in Fig. 6.17 and Fig. 6.19. Assuming the concordance cosmological model at the time of discovery, the luminosity distance can be converted into a redshift. This will help in reducing the number of candidates already *on the fly* and to cut sources outside the relevant redshift and host galaxy mass range to potentially uncover a precursor signal.

Sources at $z \approx 1$ are localized within $\simeq 0.1\,{\rm deg}^2$ when the full signal is considered, as illustrated in Fig. 6.6. Likewise, the luminosity distance and redshift, assuming a cosmology, are also known with a precision of a few percents. Considering that there are about 10^6 galaxies per ${\rm deg}^2$, projected on the sky, the redshift information from the GW signal can greatly help in weeding out galaxies in the sky error area using galaxy catalogs. Ideally, once the EM counterpart is identified, optical/near-IR imaging and spectroscopy of the host galaxy would let us study in a new and unique way the relationship between the MBH mass, inferred from the GW signal, and the galaxy mass, beside having an independent measure of the redshift to carry on estimates on the cosmological parameters [253]. Furthermore, any discrepancy between the two values of the redshifts may help detecting false positive associations, i.e. turn on AGN not having any secure connection with the GW event, given that after merger the onset of accretion might have a delay.

A multi-objects spectrograph like MOONS on VLT, with ~ 1000 fibers over a field of view of ~ 500 square arcmin would be an excellent instrument for spectroscopic follow-ups. Spectroscopic surveys or follow-ups can help select a putative EM counterpart also through AGN narrow emission lines and the presence of broad lines, although the dynamical environment close to a MBH merger can alter the "standard" picture [254]. A comparison between the MBH mass from the GW signal with that inferred using standard AGN techniques [255, and references therein] would be invaluable as consistency between the two mass measurements might reveal how the emission region changes under the highly dynamical conditions present in the post merger gaseous environment.

One important caveat is that LISA MBHs have relatively low masses, therefore they will not be bright sources in absolute terms, even if they accrete at the Eddington rate. A $10^6\,{\rm M}_\odot$ MBH at redshift $z \sim 1$ accreting at the Eddington limit would emit a [2-10] keV X-ray flux of about 8×10^{-16} in cgs units, and

could be detected with a 5 ks exposure with *Athena* with an apparent magnitude of ~ 25.4 in the B band. A host galaxy 1000 times heavier than the MBH, and on the star formation "main sequence" [256], would have magnitude $\sim 24 - 25.4$ depending on its dust content.This means that if the MBH is accreting at sub-Eddington rates the galaxy will be generally brighter than the AGN at optical wavelengths. As a consequence, in terms of identifying the GW source, optical selection cannot rely on AGN features, such color selection or broad or narrow AGN emission lines, since these will be weak except for MBHs accreting close to the Eddington rate. Study of the host galaxy, however, would be facilitated because the spectral energy distribution is in this case dominated by the galaxy properties. Optical spectroscopy near the MBH where broad lines are produced would require instruments with very high sensitivity, e.g., a long-lived James Webb Space Telescope (JWST) or Wide Field Infrared Survey Telescope (WFIRST), which can look for spectroscopic signatures of the MBH-powered AGN once the host galaxy has been identified.

6.5 Discussion

We discuss the role of each binary parameter in shaping the sky position, luminosity distance, chirp mass and mass ratio uncertainties distributions. For each of these parameters we compared different cases:

(I) $q = 0.1,\ 0.5,\ 1$ and randomly distributed in $[0.1, 1]$;

(II) $t_c = 0.5,\ 2,\ 4\,\mathrm{yr}$ and $t_c \in [0,\ 4\,\mathrm{yr}]$;

(III) $\chi_1 = \chi_2 = 0.1,\ 0.5,\ 0.9$ and $\chi_1,\ \chi_2 \in [0,\ 1]$;

(IV) inclination $i = 0,\ \pi/4,\ \pi/2$ and uniformly distributed;

(V) different sky positions.

For each case, we assume a MBHB with $\mathrm{M_{tot}} = 10^6\,\mathrm{M_\odot}$ at $z = 1$ and randomize over $\mathrm{N} = 10^3$ realizations for the other parameters.

Mass ratio

In Fig. 6.24 we show sky position uncertainties for different values of the mass ratio and for the case of random extraction in the interval $[0.1, 1]$. The sky position of systems with $q = 0.1$ is recovered better than the one for equal-mass system at all times before merger. At 1 month from coalescence, systems with $q = 0.1$ and $q = 1$ are localized with a median accuracy of $\simeq 200\,\mathrm{deg}^2$ and $\simeq 10^3\,\mathrm{deg}^2$, respectively.

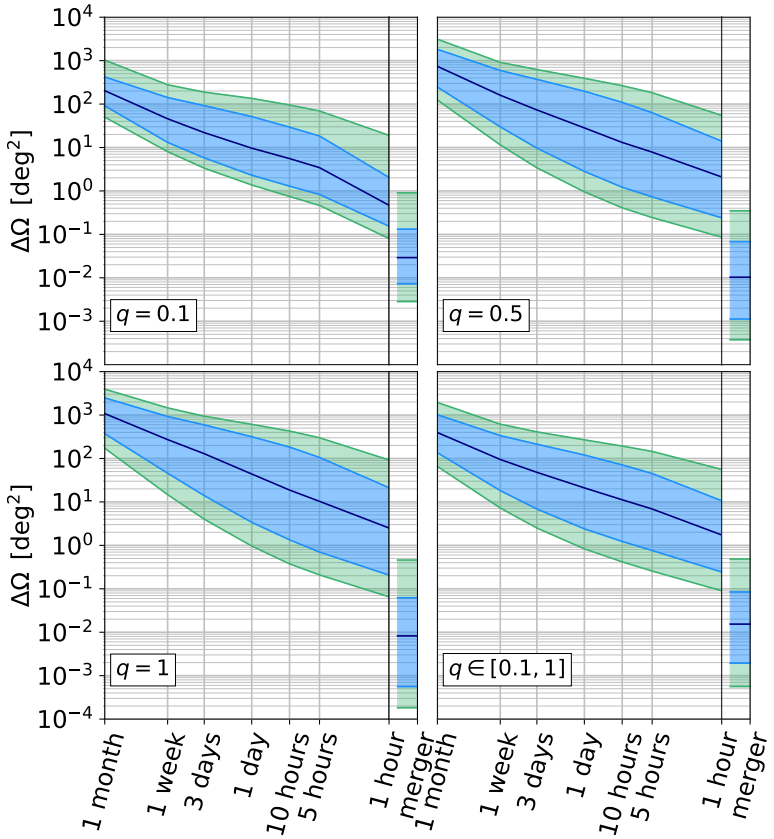

Figure 6.24: Sky localization uncertainties as function of time to coalescence for different mass ratios as given in each panel. Colors as in Fig. 6.6.

At 1 hour from merger equal-mass systems are localized with a median of $\simeq 3\,\mathrm{deg}^2$, while the uncertainties for $q = 0.1$ systems are smaller by a factor of $\simeq 5$. This is expected due to the fact that higher harmonics turns out to be important for small mass ratios and can lead to an improvement in the parameter estimation.

However at merger nearly equal-mass systems have higher S/N and the recovered area is usually smaller than the one for unequal-mass systems. In this case the increase in S/N compensates the suppression of the higher harmonics, leading to a better sky position estimate for equal-mass systems.

The distributions for unequal-mass systems are usually narrow but they still cover several orders of magnitude. In both $q = 0.1$ and $q = 1$ cases the recovered areas cover more than an order of magnitude at 1 month from coalescence and over two orders of magnitude at 1 hour from merger.

The cases for $q = 0.5$ and $q \in [0.1, 1]$ show intermediate behaviour. From these results, we choose to randomize over the mass ratio.

We find similar trend also for the luminosity distance, chirp mass and mass ratio uncertainties.

Time to coalescence

In Fig. 6.25 we show the recovered binary position errors for systems at different times to coalescence. In particular, we consider systems with coalescence time fixed at $t_c = 0.5,\ 2,\ 4\,\mathrm{yr}$ and randomly distributed in $[0,\ 4]\,\mathrm{yr}$. This time corresponds to the time left before merger and we assume that LISA is observing the full signal. In other words for the case $t_c = 4\,\mathrm{yr}$ we assume that, when LISA starts taking data for the first time, there is a system that will coalesce in exactly four years. Even if systems are detected only months before merger, the accumulated signal brings further information that lead to a better estimate of the source sky position.

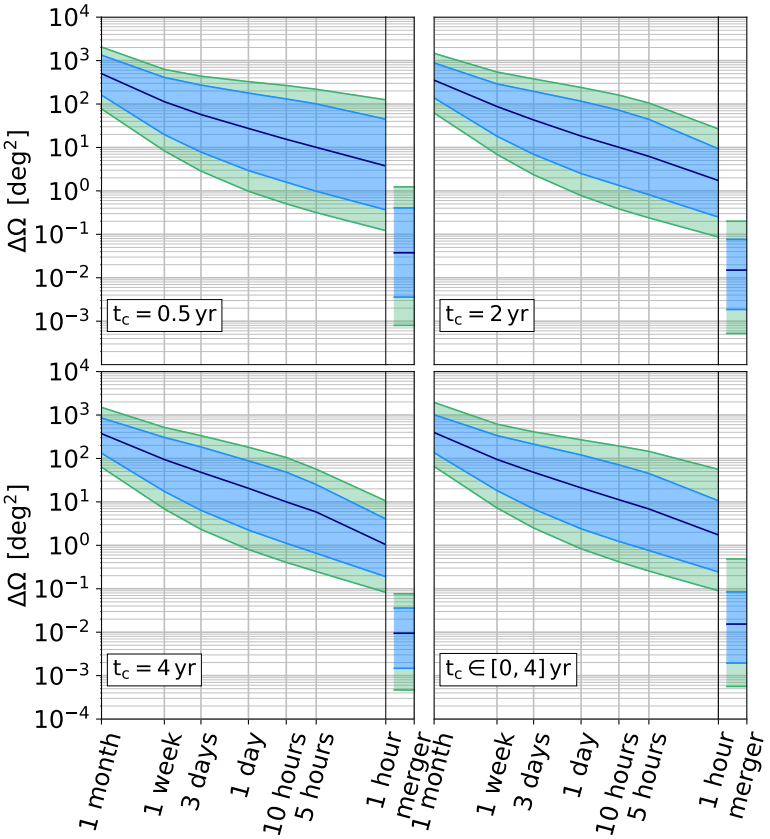

Figure 6.25: Same as Fig. 6.24 for case (II), i.e. for different coalescence times as reported in each panel.

MBHBs merging in 4 yr are localized 4 times better than systems at only 0.5 yr from coalescence at 1 hour from merger. The intermediate case with $t_c = 2\,\mathrm{yr}$ and

the case for random distributed coalescence time show intermediate behaviour. Since there is small difference between the two extreme cases, we chose to randomize over coalescence time when providing analytical formulas.

Spin magnitude

In Fig. 6.26 we give the sky uncertainty distributions for three different values of spin magnitude, namely $\chi_1 = \chi_2 = 0.1, 0.5, 0.9$, and the case where spin magnitudes are both randomly extracted in $[0, 1]$. In all cases, we leave spin directions uniformly distributed over a sphere. Higher spins help in breaking degeneracies and usually allow to recover better sky positions. At the end of the inspiral, spin-precession effects become important and high-spinning (low-spinning) systems can be localized with a median value of $\simeq 0.9\,\mathrm{deg}^2$ ($\simeq 4\,\mathrm{deg}^2$). However the distributions show similar range. Since spin values do not seem to affect significantly the recovered area, we choose to randomize over the allowed range.

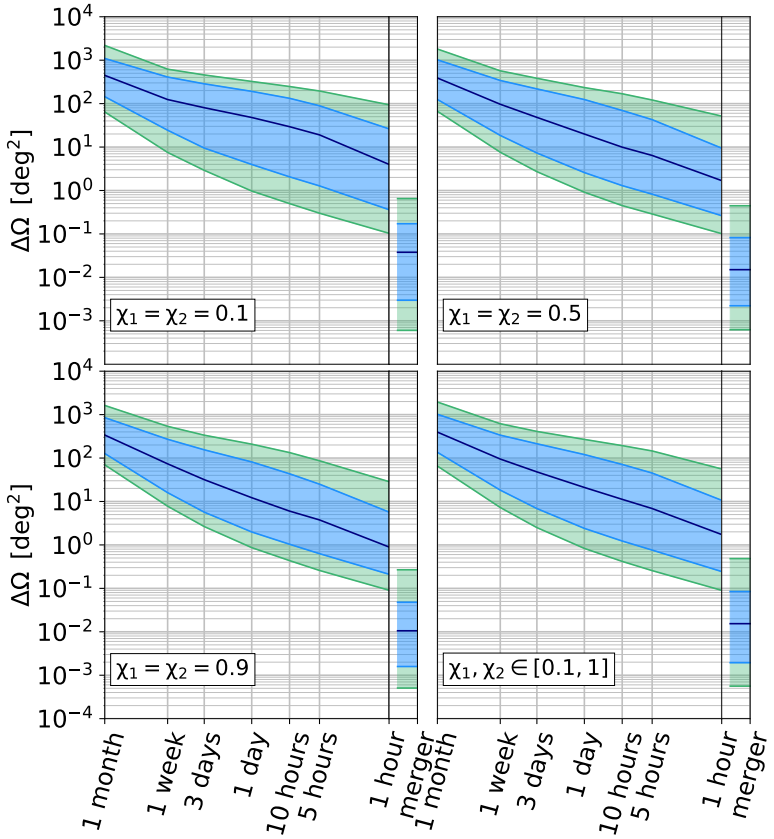

Figure 6.26: Same as Fig. 6.24 for case (III), i.e. for different spin magnitudes as reported in each panel.

Binary inclination

In Fig. 6.27 we show the sky uncertainty distribution for three different inclination values and for the case $\iota \in [0, \pi/2]$. Face-on systems are localized with a better precision during all the inspiral with uncertainties smaller of one order of magnitude at 1 hour before merger. The difference is larger at merger since face-on systems have larger S/N. Different inclination values affect only the median value, while the distributions present similar ranges. Even if the inclination affects the recovered error on the sky position, we choose to randomize over this parameter.

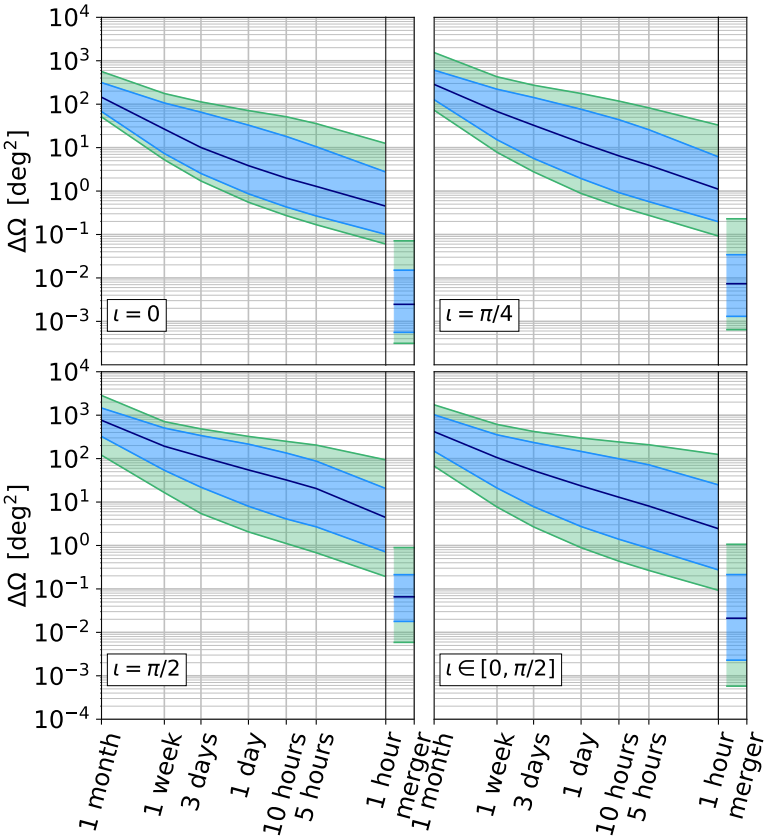

Figure 6.27: Same as Fig. 6.24 for case (IV), i.e. for different inclination values as reported in each panel.

Sky position

In Fig. 6.28 we show the uncertainties on the sky position, luminosity distance, chirp mass and mass ratio at different sky positions. Similarly to [207], we define $\mu_N = \cos(\theta_N)$ and divided the interval $\mu_N \in [-1, 1]$ in 40 bins. In each bin, we

perform $N = 10^4$ realizations, varying μ_N in the bin range. We keep $M_{tot} = 10^6\,M_\odot$ and $z = 1$.

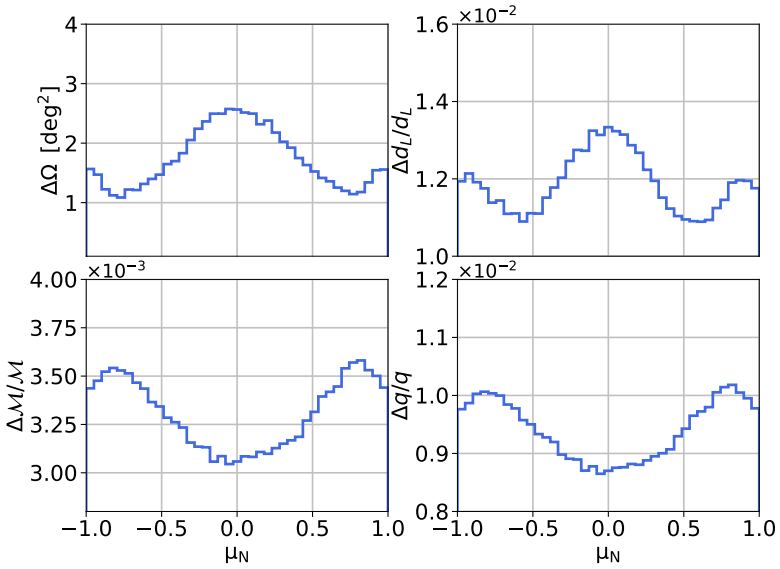

Figure 6.28: Distribution of sky position, luminosity distance, chirp mass and mass ratio uncertainties as function of μ_N for a system with $M_{tot} = 10^6$, $z = 1$.

All recovered distribution are symmetric respect to $\mu_N = 0$ as expected and the small differences are due to statistical fluctuations. LISA is able to constrain the sky position of sources lying outside the galactic plane better by a factor of 2 than sources lying in the plane. Luminosity distance uncertainties show three peaks at central value and approaching the poles. The central peak is slightly higher than the outlying ones. Chirp mass and mass ratio show opposite trends and they are recovered better for sources lying in the galactic plane with an improvement of $\simeq 10\%$ respect to sources lying outside.

Finally, we find no strong dependence for the recovered uncertainties on the polarization or the initial phase, so we average over them.

6.6 Comparison with previous studies

In this section we compare our results against previous results in the literature. In Fig. 6.29, we plot the fiducial LISA design sensitivity adopted in this study and the sensitivity adopted in past studies focusing on LISA ability to constrain source parameters during the inspiral [197, 207]. At $f = 10^{-4}$ Hz, the old LISA design sensitivity is roughly an order of magnitude higher, i.e. has a lower characteristic

strain than the current one. Also in the bucket of the curve, $f \simeq 5 \times 10^{-3}$ Hz, old LISA design had a higher sensitivity.

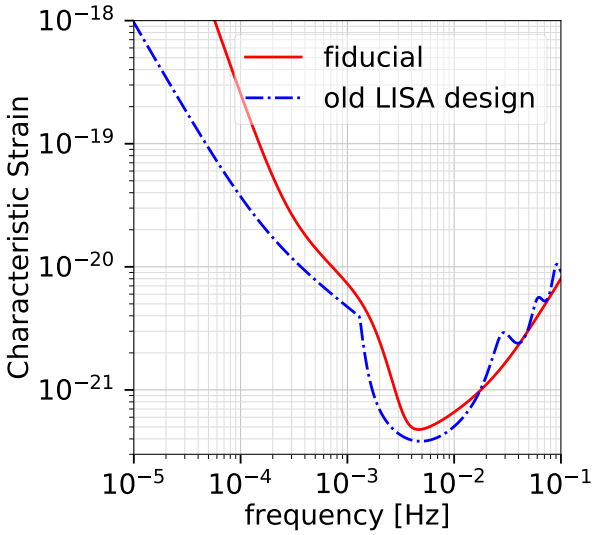

Figure 6.29: Old LISA design (dotted-dashed blue line) and current LISA design (continue red line) sensitivity.

As a consequence, in past studies, LISA sources where better localized in the sky already at 1 month from coalescence. In Fig. 6.30 we plot the sky position uncertainties as function of time to coalescence for the two sensitivity curves reported in Fig. 6.29 for a MBHB with $\mathrm{M}_{\mathrm{tot}} = 3 \times 10^6$ at $z = 1$. We change only the sensitivity curve, randomizing all the other parameters in the same range over $N = 10^3$ realizations. The improved low-frequency sensitivity of the old LISA design leads to a median sky position error of $\simeq 4\,\mathrm{deg}^2$ at 1 month from coalescence, almost three order of magnitude better compared to the current LISA design. When the system approaches merger the difference between the two configurations narrows down, leading to a median sky localization uncertainty of $\simeq 0.3\,\mathrm{deg}^2$ at 1 hour from coalescence, to be compared with a fiducial value of $\simeq 2\,\mathrm{deg}^2$. Similar considerations hold also when the full signal is considered.

6.7 Estimation of binary angular momentum

In this section we estimate the uncertainties in the direction of the binary angular momentum $\mathbf{L}$, relative to the line of sight from the source to the observer. To compute $\Delta\Omega_L$, we adopted the same formula for the sky-position $\Delta\Omega$, but replacing

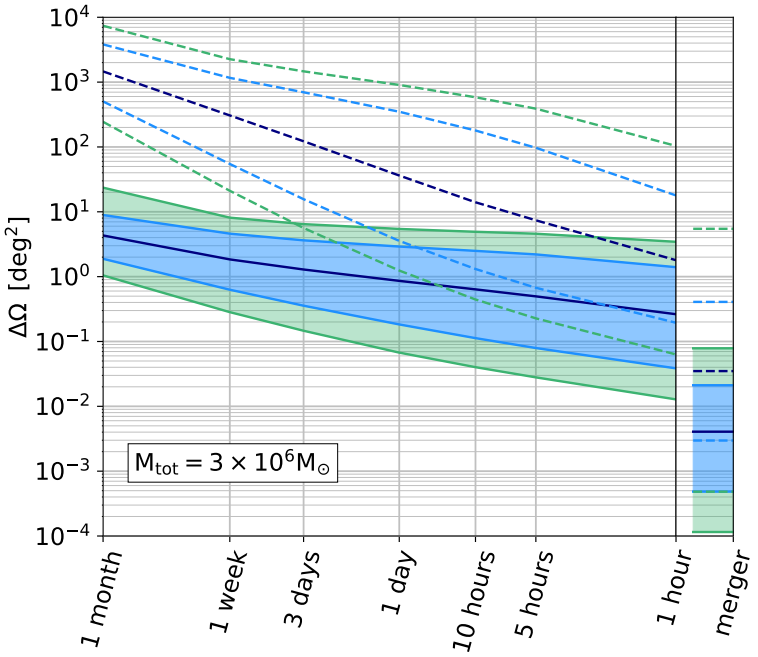

Figure 6.30: Sky position uncertainty as function of time to coalescence for a MBHB as labeled in the plot at $z = 1$. Solid (dashed) lines are obtained with the old (current) LISA sensitivity. Colors as in Fig. 6.6.

the uncertainties on $[\cos(\theta_N), \phi_N]$ with the one on $[\cos(\theta_L), \phi_L]$ (neglecting the cross-correlation term). In Fig. 6.31 we show LISA ability to constrain the binary angular momentum as function of time left before merger. At 1 month from merger, the binary angular momentum is not constrained, but, at 1 hour from merger, it is determined with an accuracy of $\simeq 10\,\mathrm{deg}^2$, corresponding to an uncertainty of ~ 3 deg. This is a key information, as the EM emission, i.e. its level of variability and spectral properties, depend on the inclination of the orbital plane relative to the observer and knowing the direction of $\mathbf{L}$ could help identifying the EM counterpart through its expected peculiar emission [192, 193]

The orbital angular momentum contributes to the total angular momentum, $\mathbf{J}$, defined as

$$\mathbf{J} = \mathbf{L} + \mathbf{S_1} + \mathbf{S_2} \tag{6.18}$$

where $\mathbf{S_1}$ and $\mathbf{S_2}$ are the BH spin vectors. Therefore it would also be interesting to investigate LISA ability to constrain on the fly the directions of the individual spins to trigger EM alerts informative of the potential directions of incipient jets. We suspect that this will be possible only when the full signal is considered. Thus, a complete and exhaustive analysis is beyond the scope of this paper.

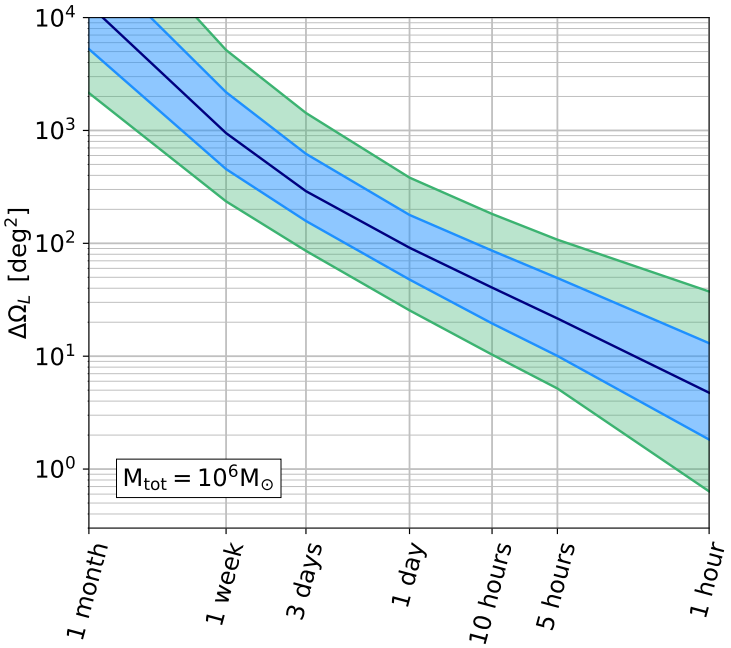

Figure 6.31: Binary angular momentum uncertainty as function of time to coalescence for a MBHB as labeled in the plot at $z = 1$. Colors as in Fig. 6.6.

Here, we would like to highlight few key points:

- During the inspiral, if each BH produces a jet, the jet is likely to be aligned with the spin direction [257]. LISA ability to constrain spin orientations might play a key role in discriminating sources for which jets are pointing towards us.

- After the merger, a jet might be launched aligned with the spin of the remnant BH and, therefore, to the total angular momentum J. However we observed that the error on the individual spin orientation is larger than that on the binary angular momentum, leading to an overall degraded estimate for J by more than an order of magnitude (on average) at the end of the inspiral.

- If spin magnitudes are small, the total angular momentum is determined basically by the binary angular momentum. This could suppress the large uncertainties connected with spin orientation.

- Gas accretion is expected to align BH spins to the binary angular momentum [220, 257]. In this case randomizing over spin orientations, as we have done

in this paper, might not be ideal. Moreover in this situation the recoil kick is in the orbital plane and it might trigger EM emission [197].

For these reasons, here we report the uncertainties on the binary angular momentum only (these data can be found at the aforementioned GitHub page)

6.8 Summary

MBHBs of $10^5 - 3\times10^7\,\mathrm{M}_\odot$ coalescing in low redshift galaxies ($z < 4$) have been the focus of this chapter. In the inspiral phase the GW signal is sufficiently long-lived to enable a pre-merger astrophysical characterization of these sources. To this aim, we carried out a parameter estimation on the fly, i.e. as a function of the time to coalescence. When the GW inspiral event is evolving in time, the signal-to-noise ratio continues to rise and uncertainties in the parameter estimates reduce. In our study we selected a sequence of times, from one month down to one hour prior to coalescence and considered the source sky localization, luminosity distance, chirp mass and mass ratio as key parameters, providing ready-to-use analytical fits of their associated uncertainties as a function of time.

Here we enumerate our key findings and concluding remarks:

- Between $3\times10^5\,\mathrm{M}_\odot$ and $3\times10^6\,\mathrm{M}_\odot$, the S/N of MBHBs at $z = 1$ rises above 8 - assumed as threshold for detection - 1 month to 1 week (for the heaviest system in this range) before coalescence. 5 hours prior merging the S/N is in the hundreds and at coalescence it reaches values in the thousands.

- Between $3\times10^5\,\mathrm{M}_\odot$ and $3\times10^6\,\mathrm{M}_\odot$, the binary chirp mass and mass ratio are determined with a fractional error $\lesssim 10\%$ 1 month to 1 week (for the heaviest system in this range) before merging. 5 hours before coalescence the accuracy narrows down at 1% level or even less (for the lightest MBHBs), and continues to improve significantly down to the end of inspiral. The luminosity distance and redshift 1 week before merging are inferred with an accuracy of about 10%.

- The median of the sky localization error $\Delta\Omega$ during the inspiral phase decreases by more than two orders of magnitude, due to the increase of the S/N as time progresses. Moreover close to merger, spin-precession effects, higher harmonics and doppler modulations help breaking degeneracies and further reduces uncertainties . However at any given time the uncertainty of $\Delta\Omega$ around the median value widens as the binary approaches coalescence. This allows the lightest sources (with masses of a few $10^5\,\mathrm{M}_\odot$) in the best (worst) configurations to be localized within $\simeq 1\,\mathrm{deg}^2$ ($\simeq 100\,\mathrm{deg}^2$) one day before coalescence. For systems of a few $10^6\,\mathrm{M}_\odot$ the uncertainty in the sky position

is larger, between $\simeq 10\,\mathrm{deg}^2$ and $\simeq 10^3\,\mathrm{deg}^2$, few days prior merging. Only at 'merger' the median of $\Delta\Omega$ plummets down to $\simeq 10^{-1}\,\mathrm{deg}^2$. Some sources can be localized with square arc-minute precision at the time of coalescence.

- Low redshift ($z \lesssim 1$), low mass MBHBs ($\mathrm{M_{tot}} \lesssim 5\times10^6\,\mathrm{M_\odot}$) can be detected first by large field-of-view telescopes as LSST and SKA from 2 days to few hours in advance if precursor emission exists, and later as time progresses by X-ray telescopes such as *Athena* at merger. These sources cover about 100 to 30 cycles before coalescence, within a sky localization uncertainty $\Delta\Omega \simeq 10\,\mathrm{deg}^2$, opening the possibility of detecting any periodicity, if present, in the EM signal possibly correlated with the periodicity in the inspiral signal.

- MBHBs with total mass around $\simeq 10^7\,\mathrm{M_\odot}$ at $z \simeq 1$ appear in the GW sky few days before merging and display a rapid increase in the S/N just in the last few hours. For these binaries the chirp mass and mass ratio is known to a precision of 10% about 3 days before merger. The sky-position remains highly uncertain across the entire inspiral phase. For these systems, the sky localization can be reconstructed at 'merger' by exploiting the amplitude and phase of the harmonics of the ringdown as shown in [210].

- Moving to higher redshift ($1 < z \leq 3$) and to binaries with masses between $3\times10^5\,\mathrm{M_\odot}$ and $3\times10^6\,\mathrm{M_\odot}$, the information on the chirp mass (mass ratio) accumulates in the last few days (few hours) reaching 10% precision. A similar trend is observed for the uncertainty in the luminosity distance. During the inspiral phase, a median sky localization of $10\,\mathrm{deg}^2$ is reached about 1 hour before coalescence. The localization improves when the full signal is recovered. MBHBs with total mass $\simeq 10^7\,\mathrm{M_\odot}$ are localized within $10\,\mathrm{deg}^2$ in their inspiral phase 10 to 1 hour prior merger up to $z \lesssim 1.3$.

- The analysis post-merger of the full GW signal allows sky localization of $\simeq 0.4\,\mathrm{deg}^2$ out to $z \simeq 3$, for those sources clustering around a mass interval between $\simeq 3\times10^5\,\mathrm{M_\odot}$ and $\simeq 10^6\,\mathrm{M_\odot}$ that could be detected by *Athena* at mergers and in the post-merger phase.

MBHB mergers are expected to be rare events in the Universe and there are large uncertainties in the predicted number of events (see [258, 259] for a recent discussion). In this paper we focus on LISA's ability to constrain source parameters without accounting for the expected number of events. To assess LISA's possibilities to detect EM counterparts, our simulations have to be convolved with a realistic population of merging MBHBs. We defer this point to later studies.

Moreover we did not include any estimate about LISA ability to estimate the time of coalescence of MBHB GW signals. This is an important information for multimessenger potential and it will be subject of later studies.

In this analysis we did not include neither the scheduled gaps in the data due to LISA communication with Earth, antennas repointing or laser locking [18], nor the gaps due to unexpected failures requiring system's reboot. Gaps would degrade our results especially in the early inspiral. However, when an event is detected, a protected period might be established around the time of the merger reducing the effect of the scheduled gaps since most of the S/N is built close to merger.

In a recent work Marsat *et al.* [211] reported the appearance of eight degenerate points in the posterior distribution for the sky position of the source when performing Bayesian parameter estimation for inspiral-merger-ringdown signals. These degeneracies can be broken close to merger with the inclusion of higher harmonics and the frequency-dependence in the LISA response function (that is what we observed with `ptmcmc`). The Fisher matrix approach is unable to track these degenerate points so our results have to be considered conservative in the early inspiral.

In this study we considered only LISA. If other space-born GW observatories [260, 261] sensitive to the same frequencies joined LISA in the sky, they might help further reducing the uncertainties , especially for the sky position of the source.

In summary, MBHBs with masses between $\simeq 3 \times 10^5\,\mathrm{M}_\odot$ and $\simeq 3 \times 10^6\,\mathrm{M}_\odot$ at $z \simeq 1$ carry exquisite information on their astrophysical parameters during the inspiral phase that can be inferred on the fly. The contribution of higher harmonics, included in this investigation, make these unequal and relatively long-lived binaries the best sources for coordinated searches of EM counterparts. GRMHD/radiative transfer simulations should focus on these systems to enhance our knowledge on their emerging spectra and variability.

Conclusion

In this Thesis I presented a detailed study and analysis of BHBs, ranging from the light BHs expected as outcome of stellar evolution to the heavy MBHs residing at the center of galaxies. I summarise the major findings of our work.

We investigated the necessary waveform accuracy to track SBHBs in their inspiral in LISA. SBHBs are expected to perform thousand of cycles in band. As a consequence, an accurate description of the waveform is necessary to prevent biases in the parameter estimation. To simulate the signal we adopted an inspiral waveform with spin precession and higher harmonics. Our waveform is computed according to the PN formalism therefore, the condition on waveform accuracy can be translated in the number of minimum PN order necessary to track the phase of the signal.

We tested the effect of total mass, mass ratio and time to coalescence on the PN accuracy requirement. We found that the main parameter affecting the waveform precision is the time to coalescence while varying the total mass or mass ratio produces null or negligible effects. As expected, systems closer to coalescence require higher PN contributions: multiband SBHBs require up to the 3PN order, while binaries at more than 5 yr from coalescence require < 1.5PN term.

We applied our code to a realistic population of SBHBs in LISA and concluded that most of the detectable sources will be properly described by waveforms with < 2PN corrections. Moreover each PN sub-populations is reasonably separate in function of time to coalescence.

Our results will help the construction of reliable and fast template bank for the parameter estimation of SBHBs in LISA.

We explored the possibility to form SBHBs above the pair-instability mass gap. Starting from SFR, metallicity and IMF, we built a coherent model to describe the formation of BHs above the mass gap, evolving single stars and combining them in binaries. We employed different models and predicted the expected number of events for current and future interferometers. We initially checked that our 'below-gap' sub-population was consistent with the results from more accurate population synthesis code and that the detected rates from 'across-gap' and

'above-gap' binaries were consistent with a non detection so far. For ground-based detector, we expect LIGO/Virgo at design sensitivity to detect few events per year in the optimistic scenario. ET should be able to detect $\simeq 10$ per year from the 'across-gap' and 'above-gap' sub-populations in the pessimistic scenario. These rates increase to $\gtrsim 200$ events in the optimistic model.

At low frequency, LISA is expect to detect 'above-gap' SBHBs even in the pessimistic scenario. In addition, $\simeq 50\%$ of detected events will be multiband sources that will be detectable by LIGO/Virgo or ET. We also predict that the unresolved 'across-gap' and 'above-gap' sources might form a stochastic background for frequency $< 10^{-3}\,\mathrm{Hz}$ comparable to the one expected from 'below-gap' binaries and galactic sources.

Moving to MBHs, we performed a preliminary study to asses the possibility to detect a premerger Doppler modulated X-ray emission in phase with the GW signal. The emission is expected to be produced by the accreting gas in mini-disk surrounding the merging MBHs while the modulation is the result of the orbital motion of the binary. Detecting the modulated EM emission in phase with the GW signal during the inspiral, would allow to pinpoint the exact source location in the relatively large area recovered by LISA. To detect the EM emission, we combined LISA and TAP, a proposed NASA mission with an X-Ray Telescope on board. We found that the modulation detection will probably come from massive unequal systems with inclination $\simeq 45^\circ$ respect to the line of sight. We also explored different observational strategies and concluded that the most promising one might be start TAP observations when LISA area drops below $\simeq 20\,\mathrm{deg}^2$ in order to free more time for other sources and avoid the observation of wide portion of sky. Assuming fiducial rates for MBHBs, we estimated few detections over LISA time mission.

We investigated LISA ability to constrain source parameter during the inspiral. In particular we focus on the sky position, luminosity distance, chirp mass and mass ratio estimates as function of time to coalescence. We simulated systems with $\mathrm{M_{tot}} \in [10^5, 3 \times 10^7]\,\mathrm{M}_\odot$ and $z \in [0.1, 4]$ and run 10^4 realisations for each combination of total mass and redshift.

At $z = 1$ light systems can be localized within $\simeq [1, 100]\,\mathrm{deg}^2$ one day before merger. Increasing the total mass of the system reduces LISA ability to constrain source parameters: MBHBs with $3 \times 10^6\,\mathrm{M}_\odot$ are localized within $\simeq [10, 10^3]\,\mathrm{deg}^2$ few days before coalescence while MBHBs with $10^7\,\mathrm{M}_\odot$ are basically not localized until the very end of the inspiral. Including merger and ringdown leads to a significant improvement of the sky localization down to $\simeq 0.1\,\mathrm{deg}^2$. In particular MBHBs between $\simeq 3 \times 10^5\,\mathrm{M}_\odot$ and $\simeq 10^6\,\mathrm{M}_\odot$ can be localised up to $z \simeq 3$ within $0.4\,\mathrm{deg}^2$. Chirp mass, mass ratio and luminosity distance are constrained at 1% at

the end of inspiral. We extensively discussed multimessenger potential combining LISA with future EM facilities like Athena or LSST.

We released the set of data on which these results are based on and provided analytical formulas to fit the running uncertainties in the range $\mathrm{M_{tot}} \in [10^5,\, 10^7]\,\mathrm{M_\odot}$ and $z \in [0.3, 3]$. Our formulas take few input parameters (the time left before merger, the total mass and the redshift) and are in good agreements with the simulations outcomes.

Appendix A

Coefficients tables

In this appendix we report the coefficients for the formulas introduced in Chapter 6 to fit the uncertainties on sky position, luminosity distance, chirp mass and mass ratio. In Tab. A.1 we report the coefficients for the uncertainties on sky position and luminosity distance during the inspiral. Similarly, in Tab. A.2 we report the chirp mass and mass ratio formula coefficients. In Tab. A.3 we report the coefficients to fit the sky position and luminosity distance at merger for systems with $M_{tot} < 3 \times 10^6 M_\odot$. In Tab. A.4 we report the same coefficients for systems with $M_{tot} > 3 \times 10^6 M_\odot$.

Coefficients	Parameters									
	$\Delta\Omega$					$\Delta d_L/d_L$				
	median	68% lower	68% upper	95% lower	95% upper	median	68% lower	68% upper	95% lower	95% upper
c_1	2568.27	3512.72	1577.58	3874.1084	297.1314	1005.79	1559.583	756.97	1988.84	−267.832
c_2	−1208.887	−1626.038	−731.275	−1797.039	−168.1976	−458.186	−711.0698	−348.628	−921.42	141.362
c_3	184.4128	245.4319	109.31	272.2114	28.8558	67.2397	105.1866	51.56386	139.1144	[z, $\log_{10}$ M_{tot}]
c_4	−9.13586	−12.08178	−5.29714	−13.47515	−1.56994	−3.1845	−5.0494	−2.4594	−6.84734	1.4809
c_5	−1796.673	−2344.484	−1108.298	−2602.995	−289.0075	−718.3414	−1024.527	−537.0054	−1285.656	129.117
c_6	846.8472	1085.9196	513.703	1208.7319	151.8264	328.787	467.3178	247.8523	595.444	−70.771
c_7	[z, $\log_{10}$ M_{tot}]	[z, $\log_{10}$ M_{tot}]	[z, $\log_{10}$ M_{tot}]	[z, $\log_{10}$ M_{tot}]	[z, $\log_{10}$ M_{tot}]	[z, $\log_{10}$ M_{tot}]	[z, $\log_{10}$ M_{tot}]	[z, $\log_{10}$ M_{tot}]	[z, $\log_{10}$ M_{tot}]	12.92974
c_8	6.49952	8.148226	3.799775	9.158112	1.36678	2.355736	3.355828	1.79838	4.45595	−0.77395
c_9	389.6703	491.046	245.2222	548.7184	79.19753	158.2055	212.1132	118.1205	263.1475	−19.987
c_{10}	−183.79561	−227.3143	−113.8672	−254.8002	−40.3808	−72.62682	−96.74195	−54.6334	−121.82422	11.4809
c_{11}	28.282011	34.4617	17.2381	38.797776	6.6287905	10.85154	14.38965	8.211404	18.45193	−2.17817
c_{12}	−1.419813	−1.708847	−0.8532665	−1.9359222	−0.355383	−0.527822	−0.6969475	−0.4018752	−0.913203	0.133935
c_{13}	−26.699734	−32.74404	−17.2392	−36.7993	−6.44256	−10.96238	−14.01813	−8.1937	−17.2456	1.01535
c_{14}	12.5929	15.13522	8.01997	17.07276	3.2388846	5.03955	6.388211	3.79471	7.97705	−0.617936
c_{15}	−1.939627	−2.2921364	−1.218924	−2.59833	−0.527868	−0.7551506	−0.9498658	−0.5720776	−1.207692	0.122496
c_{16}	0.097577	0.1136226	0.0607029	0.1296806	0.02822687	0.0369069	0.0460217	0.0281455	0.0597755	−0.0077483
d_1	−129.98573	−164.5524	−77.3729	−183.877	−25.3058	−48.84506	−69.43392	−37.05507	−90.144	−25.2
d_2	-2.54×10^{-4}	-3.18×10^{-4}	-5.04×10^{-4}	-4.34×10^{-4}	-6.6×10^{-4}	-1.1×10^{-4}	-4.9×10^{-5}	-1.8×10^{-4}	-5×10^{-5}	-9.4×10^{-4}
d_3	-2.26×10^{-3}	-2.47×10^{-3}	-1.63×10^{-3}	-3.06×10^{-3}	-2.02×10^{-3}	-8.1×10^{-4}	-5.1×10^{-4}	-6×10^{-4}	-4.8×10^{-4}	-4.1×10^{-3}
d_4	4.82×10^{-4}	4.98×10^{-4}	4.3×10^{-4}	5.95×10^{-4}	4.68×10^{-4}	1.84×10^{-4}	1.33×10^{-4}	1.6×10^{-4}	1.3×10^{-4}	1×10^{-3}
z_c	0.753	0.744	0.76	0.744	0.78	0.38	0.38	0.38	0.38	0.375

Table A.1: Coefficients for the fit reported in Section 6.4.3 for the sky position and luminosity distance uncertainties.

Coefficients	Parameters									
	$\Delta\mathcal{M}/\mathcal{M}$						$\Delta q/q$			
	median	68% lower	68% upper	95% lower	95% upper	median	68% lower	68% upper	95% lower	95% upper
c_1	265.154	204.7335	−34.7932	3031.93	−312.206	111.22	403.8919	−132.91	2670.45	−392.089
c_2	−74.012	−34.3552	63.0254	−1446.096	184.6885	−13.238	−152.5055	100.255	−1260.664	225.7991
c_3	1.539	−6.60087	−19.0848	224.992	−36.6357	−6.2392	15.513	−23.5952	193.5704	−43.6128
c_4	0.52438	1.054653	1.54848	−11.4193	2.38862	0.8533	−0.2618	1.72765	−9.65920	2.78034
c_5	−250.187	−212.7418	−61.196	−2025.58	65.1703	−192.371	−371.442	−36.698	−1793.416	119.722
c_6	$[z, \log_{10} M_{tot}]$	$[z, \log_{10} M_{tot}]$	−0.022941	$[z, \log_{10} M_{tot}]$	$[z, \log_{10} M_{tot}]$	$[z, \log_{10} M_{tot}]$	$[z, \log_{10} M_{tot}]$	−4.5964	$[z, \log_{10} M_{tot}]$	$[z, \log_{10} M_{tot}]$
c_7	−7.49936	−2.57786	$[z, \log_{10} M_{tot}]$	−151.76925	12.45644	−5.81345	−19.1958	$[z, \log_{10} M_{tot}]$	−131.5355	17.20657
c_8	0.024866	−0.293273	−0.6267496	7.763953	−0.92562	−0.0076827	0.680987	−0.567725	6.62843	−1.192362
c_9	59.854	51.8721	21.8577	426.415	4.8196	54.7792	89.8498	23.238	379.1713	−6.76903
c_{10}	−21.99511	−16.97759	−4.55444	−204.7197	1.6225	−21.48994	−38.2546	−6.8044	−180.43504	7.5663
c_{11}	2.249767	1.25226	−0.3938	32.18694	−1.071028	2.44623	5.081692	0.1906	28.059366	−2.079704
c_{12}	−0.0446262	0.018931	0.0877907	−1.655344	0.1089012	−0.067153	−0.2032869	0.047122	−1.4233821	0.165538
c_{13}	−4.22054	−3.61683	−1.77072	−28.6609	−1.15488	−4.2843	−6.4682	−2.23887	−25.5663	−0.36784
c_{14}	1.58222	1.21883	0.455984	13.78835	0.30454	1.74461	2.790075	0.791875	12.19611	−0.09896
c_{15}	−0.169695	−0.099666	0.0013989	−2.173974	0.0035938	−0.214409	−0.37913	−0.067924	−1.903058	0.072043
c_{16}	0.0041172	-2.4234×10^{-4}	−0.0044783	0.1122246	−0.00354464	0.0073079	0.015841	-1.2534×10^{-4}	0.0969823	−0.0073868
d_1	86.4775	62.2216	5.5642	969.4018	−51.8627	67.7606	153.149	5.2722	850.214	−79.8362
d_2	2.49×10^{-4}	5.2×10^{-4}	1.26×10^{-4}	2.05×10^{-3}	6.78×10^{-4}	$8.0E-05$	1.0×10^{-3}	1.82×10^{-4}	1.3×10^{-3}	-3.22×10^{-4}
d_3	8.82×10^{-3}	1.05×10^{-2}	2.15×10^{-3}	1.07×10^{-2}	2.26×10^{-3}	8.78×10^{-3}	9.21×10^{-3}	1.71×10^{-3}	9.84×10^{-3}	1.79×10^{-3}
d_4	-9.16×10^{-4}	-1.07×10^{-3}	-2.28×10^{-4}	-1.13×10^{-3}	1.61×10^{-4}	-8.3×10^{-4}	-9.39×10^{-4}	-1.91×10^{-4}	-1.08×10^{-3}	2.31×10^{-4}
z_c	0.364	0.349	0.327	0.349	0.35	0.35	0.36	0.36	0.36	0.349

Table A.2: Same as Tab. A.1 for chirp mass and mass ratio uncertainties.

Coefficients	Parameters	$\Delta\Omega$					$\Delta d_L/d_L$				
	median	68% lower	68% upper	95% lower	95% upper	median	68% lower	68% upper	95% lower	95% upper
	[z]	[z]	[z]	[z]	[z]	[z]	[z]	[z]	[z]	[z]
m_1	13.296	14.39	11.92	16.513	8.024	6.088	6.567	5.934	7.134	5.511
m_2	62.097	86.262	−3.704	93.583	−26.74	26.99	32.9	24.703	33.24	36.263
m_3	−0.858	−0.836	−0.7946	−0.8473	−0.7515	−0.385	−0.398	−0.3858	−0.4075	−0.3928
m_4	−11.4027	−15.5978	−0.0168	−16.76	3.664	−5.0583	−6.046	−4.6995	−6.0585	−6.844
m_5	0.1608	0.1576	0.1613	0.1522	0.1668	0.0794	0.0771	0.08033	0.07462	0.08179
m_6	0.6807	0.91963	0.03179	0.9788	−0.1593	0.307	0.3611	0.28916	0.3589	0.42055
m_7	−4.1	−4.511	−3.671	−5.2655	−2.34	−1.889	−2.044	−1.8422	−2.235	−1.6968
m_8	−0.0725	−0.0726	−0.0853	−0.0641	−0.0986	−0.0429	−0.038	−0.04372	−0.03373	−0.0442
m_9	0.4119	0.4477	0.382	0.5116	0.2718	0.1948	0.2061	0.192	0.2213	0.18024
m_{10}										
n_1	7.222×10^{-6}	3.852×10^{-6}	1.31×10^{-3}	2.998×10^{-6}	3.743×10^{-5}	1.91×10^{-5}	1.315×10^{-5}	2.696×10^{-5}	1.313×10^{-5}	1.3×10^{-5}
n_2	-8.6325×10^{-3}	-6.1675×10^{-3}	9.8153×10^{-2}	-5.63045×10^{-3}	1.726×10^{-2}	-2.0083×10^{-2}	-1.6227×10^{-2}	-2.234×10^{-2}	-1.5893×10^{-2}	-1.5404×10^{-2}
n_3	1.082×10^{-4}	6.092×10^{-5}	1.746×10^{-2}	4.6124×10^{-5}	5.2977×10^{-4}	2.846×10^{-4}	2.02×10^{-4}	3.89×10^{-4}	1.98×10^{-4}	2.057×10^{-4}
n_4	-5.34×10^{-5}	-2.943×10^{-5}	-8.143×10^{-3}	-2.236×10^{-5}	-2.538×10^{-4}	-1.382×10^{-4}	-9.85×10^{-5}	-1.83×10^{-4}	-9.37×10^{-5}	-9.81×10^{-5}
n_5	7.53×10^{-6}	4.114×10^{-6}	1.107×10^{-3}	3.138×10^{-6}	3.57×10^{-5}	1.947×10^{-5}	1.388×10^{-5}	2.52×10^{-5}	1.286×10^{-5}	1.37×10^{-5}

Table A.3: Coefficients for the fit reported in Section 6.4.3 for the sky position and luminosity distance uncertainties at merger for systems with $M_{tot} \leq 3 \times 10^6\, M_\odot$.

Coefficients	Parameters									
	$\Delta\Omega$					$\Delta d_L/d_L$				
	median	68% lower	68% upper	95% lower	95% upper	median	68% lower	68% upper	95% lower	95% upper
m_1	[z]	[z]	[z]	[z]	[z]	[z]	[z]	[z]	[z]	[z]
m_2	54.14	52.38	65.175	50.41	73.024	30.014	31.89	31.65	31.075	33.47
m_3	202.74	175.795	51.54	71.944	254.464	77.09	74.578	74.52	36.196	112.27
m_4	−2.303	−2.247	−2.587	−2.195	−2.75	−1.17	−1.127	−1.236	−1.11	−1.316
m_5	−27.1115	−23.352	−4.2706	−8.3389	−33.468	−9.9143	−9.5723	−9.3884	−4.0335	−14.8135
m_6	0.1833	0.184	0.185	0.1785	0.1905	0.0915	0.091	0.0930	0.0894	0.09356
m_7	1.20935	1.0344	0.06735	0.3129	1.46415	0.42342	0.4075	0.3914	0.1419	0.65054
m_8	−13.878	−13.425	−16.788	−12.831	−18.996	−7.782	−8.362	−8.1875	−8.123	−8.668
m_9	0.1188	0.11	0.157	0.1068	0.1753	0.0620	0.0565	0.0699	0.0554	0.08076
m_{10}	0.9597	0.9309	1.1507	0.886	1.3064	0.5401	0.5843	0.565	0.5668	0.5966
n_1	4.123×10^{-7}	5.01×10^{-7}	3.88×10^{-6}	2.18×10^{-6}	2.936×10^{-7}	1.397×10^{-6}	1.385×10^{-6}	1.4×10^{-6}	4.61×10^{-6}	7.2×10^{-7}
n_2	-1.9555×10^{-3}	-2.23144×10^{-3}	-5.587×10^{-3}	-4.7614×10^{-3}	-1.5454×10^{-3}	-4.9447×10^{-3}	-5.0946×10^{-3}	-5.035×10^{-3}	-9.245×10^{-3}	-3.5031×10^{-3}
n_3	6.46×10^{-6}	8.121×10^{-6}	6.27×10^{-5}	3.347×10^{-5}	4.37×10^{-6}	2.087×10^{-5}	2.194×10^{-5}	2.124×10^{-5}	6.9×10^{-5}	1.1×10^{-5}
n_4	-3.052×10^{-6}	-3.892×10^{-6}	-3.115×10^{-5}	-1.542×10^{-5}	-2.09×10^{-6}	-9.85×10^{-6}	-1.04×10^{-5}	-1.027×10^{-5}	-3.25×10^{-5}	-5.12×10^{-6}
n_5	4.2×10^{-7}	5.435×10^{-7}	4.35×10^{-6}	2.097×10^{-6}	2.857×10^{-7}	1.346×10^{-6}	1.44×10^{-6}	1.425×10^{-6}	4.47×10^{-6}	6.92×10^{-7}

Table A.4: Coefficients for the fit reported in Section 6.4.3 for the sky position and luminosity distance uncertainties at merger for systems with $M_{tot} > 3 \times 10^6\, M_\odot$.

Acknowledgments

I acknowledge partial financial support from the INFN TEONGRAV specific initiative, from the European Research Council No. 818691 'B Massive' and networking support by the COST Action CA16104.

I am finally at the end of this three years long journey. Many people have contributed to my personal and scientific growth and I would like to thank all of them.

The first person I would like to thank is my tutor Monica Colpi for mentoring me during these years and introducing me to the field of gravitational waves. She also opened the path for many collaborations and involving projects that lead to publications.

I am profoundly indebted to my supervisor Alberto Sesana for teaching and helping me over this period. He is always encouraging and is enthusiasm is definitely contagious. Moreover he is always available to listen to your ideas, no matter how crazy they are. I hope to take some of his 'life approach' to science with me in the coming years.

A huge thank goes to Matteo Bonetti for his collaboration and endless patience in answering to my questions. He has always time for discussions and he is always able to provide useful insights.

I would like to thank the GW group in Birmingham, especially Antoine Klein, and the people in the "Paris" group: Marta Volonteri, Sylvain Marsat, Tito dal Canton, Stas Babak and Antoine Petiteau. A further thanks goes to Rosa Valiante and Raffaella Schneider for allowing me to collaborate to their work.

I would like to thank the Astrophysics group of Milano-Bicocca for accompanying me during these years. Among them, I would like to thank in particular Federico Abbate and Claudio Barbieri for all the lunches spent together at the second floor of U2. I also thank Davide Rozza: his enthusiasm for Science is tireless and he involved me in several outreach activities.

I will always be indebted to my friend Marco, especially for his infinite patience in many and many occasions and his support even in the worst moments.

These years would not have been the same without my flatmates Ilaria and

Matteo. Living together has been one of the most joyful period of my life and it would not have been possible without you. I will always remember the 'in-carto: plastica'-like discussions with a bit of nostalgia. Also, Ilaria is the one who introduced me to Asimov: a difficult debt to repay.

I also would like to thank all the PH members: Luca, Andrea, Barbara, Dario, Enrico, Lorenzo, Massine, Sara, Simone, Matteo, Luca, Riccardo, Andrea, Alessio, Djibril, Filippo for all these years spent together. University would be a really boring place without you.

I also would like to thanks my friends Lorenzo and Matteo from high school.

These last months would not be the same without a special person, Silvia. Even if we met under strange circumstances, I am sure that better times await us.

The final thank is for my parents and for their constant love and support since I was a child. I would not be here without them.

Bibliography

[1] B. P. Abbott et al. "Observation of Gravitational Waves from a Binary Black Hole Merger". In: *Phys. Rev. Lett.* 116 (6 2016), p. 061102. DOI: 10.1103/PhysRevLett.116.061102. URL: https://link.aps.org/doi/10.1103/PhysRevLett.116.061102.

[2] B. P. Abbott et al. "Properties of the Binary Black Hole Merger GW150914". In: *Phys. Rev. Lett.* 116 (24 2016), p. 241102. DOI: 10.1103/PhysRevLett.116.241102. URL: https://link.aps.org/doi/10.1103/PhysRevLett.116.241102.

[3] B. P. Abbott et al. "Astrophysical Implications of the Binary Black-hole Merger GW150914". In: *The Astrophysical Journal Letters* 818.2 (2016), p. L22. URL: http://stacks.iop.org/2041-8205/818/i=2/a=L22.

[4] B. P. Abbott et al. "GWTC-1: A Gravitational-Wave Transient Catalog of Compact Binary Mergers Observed by LIGO and Virgo during the First and Second Observing Runs". In: (2018). arXiv: 1811.12907 [astro-ph.HE].

[5] B. P. Abbott et al. "Binary Black Hole Population Properties Inferred from the First and Second Observing Runs of Advanced LIGO and Advanced Virgo". In: *The Astrophysical Journal* 882.2 (2019), p. L24. DOI: 10.3847/2041-8213/ab3800. URL: https://doi.org/10.3847%2F2041-8213%2Fab3800.

[6] B. P. Abbott et al. "Tests of general relativity with the binary black hole signals from the LIGO-Virgo catalog GWTC-1". In: *Phys. Rev. D* 100 (10 2019), p. 104036. DOI: 10.1103/PhysRevD.100.104036. URL: https://link.aps.org/doi/10.1103/PhysRevD.100.104036.

[7] The LIGO Scientific Collaboration, the Virgo Collaboration, B. P. Abbott, et al. "A gravitational-wave measurement of the Hubble constant following the second observing run of Advanced LIGO and Virgo". In: *arXiv e-prints*, arXiv:1908.06060 (Aug. 2019), arXiv:1908.06060. arXiv: 1908.06060 [astro-ph.CO].

[8] B.P.Abbott et al. "Multi-messenger Observations of a Binary Neutron Star Merger". In: *ApJ, 848* (2017).

[9] B.P.Abbott et al. "Gravitational Waves and Gamma-Rays from a Binary Neutron Star Merger: GW170817 and GRB 170817A". In: *ApJ, 848* (2017).

[10] ANTARES et al. "Search for High-energy Neutrinos from Binary Neutron Star Merger GW170817 with ANTARES, IceCube, and the Pierre Auger Observatory". In: *Submitted to ApJ* (2017).

[11] J. H. Taylor and J. M. Weisberg. "A new test of general relativity - Gravitational radiation and the binary pulsar PSR 1913+16". In: *The Astrophysical Journal* 253 (Feb. 1982), pp. 908–920. DOI: 10.1086/159690.

[12] Gregory M Harry and the LIGO Scientific Collaboration. "Advanced LIGO: the next generation of gravitational wave detectors". In: *Classical and Quantum Gravity* 27.8 (2010), p. 084006. URL: http://stacks.iop.org/0264-9381/27/i=8/a=084006.

[13] F Acernese et al. "Advanced Virgo: a second-generation interferometric gravitational wave detector". In: *Classical and Quantum Gravity* 32.2 (2014), p. 024001. DOI: 10.1088/0264-9381/32/2/024001. URL: https://doi.org/10.1088%2F0264-9381%2F32%2F2%2F024001.

[14] Kentaro Somiya. "Detector configuration of KAGRA–the Japanese cryogenic gravitational-wave detector". In: *Classical and Quantum Gravity* 29.12 (2012), p. 124007. DOI: 10.1088/0264-9381/29/12/124007. URL: https://doi.org/10.1088%2F0264-9381%2F29%2F12%2F124007.

[15] C. S. Unnikrishnan. "IndIGO and Ligo-India Scope and Plans for Gravitational Wave Research and Precision Metrology in India". In: *International Journal of Modern Physics D* 22.1, 1341010 (Jan. 2013), p. 1341010. DOI: 10.1142/S0218271813410101. arXiv: 1510.06059 [physics.ins-det].

[16] M. Punturo et al. "The Einstein Telescope: a third-generation gravitational wave observatory". In: *Classical and Quantum Gravity* 27.19, 194002 (2010), p. 194002. DOI: 10.1088/0264-9381/27/19/194002.

[17] B P Abbott et al. "Exploring the sensitivity of next generation gravitational wave detectors". In: *Classical and Quantum Gravity* 34.4 (2017), p. 044001. DOI: 10.1088/1361-6382/aa51f4. URL: https://doi.org/10.1088%2F1361-6382%2Faa51f4.

[18] P. Amaro-Seoane et al. "Laser Interferometer Space Antenna". In: *ArXiv e-prints* (Feb. 2017). arXiv: 1702.00786 [astro-ph.IM].

[19] Wen-Hong Ruan et al. "Taiji Program: Gravitational-Wave Sources". In: *arXiv e-prints*, arXiv:1807.09495 (July 2018), arXiv:1807.09495. arXiv: 1807.09495 [gr-qc].

[20] Jun Luo et al. "TianQin: a space-borne gravitational wave detector". In: *Classical and Quantum Gravity* 33.3, 035010 (Feb. 2016), p. 035010. DOI: 10.1088/0264-9381/33/3/035010. arXiv: 1512.02076 [astro-ph.IM].

[21] Seiji Kawamura et al. "Current status of space gravitational wave antenna DECIGO and B-DECIGO". In: *arXiv e-prints*, arXiv:2006.13545 (June 2020), arXiv:2006.13545. arXiv: 2006.13545 [gr-qc].

[22] Sarah Burke-Spolaor et al. "The astrophysics of nanohertz gravitational waves". In: *The Astronomy and Astrophysics Review* 27.1, 5 (June 2019), p. 5. DOI: 10.1007/s00159-019-0115-7. arXiv: 1811.08826 [astro-ph.HE].

[23] Zaven Arzoumanian et al. "The NANOGrav 12.5-year Data Set: Search For An Isotropic Stochastic Gravitational-Wave Background". In: *arXiv e-prints*, arXiv:2009.04496 (Sept. 2020), arXiv:2009.04496. arXiv: 2009.04496 [astro-ph.HE].

[24] Michele Maggiore. *Gravitational Waves. Vol. 1: Theory and Experiments*. Oxford Master Series in Physics. Oxford University Press, 2007. ISBN: 9780198570745, 9780198520740.

[25] Michele Maggiore. *Gravitational Waves. Vol. 2: Astrophysics and Cosmology*. Oxford Master Series in Physics. Oxford University Press, 2018. ISBN: 9780198570899.

[26] K. Riles. "Gravitational waves: Sources, detectors and searches". In: *Progress in Particle and Nuclear Physics* 68 (Jan. 2013), pp. 1–54. DOI: 10.1016/j.ppnp.2012.08.001. arXiv: 1209.0667 [hep-ex].

[27] Monica Colpi et al. "Astro2020 science white paper: The gravitational wave view of massive black holes". In: *arXiv e-prints*, arXiv:1903.06867 (2019), arXiv:1903.06867. arXiv: 1903.06867 [astro-ph.GA].

[28] Monica Colpi and Alberto Sesana. "Gravitational Wave Sources in the Era of Multi-Band Gravitational Wave Astronomy". In: *An Overview of Gravitational Waves: Theory*. 2017, pp. 43–140. DOI: 10.1142/9789813141766_0002.

[29] Luc Blanchet. "Gravitational Radiation from Post-Newtonian Sources and Inspiralling Compact Binaries". In: *Living Reviews in Relativity* 17.1, 2 (Dec. 2014), p. 2. DOI: 10.12942/lrr-2014-2. arXiv: 1310.1528 [gr-qc].

[30] A. Buonanno and T. Damour. "Effective one-body approach to general relativistic two-body dynamics". In: *Phys. Rev. D* 59 (8 1999), p. 084006. DOI: 10.1103/PhysRevD.59.084006. URL: https://link.aps.org/doi/10.1103/PhysRevD.59.084006.

[31] Alessandra Buonanno et al. "Comparison of post-Newtonian templates for compact binary inspiral signals in gravitational-wave detectors". In: *Phys. Rev. D* 80 (8 2009), p. 084043. DOI: 10.1103/PhysRevD.80.084043. URL: https://link.aps.org/doi/10.1103/PhysRevD.80.084043.

[32] Sebastian Khan et al. "Phenomenological model for the gravitational-wave signal from precessing binary black holes with two-spin effects". In: *Phys. Rev. D* 100 (2 2019), p. 024059. DOI: 10.1103/PhysRevD.100.024059. URL: https://link.aps.org/doi/10.1103/PhysRevD.100.024059.

[33] Lionel London et al. "First Higher-Multipole Model of Gravitational Waves from Spinning and Coalescing Black-Hole Binaries". In: *Phys. Rev. Lett.* 120 (16 2018), p. 161102. DOI: 10.1103/PhysRevLett.120.161102. URL: https://link.aps.org/doi/10.1103/PhysRevLett.120.161102.

[34] B. P. Abbott et al. "GW170814: A Three-Detector Observation of Gravitational Waves from a Binary Black Hole Coalescence". In: *Phys. Rev. Lett.* 119 (14 2017), p. 141101. DOI: 10.1103/PhysRevLett.119.141101. URL: https://link.aps.org/doi/10.1103/PhysRevLett.119.141101.

[35] Massimo Tinto and Sanjeev V. Dhurandhar. "Time-Delay Interferometry". In: *Living Reviews in Relativity* 8.1, 4 (July 2005), p. 4. DOI: 10.12942/lrr-2005-4. arXiv: gr-qc/0409034 [gr-qc].

[36] B. P. Abbott et al. "GW170817: Observation of Gravitational Waves from a Binary Neutron Star Inspiral". In: *Phys. Rev. Lett.* 119 (16 2017), p. 161101. DOI: 10.1103/PhysRevLett.119.161101. URL: https://link.aps.org/doi/10.1103/PhysRevLett.119.161101.

[37] Michal Dominik et al. "Double Compact Objects III: Gravitational Wave Detection Rates". In: *Astrophys. J.* 806.2 (2015), p. 263. DOI: 10.1088/0004-637X/806/2/263. arXiv: 1405.7016 [astro-ph.HE].

[38] Alberto Mangiagli et al. "Post-Newtonian phase accuracy requirements for stellar black hole binaries with LISA". In: *Phys. Rev. D* 99 (6 2019), p. 064056. DOI: 10.1103/PhysRevD.99.064056. URL: https://link.aps.org/doi/10.1103/PhysRevD.99.064056.

[39] Tito Dal Canton and Ian W. Harry. "Designing a template bank to observe compact binary coalescences in Advanced LIGO's second observing run". In: *arXiv e-prints*, arXiv:1705.01845 (May 2017), arXiv:1705.01845. arXiv: 1705.01845 [gr-qc].

[40] Benjamin J. Owen and B. S. Sathyaprakash. "Matched filtering of gravitational waves from inspiraling compact binaries: Computational cost and template placement". In: *Phys. Rev. D* 60 (2 1999), p. 022002. DOI: 10.1103/PhysRevD.60.022002. URL: https://link.aps.org/doi/10.1103/PhysRevD.60.022002.

[41] Theocharis A. Apostolatos. "Search templates for gravitational waves from precessing, inspiraling binaries". In: *Phys. Rev. D* 52 (2 1995), pp. 605–620. DOI: 10.1103/PhysRevD.52.605. URL: https://link.aps.org/doi/10.1103/PhysRevD.52.605.

[42] Benjamin J. Owen. "Search templates for gravitational waves from inspiraling binaries: Choice of template spacing". In: *Phys. Rev. D* 53 (12 1996), pp. 6749–6761. DOI: 10.1103/PhysRevD.53.6749. URL: https://link.aps.org/doi/10.1103/PhysRevD.53.6749.

[43] Thibault Damour, Bala R. Iyer, and B. S. Sathyaprakash. "Improved filters for gravitational waves from inspiraling compact binaries". In: *Phys. Rev. D* 57 (2 1998), pp. 885–907. DOI: 10.1103/PhysRevD.57.885. URL: https://link.aps.org/doi/10.1103/PhysRevD.57.885.

[44] Lee Lindblom, Benjamin J. Owen, and Duncan A. Brown. "Model waveform accuracy standards for gravitational wave data analysis". In: *Phys. Rev. D* 78 (12 2008), p. 124020. DOI: 10.1103/PhysRevD.78.124020. URL: https://link.aps.org/doi/10.1103/PhysRevD.78.124020.

[45] Michele Vallisneri. "Use and abuse of the Fisher information matrix in the assessment of gravitational-wave parameter-estimation prospects". In: *Phys. Rev. D* 77 (4 2008), p. 042001. DOI: 10.1103/PhysRevD.77.042001. URL: https://link.aps.org/doi/10.1103/PhysRevD.77.042001.

[46] Katerina Chatziioannou et al. "Constructing gravitational waves from generic spin-precessing compact binary inspirals". In: *Phys. Rev. D* 95 (10 2017), p. 104004. DOI: 10.1103/PhysRevD.95.104004. URL: https://link.aps.org/doi/10.1103/PhysRevD.95.104004.

[47] Eric Poisson. "Gravitational radiation from a particle in circular orbit around a black hole. VI. Accuracy of the post-Newtonian expansion". In: *Phys. Rev. D* 52 (10 1995), pp. 5719–5723. DOI: 10.1103/PhysRevD.52.5719. URL: https://link.aps.org/doi/10.1103/PhysRevD.52.5719.

[48] Étienne Racine, Alessandra Buonanno, and Larry Kidder. "Recoil velocity at second post-Newtonian order for spinning black hole binaries". In: *Physical Review D* 80.4, 044010 (Aug. 2009), p. 044010. DOI: 10.1103/PhysRevD.80.044010. arXiv: 0812.4413 [gr-qc].

[49] Alejandro Bohé et al. "Quadratic-in-spin effects in the orbital dynamics and gravitational-wave energy flux of compact binaries at the 3PN order". In: *Classical and Quantum Gravity* 32.19, 195010 (Oct. 2015), p. 195010. DOI: 10.1088/0264-9381/32/19/195010. arXiv: 1501.01529 [gr-qc].

[50] Antoine Klein, Neil Cornish, and Nicolás Yunes. "Fast frequency-domain waveforms for spin-precessing binary inspirals". In: *Phys. Rev. D* 90 (12 2014), p. 124029. DOI: 10.1103/PhysRevD.90.124029. URL: https://link.aps.org/doi/10.1103/PhysRevD.90.124029.

[51] Ryuichi Fujita. "Gravitational Waves from a Particle in Circular Orbits around a Schwarzschild Black Hole to the 22nd Post-Newtonian Order". In: *Prog. Theor. Phys.* 128 (2012), p. 971. DOI: 10.1143/PTP.128.971. arXiv: 1211.5535 [gr-qc].

[52] Ryuichi Fujita. "Gravitational Waves from a Particle in Circular Orbits around a Rotating Black Hole to the 11th Post-Newtonian Order". In: *Prog. Theor. Exp. Phys.* 2015 (3 2015), 033E01. DOI: 10.1093/ptep/ptv012. arXiv: 1412.5689 [gr-qc].

[53] Luc Blanchet. "Gravitational Radiation from Post-Newtonian Sources and Inspiralling Compact Binaries". In: *Living Reviews in Relativity* 17.1 (2014), p. 2. ISSN: 1433-8351. DOI: 10.12942/lrr-2014-2. URL: https://doi.org/10.12942/lrr-2014-2.

[54] Alexandre Le Tiec, Luc Blanchet, and Bernard F. Whiting. "The First Law of Binary Black Hole Mechanics in General Relativity and Post-Newtonian Theory". In: *Phys. Rev. D* 85 (2012), p. 064039. DOI: 10.1103/PhysRevD.85.064039.

[55] Alexandre Le Tiec, Enrico Barausse, and Alessandra Buonanno. "Gravitational Self-Force Correction to the Binding Energy of Compact Binary Systems". In: *Phys. Rev. Lett.* 108 (2012), p. 131103. DOI: 10.1103/PhysRevLett.108.131103.

[56] J. R. Cash and Alan H. Karp. "A Variable Order Runge-Kutta Method for Initial Value Problems with Rapidly Varying Right-Hand Sides". In: *ACM Transactions on Mathematical Software* 16.3 (1990), p. 201. DOI: 10.1145/79505.79507.

[57] K. G. Arun et al. "The 2.5PN gravitational wave polarisations from inspiralling compact binaries in circular orbits". In: *Class. Quant. Grav.* 21 (2004), p. 3771. DOI: 10.1088/0264-9381/21/15/010. arXiv: gr-qc/0404085 [gr-qc].

[58] K. G. Arun et al. "The 2.5PN gravitational wave polarisations from inspiralling compact binaries in circular orbits". In: *Class. Quant. Grav.* 22 (2005), p. 3115. DOI: 10.1088/0264-9381/21/15/010. arXiv: gr-qc/0404085 [gr-qc].

[59] Curt Cutler. "Angular Resolution of the LISA Gravitational Wave Detector". In: *Phys. Rev. D* 57 (1998), p. 7089. DOI: 10.1103/PhysRevD.57.7089.

[60] Enrico Barausse, Alessandra Buonanno, and Alexandre Le Tiec. "Complete nonspinning effective-one-body metric at linear order in the mass ratio". In: *Phys. Rev. D* 85 (6 2012), p. 064010. DOI: 10.1103/PhysRevD.85.064010. URL: https://link.aps.org/doi/10.1103/PhysRevD.85.064010.

[61] Luc Blanchet. "On the accuracy of the postNewtonian approximation". In: *2001: A relativistic spacetime odyssey. Proceedings, 25th Johns Hopkins Workshop on Problems in particle theory, Florence, Italy, September 3-5, 2001*. 2002, pp. 411–430. DOI: 10.1142/9789812791368_0022. arXiv: gr-qc/0207037 [gr-qc].

[62] Alberto Sesana. "Prospects for Multiband Gravitational-Wave Astronomy after GW150914". In: *Phys. Rev. Lett.* 116 (23 2016), p. 231102. DOI: 10.1103/PhysRevLett.116.231102. URL: https://link.aps.org/doi/10.1103/PhysRevLett.116.231102.

[63] B. P. Abbott et al. "The Rate of Binary Black Hole Mergers Inferred from Advanced LIGO Observations Surrounding GW150914". In: *Astrophys. J.* 833.1 (2016), p. L1. DOI: 10.3847/2041-8205/833/1/L1. arXiv: 1602.03842 [astro-ph.HE].

[64] B. P. Abbott et al. "Supplement: The Rate of Binary Black Hole Mergers Inferred from Advanced LIGO Observations Surrounding GW150914". In: *Astrophys. J. Suppl.* 227.2 (2016), p. 14. DOI: 10.3847/0067-0049/227/2/14. arXiv: 1606.03939 [astro-ph.HE].

[65] Edwin E. Salpeter. "The Luminosity Function and Stellar Evolution." In: *The Astrophysical Journal* 121 (Jan. 1955), p. 161. DOI: 10.1086/145971.

[66] B. P. Abbott et al. "Binary Black Hole Mergers in the First Advanced LIGO Observing Run". In: *Phys. Rev. X* 6 (4 2016), p. 041015. DOI: 10.1103/PhysRevX.6.041015. URL: https://link.aps.org/doi/10.1103/PhysRevX.6.041015.

[67] Christopher J. Moore, Davide Gerosa, and Antoine Klein. "Are stellar-mass black-hole binaries too quiet for LISA?" In: *Monthly Notices of the Royal Astronomical Society* 488.1 (Sept. 2019), pp. L94–L98. DOI: 10.1093/mnrasl/slz104. arXiv: 1905.11998 [astro-ph.HE].

[68] P. C. Peters. "Gravitational Radiation and the Motion of Two Point Masses". In: *Phys. Rev.* 136 (4B 1964), B1224–B1232. DOI: 10.1103/PhysRev.136.B1224. URL: https://link.aps.org/doi/10.1103/PhysRev.136.B1224.

[69] Atsushi Nishizawa et al. "eLISA eccentricity measurements as tracers of binary black hole formation". In: *Phys. Rev. D* 94 (6 2016), p. 064020. DOI: 10.1103/PhysRevD.94.064020. URL: https://link.aps.org/doi/10.1103/PhysRevD.94.064020.

[70] Johan Samsing and Daniel J. D'Orazio. "Black Hole Mergers From Globular Clusters Observable by LISA I: Eccentric Sources Originating From Relativistic N-body Dynamics". In: (2018). arXiv: 1804.06519 [astro-ph.HE].

[71] Alexander Heger et al. "How massive single stars end their life". In: *Astrophys. J.* 591 (2003), pp. 288–300. DOI: 10.1086/375341. arXiv: astro-ph/0212469 [astro-ph].

[72] Mario Spera and Michela Mapelli. "Very massive stars, pair-instability supernovae and intermediate-mass black holes with the SEVN code". In: *Mon. Not. Roy. Astron. Soc.* 470.4 (2017), pp. 4739–4749. DOI: 10.1093/mnras/stx1576. arXiv: 1706.06109 [astro-ph.SR].

[73] Davide Gerosa and Emanuele Berti. "Are merging black holes born from stellar collapse or previous mergers?" In: *Phys. Rev. D* 95 (12 2017), p. 124046. DOI: 10.1103/PhysRevD.95.124046. URL: https://link.aps.org/doi/10.1103/PhysRevD.95.124046.

[74] Carl L. Rodriguez et al. "Post-Newtonian Dynamics in Dense Star Clusters: Highly Eccentric, Highly Spinning, and Repeated Binary Black Hole Mergers". In: *Phys. Rev. Lett.* 120 (15 2018), p. 151101. DOI: 10.1103/PhysRevLett.120.151101. URL: https://link.aps.org/doi/10.1103/PhysRevLett.120.151101.

[75] Valeriya Korol, Elena M. Rossi, and Enrico Barausse. "A multimessenger study of the Milky Way's stellar disc and bulge with LISA, Gaia, and LSST". In: *Monthly Notices of the Royal Astronomical Society* 483.4 (Mar. 2019), pp. 5518–5533. DOI: 10.1093/mnras/sty3440. arXiv: 1806.03306 [astro-ph.GA].

[76] Alberto Mangiagli et al. "Merger Rate of Stellar Black Hole Binaries above the Pair-instability Mass Gap". In: *The Astrophysical Journal* 883.1 (2019), p. L27. DOI: 10.3847/2041-8213/ab3f33. URL: https://doi.org/10.3847%2F2041-8213%2Fab3f33.

[77] Feryal Özel et al. "THE BLACK HOLE MASS DISTRIBUTION IN THE GALAXY". In: *The Astrophysical Journal* 725.2 (2010), pp. 1918–1927. DOI: 10.1088/0004-637x/725/2/1918. URL: https://doi.org/10.1088%2F0004-637x%2F725%2F2%2F1918.

[78] William A. Fowler and F. Hoyle. "Neutrino Processes and Pair Formation in Massive Stars and Supernovae." In: *The Astrophysical Journal Supplement Series* 9 (Dec. 1964), p. 201. DOI: 10.1086/190103.

[79] Pablo Marchant et al. "A new route towards merging massive black holes". In: *Astronomy and Astrophysics* 588, A50 (Apr. 2016), A50. DOI: 10.1051/0004-6361/201628133. arXiv: 1601.03718 [astro-ph.SR].

[80] Konstantin A. Postnov and Lev R. Yungelson. "The Evolution of Compact Binary Star Systems". In: *Living Reviews in Relativity* 17.1 (2014), p. 3. DOI: 10.12942/lrr-2014-3. URL: https://doi.org/10.12942/lrr-2014-3.

[81] Krzysztof Belczynski, Vassiliki Kalogera, and Tomasz Bulik. "A Comprehensive Study of Binary Compact Objects as Gravitational Wave Sources: Evolutionary Channels, Rates, and Physical Properties". In: *The Astrophysical Journal* 572.1 (2002), pp. 407–431. DOI: 10.1086/340304. URL: https://doi.org/10.1086%2F340304.

[82] Ph. Podsiadlowski, S. Rappaport, and Z. Han. "On the formation and evolution of black hole binaries". In: *Monthly Notices of the Royal Astronomical Society* 341.2 (May 2003), pp. 385–404. ISSN: 0035-8711. DOI: 10.1046/j.1365-8711.2003.06464.x. URL: https://dx.doi.org/10.1046/j.1365-8711.2003.06464.x.

[83] R. Voss and T. M. Tauris. "Galactic distribution of merging neutron stars and black holes – prospects for short gamma-ray burst progenitors and LIGO/VIRGO". In: *Monthly Notices of the Royal Astronomical Society* 342.4 (July 2003), pp. 1169–1184. ISSN: 0035-8711. DOI: 10.1046/j.1365-8711.2003.06616.x. URL: https://dx.doi.org/10.1046/j.1365-8711.2003.06616.x.

[84] Krzysztof Belczynski et al. "The first gravitational-wave source from the isolated evolution of two 40-100 Msun stars". In: *Nature* 534 (2016), p. 512. DOI: 10.1038/nature18322. arXiv: 1602.04531 [astro-ph.HE].

[85] S. F. Portegies Zwart et al. "Formation of massive black holes through runaway collisions in dense young star clusters". In: *Nature* 428 (Apr. 2004), pp. 724–726. DOI: 10.1038/nature02448. eprint: astro-ph/0402622.

[86] Holger Baumgardt, Pavel Kroupa, and Sambaran Banerjee. "Stellar-mass black holes in star clusters: implications for gravitational wave radiation". In: *Monthly Notices of the Royal Astronomical Society* 402.1 (Feb. 2010), pp. 371–380. ISSN: 0035-8711. DOI: 10.1111/j.1365-2966.2009.15880.x. eprint: http://oup.prod.sis.lan/mnras/article-pdf/402/1/371/18580034/mnras0402-0371.pdf. URL: https://dx.doi.org/10.1111/j.1365-2966.2009.15880.x.

[87] Brunetto Marco Ziosi et al. "Dynamics of stellar black holes in young star clusters with different metallicities – II. Black hole–black hole binaries". In: *Monthly Notices of the Royal Astronomical Society* 441.4 (June 2014), pp. 3703–3717. ISSN: 0035-8711. DOI: 10.1093/mnras/stu824. eprint: http://oup.prod.sis.lan/mnras/article-pdf/441/4/3703/4058566/stu824.pdf. URL: https://dx.doi.org/10.1093/mnras/stu824.

[88] Sambaran Banerjee. "Stellar-mass black holes in young massive and open stellar clusters and their role in gravitational-wave generation". In: *Monthly Notices of the Royal Astronomical Society* 467.1 (Jan. 2017), pp. 524–539. ISSN: 0035-8711. DOI: 10.1093/mnras/stw3392. eprint: http://oup.prod.sis.lan/mnras/article-pdf/467/1/524/10493546/stw3392.pdf. URL: https://dx.doi.org/10.1093/mnras/stw3392.

[89] Carl L. Rodriguez et al. "DYNAMICAL FORMATION OF THE GW150914 BINARY BLACK HOLE". In: *The Astrophysical Journal* 824.1 (2016), p. L8. DOI: 10.3847/2041-8205/824/1/l8. URL: https://doi.org/10.3847%2F2041-8205%2F824%2F1%2Fl8.

[90] Michela Mapelli et al. "Hierarchical mergers in young, globular and nuclear star clusters: black hole masses and merger rates". In: *arXiv e-prints*, arXiv:2007.15022 (July 2020), arXiv:2007.15022. arXiv: 2007.15022 [astro-ph.HE].

[91] Davide Gerosa et al. "Spin orientations of merging black holes formed from the evolution of stellar binaries". In: *Phys. Rev. D* 98 (8 2018), p. 084036. DOI: 10.1103/PhysRevD.98.084036. URL: https://link.aps.org/doi/10.1103/PhysRevD.98.084036.

[92] Maya Fishbach, Daniel E. Holz, and Ben Farr. "Are LIGO's Black Holes Made from Smaller Black Holes?" In: *The Astrophysical Journal* 840.2 (2017), p. L24. DOI: 10.3847/2041-8213/aa7045. URL: https://doi.org/10.3847%2F2041-8213%2Faa7045.

[93] Atsushi Nishizawa et al. "Constraining stellar binary black hole formation scenarios with eLISA eccentricity measurements". In: *Mon. Not. Roy. Astron. Soc.* 465.4 (2017), pp. 4375–4380. DOI: 10.1093/mnras/stw2993. arXiv: 1606.09295 [astro-ph.HE].

[94] Katelyn Breivik et al. "Distinguishing Between Formation Channels for Binary Black Holes with LISA". In: *Astrophys. J.* 830.1 (2016), p. L18. DOI: 10.3847/2041-8205/830/1/L18. arXiv: 1606.09558 [astro-ph.GA].

[95] J. Samsing and D. J. D'Orazio. "Black Hole Mergers From Globular Clusters Observable by LISA I: Eccentric Sources Originating From Relativistic N-body Dynamics". In: *ArXiv e-prints* (Apr. 2018). arXiv: 1804.06519 [astro-ph.HE].

[96] D. J. D'Orazio and J. Samsing. "Black Hole Mergers From Globular Clusters Observable by LISA II: Resolved Eccentric Sources and the Gravitational Wave Background". In: *ArXiv e-prints* (May 2018). arXiv: 1805.06194 [astro-ph.HE].

[97] Johan Samsing, Morgan MacLeod, and Enrico Ramirez-Ruiz. "THE FORMATION OF ECCENTRIC COMPACT BINARY INSPIRALS AND THE ROLE OF GRAVITATIONAL WAVE EMISSION IN BINARY-SINGLE STELLAR ENCOUNTERS". In: *The Astrophysical Journal* 784.1 (2014), p. 71. DOI: 10.1088/0004-637x/784/1/71. URL: https://doi.org/10.1088%2F0004-637x%2F784%2F1%2F71.

[98] Fabio Antonini and Hagai B. Perets. "SECULAR EVOLUTION OF COMPACT BINARIES NEAR MASSIVE BLACK HOLES: GRAVITATIONAL WAVE SOURCES AND OTHER EXOTICA". In: *The Astrophysical Journal* 757.1 (2012), p. 27. DOI: 10.1088/0004-637x/757/1/27. URL: https://doi.org/10.1088%2F0004-637x%2F757%2F1%2F27.

[99] Johan Samsing. "Eccentric black hole mergers forming in globular clusters". In: *Phys. Rev. D* 97 (10 2018), p. 103014. DOI: 10.1103/PhysRevD.97.103014. URL: https://link.aps.org/doi/10.1103/PhysRevD.97.103014.

[100] Fabio Antonini et al. "BLACK HOLE MERGERS AND BLUE STRAGGLERS FROM HIERARCHICAL TRIPLES FORMED IN GLOBULAR CLUSTERS". In: *The Astrophysical Journal* 816.2 (2016), p. 65. DOI: 10.3847/0004-637x/816/2/65. URL: https://doi.org/10.3847%2F0004-637x%2F816%2F2%2F65.

[101] Giacomo Fragione and Bence Kocsis. "Black Hole Mergers from Quadruples". In: (2019). arXiv: 1903.03112 [astro-ph.GA].

[102] Michal Dominik et al. "Double Compact Objects II: Cosmological Merger Rates". In: *Astrophys. J.* 779 (2013), p. 72. DOI: 10.1088/0004-637X/779/1/72. arXiv: 1308.1546 [astro-ph.HE].

[103] Krzysztof Belczynski et al. "Compact Binary Merger Rates: Comparison with LIGO/Virgo Upper Limits". In: *Astrophys. J.* 819.2 (2016), p. 108. DOI: 10.3847/0004-637X/819/2/108. arXiv: 1510.04615 [astro-ph.HE].

[104] Michela Mapelli and Nicola Giacobbo. "The cosmic merger rate of neutron stars and black holes". In: *Monthly Notices of the Royal Astronomical Society* 479.4 (June 2018), pp. 4391–4398. ISSN: 0035-8711. DOI: 10.1093/mnras/sty1613. eprint: http://oup.prod.sis.lan/mnras/article-pdf/479/4/4391/25180521/sty1613.pdf. URL: https://dx.doi.org/10.1093/mnras/sty1613.

[105] Carl L. Rodriguez, Sourav Chatterjee, and Frederic A. Rasio. "Binary black hole mergers from globular clusters: Masses, merger rates, and the impact of stellar evolution". In: *Phys. Rev. D* 93 (8 2016), p. 084029. DOI: 10.1103/PhysRevD.93.084029. URL: https://link.aps.org/doi/10.1103/PhysRevD.93.084029.

[106] Fabio Antonini and Frederic A. Rasio. "MERGING BLACK HOLE BINARIES IN GALACTIC NUCLEI: IMPLICATIONS FOR ADVANCED-LIGO DETECTIONS". In: *The Astrophysical Journal* 831.2 (2016), p. 187. DOI: 10.3847/0004-637x/831/2/187. URL: https://doi.org/10.3847%2F0004-637x%2F831%2F2%2F187.

[107] S. E. de Mink et al. "Rotational mixing in massive binaries. Detached short-period systems". In: *Astronomy and Astrophysics* 497.1 (Apr. 2009), pp. 243–253. DOI: 10.1051/0004-6361/200811439. arXiv: 0902.1751 [astro-ph.SR].

[108] Pablo Marchant et al. "A new route towards merging massive black holes". In: *Astronomy and Astrophysics* 588, A50 (Apr. 2016), A50. DOI: 10.1051/0004-6361/201628133. arXiv: 1601.03718 [astro-ph.SR].

[109] Lise du Buisson et al. "Cosmic Rates of Black Hole Mergers and Pair-Instability Supernovae from Chemically Homogeneous Binary Evolution". In: *arXiv e-prints*, arXiv:2002.11630 (Feb. 2020), arXiv:2002.11630. arXiv: 2002.11630 [astro-ph.HE].

[110] Yang Yang et al. "Hierarchical Black Hole Mergers in Active Galactic Nuclei". In: *arXiv e-prints*, arXiv:1906.09281 (2019), arXiv:1906.09281. arXiv: 1906.09281 [astro-ph.HE].

[111] B. McKernan et al. "Monte-Carlo simulations of black hole mergers in AGN disks: Low $\chi_{\rm eff}$ mergers and predictions for LIGO". In: *arXiv e-prints*, arXiv:1907.04356 (2019), arXiv:1907.04356. arXiv: 1907.04356 [astro-ph.HE].

[112] Misao Sasaki et al. "Primordial Black Hole Scenario for the Gravitational-Wave Event GW150914". In: *Phys. Rev. Lett.* 117 (6 2016), p. 061101. DOI: 10.1103/PhysRevLett.117.061101. URL: https://link.aps.org/doi/10.1103/PhysRevLett.117.061101.

[113] Krzysztof Belczynski et al. "Compact Object Modeling with the StarTrack Population Synthesis Code". In: *The Astrophysical Journal Supplement Series* 174.1 (2008), pp. 223–260. DOI: 10.1086/521026. URL: https://doi.org/10.1086%2F521026.

[114] N. Giacobbo, M. Mapelli, and M. Spera. "Unravelling the progenitors of merging black hole binaries". In: *Gravitational-waves Science Symposium*. Mar. 2018, p. 27. arXiv: 1807.07568 [astro-ph.HE].

[115] Jim W. Barrett et al. "Accuracy of inference on the physics of binary evolution from gravitational-wave observations". In: *Monthly Notices of the Royal Astronomical Society* 477.4 (July 2018), pp. 4685–4695. DOI: 10.1093/mnras/sty908. arXiv: 1711.06287 [astro-ph.HE].

[116] R. Abbott et al. "GW190814: Gravitational Waves from the Coalescence of a 23 Solar Mass Black Hole with a 2.6 Solar Mass Compact Object". In: *The Astrophysical Journal* 896.2 (2020), p. L44. DOI: 10.3847/2041-8213/ab960f. URL: https://doi.org/10.3847%2F2041-8213%2Fab960f.

[117] B. P. Abbott et al. "GW190425: Observation of a Compact Binary Coalescence with Total Mass $\sim$ 3.4 M $\odot$". In: *The Astrophysical Journal* 892.1 (2020), p. L3. DOI: 10.3847/2041-8213/ab75f5. URL: https://doi.org/10.3847%2F2041-8213%2Fab75f5.

[118] R. Abbott et al. "GW190521: A Binary Black Hole Merger with a Total Mass of 150 $M_{\odot}$". In: *Phys. Rev. Lett.* 125 (10 2020), p. 101102. DOI: 10.1103/PhysRevLett.125.101102. URL: https://link.aps.org/doi/10.1103/PhysRevLett.125.101102.

[119] Mario Spera et al. "Merging black hole binaries with the SEVN code". In: *Monthly Notices of the Royal Astronomical Society* 485 (2019), pp. 889–907. DOI: 10.1093/mnras/stz359. arXiv: 1809.04605 [astro-ph.HE].

[120] Ugo N Di Carlo et al. "Merging black holes in young star clusters". In: *Monthly Notices of the Royal Astronomical Society* 487.2 (May 2019), pp. 2947–2960. ISSN: 0035-8711. DOI: 10.1093/mnras/stz1453. eprint: http://oup.prod.sis.lan/mnras/article-pdf/487/2/2947/28830139/stz1453.pdf. URL: https://doi.org/10.1093/mnras/stz1453.

[121] Maya Fishbach and Daniel E. Holz. "Where Are LIGO's Big Black Holes?" In: *The Astrophysical Journal* 851.2 (2017), p. L25. DOI: 10.3847/2041-8213/aa9bf6. URL: https://doi.org/10.3847%2F2041-8213%2Faa9bf6.

[122] Colm Talbot and Eric Thrane. "Measuring the binary black hole mass spectrum with an astrophysically motivated parameterization". In: *Astrophys. J.* 856.2 (2018), p. 173. DOI: 10.3847/1538-4357/aab34c. arXiv: 1801.02699 [astro-ph.HE].

[123] Marta Volonteri. "Formation of supermassive black holes". In: *The Astronomy and Astrophysics Review* 18.3 (2010), pp. 279–315. DOI: 10.1007/s00159-010-0029-x. arXiv: 1003.4404 [astro-ph.CO].

[124] Rosa Valiante et al. "From the first stars to the first black holes". In: *Monthly Notices of the Royal Astronomical Society* 457.3 (Jan. 2016), pp. 3356–3371. ISSN: 0035-8711. DOI: 10.1093/mnras/stw225. eprint: http://oup.prod.sis.lan/mnras/article-pdf/457/3/3356/8002517/stw225.pdf. URL: https://doi.org/10.1093/mnras/stw225.

[125] Belczynski et al. "The effect of pair-instability mass loss on black-hole mergers". In: *A&A* 594 (2016), A97. DOI: 10.1051/0004-6361/201628980. URL: https://doi.org/10.1051/0004-6361/201628980.

[126] Michela Mapelli et al. "The properties of merging black holes and neutron stars across cosmic time". In: *Monthly Notices of the Royal Astronomical Society* 487.1 (2019), pp. 2–13. DOI: 10.1093/mnras/stz1150. arXiv: 1902.01419 [astro-ph.HE].

[127] Coenraad J. Neijssel et al. "The effect of the metallicity-specific star formation history on double compact object mergers". In: *arXiv e-prints*, arXiv:1906.08136 (2019), arXiv:1906.08136. arXiv: 1906.08136 [astro-ph.SR].

[128] Ataru Tanikawa et al. "Merger rate density of Population III binary black holes below, above, and in the pair-instability mass gap". In: *arXiv e-prints*, arXiv:2008.01890 (Aug. 2020), arXiv:2008.01890. arXiv: 2008.01890 [astro-ph.HE].

[129] R. Schneider, V. Ferrari, and S. Matarrese. "Stochastic backgrounds of gravitational waves from cosmological populations of astrophysical sources". In: *Nuclear Physics B Proceedings Supplements* 80 (Jan. 2000), pp. 07/22. arXiv: astro-ph/9903470 [astro-ph].

[130] S. Marassi et al. "Imprint of the merger and ring-down on the gravitational wave background from black hole binaries coalescence". In: *Phys. Rev. D* 84 (12 2011), p. 124037. DOI: 10.1103/PhysRevD.84.124037. URL: https://link.aps.org/doi/10.1103/PhysRevD.84.124037.

[131] Irina Dvorkin et al. "Metallicity-constrained merger rates of binary black holes and the stochastic gravitational wave background". In: *Monthly Notices of the Royal Astronomical Society* 461 (2016), pp. 3877–3885. DOI: 10.1093/mnras/stw1477. arXiv: 1604.04288 [astro-ph.HE].

[132] Piero Madau and Tassos Fragos. "Radiation Backgrounds at Cosmic Dawn: X-Rays from Compact Binaries". In: *The Astrophysical Journal* 840.1, 39 (2017), p. 39. DOI: 10.3847/1538-4357/aa6af9. arXiv: 1606.07887 [astro-ph.GA].

[133] Piero Madau and Mark Dickinson. "Cosmic Star-Formation History". In: *Annual Review of Astronomy and Astrophysics* 52 (2014), pp. 415–486. DOI: 10.1146/annurev-astro-081811-125615. arXiv: 1403.0007 [astro-ph.CO].

[134] D. J. McLeod, R. J. McLure, and J. S. Dunlop. "The z = 9-10 galaxy population in the Hubble Frontier Fields and CLASH surveys: the z = 9 luminosity function and further evidence for a smooth decline in ultraviolet luminosity density at z ⩾ 8". In: *Monthly Notices of the Royal Astronomical Society* 459.4 (Apr. 2016), pp. 3812–3824. ISSN: 0035-8711. DOI: 10.1093/mnras/stw904. eprint: https://academic.oup.com/mnras/article-pdf/459/4/3812/8192037/stw904.pdf. URL: https://doi.org/10.1093/mnras/stw904.

[135] Pavel Kroupa and Carsten Weidner. "Galactic-Field Initial Mass Functions of Massive Stars". In: *The Astrophysical Journal* 598.2 (2003), pp. 1076–1078. DOI: 10.1086/379105. URL: https://doi.org/10.1086%2F379105.

[136] Louis-Gregory Strolger et al. "TheHubbleHigherzSupernova Search: Supernovae toz≈ 1.6 and Constraints on Type Ia Progenitor Models". In: *The Astrophysical Journal* 613.1 (2004), pp. 200–223. DOI: 10.1086/422901. URL: https://doi.org/10.1086%2F422901.

[137] Piero Madau, Lucia Pozzetti, and Mark Dickinson. "The Star Formation History of Field Galaxies". In: *The Astrophysical Journal* 498.1 (1998), pp. 106–116. DOI: 10.1086/305523. URL: https://doi.org/10.1086%2F305523.

[138] M. Giavalisco et al. "The Rest-Frame Ultraviolet Luminosity Density of Star-forming Galaxies at Redshifts z > 3.5". In: *The Astrophysical Journal* 600.2 (2004), pp. L103–L106. DOI: 10.1086/381244. URL: https://doi.org/10.1086%2F381244.

[139] Pavel Kroupa, Christopher A. Tout, and Gerard Gilmore. "The distribution of low-mass stars in the Galactic disc". In: *Monthly Notices of the Royal Astronomical Society* 262.3 (June 1993), pp. 545–587. ISSN: 0035-8711. DOI: 10.1093/mnras/262.3.545. eprint: http://oup.prod.sis.lan/mnras/article-pdf/262/3/545/3370565/mnras262-0545.pdf. URL: https://dx.doi.org/10.1093/mnras/262.3.545.

[140] Maya Fishbach and Daniel E. Holz. "Picky Partners: The Pairing of Component Masses in Binary Black Hole Mergers". In: *arXiv e-prints*, arXiv:1905.12669 (2019), arXiv:1905.12669. arXiv: 1905.12669 [astro-ph.HE].

[141] Michal Dominik et al. "DOUBLE COMPACT OBJECTS. I. THE SIGNIFICANCE OF THE COMMON ENVELOPE ON MERGER RATES". In: *The Astrophysical Journal* 759.1 (2012), p. 52. DOI: 10.1088/0004-637x/759/1/52. URL: https://doi.org/10.1088%2F0004-637x%2F759%2F1%2F52.

[142] The LIGO Scientific Collaboration, the Virgo Collaboration, Abbott, et al. "Binary Black Hole Population Properties Inferred from the First and Second Observing Runs of Advanced LIGO and Advanced Virgo". In: *arXiv e-prints*, arXiv:1811.12940 (2018), arXiv:1811.12940. arXiv: 1811.12940 [astro-ph.HE].

[143] J Abadie et al. "Predictions for the rates of compact binary coalescences observable by ground-based gravitational-wave detectors". In: *Classical and Quantum Gravity* 27.17 (2010), p. 173001. DOI: 10.1088/0264-9381/27/17/173001. URL: https://doi.org/10.1088%2F0264-9381%2F27%2F17%2F173001.

[144] LIGO Scientific Collaboration. *LIGO Algorithm Library - LALSuite*. free software (GPL). 2018. DOI: 10.7935/GT1W-FZ16.

[145] Sascha Husa et al. "Frequency-domain gravitational waves from nonprecessing black-hole binaries. I. New numerical waveforms and anatomy of the signal". In: *Phys. Rev. D* 93 (4 2016), p. 044006. DOI: 10.1103/PhysRevD.93.044006. URL: https://link.aps.org/doi/10.1103/PhysRevD.93.044006.

[146] Sebastian Khan et al. "Frequency-domain gravitational waves from nonprecessing black-hole binaries. II. A phenomenological model for the advanced detector era". In: *Phys. Rev. D* 93 (4 2016), p. 044007. DOI: 10.1103/PhysRevD.93.044007. URL: https://link.aps.org/doi/10.1103/PhysRevD.93.044007.

[147] L. Santamaría et al. "Matching post-Newtonian and numerical relativity waveforms: Systematic errors and a new phenomenological model for nonprecessing black hole binaries". In: *Phys. Rev. D* 82 (6 2010), p. 064016. DOI: 10.1103/PhysRevD.82.064016. URL: https://link.aps.org/doi/10.1103/PhysRevD.82.064016.

[148] B. P. Abbott et al. "Prospects for Observing and Localizing Gravitational-Wave Transients with Advanced LIGO and Advanced Virgo". In: *Living Reviews in Relativity* 19.1 (2016), p. 1. ISSN: 1433-8351. DOI: 10.1007/lrr-2016-1. URL: https://doi.org/10.1007/lrr-2016-1.

[149] G. M. Harry and LIGO Scientific Collaboration. "Advanced LIGO: the next generation of gravitational wave detectors". In: *Classical and Quantum Gravity* 27.8, 084006 (Apr. 2010), p. 084006. DOI: 10.1088/0264-9381/27/8/084006.

[150] S. Hild et al. "Sensitivity studies for third-generation gravitational wave observatories". In: *Classical and Quantum Gravity* 28.9, 094013 (2011), p. 094013. DOI: 10.1088/0264-9381/28/9/094013. arXiv: 1012.0908 [gr-qc].

[151] Travis Robson, Neil J Cornish, and Chang Liu. "The construction and use of LISA sensitivity curves". In: *Classical and Quantum Gravity* 36.10 (2019), p. 105011. DOI: 10.1088/1361-6382/ab1101. URL: https://doi.org/10.1088%2F1361-6382%2Fab1101.

[152] Eric Thrane and Joseph D. Romano. "Sensitivity curves for searches for gravitational-wave backgrounds". In: *Physical Review D* 88.12, 124032 (2013), p. 124032. DOI: 10.1103/PhysRevD.88.124032. arXiv: 1310.5300 [astro-ph.IM].

[153] Alberto Sesana. "Prospects for Multiband Gravitational-Wave Astronomy after GW150914". In: *Physical Review Letters* 116.23, 231102 (2016), p. 231102. DOI: 10.1103/PhysRevLett.116.231102. arXiv: 1602.06951 [gr-qc].

[154] Martyna Chruslinska, Gijs Nelemans, and Krzysztof Belczynski. "The influence of the distribution of cosmic star formation at different metallicities on the properties of merging double compact objects". In: *Monthly Notices of the Royal Astronomical Society* 482.4 (Nov. 2018), pp. 5012–5017. ISSN: 0035-8711. DOI: 10.1093/mnras/sty3087. eprint: http://oup.prod.sis.lan/mnras/article-pdf/482/4/5012/26823152/sty3087.pdf. URL: https://doi.org/10.1093/mnras/sty3087.

[155] Davide Gerosa et al. "Multiband gravitational-wave event rates and stellar physics". In: *Phys. Rev. D* 99 (10 2019), p. 103004. DOI: 10.1103/PhysRevD.99.103004. URL: https://link.aps.org/doi/10.1103/PhysRevD.99.103004.

[156] Chiara Caprini et al. "Reconstructing the spectral shape of a stochastic gravitational wave background with LISA". In: *arXiv e-prints*, arXiv:1906.09244 (2019), arXiv:1906.09244. arXiv: 1906.09244 [astro-ph.CO].

[157] Alison J. Farmer and E. S. Phinney. "The gravitational wave background from cosmological compact binaries". In: *Monthly Notices of the Royal Astronomical Society* 346.4 (2003), pp. 1197–1214. DOI: 10.1111/j.1365-2966.2003.07176.x. arXiv: astro-ph/0304393 [astro-ph].

[158] B. P. Abbott et al. "Upper Limits on the Stochastic Gravitational-Wave Background from Advanced LIGO's First Observing Run". In: *Phys. Rev. Lett.* 118 (12 2017), p. 121101. DOI: 10.1103/PhysRevLett.118.121101. URL: https://link.aps.org/doi/10.1103/PhysRevLett.118.121101.

[159] The LIGO Scientific Collaboration, the Virgo Collaboration, et al. "A search for the isotropic stochastic background using data from Advanced LIGO's second observing run". In: *arXiv e-prints*, arXiv:1903.02886 (2019), arXiv:1903.02886. arXiv: 1903.02886 [gr-qc].

[160] Paul A. Crowther et al. "The R136 star cluster hosts several stars whose individual masses greatly exceed the accepted 150$M_\odot$ stellar mass limit". In: *Monthly Notices of the Royal Astronomical Society* 408 (2010), pp. 731–751. DOI: 10.1111/j.1365-2966.2010.17167.x. arXiv: 1007.3284 [astro-ph.SR].

[161] Edwige Pezzulli, Rosa Valiante, and Raffaella Schneider. "Super-Eddington growth of the first black holes". In: *Monthly Notices of the Royal Astronomical Society* 458.3 (Mar. 2016), pp. 3047–3059. ISSN: 0035-8711. DOI: 10.1093/mnras/stw505. eprint: http://oup.prod.sis.lan/mnras/article-pdf/458/3/3047/8007188/stw505.pdf. URL: https://doi.org/10.1093/mnras/stw505.

[162] Rosa Valiante et al. "Chasing the observational signatures of seed black holes at z > 7: candidate statistics". In: *Monthly Notices of the Royal Astronomical Society* 474.3 (Nov. 2017), pp. 3825–3834. ISSN: 0035-8711. DOI: 10.1093/mnras/stx3028. eprint: http://oup.prod.sis.lan/mnras/article-pdf/474/3/3825/23002592/stx3028.pdf. URL: https://doi.org/10.1093/mnras/stx3028.

[163] Haruki Uchida et al. "Black Hole Formation and Explosion from Rapidly Rotating Very Massive Stars". In: *The Astrophysical Journal* 870.2 (2019), p. 98. DOI: 10.3847/1538-4357/aaf39e. URL: https://doi.org/10.3847%2F1538-4357%2Faaf39e.

[164] Isobel Romero-Shaw et al. "GW190521: Orbital Eccentricity and Signatures of Dynamical Formation in a Binary Black Hole Merger Signal". In: *The Astrophysical Journal Letters* 903.1, L5 (Nov. 2020), p. L5. DOI: 10.3847/2041-8213/abbe26. arXiv: 2009.04771 [astro-ph.HE].

[165] Mohammadtaher Safarzadeh and Zoltán Haiman. "Formation of GW190521 via Gas Accretion onto Population III Stellar Black Hole Remnants Born in High-redshift Minihalos". In: *The Astrophysical Journal Letters* 903.1, L21 (Nov. 2020), p. L21. DOI: 10.3847/2041-8213/abc253. arXiv: 2009.09320 [astro-ph.HE].

[166] Chase Kimball et al. "Evidence for hierarchical black hole mergers in the second LIGO–Virgo gravitational-wave catalog". In: *arXiv e-prints*, arXiv:2011.05332 (Nov. 2020), arXiv:2011.05332. arXiv: 2011.05332 [astro-ph.HE].

[167] H. Umeda et al. "The Final Fates of Accreting Supermassive Stars". In: *The Astrophysical Journal Letters* 830, L34 (Oct. 2016), p. L34. DOI: 10.3847/2041-8205/830/2/L34. arXiv: 1609.04457 [astro-ph.SR].

[168] R. Valiante et al. "From the first stars to the first black holes". In: *Monthly Notices of the Royal Astronomical Society* 457 (Apr. 2016), pp. 3356–3371. DOI: 10.1093/mnras/stw225. arXiv: 1601.07915.

[169] J. L. Johnson and F. Haardt. "The Early Growth of the First Black Holes". In: *Publications of the Astronomical Society of Australia* 33, e007 (Mar. 2016), e007. DOI: 10.1017/pasa.2016.4. arXiv: 1601.05473.

[170] Martin G. Haehnelt. "Low frequency gravitational waves from supermassive black holes". In: *Mon. Not. Roy. Astron. Soc.* 269 (1994), p. 199. DOI: 10.1093/mnras/269.1.199. arXiv: astro-ph/9405032 [astro-ph].

[171] Andrew H. Jaffe and Donald C. Backer. "Gravitational waves probe the coalescence rate of massive black hole binaries". In: *Astrophys. J.* 583 (2003), pp. 616–631. DOI: 10.1086/345443. arXiv: astro-ph/0210148 [astro-ph].

[172] J. Stuart B. Wyithe and Abraham Loeb. "Low - frequency gravitational waves from massive black hole binaries: Predictions for LISA and pulsar timing arrays". In: *Astrophys. J.* 590 (2003), pp. 691–706. DOI: 10.1086/375187. arXiv: astro-ph/0211556 [astro-ph].

[173] Motohiro Enoki et al. "Gravitational waves from supermassive black hole coalescence in a hierarchical galaxy formation model". In: *Astrophys. J.* 615 (2004), p. 19. DOI: 10.1086/424475. arXiv: astro-ph/0404389 [astro-ph].

[174] Alberto Sesana et al. "Low-Frequency Gravitational Radiation from Coalescing Massive Black Hole Binaries in Hierarchical Cosmologies". In: *The Astrophysical Journal* 611.2 (2004), pp. 623–632. DOI: 10.1086/422185. URL: https://doi.org/10.1086%2F422185.

[175] A. Sesana et al. "The gravitational wave signal from massive black hole binaries and its contribution to the LISA data stream". In: *Astrophys. J.* 623 (2005), pp. 23–30. DOI: 10.1086/428492. arXiv: astro-ph/0409255 [astro-ph].

[176] Kirsty J. Rhook and J. Stuart B. Wyithe. "Realistic event rates for detection of supermassive black hole coalescence by LISA". In: *Monthly Notices of the Royal Astronomical Society* 361.4 (Aug. 2005), pp. 1145–1152. ISSN: 0035-8711. DOI: 10.1111/j.1365-2966.2005.08987.x. URL: https://dx.doi.org/10.1111/j.1365-2966.2005.08987.x.

[177] Enrico Barausse. "The evolution of massive black holes and their spins in their galactic hosts". In: *Monthly Notices of the Royal Astronomical Society* 423.3 (June 2012), pp. 2533–2557. ISSN: 0035-8711. DOI: 10.1111/j.1365-2966.2012.21057.x. URL: https://dx.doi.org/10.1111/j.1365-2966.2012.21057.x.

[178] Antoine Klein et al. "Science with the space-based interferometer eLISA: Supermassive black hole binaries". In: *Phys. Rev. D* 93 (2 2016), p. 024003. DOI: 10.1103/PhysRevD.93.024003. URL: https://link.aps.org/doi/10.1103/PhysRevD.93.024003.

[179] M. J. Rees and S. D. M. White. "Core condensation in heavy halos: a two-stage theory for galaxy formation and clustering". In: *Monthly Notices of the Royal Astronomical Society* 183.3 (July 1978), pp. 341–358. ISSN: 0035-8711. DOI: 10.1093/mnras/183.3.341. URL: https://dx.doi.org/10.1093/mnras/183.3.341.

[180] Martin Haehnelt and Guinevere Kauffmann. "A unified model for the evolution of galaxies and quasars". In: *Monthly Notices of the Royal Astronomical Society* 311.3 (Jan. 2000), pp. 576–588. ISSN: 0035-8711. DOI: 10.1046/j.1365-8711.2000.03077.x. URL: https://dx.doi.org/10.1046/j.1365-8711.2000.03077.x.

[181] Marta Volonteri, Francesco Haardt, and Piero Madau. "The Assembly and Merging History of Supermassive Black Holes in Hierarchical Models of Galaxy Formation". In: *The Astrophysical Journal* 582.2 (2003), pp. 559–573. DOI: 10.1086/344675. URL: https://doi.org/10.1086%2F344675.

[182] Alberto Sesana, Marta Volonteri, and Francesco Haardt. "The imprint of massive black hole formation models on the LISA data stream". In: *Monthly Notices of the Royal Astronomical Society* 377.4 (May 2007), pp. 1711–1716. ISSN: 0035-8711. DOI: 10.1111/j.1365-2966.2007.11734.x. URL: https://dx.doi.org/10.1111/j.1365-2966.2007.11734.x.

[183] Miroslav Micic et al. "Supermassive black hole growth and merger rates from cosmological N-body simulations". In: *Monthly Notices of the Royal Astronomical Society* 380.4 (Sept. 2007), pp. 1533–1540. ISSN: 0035-8711. DOI: 10.1111/j.1365-2966.2007.12162.x. URL: https://dx.doi.org/10.1111/j.1365-2966.2007.12162.x.

[184] Monica Colpi. "Massive Binary Black Holes in Galactic Nuclei and Their Path to Coalescence". In: *Space Science Reviews* 183.1-4 (2014), pp. 189–221. DOI: 10.1007/s11214-014-0067-1. arXiv: 1407.3102 [astro-ph.GA].

[185] S. Chandrasekhar. "Dynamical Friction. I. General Considerations: the Coefficient of Dynamical Friction." In: *The Astrophysical Journal* 97 (Mar. 1943), p. 255. DOI: 10.1086/144517.

[186] Matteo Bonetti et al. "Post-Newtonian evolution of massive black hole triplets in galactic nuclei – IV. Implications for LISA". In: *Monthly Notices of the Royal Astronomical Society* 486.3 (Mar. 2019), pp. 4044–4060. ISSN: 0035-8711. DOI: 10.1093/mnras/stz903. eprint: https://academic.oup.com/mnras/article-pdf/486/3/4044/28559349/stz903.pdf. URL: https://doi.org/10.1093/mnras/stz903.

[187] Alberto Sesana et al. "Reconstructing the massive black hole cosmic history through gravitational waves". In: *Phys. Rev. D* 83 (4 2011), p. 044036. DOI: 10.1103/PhysRevD.83.044036. URL: https://link.aps.org/doi/10.1103/PhysRevD.83.044036.

[188] Philip J. Armitage and Priyamvada Natarajan. "Accretion during the Merger of Supermassive Black Holes". In: *The Astrophysical Journal* 567.1 (2002), pp. L9–L12. DOI: 10.1086/339770. URL: https://doi.org/10.1086%2F339770.

[189] Milos Milosavljevic and E. S. Phinney. "The Afterglow of massive black hole coalescence". In: *Astrophys. J.* 622 (2005), pp. L93–L96. DOI: 10.1086/429618. arXiv: astro-ph/0410343 [astro-ph].

[190] Massimo Dotti et al. "On the search of electromagnetic cosmological counterparts to coalescences of massive black hole binaries". In: *Mon. Not. Roy. Astron. Soc.* 372 (2006), pp. 869–875. DOI: 10.1111/j.1365-2966.2006.10905.x. arXiv: astro-ph/0605624 [astro-ph].

[191] Bence Kocsis et al. "Finding the Electromagnetic Counterparts of Cosmological Standard Sirens". In: *The Astrophysical Journal* 637.1 (2006), pp. 27–37. DOI: 10.1086/498236. URL: https://doi.org/10.1086%2F498236.

[192] Yike Tang, Zoltán Haiman, and Andrew MacFadyen. "The late inspiral of supermassive black hole binaries with circumbinary gas discs in the LISA band". In: *Monthly Notices of the Royal Astronomical Society* 476.2 (Feb. 2018), pp. 2249–2257. ISSN: 0035-8711. DOI: 10.1093/mnras/sty423. URL: https://doi.org/10.1093/mnras/sty423.

[193] Stéphane d'Ascoli et al. "Electromagnetic Emission from Supermassive Binary Black Holes Approaching Merger". In: *The Astrophysical Journal* 865.2 (2018), p. 140. DOI: 10.3847/1538-4357/aad8b4. URL: https://doi.org/10.3847%2F1538-4357%2Faad8b4.

[194] Dennis B. Bowen et al. "Quasi-periodic Behavior of Mini-disks in Binary Black Holes Approaching Merger". In: *The Astrophysical Journal* 853.1 (2018), p. L17. DOI: 10.3847/2041-8213/aaa756. URL: https://doi.org/10.3847%2F2041-8213%2Faaa756.

[195] Tito Dal Canton et al. "Detectability of Modulated X-Rays from LISA's Supermassive Black Hole Mergers". In: *The Astrophysical Journal* 886.2 (2019), p. 146. DOI: 10.3847/1538-4357/ab505a. URL: https://doi.org/10.3847%2F1538-4357%2Fab505a.

[196] Sean McGee, Alberto Sesana, and Alberto Vecchio. "Linking gravitational waves and X-ray phenomena with joint LISA and Athena observations". In: *Nature Astronomy* 4 (Jan. 2020), pp. 26–31. DOI: 10.1038/s41550-019-0969-7. arXiv: 1811.00050 [astro-ph.HE].

[197] Bence Kocsis, Zoltán Haiman, and Kristen Menou. "Premerger Localization of Gravitational Wave Standard Sirens withLISA: Triggered Search for an Electromagnetic Counterpart". In: *The Astrophysical Journal* 684.2 (2008), pp. 870–887. DOI: 10.1086/590230. URL: https://doi.org/10.1086%2F590230.

[198] Kirpal Nandra et al. "The Hot and Energetic Universe: A White Paper presenting the science theme motivating the Athena+ mission". In: *arXiv e-prints*, arXiv:1306.2307 (June 2013), arXiv:1306.2307. arXiv: 1306.2307 [astro-ph.HE].

[199] Nicola Tamanini et al. "Science with the space-based interferometer eLISA. III: probing the expansion of the universe using gravitational wave standard sirens". In: *Journal of Cosmology and Astroparticle Physics* 2016.04 (2016), p. 002. URL: http://stacks.iop.org/1475-7516/2016/i=04/a=002.

[200] Zoltán Haiman. "Electromagnetic chirp of a compact binary black hole: A phase template for the gravitational wave inspiral". In: *Phys. Rev. D* 96 (2 2017), p. 023004. DOI: 10.1103/PhysRevD.96.023004. URL: https://link.aps.org/doi/10.1103/PhysRevD.96.023004.

[201] Curt Cutler. "Angular resolution of the LISA gravitational wave detector". In: *Phys. Rev. D* 57 (12 1998), pp. 7089–7102. DOI: 10.1103/PhysRevD.57.7089. URL: https://link.aps.org/doi/10.1103/PhysRevD.57.7089.

[202] Leor Barack and Curt Cutler. "LISA capture sources: Approximate waveforms, signal-to-noise ratios, and parameter estimation accuracy". In: *Phys. Rev. D* 69 (8 2004), p. 082005. DOI: 10.1103/PhysRevD.69.082005. URL: https://link.aps.org/doi/10.1103/PhysRevD.69.082005.

[203] Scott A. Hughes. "Untangling the merger history of massive black holes with LISA". In: *Monthly Notices of the Royal Astronomical Society* 331.3 (Apr. 2002), pp. 805–816. ISSN: 0035-8711. DOI: 10.1046/j.1365-8711.2002.05247.x. URL: https://doi.org/10.1046/j.1365-8711.2002.05247.x.

[204] Emanuele Berti, Alessandra Buonanno, and Clifford M. Will. "Estimating spinning binary parameters and testing alternative theories of gravity with LISA". In: *Phys. Rev. D* 71 (8 2005), p. 084025. DOI: 10.1103/PhysRevD.71.084025. URL: https://link.aps.org/doi/10.1103/PhysRevD.71.084025.

[205] Alberto Vecchio. "LISA observations of rapidly spinning massive black hole binary systems". In: *Phys. Rev. D* 70 (4 2004), p. 042001. DOI: 10.1103/PhysRevD.70.042001. URL: https://link.aps.org/doi/10.1103/PhysRevD.70.042001.

[206] K. G. Arun et al. "Higher signal harmonics, LISA's angular resolution, and dark energy". In: *Phys. Rev. D* 76 (10 2007), p. 104016. DOI: 10.1103/PhysRevD.76.104016. URL: https://link.aps.org/doi/10.1103/PhysRevD.76.104016.

[207] Ryan N. Lang and Scott A. Hughes. "Localizing Coalescing Massive Black Hole Binaries with Gravitational Waves". In: *The Astrophysical Journal* 677.2 (2008), pp. 1184–1200. DOI: 10.1086/528953. URL: https://doi.org/10.1086%2F528953.

[208] Miquel Trias and Alicia M. Sintes. "LISA observations of supermassive black holes: Parameter estimation using full post-Newtonian inspiral waveforms". In: *Phys. Rev. D* 77 (2 2008), p. 024030. DOI: 10.1103/PhysRevD.77.024030. URL: https://link.aps.org/doi/10.1103/PhysRevD.77.024030.

[209] Sean T. McWilliams et al. "Sky localization of complete inspiral-merger-ringdown signals for nonspinning massive black hole binaries". In: *Phys. Rev. D* 84 (6 2011), p. 064003. DOI: 10.1103/PhysRevD.84.064003. URL: https://link.aps.org/doi/10.1103/PhysRevD.84.064003.

[210] Vishal Baibhav, Emanuele Berti, and Vitor Cardoso. "LISA parameter estimation and source localization with higher harmonics of the ringdown". In: *arXiv e-prints*, arXiv:2001.10011 (Jan. 2020), arXiv:2001.10011. arXiv: 2001.10011 [gr-qc].

[211] Sylvain Marsat, John G. Baker, and Tito Dal Canton. "Exploring the Bayesian parameter estimation of binary black holes with LISA". In: (Feb. 2020). arXiv: 2003.00357 [gr-qc].

[212] J. Camp and Transient Astrophysics Probe Team 2018. "Transient Astrophysics Probe (TAP) Concept". In: *American Astronomical Society Meeting Abstracts, Vol.231, American Astronomical Society Meeting Abstracts 231, 121.05* (2018).

[213] K. M. Górski et al. "HEALPix: A Framework for High-Resolution Discretization and Fast Analysis of Data Distributed on the Sphere". In: *The Astrophysical Journal* 622.2 (Apr. 2005), pp. 759–771. DOI: 10.1086/427976. arXiv: astro-ph/0409513 [astro-ph].

[214] E. Lusso et al. "Bolometric luminosities and Eddington ratios of X-ray selected active galactic nuclei in the XMM-COSMOS survey". In: *Monthly Notices of the Royal Astronomical Society* 425.1 (Sept. 2012), pp. 623–640. DOI: 10.1111/j.1365-2966.2012.21513.x. arXiv: 1206.2642 [astro-ph.CO].

[215] A. Marconi et al. "Local supermassive black holes, relics of active galactic nuclei and the X-ray background". In: *Monthly Notices of the Royal Astronomical Society* 351.1 (June 2004), pp. 169–185. DOI: 10.1111/j.1365-2966.2004.07765.x. arXiv: astro-ph/0311619 [astro-ph].

[216] Benny Trakhtenbrot et al. "BAT AGN Spectroscopic Survey (BASS) – VI. The $\Gamma_X \breve{} L/L_{Edd}$ relation". In: *Monthly Notices of the Royal Astronomical Society* 470.1 (May 2017), pp. 800–814. ISSN: 0035-8711. DOI: 10.1093/mnras/stx1117. eprint: https://academic.oup.com/mnras/article-pdf/470/1/800/17872358/stx1117.pdf. URL: https://doi.org/10.1093/mnras/stx1117.

[217] Bernard J. Kelly et al. "Prompt electromagnetic transients from binary black hole mergers". In: *Phys. Rev. D* 96 (12 2017), p. 123003. DOI: 10.1103/PhysRevD.96.123003. URL: https://link.aps.org/doi/10.1103/PhysRevD.96.123003.

[218] Constanze Roedig, Julian H. Krolik, and M. Coleman Miller. "OBSERVATIONAL SIGNATURES OF BINARY SUPERMASSIVE BLACK HOLES". In: *The Astrophysical Journal* 785.2 (2014), p. 115. DOI: 10.1088/0004-

637x/785/2/115. URL: https://doi.org/10.1088%2F0004-637x%2F785%2F2%2F115.

[219] S. Paltani. "Searching for periods in X-ray observations using Kuiper's test. Application to the ROSAT PSPC archive". In: *Astronomy and Astrophysics* 420 (June 2004), pp. 789–797. DOI: 10.1051/0004-6361:20034220. arXiv: astro-ph/0403186 [astro-ph].

[220] M. Dotti et al. "Dual black holes in merger remnants – II. Spin evolution and gravitational recoil". In: *Monthly Notices of the Royal Astronomical Society* 402.1 (Feb. 2010), pp. 682–690. ISSN: 0035-8711. DOI: 10.1111/j.1365-2966.2009.15922.x. eprint: https://academic.oup.com/mnras/article-pdf/402/1/682/18587970/mnras0402-0682.pdf. URL: https://doi.org/10.1111/j.1365-2966.2009.15922.x.

[221] Alberto Mangiagli et al. "On the inspiral of coalescing massive black hole binaries with LISA in the era of Multi-Messenger Astrophysics". In: *arXiv e-prints*, arXiv:2006.12513 (June 2020), arXiv:2006.12513. arXiv: 2006.12513 [astro-ph.HE].

[222] Michele Armano et al. *LISA Pathfinder*. 2019. arXiv: 1903.08924 [astro-ph.IM].

[223] Neil J Cornish and Edward K Porter. "The search for massive black hole binaries with LISA". In: *Classical and Quantum Gravity* 24.23 (2007), pp. 5729–5755. DOI: 10.1088/0264-9381/24/23/001. URL: https://doi.org/10.1088%2F0264-9381%2F24%2F23%2F001.

[224] Edward K. Porter and Neil J. Cornish. "Fisher versus Bayes: A comparison of parameter estimation techniques for massive black hole binaries to high redshifts with eLISA". In: *Phys. Rev. D* 91 (10 2015), p. 104001. DOI: 10.1103/PhysRevD.91.104001. URL: https://link.aps.org/doi/10.1103/PhysRevD.91.104001.

[225] Travis Robson, Neil Cornish, and Chang Liu. "The construction and use of LISA sensitivity curves". In: (2018). arXiv: 1803.01944 [astro-ph.HE].

[226] Stanislav Babak et al. "Science with the space-based interferometer LISA. V. Extreme mass-ratio inspirals". In: *Phys. Rev. D* 95 (10 2017), p. 103012. DOI: 10.1103/PhysRevD.95.103012. URL: https://link.aps.org/doi/10.1103/PhysRevD.95.103012.

[227] LISA Science Study Team. "LISA science requirements document". In: *Technical Report ESA-L3-EST-SCI-RS-001. European Space Agency* (2018). URL: https://www.cosmos.esa.int/documents/678316/1700384/SciRD.pdf/25831f6b-3c01-e215-5916-4ac6e4b306fb?t=1526479841000.

[228] LISA Science Group. "Science questions and figures of merit affected by low-frequency sensitivity". LISA-LCST-XXX-TN-001, Unpublished.

[229] Lionel London et al. "First Higher-Multipole Model of Gravitational Waves from Spinning and Coalescing Black-Hole Binaries". In: *Phys. Rev. Lett.* 120 (16 2018), p. 161102. DOI: 10.1103/PhysRevLett.120.161102. URL: https://link.aps.org/doi/10.1103/PhysRevLett.120.161102.

[230] Ryan N. Lang and Scott A. Hughes. "Measuring coalescing massive binary black holes with gravitational waves: The impact of spin-induced precession". In: *Phys. Rev. D* 74 (12 2006), p. 122001. DOI: 10.1103/PhysRevD.74.122001. URL: https://link.aps.org/doi/10.1103/PhysRevD.74.122001.

[231] Justin Ellis and Rutger van Haasteren. *jellis18/PTMCMCSampler: Official Release*. Oct. 2017. DOI: 10.5281/zenodo.1037579. URL: https://doi.org/10.5281/zenodo.1037579.

[232] W. D. Vousden, W. M. Farr, and I. Mandel. "Dynamic temperature selection for parallel tempering in Markov chain Monte Carlo simulations". In: *Monthly Notices of the Royal Astronomical Society* 455.2 (Nov. 2015), pp. 1919–1937. ISSN: 0035-8711. DOI: 10.1093/mnras/stv2422. URL: https://doi.org/10.1093/mnras/stv2422.

[233] Michael L. Katz et al. "GPU-accelerated massive black hole binary parameter estimation with LISA". In: (May 2020). arXiv: 2005.01827 [gr-qc].

[234] Enrico Barausse. "The evolution of massive black holes and their spins in their galactic hosts". In: *Monthly Notices of the Royal Astronomical Society* 423.3 (June 2012), pp. 2533–2557. ISSN: 0035-8711. DOI: 10.1111/j.1365-2966.2012.21057.x. URL: https://doi.org/10.1111/j.1365-2966.2012.21057.x.

[235] Yun Wang, Daniel E. Holz, and Dipak Munshi. "A Universal Probability Distribution Function for Weak-lensing Amplification". In: *The Astrophysical Journal* 572.1 (2002), pp. L15–L18. DOI: 10.1086/341604. URL: https://doi.org/10.1086%2F341604.

[236] C. Shapiro et al. "Delensing gravitational wave standard sirens with shear and flexion maps". In: *Monthly Notices of the Royal Astronomical Society* 404.2 (May 2010), pp. 858–866. ISSN: 0035-8711. DOI: 10.1111/j.1365-2966.2010.16317.x. URL: https://doi.org/10.1111/j.1365-2966.2010.16317.x.

[237] William H. Press et al. *Numerical Recipes 3rd Edition: The Art of Scientific Computing*. 3rd ed. USA: Cambridge University Press, 2007. ISBN: 0521880688.

[238] James M. Bardeen and Jacobus A. Petterson. "The Lense-Thirring Effect and Accretion Disks around Kerr Black Holes". In: *Astrophys. J.* 195 (1975), p. L65. DOI: 10.1086/181711.

[239] A. R. King, J. E. Pringle, and J. A. Hofmann. "The evolution of black hole mass and spin in active galactic nuclei". In: *Monthly Notices of the Royal Astronomical Society* 385.3 (Apr. 2008), pp. 1621–1627. DOI: 10.1111/j.1365-2966.2008.12943.x. arXiv: 0801.1564 [astro-ph].

[240] Emanuele Berti and Marta Volonteri. "Cosmological Black Hole Spin Evolution by Mergers and Accretion". In: *The Astrophysical Journal* 684.2 (Sept. 2008), pp. 822–828. DOI: 10.1086/590379. arXiv: 0802.0025 [astro-ph].

[241] A. Perego et al. "Mass and spin co-evolution during the alignment of a black hole in a warped accretion disc". In: *Monthly Notices of the Royal Astronomical Society* 399.4 (Nov. 2009), pp. 2249–2263. DOI: 10.1111/j.1365-2966.2009.15427.x. arXiv: 0907.3742 [astro-ph.CO].

[242] M. Dotti et al. "On the Orientation and Magnitude of the Black Hole Spin in Galactic Nuclei". In: *The Astrophysical Journal* 762.2, 68 (Jan. 2013), p. 68. DOI: 10.1088/0004-637X/762/2/68. arXiv: 1211.4871 [astro-ph.CO].

[243] Tamara Bogdanović, Christopher S. Reynolds, and M. Coleman Miller. "Alignment of the Spins of Supermassive Black Holes Prior to Coalescence". In: *The Astrophysical Journal Letters* 661.2 (June 2007), pp. L147–L150. DOI: 10.1086/518769. arXiv: astro-ph/0703054 [astro-ph].

[244] Yohan Dubois, Marta Volonteri, and Joseph Silk. "Black hole evolution - III. Statistical properties of mass growth and spin evolution using large-scale hydrodynamical cosmological simulations". In: *Monthly Notices of the Royal Astronomical Society* 440.2 (May 2014), pp. 1590–1606. DOI: 10.1093/mnras/stu373. arXiv: 1304.4583 [astro-ph.CO].

[245] A. Sesana et al. "Linking the Spin Evolution of Massive Black Holes to Galaxy Kinematics". In: *The Astrophysical Journal* 794.2, 104 (Oct. 2014), p. 104. DOI: 10.1088/0004-637X/794/2/104. arXiv: 1402.7088 [astro-ph.CO].

[246] Davide Fiacconi, Debora Sijacki, and J. E. Pringle. "Galactic nuclei evolution with spinning black holes: method and implementation". In: *Monthly Notices of the Royal Astronomical Society* 477.3 (July 2018), pp. 3807–3835. DOI: 10.1093/mnras/sty893. arXiv: 1712.00023 [astro-ph.GA].

[247] P. E. Dewdney et al. "The Square Kilometre Array". In: *IEEE Proceedings* 97.8 (Aug. 2009), pp. 1482–1496. DOI: 10.1109/JPROC.2009.2021005.

[248] LSST Science Collaboration et al. "LSST Science Book, Version 2.0". In: *arXiv e-prints*, arXiv:0912.0201 (Dec. 2009), arXiv:0912.0201. arXiv: 0912.0201 [astro-ph.IM].

[249] A. Rau et al. "The Hot and Energetic Universe: The Wide Field Imager (WFI) for Athena+". In: *arXiv e-prints*, arXiv:1308.6785 (Aug. 2013), arXiv:1308.6785. arXiv: 1308.6785 [astro-ph.IM].

[250] C. Palenzuela, L. Lehner, and S. L. Liebling. "Dual Jets from Binary Black Holes". In: *Science* 329.5994 (Aug. 2010), pp. 927–930. DOI: 10.1126/science.1191766. arXiv: 1005.1067 [astro-ph.HE].

[251] Philip J. Armitage and Priyamvada Natarajan. "Accretion during the Merger of Supermassive Black Holes". In: *The Astrophysical Journal Letters* 567.1 (Mar. 2002), pp. L9–L12. DOI: 10.1086/339770. arXiv: astro-ph/0201318 [astro-ph].

[252] Z. Ivezic et al. "Large Synoptic Survey Telescope: From Science Drivers To Reference Design". In: *Serbian Astronomical Journal* 176 (June 2008), pp. 1–13. DOI: 10.2298/SAJ0876001I.

[253] B. F. Schutz. "Determining the Hubble constant from gravitational wave observations". In: *Nature* 323.6086 (1986), pp. 310–311. DOI: 10.1038/323310a0.

[254] Julian H. Krolik et al. "Population Estimates for Electromagnetically Distinguishable Supermassive Binary Black Holes". In: *The Astrophysical Journal* 879.2, 110 (July 2019), p. 110. DOI: 10.3847/1538-4357/ab24c9. arXiv: 1905.10450 [astro-ph.GA].

[255] Kelly D. Denney et al. "Systematic Uncertainties in Black Hole Masses Determined from Single-Epoch Spectra". In: *The Astrophysical Journal* 692.1 (Feb. 2009), pp. 246–264. DOI: 10.1088/0004-637X/692/1/246. arXiv: 0810.3234 [astro-ph].

[256] J. S. Speagle et al. "A Highly Consistent Framework for the Evolution of the Star-Forming "Main Sequence" from z ~0-6". In: *The Astrophysical Journal Supplement Series* 214.2, 15 (Oct. 2014), p. 15. DOI: 10.1088/0067-0049/214/2/15. arXiv: 1405.2041 [astro-ph.GA].

[257] C. Palenzuela, L. Lehner, and S. L. Liebling. "Dual Jets from Binary Black Holes". In: *Science* 329.5994 (Aug. 2010), pp. 927–930. DOI: 10.1126/science.1191766. arXiv: 1005.1067 [astro-ph.HE].

[258] Michael L Katz et al. "Probing massive black hole binary populations with LISA". In: *Monthly Notices of the Royal Astronomical Society* 491.2 (Nov. 2019), pp. 2301–2317. ISSN: 0035-8711. DOI: 10.1093/mnras/stz3102. URL: https://doi.org/10.1093/mnras/stz3102.

[259] Marta Volonteri et al. "Black hole mergers from dwarf to massive galaxies with the NewHorizon and Horizon-AGN simulations". In: (May 2020). arXiv: 2005.04902 [astro-ph.GA].

[260] Hai-Tian Wang et al. "Science with the TianQin observatory: Preliminary results on massive black hole binaries". In: *Phys. Rev. D* 100 (4 2019), p. 043003. DOI: 10.1103/PhysRevD.100.043003. URL: https://link.aps.org/doi/10.1103/PhysRevD.100.043003.

[261] Wen-Hong Ruan et al. "The LISA-Taiji network: precision localization of massive black hole binaries". In: (Sept. 2019). arXiv: 1909.07104 [gr-qc].